University of Alberta

A MEMS-based Fixed-Fixed Folded Spring Piezoelectric Energy Harvester

by

Jonathan Sierzant Lueke

A thesis submitted to the Faculty of Graduate Studies and Research
in partial fulfillment of the requirements for the degree of

Doctor of Philosophy

Department of Mechanical Engineering

© Jonathan Sierzant Lueke
Spring 2014
Edmonton, Alberta

Dedication

To my loving wife, Nicole: this work would have not been possible without your love, support and patience. I look forward to building our lives together and tackling the next challenge. I love you.

To my parents: without your support and guidance, this would not have been possible. Thank you for providing every opportunity to broaden my horizons and to strive for my goals.

To Jason and Marie; Nathaniel and Benjamin: Thank you for your support and showing me it is possible to balance ambitious goals and a family. In the years to come, I fully expect the boys to make our accomplishments look small.

To Papa: thank you for showing me that a life well lived is built around family and friends. Thank you for teaching me not to forget the good things in life - throwing the best parties, buying the best pants, and drinking the best alcohol. I wish I could have shared this achievement with you.

To Dr. Moussa: thank you for your patience, guidance and advice. It has not been an easy road - when others would have given up and let me fail, you dragged me along and pushed me towards success

To Dr. Lou: thank you for guiding me through the electrical portion of this project. Your knowledge and experience helped immensely.

To my supervisory committee, Dr. Toogood and Dr Carey: your guidance and advice throughout this project has been invaluable. Thank you for being a sounding board for ideas and reminding me that clarity and brevity are virtues. I tried to keep the thesis short – I really did! (*audible Dr. Toogood groan*).

To my Labmates: throughout this journey, I have had the pleasure of working alongside you for many years. Working with all of you has been a pleasure. I hope that I have had the opportunity to enrich your work as you have done mine. To those who have graduated before: Dr. Noor Al Quddus, Dr. Hossam Garib, Dr. David Benfield, and Dr. Ryan Saunders; thank you for your advice and support throughout the years – it has been invaluable. To Mehdi: I know we have not always agreed on the various issues/concepts with our work, however, I believe our discussions have made me a better researcher. Thank you for the debates and the hard questions. I wish you nothing but success. To Else: it has been a pleasure to work with you. Thank you for reminding me on multiple occasions to evaluate the problem as a while rather than jumping headlong into finding a solution. You may not know it – but you saved me a lot of headaches. To Alia, Gowini, and

Suzan, the three of you have always helped me to stay grounded and focused. Thank you for listening to many rants about fabrication problems and random testing issues. It is always comforting to have an attentive listener willing to help. To Shichao, although your journey with the group is relatively starting, thanks for reminding me about my own enthusiasm for my work. Remember, there is always a solution to a problem – work hard and you will find it.

To the Nanofab Staff: thank you for putting up with me over the years. From pushing boundaries, helping me to develop and diagnosing fabrication processes, to straight out destroying wetdecks, the fabrication of the harvesters would not have been possible without your help and support. To Dr. Eric Flaim, Les Schowalter, Stephanie Bozic, Scott Munro, Keith Franklin, and Melissa Hawrelechko – thank you for helping me turn my ideas into a physical reality.

To Rick Conrad: I would have not been able to make sense of the "electrical voodoo" without your help. Designing a circuit is one thing, building it is another story. Thank you for showing me how to turn a circuit diagram into a physical component and answering so many confused, silly questions.

To Jon Clark: Thanks for all the trips for coffee and random chats about how to keep my computers operational. I still mourn the slow death of the motivational Corgi poster.

To Mike Poznanski: You have been standing by me for almost my entire life, supporting me in whatever endeavour I set upon. I honestly have no clue where I would be right now if it was not for your wise opinions and support. I hope I can repay the favor someday.

To Joe Balaneski: Hi. Now you can call me Dr. Jibbs, like you have been threatening for several years.

To the furballs Dexter and Burnie, and Odin the Gecko: thank you for listening to all my complaining and reminding me there is more to life than research.

Abstract

Energy harvesting is an important developing field in Microelectromechanical Systems (MEMS) research. In this thesis, a fixed-fixed folded spring-based harvester is presented as an alternative mechanical element for beam-based piezoelectric harvesters to reduce its natural frequency for low frequency applications (30-300 Hz). The research focused on decreasing the natural frequency of the harvester through mechanical stiffness reduction, which leads to an increase in output power. Two classes of folded spring-based energy harvesters were produced in order to characterize the frequency response of the folded spring harvesters - single folded spring harvesters and harvesters consisting of arrays of folded springs and proof masses. The critical parameters of the folded spring harvester were identified: the length of the individual beam elements and the thickness of the folded spring. Through the manipulation of these parameters, it was found that the fixed-fixed folded spring geometry allowed for a large increase of beam length, reducing the natural frequency of the structure without generating significant length-enhanced residual stress stiffening. Additionally, the folded spring structure increased the quasi-linear stiffness range of the harvester, allowing for the correct match of load resistance without potential drift and losses due to non-linear spring stiffening.

To experimentally test the energy harvesters, a microfabrication process flow was developed to produce the piezoelectric harvesters with the chosen materials and cross section. This process flow, combined with the folded spring methodology, resulted in several publications and a US Patent Application (Serial No.

14/032,018). Packaging and testing methodologies were developed in order to allow the harvesters to be tested under a base excitation. The frequency reduction methodology applied to the harvester allowed for wide frequency range of input vibration to be captured by the harvesters, ranging from 45 to 3667 Hz. The maximum power harvested by a single harvester was 690.50 nW at 226.25 Hz, with a PZT layer thickness of 0.24 μm. The natural frequency reduction methodology presented in this thesis can be applied to any MEMS-based energy harvesting scheme that requires high amplitude, low frequency, out of plane displacement to maximize the energy harvested.

Acknowledgements

Table of Contents

List of Tables

List of Figures

1 Chapter 1: Introduction

1.1 Motivation

Microelectromechanical Systems (MEMS)-based sensors are gaining popularity for a variety of applications due to their small size, low power consumption, and high integratability into microelectronic systems. Generally MEMS devices have one, if not all, of their major dimensions in the micrometer range, many being not much bigger than a few tens of cubic millimeters when packaged. For biomedical and implantable applications, MEMS-based devices can be used in a multitude of roles such as sensing physical loads on joints and implants, vital signs, measuring bone density, evaluating osseointegration, enabling targeted drug delivery and diagnosis through lab-on-a-chip devices [1]. MEMS are typically attractive for biomedical applications due to their scale – they are less invasive to implant than larger macro-scale sensors, allowing for use in a variety of locations in the body where macro-scale devices may not be suitable [2]. MEMS-based devices are additionally used in a variety of applications such as accelerometers for commercial products and motor vehicles, stress/strain measurement for structural health monitoring for bridges and large equipment, and various optical applications such as micromirrors [2]. In general, these MEMS-based devices have very low power consumption, when coupled with active power management, such as sleep/standby modes, can allow for MEMS-based sensors to operate for long periods of time across all applications.

Energy harvesting is an important developing field in MEMS research. Energy harvesting can allow for the augmentation and improvement of traditional power schemes, such as batteries, for wireless MEMS-based sensors and devices. Long term MEMS-based biomedical applications, such as permanent implants instrumented with MEMS sensors for various applications are an especially attractive application for energy harvesting. The ability to supplement or replace the power supply of a MEMS-based medical implant would not only increase the battery lifespan of the device, but increase the level of patient care. For wireless MEMS-based sensors, an energy harvester could allow for the sensor to operate

autonomously, with little or no outside support. This could be very important for wireless sensing systems such as weather stations or structural health monitoring in remote/dangerous locations. Additionally, MEMS-based energy harvesting technologies could be extended to consumer and personal electronics to augment and lengthen the lifespan of current battery technology.

There are a variety of energy harvesting methods available including photovoltaic, micro fuel cells, thermoelectric, electromagnetic, electrostatic, and piezoelectric methods [1,3-6]. Typically, vibration-based schemes, such as piezoelectric energy harvesters are more universal in application than the other methods of energy harvesting [1,3,7]. Piezoelectric energy harvesting converts ambient vibrational energy into electricity via the piezoelectric effect [5,8]. Since piezoelectric energy harvesting can produce high power output at low operational frequencies (>300 Hz), piezoelectric energy harvesting is an attractive technology for a variety of biomedical and consumer electronics applications [2,9]. Therefore, it is critical to optimize the dynamics of the piezoelectric MEMS-based harvesters to reduce natural frequency and increase output power to meet these applications.

It has been shown [5,10] that the performance of piezoelectric energy harvesters is directly tied to the dynamic performance of the structural element used in the device. First, the operational frequency of the energy harvester should match the first natural frequency of the mechanical element of the energy harvester. This ensures that the maximum deflection and strain on the piezoelectric film is achieved at the operational frequency. Second, the natural frequency of the energy harvester should be as low as possible [5,10]. The lower the natural frequency, the more likely the structure of the energy harvester will be actuated by ambient vibrations present *in-situ*. Additionally, displacements and strains applied to the films at lower frequency will be higher magnitude, allowing for higher voltage and power output. Therefore, the most important parameters of the piezoelectric energy harvester are the natural/operational frequency and the strain applied to the piezoelectric elements produced through beam bending.

The motivation in studying the dynamics of the MEMS-based piezoelectric energy harvesters was to provide a suitable mechanical alternative to cantilever-based harvesting systems. The work in this thesis focuses on an alternative mechanical spring element to cantilever based systems, in order to reduce the natural frequency of the harvester, to reduce the negative stiffening effects of fabrication created residual stresses, and to allow for complex array systems of harvesting elements to increase the overall power generation.

1.2 Proposed Approach

In literature, cantilever-based energy harvesters are the most common piezoelectric energy harvesters due to their well known dynamics, ease of optimization, and ease of fabrication [5,10-12]. The typical methods of optimizing the natural frequency of the cantilever beam-based harvester are reducing the mechanical stiffness of the harvester and adding mass to the system. To reduce the stiffness of the cantilever beam, the most common method is to increase the length of the beam. Fabrication-based residual stresses in cantilever systems relax through an out of plane curling of the beam. At increased beam lengths, this out of plane curling increases, adding additional mechanical stiffness to the system hindering the attempt at frequency reduction. An alternative structure, known as a folded beam, is suggested in this thesis as an alternative to the cantilever based systems, allowing for a high degree of customization, natural frequency reduction and strain optimization, while providing insensitivity to fabrication-based residual stress stiffening.

The folding of the spring allows for the increase of the effective length of the beam that experiences bending under vibration. This allows for an efficient reduction of natural frequency while not greatly increasing device footprint. Additionally, the fixed-fixed beam configuration used in this thesis allows for the unhindered expansion or contraction of each individual beam member to release residual stresses [13-15]. The suspended proof masses used in the second generation of energy harvesters studied in this thesis are allowed to rotate freely, preventing residual stresses from developing [13-15].

To study the proposed structural changes a variety of designs of folded spring energy harvester, using the same fabrication and testing methodology, will be produced. The first class of devices focuses upon the folded springs that have been postulated to be a replacement elastic member for piezoelectric energy harvesters. These are proof-of-concept devices that will allow for the development of a universal microfabrication process for PZT-based energy harvesters and proof of design concept. Through the development of the Class I Harvesters, the fabrication process, needed fabrication equipment, testing methodology, and packaging scheme will be developed. The important geometric parameters of the folded spring harvester will be determined, allowing for design rules and a greater understanding to be applied to the second class of harvester. It is expected that these devices will have a higher natural frequency and lower power output than both the Class II harvesters and goal outputs.

The Class II Harvesters are composed of arrays of masses and folded spring energy harvesters that have a target operational/natural frequency of 30-300Hz, and power output goals of tens to hundreds of microwatts. In addition to the decrease of natural frequency and increase of power output through arrays of harvesters, it is possible to examine the benefits of parallel and series arrays of springs on both the frequency response and power output. The simulation, fabrication, and testing /characterization methodologies that were developed with the previous class of devices are applied to this class of energy harvester.

1.3 Research Objectives

The research in this thesis has a number of objectives, including the following:

- Apply a fixed-fixed folded spring as the mechanical element of the energy harvester to reduce the natural frequency. This allows for a reduction of natural frequency of the harvester without the residual stress based stiffening issues encountered in natural frequency reduction of cantilever-based systems.

4

- Identify the critical design parameters of the fixed-fixed folded spring. Manipulate these parameters to reduce the natural frequency of the structure while maintaining mechanical stability.
- Determine if the fixed-fixed folded spring increases the linear stiffness range of the harvester. If the harvester behaves non-linearly, the natural frequency of the harvester may drift. This is important for matching the load resistance of the conditioning circuit to the input impedance of the harvester for maximum power transfer.
- Use arrays of folded springs in parallel and series configurations to allow for the balancing of natural frequency and mechanical stability. This will allow the energy harvester to be optimized to a variety of applications.
- Develop a robust and universal silicon-based microfabrication procedure. The fabrication flow must be capable of fabricating harvesters of any planar design, with or without seismic masses, with multiple piezoelectric materials and related electrode materials. Develop any required microfabrication processes or equipment needed to facilitate the research.
- Develop a research-based packaging scheme for the energy harvesters to allow for characterization under a base excitation.

1.4 Thesis Outline

The entire thesis outlines the motivation, methodology, theory, and experimental work undertaken to study the application of the fixed-fixed folded spring geometry to the mechanical spring elements of the piezoelectric MEMS-based energy harvester. The thesis is divided into eight chapters, according to Figure 1.1.

```
                    ┌─────────────────────────────┐
                    │  Chapter 1 - Introduction   │
                    └─────────────────────────────┘
                    ┌─────────────────────────────┐
                    │ Chapter 2 - Literature Review│
                    └─────────────────────────────┘
                    ┌─────────────────────────────┐
                    │  Chapter 3 - Design and     │
                    │       Methodology           │
                    └─────────────────────────────┘
  Design Considerations ┌──────────────────────────┐
  From Microfabrication │ Chapter 4 - Microfabrication│
  Constraints/Procedures│   Process and Development │
                        └──────────────────────────┘
                    ┌─────────────────────────────┐
                    │ Chapter 5 - Packaging and    │  Simulations of Designs for
                    │     Testing Methodology      │  Comparison with
                    └─────────────────────────────┘  Experimental Results
                    ┌─────────────────────────────┐
                    │ Chapter 6 - Results and      │
                    │ Discussion of Class I Harvesters│
                    └─────────────────────────────┘
  Testing Results   ┌─────────────────────────────┐
  Influencing Design│ Chapter 7 - Results and      │
  of Class II Harvesters│ Discussion of Class II Harvesters│
                    └─────────────────────────────┘
                    ┌─────────────────────────────┐
                    │  Chapter 8 - Conclusions    │
                    └─────────────────────────────┘
```

Figure 1.1 – A schematic representation of the interdependencies of the Thesis Chapters. Major dependencies between the chapters are shown.

Chapter 1 is a brief explanation of the study, an overview of the motivation of the research, an overview of the research undertaken in the thesis and the methodology undertaken. Chapter 2 is a literature review of the field of piezoelectric energy harvesting, highlighting key results relevant to this work. The challenges in the field that this research hopes to address are identified and highlighted. Chapter 3 is a discussion of the theory behind beam based energy harvesting and the methodology undertaken to study the folded spring geometry. This includes a detailed discussion of cantilever and folded spring energy harvesting including the motivation of using the folded spring geometry. The design methodology used in the study will be explored in detail. Chapter 4 is an outline of the microfabrication process that was developed for this study. The fabrication technologies, required equipment developed to enable the fabrication, and the entire fabrication process flow of the harvesters will be discussed at length. Chapter 5 is a review of the packaging and testing methods available and a discussion of the specific methods developed and adapted for use in this research.

The specific packaging scheme developed allows for the full in-situ characterization of the harvesters in a variety of typical electronics packaging situations. The testing methodology includes both the mechanical and electrical testing methodologies that allow for the full characterization of the harvesters. Chapters 6 and 7 are the results and discussion of the characterization for both the Class I and Class II harvesters respectively. Chapter 8 is a summary of conclusions derived from the entirety of the work.

As shown in Figure 1.1, the simulation work undertaken to design the classes of harvesters in Chapter 3 is used for comparison in Chapters 6 and 7 of the simulated and experimental results. Additionally, the characterization of the microfabrication processes helps diagnose problems with the fabrication process in Chapter 4 and provided design constraints for Chapter 3. The characterization of the Class I Harvesters in Chapters 6 allowed for the design of the Class II Harvesters to proceed in Chapter 3. The interdependencies of the chapters allowed for the fluid development of functioning, frequency optimized energy harvesters. Before the development of the fixed-fixed folded spring-based energy harvesters could begin, the field of energy harvesting had to be examined, as discussed in the following chapter.

1.5   References:

[1]   J. Lueke and W. A. Moussa, "MEMS-Based Power Generation Techniques for Implantable Biosensing Applications," *Sensors,* vol. 11, pp. 1433-1460, 2011.

[2]   N. E. DuToit, B. L. Wardle, and S. G. Kim, "Design considerations for MEMS-scale piezoelectric mechanical vibration energy harvesters," in *Integrated Ferroelectrics*, Cancun, 2005, pp. 121-160.

[3]   K. A. Cook-Chennault, N. Thambi, and A. M. Sastry, "Powering MEMS portable devices - a review of non-regenerative and regenerative power supply systems with special emphasis on piezoelectric energy harvesting systems," *Smart Materials & Structures,* vol. 17, p. 33, Aug 2008.

[4]   S. P. Beeby, M. J. Tudor, and N. M. White, "Energy harvesting vibration sources for microsystems applications," *Measurement Science & Technology,* vol. 17, pp. R175-R195, Dec 2006.

[5]   S. Roundy and P. K. Wright, "A piezoelectric vibration based generator for wireless electronics," *Smart Materials and Structures,* vol. 13, pp. 1131-1142, 2004.

[6]   H. A. Sodano, G. Park, D. J. Leo, and D. J. Inman, "Use of piezoelectric energy harvesting devices for charging batteries," San Diego, CA, United states, 2003, pp. 101-108.

[7]   B.-S. Lee, P.-J. Shih, J.-J. He, W.-P. Shih, and W.-J. Wu, "A study of implantable power harvesting transducers," in *Proceedings of SPIE - The International Society for Optical Engineering*, San Diego, CA, United states, 2007, pp. SPIE; American Society of Mechanical Engineers, ASME.

[8]   F. Lu, H. P. Lee, and S. P. Lim, "Modeling and analysis of micro piezoelectric power generators for micro-electromechanical-systems applications," *Smart Materials & Structures,* vol. 13, pp. 57-63, FEB 2004.

[9]   Y. Rao, S. Cheng, and D. P. Arnold, "An energy harvesting system for passively generating power from human activities," *Journal of Micromechanics and Microengineering,* vol. 23, p. 114012, 2013.

[10]   S. Roundy, E. S. Leland, J. Baker, E. Carleton, E. Reilly, E. Lai, B. Otis, J. M. Rabaey, P. K. Wright, and V. Sundararajan, "Improving power output for vibration-based energy scavengers," *Ieee Pervasive Computing,* vol. 4, pp. 28-36, 2005.

[11]   S. Roundy, P. K. Wright, and K. S. J. Pister, "Micro-Electrostatic Vibration-to-Electricity Converters," in *ASME International Mechanical Engineering Congress and Exposition*, 2002.

[12]   R. Elfrink, T. M. Kamel, M. Goedbloed, S. Matova, D. Hohlfeld, Y. Van Andel, and R. Van Schaijk, "Vibration energy harvesting with aluminum nitride-based piezoelectric devices," *Journal of Micromechanics and Microengineering,* vol. 19, 2009.

[13]   K. B. Lee, "Statics," in *Principles of Microelectromechanical Systems*: John Wiley & Sons, Inc., pp. 64-143.

[14]   K. B. Lee, "Static Behavior of Microstructures," in *Principles of Microelectromechanical Systems*: John Wiley & Sons, Inc., pp. 144-234.

[15]   K. B. Lee, "Dynamics," in *Principles of Microelectromechanical Systems*: John Wiley & Sons, Inc., pp. 235-324.

2   Chapter 2: Background and Literature Review

2.1   Introduction

Energy harvesting is an attractive technology for a variety of applications, including consumer electronics, military applications, and implantable biosensing. Microelectromechanical (MEMS)-based generation techniques can allow for the autonomous operation of implantable biosensors by generating electrical power to replace or supplement existing battery-based power systems. By supplementing existing battery-based power systems for implantable biosensors, the operational lifetime of the sensor can be increased. In addition, the potential for a greater amount of available power allows additional components to be added to the sensing module, such as computational and wireless and components, improving functionality and performance of the sensor. The main methods of energy harvesting that are applicable for biosensing applications are photovoltaic, thermovoltaic, micro fuel cell, electrostatic, electromagnetic, and piezoelectric based generation schemes. MEMS-based generation techniques that harvest ambient energy, such as vibration, are much better suited for implantable biosensing applications than fuel-based approaches, producing up to milliwatts of electrical power. High power density MEMS-based approaches, such as piezoelectric and electromagnetic schemes, allow for supplemental and replacement power schemes for biosensing applications to improve device capabilities and performance. In addition, this may allow for the biosensor to be further miniaturized, reducing the need for relatively large batteries with respect to device size. This would cause the implanted biosensor to be less invasive, increasing the quality of care received by the patient.

Conventional and thin-film batteries are the most common power source for MEMS-based wireless sensors. Normally, the battery system is the limiting factor to the lifespan and applicability of many microbiosensors. Although some biocompatible batteries may have long life spans, the battery will eventually

require replacement or recharging. For short term applications, a battery may provide a sufficient device lifespan, but for long term or high duty cycle applications, alternative power schemes may be preferable to replacing dead batteries, especially if the replacement/recharge procedure is invasive. For example, pacemakers are a common implantable system that requires an independent power source that functions completely autonomously from the outside world. The current standard for pacemaker operation is to utilize a high-life battery that supplies approximately 0.65 to 2.8 Ampere hours for 5.1 to 9 years [1]. Eventually, the battery for this system will need to be replaced, requiring surgery. Although a pacemaker is not necessarily a biosensing device, or a MEMS scale device, the power supply has been augmented by an electromagnetic-based MEMS generator. Roberts *et al.* [2] developed a system by which an electromagnetic MEMS-based generator captures the vibrational energy produced by the heart muscle to generate power to supplement the pacemaker's internal battery. In initial clinical trials, it was possible to produce up to 17% of the energy required to operate a conventional pacemaker [2]. Further development of this technology may be able to eliminate the costly and invasive surgeries required to maintain the pacemaker, both decreasing medical cost and improving the quality of care for the patient. A direct analogy can be drawn to the possible applications of this strategy to implantable biosensing. Any number of implantable biosensing platforms could have their power systems replaced or augmented by MEMS-based power generators. The addition of MEMS-based generators to the conventional power systems of these sensors would allow for increased lifespan and the ability to add components to the sensing platform that may have been too energy-costly to initially add to the system. Additional hardware could also be integrated into these sensing packages, allowing for wireless communications and on-board computing to further increase the functionality and usefulness of said MEMS-based implantable sensors.

Although micro scale power generation has many forms, the same general operational principles are used as in macro scale power generation—a specific form of energy is converted into electricity via a specific physical phenomenon.

The major difference between micro and macro scale power generation is the scale at which the generation takes place. As you decrease the size of a device into the micro regime; the relative strengths of all physical forces change. For example, highly length-dependant forces, such as electrostatic forces, become increasingly dominant over gravity. Therefore, the MEMS devices are more likely to be influenced by what would be considered to be ambient forces on a macro scale. Ambient forces and energy are non-negligible for MEMS devices, and in some cases, this ambient energy can be harvested to produce electricity.

To examine the field of energy harvesting, the general types of energy harvesting will be explored, including solar harvesting, thermoelectric harvesting, micro fuel cells, and vibration-based energy harvesting. The vibration-based techniques will be examined in detail, including electrostatic, electromagnetic, and piezoelectric harvesting. Since piezoelectric harvesting is the focus of this research, the methods of piezoelectric harvesting will be further discussed.

Solar harvesting is the most common technique of energy harvesting, converting ambient light into electricity using photovoltaic cells [3-14]. Ambient thermal energy can be converted into electricity using thermoelectric harvesting [15-23]. In addition to harvesting techniques, chemistry-based techniques, such as micro fuel cells [9,24-36] can be used to supplement battery-based power schemes. Micro fuel cells use a variety of electrochemical reactions to produce electricity. Some micro fuel cells can regenerate their fuel and oxidation agents through the electrochemical reactions that take place within the fuel cell allowing for long term operation [9,24-36]. Vibration driven techniques have good energy densities and have good versatility depending upon the conversion physics involved. Electrostatic generation has a high energy density, and many specific different methods/arrangements that allow for generation [12,37-47]. Electromagnetic generation, although robust to off-axis non-ideal actuation, requires a large displacement to produce a meaningful amount of power [2,48-59]. Piezoelectric vibration has high energy density at comparatively low displacement in comparison to the other generation physics [60-86]

11

2.2 Methods of Energy Harvesting

2.2.1 *Photovoltaic Generation*

Photovoltaic cells are the most recognizable energy harvesting technique currently in use, both in small and large scale applications, ranging from hand-held calculators to commercially generated electricity. MEMS-based solar cells are based upon electronic asymmetry, such as a p-n junction, found in semiconductors. As this electrical asymmetry is excited, incident photons cause electron hole pairs to form, promoting local electron mobility. If connected to a load, free electrons will flow through the load and then back to the solar cell, where vacant electron holes are located [10]. In order for photovoltaic cells to be efficient they must be placed in direct, bright sunlight. Without direct, high intensity light, the generating capacity of a photovoltaic cell can diminish significantly from 15 mW/cm^2 in direct sunlight to 10 μW/cm^2 in normal office lighting [12]. Photovoltaic cell materials need to be carefully chosen, since the measured output power can vary over three orders of magnitude at low illumination levels [4]. MEMS-based solar cells can be fabricated from a variety of materials, including single crystal silicon, thin film polysilicon, gallium arsenide, cadmium telluride, hydrogenated amorphous silicon and ferroelectric films such as lead lanthanum zirconate titanate (PLZT) [3,8,10]. These materials are chosen due to their suitable semiconductor band gaps of 1.4–1.6 eV [10]. Solar cells using hydrogenated amorphous silicon, such as those developed by Lee *et al.* [10] produce a usable amount of electrical power, due to the large band gap (1.55 eV) present in the specific silicon. This solar cell can produce open circuit voltages of 1.5 V per cell in series and short circuit current of 0.28 μA per cell.

Indium gallium arsenide photocells have been developed for use in fiber optic networks to power optical switches and controllers far down-cable. The integration of this harvester with the fibre optic cable may provide the required high intensity light to be directly channeled to the photocell, removing the requirement for direct, ambient light. High efficiency photodiodes are available

for this application [5-7,13] which convert the long wavelength light (1,300–1,550 nm) into electricity. These photodiodes are highly efficient, however, the voltage available from these relatively small band gap diodes is too small for many switching and controlling applications. Dentai *et al.* connected 30 diode segments in a favorable configuration in order to increase the overall electricity generation from approximately 1 V to 10.5 V at 500 µW, converting 1,554 nm incident light [6]. The photodiodes are arranged in complete circle of 30 pie-shaped photodiodes. This arrangement allows for increased conversion area, reduction of contact resistance, the ability to use anti-reflection coatings on the incident surface of the photodiode, and the ability to metalize the backside of the photodiode to allow unconverted light to have a second pass through the photodiode [6]. Similar photovoltaic cells fabricated from gallium arsenide have generated upwards of 1 W of electrical power using concentrated incident light as a power source [11].

Solar-based schemes also can use photosynthesis as the driving force behind energy harvesting in a hybrid photoelectric fuel cell [9]. In this fuel cell, sub-cellular thylakoid photosystems, isolated from spinach cells, provide the chemical reactions necessary to generate electricity. During photosynthesis, water is split to produce protons (H^+) and electrons which are both collected by the anode of the cell. The current from the anode drives the connected device and then is returned to the cell through the cathode, either reducing O_2 or regenerating the ferricyanide used in the cell as charge carriers. This process not only produces electricity for use in a device, but regenerates the chemical reagents used in the initial reaction. This photo-driven fuel cell can produce power densities of up to 5.4 pW/cm^2 [9]. For biological applications the photosynthesis-based micro fuel cell is attractive for its biocompatibility, having no bio-incompatible fuels or chemical reactions.

2.2.2 *Thermoelectric Energy Harvesting*

Direct thermoelectric energy harvesters utilize the Seebeck Effect to generate electricity. The Seebeck Effect is the direct conversion of a temperature

difference between a material pair junction into an electrical potential [16,17]. Thermoelectric energy harvesters composed of aluminum, n-poly-Si, p-$Bi_{0.5}Sb_{1.5}T_3$, and n-$Bi_{0.87}Sb_{0.13}$ thermocouples were developed by Huegsen, Woias, and Kockmann [16,17]. In this case, thin film thermocouples of the above composition were fabricated and then connected in series to form thermopiles. In order to maximize the power generation of the thermoelectric generator, a large thermal contact area is required. To allow for a large thermal contact area, the heat flow path is guided by thermal connectors to be perpendicular to the surface of the thermopiles. This method shapes the thermal profile of the thermopile, allowing for 95% of the entire temperature difference to be located between the two thermopile junctions, maximizing the total heat that can be used in conversion. Power factors as high as 3.63×10^{-3} W/mm^{2}K^2 and 8.14×10^{-3} W/mm^{2}K^2 can be achieved through this method [16,17]. As long as heat energy is available to the energy harvester, energy conversion will continue without interruption. The maximum energy that could be converted from thermal to electric energy is determined by the Carnot efficiency of the generating situation [20]. Since the efficiency of the thermal-to-electricity conversion is limited by the Carnot efficiency, small thermal gradients will not be efficient in producing electricity. For thermopile arrays, it has been reported for temperature differences of 180 °C (200–20 °C) the efficiency of the thermopile array is 10%. In comparison for a temperature difference of 20 °C (40–20 °C), the same thermopile array has an efficiency of 1% [20,21].

Thermoelectric harvesters, using the human body as a heat source, have been explored by Leonov *et al.* [18]. With a wide range of tissues and fluids having their own unique material and thermal properties, the human body has an inherent non-uniform temperature distribution. Thermal profiles in different regions of the body may vary due to proximity to blood vessels and function of surrounding tissues and organs. Areas such as wrists and ankles will be considerably warmer due to the proximity of major blood vessels to the skin and the external environment, therefore, it is advantageous to strategically place thermoelectric generators in these locations to maximize generation [18]. The

energy harvester itself is a microfabricated array of polysilicon-germanium (poly-SiGe) thermocouples, which are sandwiched between two silicon wafers and interconnected in series to form thermopiles. The energy harvester was integrated into a wrist-mounted package approximately $3 \times 3 \times 1$ cm^3 in size, in order to allow for heat absorption directly from the radial artery of the wrist [18]. These poly-SiGe thermopiles can produce upwards of 4.5 µW/cm^2 of power on the radial artery [18]. This location was chosen since it has the maximum temperature difference between the body and the outside environment, thus maximizing generation. A second thermoelectric generator was produced with commercially available BiTe thermopiles that were developed for the same application, for comparison, using a similar wrist mounted package. Poly-SiGe thermopiles are a more cost effective and mature technology in comparison to the BiTe thermopiles. However, the BiTe thermocouple-based thermoelectric generator was able to produce on average 100 µW of power, which was then stored in 2 NiMH batteries. The BiTe energy harvester was composed of 128 BiTe thermocouples, forming 48 thermopiles, taking a volume of $8.2 \times 8.9 \times 2.4$ mm^3 [18]. In comparison, the BiTe-based thermoelectric generator produced a power density of approximately 571 µW/cm^2, in comparison to the poly-SiGe thermoelectric generator that produced 4.5 µW/cm^2. The volume savings of using a more effective thermocouple is significant in this case. The BiTe-based thermoharvester produced a much higher power density with a much smaller device. This technology has been adapted for wrist watches, and is currently being used by multiple commercial watch companies in thermo-electrically driven watches. It has been reported that up to ten similar thermoelectric modules as the above are used to produce the required electricity to power these watches [20].

In addition to direct thermoelectric conversion, there has been work dedicated to the conversion of heat to electricity using a thermally driven actuator [22]. To achieve out of plane displacement, two similarly shaped cantilever beams are fabricated one on top of the other. The top beam is approximately 25% thinner than the bottom beam. When connected to each other at their respective free ends forming a U-shape, the thermal expansion of these cantilever beams becomes

linked. Therefore, as this structure is heated, asymmetric thermal expansion between the two connected beams allows for the U-shaped structure to actuate out of plane. To achieve in plane actuation, cantilever beams are connected perpendicularly to an actuator. The beams are constrained versus axial thermal expansion. When heated, these beams will expand, and eventually will start to buckle. This symmetric thermal expansion and buckling will actuate the central beam in-plane [22]. In addition, rotary motors, including Brayton Cycle micro-gas turbine engines [19] and Otto Cycle based heat engines [15], can be used to produce harvestable rotation from hydrocarbons on a micro scale. For example, the linear actuation schemes can be used to actuate electrostatic, electromagnetic, and piezoelectric based generation schemes. The rotary actuation schemes can be used to actuate rotary electromagnetic MEMS-based generation schemes.

Thermoelectric generation also entails the use of heat engines to produce electricity on a micro scale. Heat engines, such as the P^3 micro heat engine developed by Whalen *et al.* [23] can convert hydrocarbon fuels to electricity on a micro scale. The P^3 heat engine is comprised of two major systems: a combustion chamber and a two-phase working fluid. The heat supplied by the combustion chamber to the two-phase working fluid causes the fluid to expand and apply pressure to a piezoelectric membrane. The piezoelectric membrane converts the applied mechanical strain into electricity via the piezoelectric effect. The heat engine has a four phase working cycle: compression, isothermal high temperature heat addition, expansion, and isothermal low temperature heat rejection. The piezoelectric membrane is deflected during the compression and expansion phases experienced by the two-phase working fluid. For characterization, a resistance heater was used to provide the thermal energy required in order to actuate the piezoelectric membrane. The resistance heater was operated using a square wave, with a 1 ms pulse width, at voltage amplitude of 3.2 V. The resistance heater, having a resistance of 1.7 Ω, delivered 1.45 W of thermal energy to the working fluid. The piezoelectric membrane produced a voltage varying between 63 and 135 mV at a frequency of 240 Hz. With a load resistance of 14 kΩ, the P^3 heat engine produced 0.8 μW at these conditions.

2.2.3 Micro-Fuel Cells

Micro fuel cells produce electricity by harvesting electrons from controlled electrochemical reactions. Depending upon the fuel and oxidizing agents reacting in the micro fuel cell, it can be considered either a regenerative or non-regenerative generation technique. If the electrochemical reactions that take place are self-sustaining, such that the reactants are not irreversibly consumed, the fuel cell is regenerative. For example, glucose-based, self contained fuel cells [24,87] are completely regenerative, able to operate for extended periods of time without outside intervention. The electrochemical reactions that take place in the glucose-based fuel cell can occur continuously without exhausting fuel or oxidation chemical supplies. Non-regenerative fuel cells usually have solid oxide fuels, methanol, or hydrogen as a fuel utilizing a non-reversible reaction to produce free electrons. These fuels have higher energy densities, but consume the fuel during the electrochemical reaction.

Glucose-based micro fuel cells for biomedical applications are well researched. This type of fuel cell relies on the electrochemical reaction of oxygen and glucose – two substances commonly found in the body. For *in vivo* applications, a glucose-based fuel cell may have an unlimited fuel supply [24,87]. Glucose-based fuel cells can be categorized into three specific types: enzymatic, microbial and abiotic. Enzymatic refers to glucose fuel cells that employ enzymes to facilitate the required chemical reactions to produce electricity. Microbial glucose fuel cells employ specific micro-organisms that convert the glucose found in a system to electricity [9]. Abiotic fuel cells use non-biological catalysts in order to ensure that conversion of glucose to electricity takes place. As in all fuel cells, electricity is generated by the electrochemical reaction of a fuel and an oxidant at two separated electrodes. Regardless of the fuel or the method of which is taken to catalyze the reaction, electrons released from the oxidation of the fuel are collected by the anode, flow through the load to the cathode, upon where a terminal electron acceptor is reduced. The electron flow is driven by the difference in electrochemical potential of the anode and cathode redox pairs [28].

One molecule of glucose can be completely oxidized into carbon dioxide and water, releasing 24 electrons per molecule, as shown below [28]:

$$Anode: C_6H_{12}O_6 + 24OH^- \longrightarrow 6CO_2 + 18H_2O + 24e^- \qquad (1)$$

$$Cathode: 6O_2 + 12H_2O + 24e^- \longrightarrow 24OH^- \qquad (2)$$

$$Overall: C_6H_{12}O_6 + 6O_2 \longrightarrow 6CO_2 + 6H_2O \qquad (3)$$
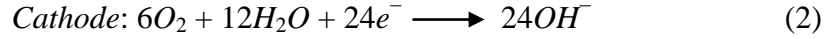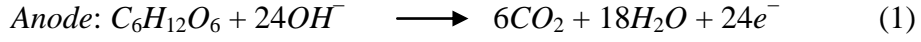
Theoretically, it is possible to collect and use all 24 electrons that are generated in this reaction. However, in practice this has not been achieved [28]. In addition, this single reaction would generate a theoretical voltage of 1.24 V [28]. The major attraction for the glucose fuel-cell the biocompatibility and suitability for *in vivo* MEMS-based applications. Glucose-based micro fuel cells have been reported to produce 50 $\mu W/cm^2$ to 430 $\mu W/cm^2$ for long-term constant generation [26].

Solid oxide fuel cells (SOFC) have also been explored for MEMS-based energy harvesting [25]. These fuel cells use a novel microfabrication method of directly printing the anodes and cathodes used in the system. They are deposited using a direct-write system, where suspensions of 55 wt% NiO/45 wt% YSZ (anode) and $(La_{0.8}Sr_{0.2})_{0.98}MnO_3$ (cathode) powders are deposited as a paste onto the fuel cell's surface through a robotically controlled micronozzle system. This allows for a variety of possible electrode configurations, maximizing electrode/reactant surface area contact. In addition, by using these specific electrode materials, it is possible to use hydrocarbons as a fuel, since the operational temperature of this fuel cell can be significantly higher than comparable cells. Hydrocarbon-based fuel cells have higher energy densities than other fuel cells [25]. A mixture of methanol and air is used as the fuel in this fuel cell, producing an open circuit voltage of 0.9 V and a peak power density of 2.3 mW/cm^2 at 700 °C. In comparison, this type of micro fuel cell has a much higher operational temperature than the previous ones, but produces much more energy [25]. When applied to other types of fuel cells, this approach may help with further miniaturization and optimization of power output, especially for size critical applications.

18

Direct Methanol Fuel Cells (μDMFC) are an additional type of fuel cell. Common power generation values range from 200 mV–1 V, and microwatts of power. For example, a micro fuel cell developed by Sim, Kim and Yang for the biological application uses methanol as a fuel [34]. Although methanol is toxic to biological systems, it is a good example of the technology. The operation of these systems is based on the electrochemical reaction shown below:

$$CH_3OH + H_2O \longrightarrow CO_2 + 6H^+ + 6e^- \qquad (4)$$
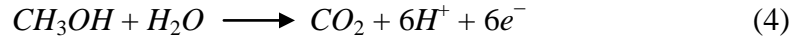
The μDMFC is a Proton Exchange Membrane Fuel Cell (PEMFC) [31], which relies on both the collection of electrons at the anode to produce a current and the migration of protons (H^+) to the cathode to allow the hydrogen to form water, completing the electrical circuit. Size is a limiting factor to the application of these specific fuel cells. A typical footprint for these devices is $16 \times 16 \times 1.2$ mm, which may be too large for some applications. The second limiting factor to the lifespan of the device, barring any physical damage, is the amount of fuel available to the system [36]. Generally, this type of fuel cell is constructed of two silicon wafers with a membrane electrode assembly patterned onto a membrane, such as Nafion, sandwiched in between. The silicon wafers are micromachined with through-holes in order to allow both the methanol fuel and oxygen catalyst to reach the membrane/electrode assembly to allow for the electrochemical reaction to take place [31]. The through hole or microchannels are designed to be very small, roughly 80×80 μm, to ensure that the capillary forces passively transporting the methanol to the membrane/electrode assembly are dominant over gravity [29]. This type of passive μDMFC is able to produce 9 mW/cm^2 for about 50 minutes operation—the time required to exhaust the methanol fuel source [31].

Motokawa *et al.* [33] have developed a novel parallel microchannel system for μDMFCs that allows for a greater active area on the membrane interface that transports protons. The micro fuel cell is composed of two parallel microchannels, connected on the top surface by a DuPont Nafion 112 proton membrane. The multiple anodes and cathodes used in this micro fuel cell are located on the bottom and sides of the microfluidic channels, which allow for high

efficiency collection of electrons by the anodes and high efficiency transportation of protons to the cathodes. The travel distance from anode to cathode is very short, causing the system to be less sensitive to the resistance of the solution and the electrodes [33]. In addition, this approach isolates the fuel and oxidant in the fuel cell, preventing any cross-mixing of fuel and oxidant that may occur. This novel technique prevents some traditional problems in micro fuel cell design, but does not produce as much power as other designs, only producing 0.78 mW/cm^2 [33]. In addition to travel distance, the geometry of the fuel cell plays an important role in the efficiency and generation potential of the μDMFC. Generally, the anode flow field plate is designed to maximize the surface area upon which the required electrochemical reactions take place. By maximizing the surface area by using a double serpentine structure rather than a pin-type flow plate, the peak power output of the μDMFC can be increased by upwards of 20.7% [30]. In addition to previous schemes used to increase the surface reactive area of fuel cells, stacks of fuel cells can be arranged in a "flip flop" configuration where a common bipolar plate, containing both an anode and cathode, can be used to achieve long continuous stacks of fuel cells [35]. By connecting one anode side of a common plate to a cathode side of a different common plate, long stacks can be created, increasing the generation potential and minimizing the connection resistance of that single, "flip flopped", fuel cell. This scheme, when fueled with 2 M methanol, produced 2.7 V of open circuit voltage, with a peak power output density of 2.2 mW/cm^2 [35].

Carbon Nanotubes have been pursued as both a catalyst support layer and a gas transport method for micro-fuel cells [32]. A honeycomb-type arrangement of carbon nanotubes has been used to transport both the fuel and oxidant between reaction sides of the fuel cell. In this case, an air/hydrogen mixture is used as fuel. Studies conducted by Kuriyama *et al.* [32] focused on demonstrating that carbon nanotubes were a viable structural material for both material transport and as a support layer. The micro fuel cell using carbon nanotubes as a transport medium for catalysts was able to produce an energy density of 0.75 W/cm^2 [32]. The carbon nanotube transport system also allowed for a more uniform and predictable

transportation of materials around the fuel cell. In traditional fuel cells, pressure driven diffusion across a membrane is the primary method of reactant transportation. With carbon nanotubes, it is possible to easily transport materials without a pressurizing mechanism, allowing for greater reliability and standardization of specifications between similar fuel cells [32].

2.2.4   *Electrostatic Vibration-to-Electricity Conversion*

Electrostatic vibration-to-electricity energy harvesting most often utilizes a comb drive to generate electricity from an applied vibration. These devices generate power through a vibration-driven capacitance variance which causes charge transfer and current flow. The capacitors must be held at a constant charge to promote power generation; therefore, a polarization source must be present in order to generate additional power. The charge required for the system to operate can be supplied actively from a power source or passively through use of an electret layer [37,39] or a charge pump [38,40]. An electret-driven energy harvester uses an electret layer to provide the necessary polarization to the variable capacitor. The electrets are microfabricated on silicon wafers, with deposited layers of silicon oxide and silicon nitride. The wafer is subject to a corona charge, which deposits a significant amount of charge in the silicon nitride layer. After a heat treatment, the charge is trapped within the electret. The average lifetime of the electret under regular operation is approximately 50 years [41]. The charge quantity from an electret directly influences the power generated, up to as much as a few orders of magnitude. A 10 V electret will allow a electrostatic generator to produce 2 nW continually, while a 100 V electret will allow a electrostatic generator to produce upwards of 5 µW [39]. The charge pump is functionally different than an electret, but performs the same task. Instead of slowly releasing charge over time to polarize the variable capacitors, a charge pump, once primed with an externally supplied charge, will siphon the required energy from the energy generated to maintain the generation cycle. To prevent charge saturation, the charge pump requires a flyback circuit and a charge reservoir, such as a battery or capacitor [40]. Once operating, the charge pump

will continually charge the variable capacitors until either a lack of vibration or some other interruption occurs disrupting the cycle long enough for a complete draining of the charge reservoir [40].

Generally, the concept of generating power through electrostatic harvesting can be summarized in three steps: charge the variable capacitor when the capacitance is high, reduce the capacitance of the variable capacitor through mechanical vibrations, and discharge the capacitor when it is suitable to do so [44]. There are three different types of electrostatic harvesters which differ by actuation direction. The harvester shown in Figure 2.1 is referred to as an in-plane gap closing electrostatic harvester. This harvester develops a capacitance variance by vibrating in the plane of the device, in the direction shown in Figure 2.1.
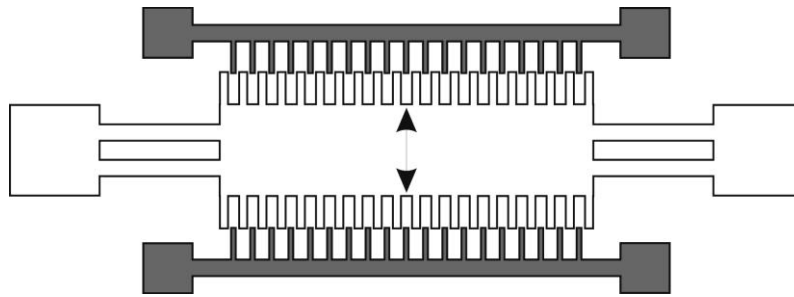
Figure 2.1 - Schematic of an in-plane overlap electrostatic energy harvester, direction of travel indicated [88].

This motion causes the overlap area of the teeth of the comb drive to vary, thereby causing the required capacitance change. The actuation of this device is limited by the spacial gap in the direction of the actuation. In order to prevent damage to the structure, either through impact or stiction, mechanical stops must be fabricated [12]. The mechanical stops limit the minimum dielectric gap in the interdigitated fingers, thereby determining the maximum capacitance of the system. As for power output, this device can produce up to 20 μW/cm^2 [12]. The potential power output for this type of electrostatic energy harvester has been shown through simulation to be upwards of 10 μW of power, driven at 120 Hz, under a 3.5 m/s^2 acceleration [46]. However, due to the design of the comb drives

involved off-axis actuation can cause rotation, which promotes electrical contact, shorting, and stiction, as shown in Figure 2.2.

Under Normal Operation

Under Off-Axis Actuation
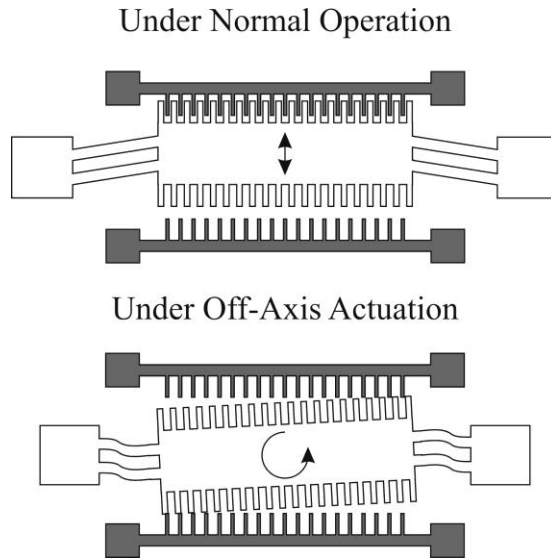
Figure 2.2 - Detrimental rotation of the in-plane overlap electrostatic energy harvester [88].

The in-plane gap closing electrostatic energy harvester, as shown in Figure 2.3, is of the same configuration as in-plane overlap electrostatic energy harvester; with a perpendicular actuation direction. With this device, the capacitance variation is driven through varying the gap between the teeth of the combs.
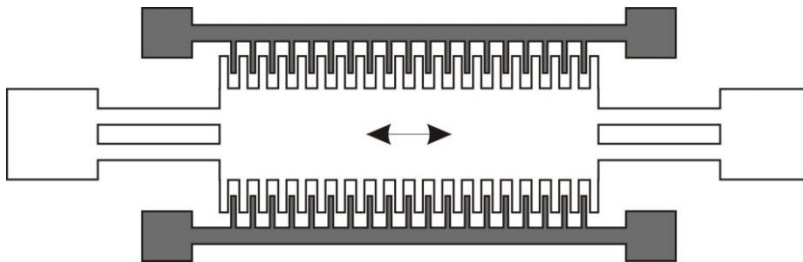
Figure 2.3 - Schematic of an in-plane gap closing electrostatic energy harvester, direction of travel indicated [88].

As before, this device has the same minimum gap restriction, requiring mechanical stops to prevent damage to the system. It is reported by Roundy *et al.* [12] that this design is more manageable and less prone to detrimental in-plane

rotation, and therefore, was chosen to be optimized. The optimized in-plane gap converter was able to harvest up to 116 µW/cm^2 vibrating at 2.25 m/s^2 at 120 Hz [12]. Murillo *et al.* [45] have developed an in-plane closing gap electrostatic energy harvester that can produce 76.67 nW of power at a frequency of 100 Hz. The strength of this electrostatic energy harvester system is the array-like integration which was the focus of Murrilo *et al.'s* research. One hundred energy harvesters were integrated into a chip an area of 2.84 × 3.67 mm, increasing the power output from 76.67 nW to 0.958 µW [45].

The last design, as shown in Figure 2.4, is the out-of-plane gap electrostatic harvester. It is of similar form to the previous in-plane electrostatic harvesters, but is actuated out of plane.
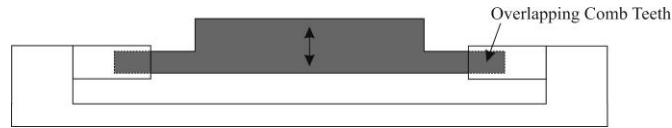
Figure 2.4 - Schematic of an out-of-plane gap closing electrostatic
energy harvester, direction of travel indicated [88].

As in other iterations of this harvesting scheme, the out of plane actuation provides the necessary capacitance change to produce electricity. The out-of-plane gap harvester is greatly influenced by thin-film damping and stiction. For this device to produce appreciable power, it must be packaged in a vacuum to avoid thin film damping, improving the power generation from 1 nW/cm^2 to 20 µW/cm^2. Depending on the application, packaging the harvester in a vacuum may or may not be possible. To further make the harvester viable, mechanical stops would have to be fabricated in order to prevent the out-of-plane gap converter from contacting the substrate, preventing shorting and stiction. These mechanical stops are extremely difficult to fabricate since there is no geometrical freedom to produce them [12]. A similar device to the out-of-plane harvester was proposed by Sterken *et al.* [47]. The device consists of two capacitors, one stationary, and one mobile. As the capacitance of the system varies via the free capacitor, the

change in capacitance will cause a current in a similar manner to the previously discussed designs. This device is capable of generating 100 μW while excited at 1200 Hz [47]. This energy harvester was optimized to allow the operational frequency to be as close as possible to the natural frequency of the harvester, maximizing the displacement of the free capacitor, thereby maximizing the possible power output. As with previous incarnations of electrostatic MEMS-based harvesters, this design requires a polarization source to charge the capacitors prior to generation.

A comb-based electrostatic energy harvester was developed by Ma *et al.* [43] using an out of plane vertical comb drive rather than a typical horizontal comb drive. In this case, a variable capacitor is formed between a floating, heavily doped insulated poly-silicon electrode suspended above a metal electrode. The gap between electrodes does not change. The energy harvester is actuated horizontally to create the required capacitance change for energy harvesting. The capacitance change is largely caused by the fringing of dielectric fields, rather than the more direct overlapping of previous designs. This energy harvester was capable of producing 65 nW of power under a resistance load of 50 MΩ, driven at near-resonance, at a displacement of 2.2 μm [43]. This specific harvesting scheme uses capacitor polarization that is provided by electron tunneling, similar to the process found in non-volatile memory devices [42].

2.2.5   *Electromagnetic Energy Harvesting*

Electromagnetic energy harvesting has been used to generate power since the discovery of electromagnetic induction by Faraday, which led to the development of the first magneto by Pixii [89]. Since that initial discovery, the principle of generating power from oscillating magnetic fields and a conductor has been extensively used both in large and small scales. Electromagnetic vibration-to-electricity conversion is a fundamentally regenerative energy harvesting scheme as long as the actuation is ambient. Electromagnetic generation has been used for MEMS-based biological energy harvesting, as shown by Roberts *et al.*[2]. This scheme uses a MEMS-based electromagnetic energy

harvester to augment the power supply for pacemaker batteries in clinical trials. An example electromagnetic MEMS-based energy harvester is schematically shown in Figure 2.5.
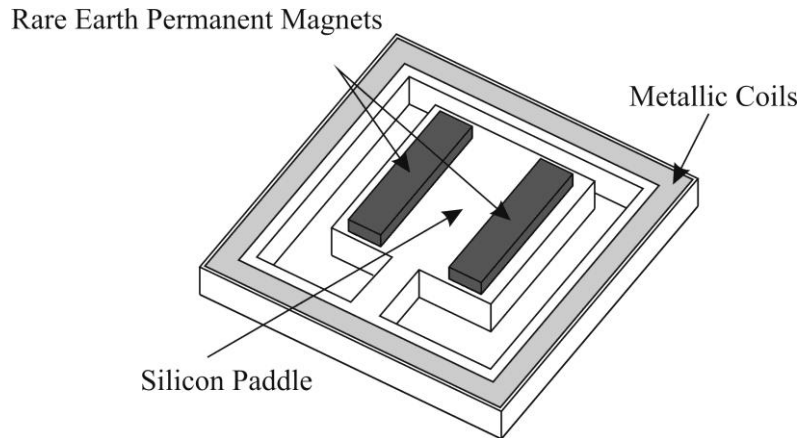
Figure 2.5 - Schematic of an example electromagnetic energy harvester. [88]

Generally, electromagnetic energy harvesters consist of an arrangement of permanent magnets and metallic coils that oscillate relative to one another, as shown in Figure 2.5. A coil is contained within the silicon beam layer, running the perimeter of the etched well. As the beam vibrates out of plane, the magnetic field oscillates relative to the coils on the well's edge, causing the coils to be subject to a magnetic flux. The flux imparts an electromotive force on the coils, causing a current to flow in the coils. This device is capable of significant power generation at operating frequencies of 30–350 Hz, well below the reported natural frequencies of the device, which range from 6.4 to 12.6 kHz [48]. Since the performance of an electromagnetic energy harvester is tied to the magnetic flux that is produced from vibration, optimizing the amount of vibration characteristics of the energy harvester is important. The optimizations of the harvester include, improving the linear behavior, reducing the parasitic damping, and tuning the frequency response of the generator to the ambient vibrations that the energy harvester is exposed to [53]. To this end, both the geometry and the materials that are used in the energy harvester must be optimized. Silicon based materials, such

as Si, SiO$_2$, and Si$_3$N$_4$ are preferable to polymeric materials, such as Kapton, due to lower mechanical losses and lack of spring stiffening effects at large excitation amplitudes [52].

Reissman *et al.* [51], have developed a similar method of harvesting electricity through electromagnetic induction on a MEMS scale. A NdFeB permanent rare earth magnet provides the strong magnetic fields required for this energy harvester. The permanent magnet is suspended via a rigid beam 2 mm above a micro-coil of copper, fabricated from CMOS processes. In this configuration, the fringing of the suspended NdFeB magnet is supplying the magnetic flux to the copper micro-coil. At a frequency of 27 Hz, the device is able to produce 12.5 µW of power per copper coil layer [51].

Serre *et al.*[53] developed a membrane based energy harvester that uses Kapton, a polymer-based membrane. The Kapton membrane, having a Young's Modulus much lower than other possible membrane materials such as silicon, is a suitable material for low frequency actuation applications. A Kapton membrane of 127 µm thickness was used to suspend a NdFeB rare earth magnet inside a micromachined well. Coils were deposited on the top surface of the wafer, above the wells. A prototype energy harvester, with a 7 × 7 × 4 mm^3 magnet and a 13 × 13 mm^2 Kapton membrane with a resonant frequency of 360 Hz was able to produce a peak power output of 45 nW [53]. An optimization of this harvester was undertaken in order to increase the power output [52]. The geometry of the Kapton membrane was optimized to provide greater displacement to the permanent magnet, to maximize the magnetic flux that would be produced. Parasitic damping, caused by spring stiffening effects, increases as the membrane deflection increases, adding losses to the system with increased deflection. To further increase the power generation that this type of energy harvester can produce, thicker electroplated copper coils have been suggested by Serre *et al.* to increase the peak power generation from 45 nW to between 60 to 120 µW [52].

A rotary electromagnetic generator was produced by Pan *et al.* [50]. The energy harvester consists of two disks: one disc consisting of an 8-pole NdFeB magnet, and the other consisting of various layers of copper multipolar coils with a line width of 30 μm. These two discs were separated by one millimeter. The magnetic disc is suspended on a rotary mechanism, while the coils attached to a static platform. To increase the generation potential of the rotary harvester, four layers of copper coils were added to the system. Running the rotating platform at 150 Hz, the maximum induced voltage from a four layer coil disc is 111.2 mV, with a maximum power output of 386.42 μW. Another rotary generator was developed by Herrault *et al.* [49] uses an air turbine as an actuation mechanism for its rotary energy harvester. As with other electromagnetic energy harvesters, a NdFeB permanent magnet will be used to provide the strong magnetic field required. The design of the energy harvester in this case is similar to Pan *et al.* [50], however the stator coils are of a more complex design. Coils that will experience the same electrical phase are connected, thereby maximizing the electricity generated at a specific electrical phase. The poles of the coil assembly were equally spaced in the stator design. In addition, to maximize the generated power, the speed at which the rotor is driven was increased, above the typical speeds of micro scale devices. This rotary harvester was driven at 392 kRPM, producing 6.6 mW of electrical power. These energy harvesters produce a fair amount of electricity; however rotation is not a convenient motion of vibration to harvest energy from on a MEMS scale. A MEMS-based turbine or rotational engine will be required provide the necessary mechanical rotation for these electromagnetic harvesting schemes.

2.2.6   Piezoelectric Harvesting

Piezoelectric generation is a well researched method of harvesting electricity from mechanical vibrations. When the crystal structure of the piezoelectric material is loaded, the micro-structure of the crystal is distorted. In order to maintain electrical equilibrium within the crystal the electrons become mobile to equalize the imbalance, creating a current. This is referred to as the

direct piezoelectric effect. Alternatively, the exact opposite phenomenon, the converse piezoelectric effect, can also take place. The direct piezoelectric effect is used for energy harvesting and sensing purposes, while the converse piezoelectric effect is used for actuation. Piezoelectric energy harvesting is frequency dependant, maximized as the frequency at which the system is driven matches the natural frequency of the harvester [63]. This maximizes the displacement of the harvester and strain applied to the piezoelectric element. There are three main types of piezoelectric energy harvesting in literature: beam-based, membrane-based, and fibre-based.

Beam-based piezoelectric energy harvesting is the most common method of piezoelectric-based energy harvesting. The typical configuration, as shown in Figure 2.6 [88], of the beam-based harvester provides tension/compression to the piezo film through beam bending, allowing for the 31-mode of the piezoelectric material to be accessed easily, maximizing the voltage output of the piezoelectric material, especially in low strain realms [65].
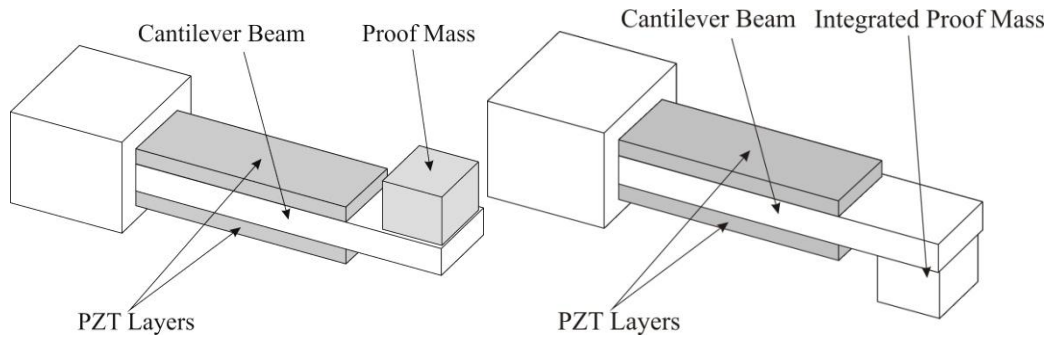
Figure 2.6 - Schematic of a typical piezoelectric cantilever-based energy harvester. [88].

The "mode" of the piezoelectric material refers to the direction of both the mechanical force applied and electric charge collected. The modes of the piezoelectric material are shown schematically in Figure 2.7.
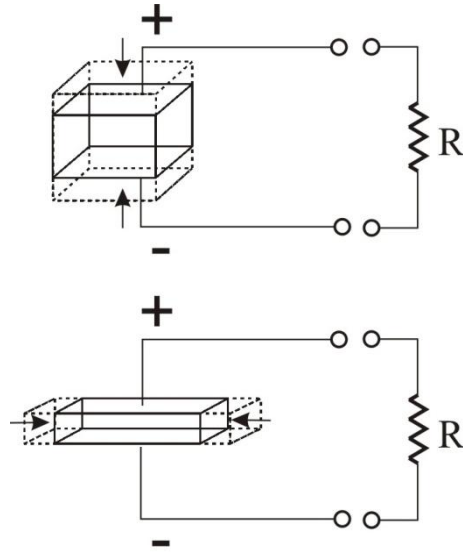
Figure 2.7 **-** The 33-mode (top) and 31-mode (bottom) of a piezoelectric material [88].

The top of Figure 2.7 shows the 33-mode of the piezoelectric material, where the charge is being collected (or applied) on the surface perpendicular to the polarization axis while the mechanical displacement is applied (or experienced) along the polarization axis. The 33-mode of the piezoelectric material is useful for pressure sensing and some actuation applications [90]. This mode of the piezoelectric material is desirable when the overall thickness of the sensor is not a design constraint [63]. An increase of PZT thickness can amplify the response of the piezoelectric element – either the electrical signal produced from a pressure or the actuation produced by an applied voltage. Conversely, the bottom of Figure 2.7 shows the 31-mode of a piezoelectric material, where the charge is being collected (or applied) on the surface perpendicular to the polarization axis, and the mechanical displacement is being applied (or experienced) perpendicular to the polarization axis. This arrangement is more desirable for sensors that can take advantage of bending structures, such as cantilever beams, for limited thickness, low-pressure applications, or energy harvesting applications [63]. The 31-mode is the typical mode used in out of plane piezoelectric actuation [63].

The majority of the research into piezoelectric energy harvesters centers on optimizing the performance and efficiency of the harvester. Specifically, the work deals with optimizing the amount of power generated by tuning the dynamics of the system and optimizing the conditioning circuits that are used to collect and store the generated power [63,65]. The power that a piezoelectric harvester is capable of generating is directly proportional to the strain the piezoelectric crystals are subject to, as shown by equations (5) and (6).

$$\sigma = E\varepsilon = Eu_x \tag{5}$$

$$[T] = [c][S] - [e^t]\bar{E} \tag{6}$$

where, in (6) *[T]* is the Stress Field Tensor, *[c]* is the Elastic Stiffness Tensor, *[S]* is the Strain Field Tensor, *[e^t]* is the transpose of the crystal symmetry tensor specific to the piezoelectric material, and *E* is the Electric Field Vector. To achieve maximum strain to increase the output power, the deflection the harvester undergoes must be maximized as well. Typically, the maximum displacement for the beam-based piezoelectric systems is maximized at resonance [63].

Roundy *et al.* [66] have examined the properties and generation potential of the piezoelectric cantilever energy harvesters. The harvesters developed by Roundy *et al.* are very large for MEMS devices; however, important results have been gained from their work. Their energy harvesters were limited to 1 cm^3 total volume, using tungsten proof masses to tune the frequency-based characteristics of the energy harvesters. Roundy *et al.* observed several key results to aid in the optimization of this type of MEMS-based harvester:

- The energy harvester's resonant frequency should be as close to the operational frequency of the harvester as possible [66]. This ensures that the cantilever-based energy harvester will experience maximum displacement and strain, thereby maximizing the mechanical-electrical conversion in the piezoelectric material.

- The power output of the system is inversely proportional to the driving and resonant frequency of the device [66]. This result is intuitive – lower frequency vibration typically has higher displacement amplitudes.

- The power output of the energy harvester is proportional to the proof mass of the beam-based harvester [66]. Higher mass reduces the natural frequency of the energy harvester, increasing the output power.

- The energy removed from the generator will act as mechanical damping to the system due to the piezoelectric coupling [66].

While developing these design rules, Roundy *et al.* were able to produce cantilever-based piezoelectric energy harvesters that were capable of harvesting 375 µW from driving vibrations of 2.5 m/s^2 at 120 Hz [66].

Aluminum nitride (AlN)-based cantilever energy harvesters are being explored for piezoelectric energy harvesting applications. As discussed by Elfrink *et al.* [61], the major advantage of using AlN-based piezoelectric harvesters, in comparison to a PZT-based harvesters, is the higher optimum load resistance of AlN. For AlN, Elfrink reported an optimum load resistance of 0.1–1.0 MΩ, where PZT based energy harvesters generally have optimum load resistances of a few kΩ [61]. This difference in load resistance causes AlN to generally have higher output voltages in comparison for PZT for equivalent power outputs. That may be desirable for certain energy harvesting applications requiring higher output voltages and lower output currents. The AlN-based harvesters are fairly large for MEMS-based harvesting, up to 7 × 7 mm in footprint, with beam thicknesses of approximately 45 µm, which allowed for natural beam frequencies as low as 277 Hz. The maximum power output from this scheme was 60 µW at an operational/natural frequency of 572 Hz [61]. To be efficient, this energy harvester needs to be packaged in a vacuum, since air damping will reduce the displacement of the proof mass, reducing the output power.

Choi *et al.* [75] and Lee *et al.* [81] produced lead zirconate titanate (PZT)-based cantilever energy harvesters that utilized interdigitated electrodes in order to collect the charge produced through actuation. The interdigitated electrodes allowed for the collection of the charge to occur on one side of the piezoelectric film, rather than the lower/upper electrode configuration. This allows for the collection of charge in the 33-mode of the piezoelectric material, rather than the 31-mode of the piezoelectric material. These harvesters were capable of producing 1 µW at 2.4 V [75] and 1.3 µW at an applied acceleration of 19.62 m/s^2 [81].

Duggirala *et al*. [76] studied an alternate, perpetual method of driving a cantilever-based piezoelectric harvester. The novel actuation method in this study involved a radioactive source emitting beta particles, charging a collector mass, to produce an electrostatic force to actuate the beam. Once the mass contacts the grounded electrode, the charge on the collector mass is dissipated, causing the beam to return to equilibrium. The entire cycle is then repeated until the radioactive source is exhausted [76]. There were two sizes of harvesters produced for this harvester a 1 cm and 5 mm cantilever, producing 1.13 µW and 170 nW respectively at 38 Hz [76].

Different types of proof masses have been used to provide the required natural frequency reduction to increase the output energy of the harvesters. Fang *et al.* [77] utilizes a dense nickel proof mass to reduce the natural frequency, in order to produce 2.16 µW at a 9.81 m/s^2 acceleration applied at 609Hz. Shen *et al.* [86] studied cantilever-based energy harvesters with integrated proof masses, similar to the harvester shown in Figure 2.6. These harvesters were capable of producing 2.15 µW at an operational frequency of 461.15 Hz.

Arrays of cantilever-based energy harvesters have been used to capture a wide bandwidth of operational frequencies in one device. The harvester produced by Liu *et al.* [85] was composed of multiple cantilever harvesters that

encompassed a natural frequency bandwidth of 226-234 Hz. This methodology was capable of producing 3.98 µW over the bandwidth of the device.

Membrane-based energy harvesters have been investigated for both implantable and ambient uses. Generally, a circular membrane of PZT is used [64] due to its axisymmetry. The most basic membrane-based piezo harvesters are simple circular diaphragms of PZT subject to a pressure load. For example, Kuehne *et al.* [80] produced a 25 mm^2 circular piezoelectric membrane capable of producing 1 µW under resonance. In biomedical applications, a circular membrane piezoelectric energy harvester can be tuned to actuate from pressure differences found in the body, such as those generated by breathing, muscle contractions or blood flow. A circular piezoelectric energy harvester [64] was designed to be actuated from the pressure difference (40 mmHg) that is produced from a typical human pulse. This device was able to generate 61 µW experimentally from the 40 mmHg pressure load. Ramsay and Clark [65] have also examined using blood pressure as a power source for piezoelectric membrane energy harvesters. It has been reported that the power available from variations in blood pressure is as high as 0.373 W [67]. Even with the relatively low conversion efficiency of 34% of the PZT-5A material used in the analysis, it is theoretically possible to produce membrane-based piezoelectric energy harvesters that could easily provide 10 mW. However, Ramsay and Clark discovered that although the generation potential was sufficient, the size of the membrane would be a limiting factor in generation. With membranes limited to 1 cm^2 it was not possible to produce 10 mW of continuous power. Using blood pressure (40 mmHg) alone as an actuation method for the piezoelectric energy harvester, and limiting the size of the membrane in the energy harvester to 1 cm^2, it was possible to continuously supply microwatts of continuous power, while being able to provide milliwatts range power intermittently when the displacement of the energy harvester is maximum. Lee *et al.* [82] packaged a bulk PZT disk for energy harvesting from bioapplications. The fully packaged bulk PZT harvester was implanted in pigs and tested for subcutaneous energy harvesting. It was capable of producing 0.15 µW at 1508 Hz in *in vivo* testing in animals.

Fibre-based piezoelectric energy harvesters have been developed by Churchill *et al.* [84], utilizing long, unidirectional 250 µm diameter PZT fibers embedded in the resin matrix. This harvester will act similarly to the beam-based harvesters, where the elongation of the embedded fibers will produce the required strain to harvest electricity. This harvester was capable of producing 0.1-0.8 mW for various strains applied at 180 Hz [84]. For biomedical applications, a PZT microfiber harvester was developed by Ishisaka *et al.* [62] in which the contractions of a heart muscle are used to actuate the harvester. The piezoelectric microfibers are fabricated by depositing PZT onto a platinum wire and then plating the wire with nickel in order to complete the electrical circuit. A PDMS membrane is then placed between the fiber and the heart muscle to provide biocompatibility. As the heart muscle contracts, the PDMS membrane is deflected, which in turn causes the embedded PZT microfiber to deflect. In experiments, cultured cardiomyocytes were used for actuation. These lab-grown cells actuated the piezoelectric harvester at a frequency of 1.1 Hz, producing between 40–80 mV, for a single ~100 µm fiber. The strength of this energy harvester is the high biocompatibility of the PDMS membrane encapsulation that prevents contact between the PZT and the cardiomyocytes. Not only is the material highly flexible, allowing for actuation, it is completely biocompatible.

Additionally, zinc oxide (ZnO) nanowires have been used to harvest electricity on a micro scale. The ZnO nanowires were grown using a wet chemistry method to deposit the nanowires on a plastic substrate [69]. The wet chemistry method can be altered for different orientations and densities of ZnO nanowires. The flexibility of the plastic substrate allows for the ZnO nanowires to be used in a flexible application, such as implantable biosensors [69]. ZnO wires with a 300 nm diameter, 1 µm long, produced an output power of approximately 5 pW at 45mV, under a 5 nN contact force load through AFM actuation [69]. Xu *et al.* [71] have developed ZnO nanowire-based array energy harvesters deposited on Kapton, using a similar process as above. The deposited ZnO nanowire array is then encapsulated by a soft polymer, such as photoresist, to protect the nanowires from the environment. This harvester was capable of generating 1.26 V at a strain

of 0.19% [71], producing a peak power output density of 2.7 mW/cm^3. A similar energy harvester has been used in clinical trials by Li *et al.* [70] to generate power using a ZnO nanowire harvester in an *in vivo* application. This energy harvester has bigger nanowires than the previous energy harvesters having a diameter of 100–800 nm and length of 100–500 μm [70], packaged in a similar manner using flexible polymer materials. The energy harvester was implanted on the diaphragm muscle and heart of live rats in order to test the energy harvester in an implantable application. For the expansion and contraction of the diaphragm during breathing, the ZnO nanowire harvester was able to generate 1 mV at 1 pA [70]. The generator was able to generate more power from the heart beat of the rat, generating 3 mV and 30 pA [70]. Although this experiment produced significantly less power than the previous studies using mechanical stimulation, it is an important first step for ZnO nanowire-based *in vivo* energy harvesters.

A summary of the discussed vibration-driven piezoelectric energy harvesters is shown in Table 2.1.

Table 2.1 - Summary of Piezoelectric Energy Harvesters

Method of Piezo-Energy Harvesting	Author	Description	Power Generation Potential
Bimorph Cantilever	Roundy/Wright	Simplified microfabrication- Ability to add large seismic masses for optimization	375 μW [66]
Membrane-based	Ramsay	Membrane can exhibit strain stiffening, depending upon the materials used. Versatility in application	10 mW [65]
Cantilever-based with Interdigitated Electrodes	Choi	Interdigitated rather than top/bottom for charge collection.	1 μW @ 2.4 VDC [75]
Long PZT Fibers Under Strain	Churchill	Unidirectional 250 μm diameter PZT fibres embedded in a resin matrix	0.1-0.8 mW @ 180 Hz.[84]
Radioisotope-controlled Cantilever	Duggirala	Cantilever driven by radioactive decay/electrostatic attraction cycle.	1.13 μW (1 cm cantilever) 170 nW (5 mm cantilever) 38 Hz [76]
Single PZT layer Cantilever w/Nickel Proof Mass	Fang	Composite Pt/Ti/PZT/Pt/Ti stack structure with nickel proof mass.	2.16 μW @ 609 Hz @ 9.81 m/s^2 [77]
ZnO Nanowires.	Gao	ZnO Nanowires deposited on plastic substrate	1-2 mW/cm^2 [69]
Heart-muscle Actuated PZT Wires.	Ishisaka	PZT deposited on platinum wire, plated with nickel. PDMS membrane between wire and muscle. Muscle contractions deflect whole device.	40-80 mV per fiber @ 1-2 Hz [62]
Bowed Cantilever with transverse PZT	Jeon	Cantilever with specific orientation of PZT. Proof Mass.	1 μW at 2.4V dc [79] 13.9 kHz
Piezoelectric Diaphragm	Kuehne	25 mm^2 circular diaphragm subject to pressure loads	~1 μW under resonance.[80]
Disc Shaped Bulk PZT	Lee	Bulk PZT harvesting disc. *In vivo* tests. Used for subcutaneous energy harvesting.	0.15 μW @ 1508 Hz [82]
Cantilever w/ Interdigitated Electrodes	Lee	Integrated proof mass with interdigitated electrodes.	1.3 μW @ 19.62 m/s^2 [81]

Table 2.1 - Summary of Piezoelectric Energy Harvesters (Continued)

Method of Piezo-Energy Harvesting	Author	Info	Power Generation Potential
Array of Cantilevers	Liu	Cantilever array of three beams	226-234 Hz bandwidth. 3.98 µW [85]
Circular Membrane PZT for Blood Pressure Actuation	Mo	Circular PZT membrane designed to be actuated by 40mmHg	30-40 V [64]
Cantilever with Integrated Proof Mass	Shen	Typical arrangement of PT/PZT stack µm-size cantilever with integrated mm-size Si proof mass.	2.15 µW 461.15 Hz [86]
Zinc Oxide Nanowires on Kapton	Xu	Zinc Oxide Nanowires on Kapton	1.26 V at a strain of 0.19% [71]
Aluminum Nitride-based Cantilever Harvesters	Elfrink	AlN-based energy harvesting cantilevers. AlN gives a higher optimum load resistance, therefore higher voltage output.	60 µW @ 572 Hz [61].
Zinc Oxide Nanowires for *In vivo* Harvesting	Li	Encapsulated zinc oxide nanowires tested in vivo in rats. Vibrations from muscle and heart used.	1 mV @ 1 pA (muscle), 3 mV @ 30 pA (heart) [70].

2.3   Discussion and Summary of Harvesting Methods

The type of MEMS-based energy harvester chosen for a specific application depends on the type of input energy that is available for the application. Although, solar energy harvesting uses the most plentiful source of input energy available, major issues arise with light intensity. For example, the efficiency of a photoelectric harvester suffers greatly from diminished light intensity, up to a 94% loss in efficiency from not being in direct sunlight [12]. For an implantable or "dark" system, this could be troublesome and would cause solar-based schemes to be unsuitable. Ambient heat is an abundant energy source for energy harvesting. For example, the body constantly generates heat from the various biological processes required to sustain life. To maximize efficiencies for the biological application, the areas of the body with maximum temperature differentials should be prioritized. For example, locations where blood vessels are in close proximity to the exterior of the body such as the neck, wrists, and ankles, would be prime harvesting locations. Ambient vibration is also a plentiful ambient power source. Vibrations from a variety of sources, such as rotary motion, a beating heart, expanding diaphragm, a pulse from an artery, or shock/movement from walking can all be harvested for electricity. However, to harvest meaningful quantities of electricity from these situations, specific tuning of the energy harvester to operate near the frequency of ambient vibration is required. In addition, arrays of vibration driven energy harvesters may be arranged to capture a wide frequency band of actuation, each energy harvester in the array tuned to a specific subsection of that frequency band.

Table 2.2 briefly states the advantages, disadvantages, and power generation potential of each type of power generation explored.

Table 2.2 - Comparison of energy harvesting techniques.

Method of Energy Harvesting	Advantages	Disadvantages	Power Generation Potential	Input Energy Source
Photovoltaic	Abundant Input Energy	Efficiency and output is tied to light intensity.	500 µW [6] – 1 W [11]	Light/Photons
Thermovoltaic	Abundant Input Energy	Requires large temperature difference for efficient generation.	4.5 µW – 100 µW [20] (Thermopiles) 0.8 µW [23] (P^3 Micro-heat engine)	Ambient or supplied heat.
Micro Fuel Cells	Reasonable energy density.	Hydrocarbon fuels (highest energy) are not biocompatible.	50 µW/cm^2 – 430 µW/cm^2 [26] (Glucose based) 9 mW/cm^2 – 750 mW/cm^2 [31,32] (Hydrocarbon Based)	Supplied fuels such as Glucose or Hydrocarbons
Electrostatic	Can be self-sustaining with electrets and charge pumps.	Requires energy to produce energy.	20 µW/cm^2 – 116 µW/cm^2 [12] (In-plane gap closing type) 100 µW/cm^2 [47] (out-of-plane type)	Ambient or supplied vibration.
Electromagnetic	High power Density.	Poor length-scale based scaling.	12.5 µW [51] (Cantilever) 45 nW [53] (Membrane) 386.46 µW [50] – 6.6 mW [49]	Ambient or supplied vibration.
Piezoelectric	High power density. Customizable	Possible bio-compatibility issue. Highly frequency dependant.	375 µW [66] (Bimorph) 10 mW [65] (Membrane) 2.7 mW/cm^3 [71] (ZnO Nanowire) 1 µW [75] - 375 µW [66] (Cantilever) 1 µW [80] - 10 mW [65] (Membrane) 0.1-0.8 mW [84] (Long PZT Fibers)	Ambient or supplied vibration.

The application of the energy harvester ultimately defines the harvesting methodology used. For the example case of implantable biosensing power systems, there are a variety of possible harvesting methods that could allow existing power systems to be augmented. First, the harvesters must be biocompatible. Either all components must be suitable for implantation, or sufficient packaging must be in place to prevent possible biocompatibility issues. This is usually accomplished by packaging the energy harvesters or biosensing platform in polymeric or silicone gel encapsulation [91]. This type of packaging is required to ensure biocompatibility both for the patient and the implant. The patient must be protected from possible cytotoxic materials, while the implant itself must be protected from environmental factors *in vivo* that may reduce their generation effectiveness. The majority of materials used in MEMS devices, including silicon, silicon oxide, polysilicon, silicon nitride, titanium, and some photoresists, such as SU-8, have been proven to be non-cytotoxic [91]. However, there are some materials, such as lead zirconate titanate (PZT) that can be cytotoxic if improperly packaged. In addition, the topology of various MEMS devices may cause many sharp edges to be present on the cellular level, allowing for the potential of localized cell damage through direct contact. For these reasons, MEMS devices used in implantable biosensing are usually packaged in a biocompatible manner, regardless of the cytotoxicity of the materials involved.

Unless high intensity light is transported subcutaneously to an implanted photovoltaic system via fiber optics or the power harvested on the surface of the skin can be transmitted to the biosensor, photovoltaic harvesting will suffer from low conversion efficiency and power output. However, if the harvester could be worn or integrated into a piece of clothing and the harvested power transmitted into the body, photovoltaic harvesting may be suitable for implantable biosensing. Although there have been advances in the technology to allow for improved conversion rates and adaption of the technology to overcome the challenges inherent to the harvesting scheme; the majority of implantable biosensing applications are not applicable for use with photovoltaic schemes.

Thermoelectric harvesting is an interesting alternative to batteries for biosensing applications due to of the availability of ambient heat energy and the reasonable power generation potential at optimal harvesting sites. Direct thermoelectric generation is an energy harvesting technique that can be effective with small temperature differentials, while maximized with high temperature differentials. With increasing efficiency of various thermopile designs, the average size of direct thermoelectric harvesters has decreased, making them increasingly attractive for implantable biosensing applications. Combustion, *in vivo*, could have significant packaging challenges such as reactant and product handling challenges, not to mention the localized heating. In addition, the operational location of the thermoelectric-based energy harvesters is of great importance, since the body has an inhomogeneous thermal profile. The possible applications of thermoelectric generation may be limited by the thermal profile of the body at the required implantation site. Without a sufficient thermal gradient at the implantation site, it may not be feasible to use thermoelectric harvesting to produce sufficient operational power in implantable biosensing applications.

Micro fuel cells are a suitable power generation scheme for implantable biosensing as long as the fuel cell is biocompatible. Regenerative fuel cells, such as glucose based fuel cells, can be implanted for long term operation since the fuel and oxidation reagent is replenished constantly through the electrochemical reactions that generate power. In addition, glucose is readily available in the body, thus additional fuel for glucose-based micro fuel cells is available if needed. Micro fuel cells using non-biocompatible reactants generally produce more power than those using biocompatible fuels. There are intrinsic difficulties when dealing with non-biocompatible reactants and implantation, such as the possibility of insufficient packaging causing the potential leaching of reactants out of the fuel cell damaging surrounding tissues. The smaller and more efficient a micro fuel cell, the more applicable it will be to implantable applications. Micro fuel cells are the only location independent MEMS-based generation technique, not relying on a specific implantation location or physical phenomenon to supply the specific input energy required to produce power. As long as the implantation location can

accommodate the size of the micro fuel cell and does not impart any specific loading to the micro fuel cell that may damage its packaging, it would be applicable for implantable biosensing techniques.

Electrostatic MEMS-based energy harvesting requires predictable vibrations in order to produce an optimum amount of electricity. The strength of electrostatic MEMS-based harvesting lies within the multiple actuation directions and arrangements that are possible. This is important for biosensing applications, since conceivably, electrostatic harvesting could be used in a multitude of orientations, many of which would not be possible with other vibration-based harvesting schemes. However, rotation and off axis motion is troublesome for electrostatic based schemes, causing potential damage through collision and stiction. In addition, in order to generate power, the electrostatic harvester must be pre-charged in order to take full advantage of the motion-induced capacitance changes. Efficiency of these systems is improved by using self-charging mechanisms such as electrets and charge pumps. Using these self-charging mechanisms, the electrostatic MEMS-based energy harvesters are a self-contained system suitable for a multitude of implantable biosensing applications where known planar motions and vibrations are present.

Electromagnetic energy harvesting is currently used in some high profile implantable applications, such as harvesting supplementary power for pacemaker batteries [2]. As with electrostatic-based harvesting, electromagnetic harvesting has directional actuation dependence, therefore knowledge of the implantation site conditions is critical. However, electromagnetic harvesting is significantly more robust than electrostatic, since any out of plane actuation is usable—off axis actuation is not detrimental or damaging to the electromagnetic harvester. Optimization of the power generated through this strategy is achieved by maximizing the magnetic flux experienced by the coils of the harvester. Rotary electromagnetic harvesting is a well known method to maximize the magnetic flux possible on a macro-scale. Although a novel MEMS application and relatively high power density scheme, rotary motion may be difficult to supply to

the energy harvester in comparison to linear actuation. Therefore, linearly actuated electromagnetic MEMS-based energy harvesting techniques would have more possible implantable applications than rotary ones. Electromagnetic harvesting, although having reasonable power densities, can have scaling issues with miniaturization. As the scale of the electromagnetic harvesters decreases, it has been suggested by Beeby *et al.* [55] that the power output potential of the energy harvester decreases as well. The power density and power output of electromagnetic based schemes can lag behind other similar techniques in this size regime.

Piezoelectric based harvesting is suitable for implantable biosensing having high power densities allowing for sufficient power generation for many applications. For high power density piezoelectric MEMS-based harvesters using PZT films, the major challenge in regards to implantable applications is biocompatibility. Advancements toward biocompatible PZT-based piezoelectric harvesters have been made. Biocompatible packaging, such as PDMS will be required in order to allow piezoelectric schemes to be used in implantable biosensing applications. Although AlN and ZnO-based energy harvesters have less power generation potential according to the material properties of the respective piezoelectric films, important advances have been made towards using energy harvesters based on these materials in *in vivo* applications. The recent advances and inherent biocompatibility of AlN and ZnO-based piezoelectric generators give an interesting alternative to PZT-based systems for implantable applications. As with electromagnetic generation, off-axis actuation is non-optimal, but will not prevent harvesting or cause damage. Optimization of the frequency response is required in order to maximize the power generated. The vibrations that actuate the piezoelectric energy harvesters can be low frequency and low amplitude, which are easily achievable for implantable biosensing. The piezoelectric energy harvesters can be tuned to specific frequency responses found at the implantation site, allowing the energy harvesters to be designed to maximize the local power generation possible at an implantation site.

Determining the correct energy harvesting scheme for a specific implantable biosensing application can be a difficult task. Power density is important for implantable biosensing power harvesting. The smaller an energy harvester can be in this case, the less invasive the implant. Therefore, energy harvesters with high power densities, for example, those using piezoelectric and electromagnetic schemes would be the least invasive for a vibration-based application, requiring the smallest volume to provide a necessary power level. In situations where more than one generation physics can be utilized, power density should be a major consideration in order to reduce the power system's overall size.

For a general application, the most significant factor used in determining the most applicable energy harvesting technique to use is the ambient energy available. Whether the energy available is solar energy, heat, or vibration, the energy harvesting technologies studied are exclusive in terms of their input energy. For the work of this thesis, vibration was chosen initially due to the applicability with implantable biosensing. Through the development of the project, the motivation to harvest electricity through vibration branched into more general low frequency vibration-driven applications, such as consumer, structural health monitoring and military human-actuated energy harvesting. Regardless of the specific application to which a specific vibrational harvester is to be applied, the goal remains the same – maximize the harvested energy. Given the specific methods of vibration-based energy harvesting, the most suitable harvesting method for a generalized application is piezoelectric energy harvesting. Electrostatic-based methods have very rigid vibration direction and amplitude restrictions to prevent mechanical damage. Additionally, the typical electrostatic harvester requires input electricity to harvest electricity. The electromagnetic schemes do not have a directional dependency, however, scale very poorly as they are miniaturized. Although the piezoelectric schemes do suffer from losses from non-optimal off-axis vibration, the flexibility of design, fewer constraints on input vibration, and good length based scaling make piezoelectric energy harvesting the clear choice to pursue in this thesis. Of the piezoelectric energy harvesting

methods, the beam-based methods are the most universal methods of harvesting energy from an ambient vibration. The general designs of the beam-based harvesters have certain mechanical limitations that this thesis will address. Due to scaling and microfabrication processes, residual stresses in thin structures become a major challenge. For example, Choi *et al.* [75] experienced this problem with the curling of their cantilever-based harvester, as seen in Figure 2.8.
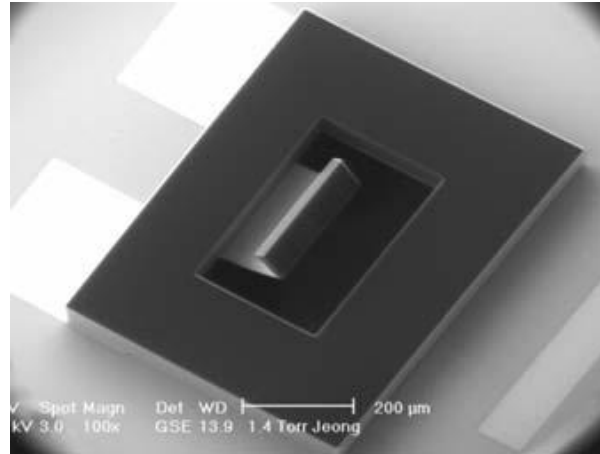
Figure 2.8 – Residual stresses curling a cantilever piezoelectric energy harvester produced by Choi *et al.* [75] (Reproduced with permission).

As will be discussed in Chapter 3, the residual stress and curling mechanically stiffen cantilever-based harvesters in general. This ultimately complicates attempts of natural frequency reduction. In this Chapter 3, a novel design using a folded fixed-fixed spring will be discussed to overcome this challenge.

Additionally, as discussed earlier this chapter, arrays of beam-based piezoelectric harvesters are used by Liu *et al.* [85] to increase the natural frequency bandwidth of the harvester. This harvesting system can be seen in Figure 2.9.
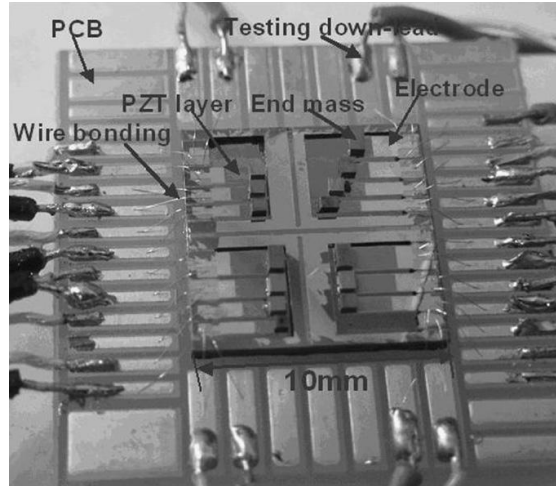
Figure 2.9 – The array-based piezoelectric energy harvester produced by Liu *et al.* [85] (Reproduced with permission).

Additional to widening the bandwidth, this arrangement of harvesters can be used to increase the power output by electrically arraying the harvesters. If the harvesters are all driven at the same natural frequency, rather than spreading out the operational frequencies as the harvester in Figure 2.9, the harvester array can be used to maximize the power output. The evolution of the fixed-fixed folded spring design, as described in Chapter 3 integrating proof masses into the system, will utilize the array methodology to reduce the natural frequency and increase the power output of the harvesters.

2.4 Piezoelectric Materials

The energy harvester to be examined in this thesis requires a piezoelectric thin film to convert the harvested strain into electricity. There are three materials used in literature that can be used for this application: lead zirconate titanate (PZT), zinc oxide, and aluminum nitride. In literature, PZT is the dominantly used for power generation purposes. Zinc oxide and aluminum nitride are more commonly used in actuation and sensing. In terms of microfabrication, zinc oxide and aluminum nitride are less complicated and have fewer equipment contamination issues than PZT. The material properties of these thin films are shown in Table 2.3.

Table 2.3 - Thin Film Piezoelectric Materials [88]

Thin Film Piezoelectric Material	Fabrication Method	Fabrication Difficulty (Easy/Medium/ Difficult)	Piezoelectric Coefficient d_{31} (pC/N)	Piezoelectric Coefficient d_{33} (pC/N)
Aluminum Nitride	Sputtering	Easy (Sputtering)	0.7	2.0
Lead Zirconate Titanate (PZT)	Sputtering, Sol-Gel Deposition, Metal Oxide Chemical Vapor Deposition (MOCVD)	Easy (Sputtering) Medium (Sol-Gel Deposition, MOCVD)	-60 (PZT-2) -171 (PZT-5) -220 (PZT-5J)	152 (PZT-2) 374 (PZT-5) 500 (PZT-5J)
Zinc Oxide	Sputtering	Easy (Sputtering)	-5.43	11.67

As shown in Table 2.3, the piezoelectric coefficients for a variety of PZT materials are much higher in magnitude than aluminum nitride and zinc oxide thin films. The energy harvesters designed utilize the 31-mode, or "beam bending" mode of the piezoelectric material, therefore higher piezoelectric coefficients, especially the d_{31} coefficient, are desirable [60]. In addition, although PZT can have significant fabrication-based challenges, the variety of materials and deposition technologies allows for greater control over the material properties and deposition thicknesses of the film which is beneficial for further optimization of the generator itself. Although there have been recent advances in using aluminum nitride/zinc oxide in energy harvesting applications, as discussed earlier in this chapter, PZT will be the primary piezoelectric material used in this stiffness optimized energy harvester.

For PZT films to exhibit their desirable mechanical, ferroelectric and dielectric properties, it is necessary for the film to exhibit the proper perovskite crystal structure. The films enter this crystal phase when annealed at the appropriate crystallization temperature [92].

Usually, the composition of PZT is described as $PbZr_xTi_{1-x}O_3$, where x denotes the finite range where there the morphotropic phase boundary involves a coexistence of tetragonal and rhombohedral crystal phases [93]. When both of these phases coincide, a local fluctuation in the composition is present, which in turn generates a local fluctuation in the lattice parameters, which greatly affects

the ferroelectric properties of the PZT, as seen by the large range of material properties [92-96]. Usually, for PZT, the parameter *x* can vary between 0.4 and 0.6, depending on the desired material properties.

There are several important thickness-dependant material properties of the PZT that will have significant consequences to the harvester. For example, the relative permittivity of the PZT film is dependent upon the thickness of the film [97]. Additionally, thinner films have the tendency to release lead during the required crystallization anneals, producing low-lead pyrochlore PZT with reduced permittivity [98]. The relation between the PZT thickness and the relative permittivity for the specific PZT material used in this study can be seen in Figure 2.10.
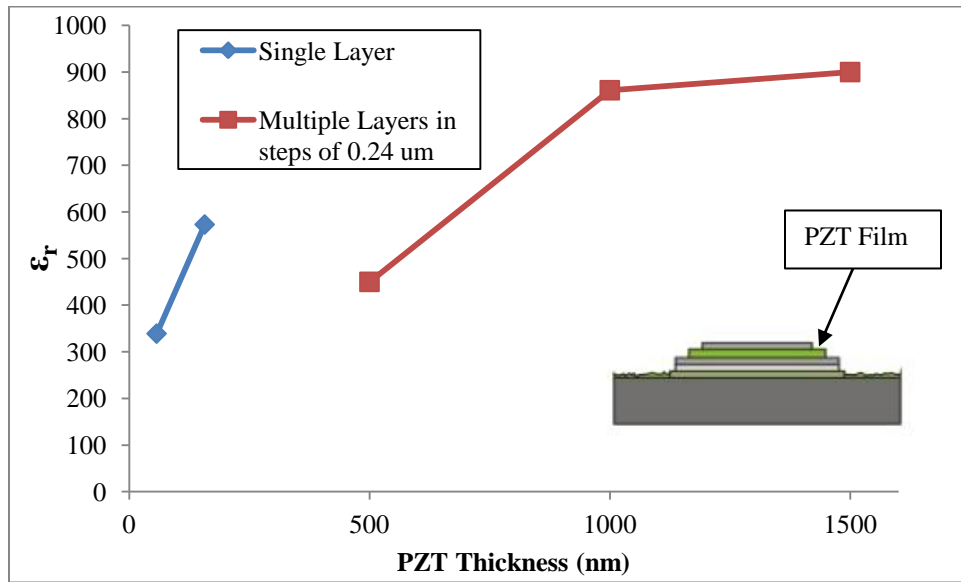
Figure 2.10 – The dependence of the relative permittivity versus the PZT thickness. Single layer thickness was approximately 0.24 μm, Multilayer thickness started at 0.48 μm and incremented in steps of 0.24 μm.[97] (Reproduced with Permission)

Although a thicker film will increase the output voltage produced due to the increase of strain applied to the PZT layer, the thickness will directly affect the input impedance of the harvester as described in equations (7) and (8):

$$C = \frac{\varepsilon_o \varepsilon_r A}{d} \qquad (7)$$

$$Z = \frac{1}{2\pi\omega C} \qquad (8)$$

Where C is the capacitance of the PZT layer, ε_o is the permittivity of free space, ε_r is the relative permittivity, A is the active area of the PZT layer, d is the thickness of the PZT layer, Z is the input impedance of the harvester, and ω is the operational frequency of the harvester. It is clear from (7) and (8) that the input impedance of the harvester is directly tied to permittivity of the PZT layer through the thickness of the PZT layer. Although there will be an increased voltage output from the increase of strain on the PZT film through increasing the film thickness, the input impedance and optimum load resistance will increase as well, causing the current produced to increase at a smaller rate. If these values are used in equation (1) of Chapter 3, the maximum power output of the harvester can be calculated analytically. The interdependence of these two values will change the ratio of current to voltage produced as output power.

2.5   Summary

Piezoelectric generation is a very flexible and robust method of generating electricity on a micro-scale. Devices centered on piezoelectric generation are highly customizable, and can be designed for many applications. The majority of the research into piezoelectric energy harvesters centers on optimizing the performance of the generator through manipulation of the frequency spectrum of the device.

The research in this project will focus on the further optimization of the piezoelectric energy harvester by manipulating the mechanical stiffness of the energy harvester to reduce the natural frequency to optimum generation levels. The majority of research in the field focuses on cantilever based methods where some limited attempts at structural optimization have occurred. This thesis will focus on applying a fixed-fixed folded spring as an alternative structural element to the traditional cantilever typically used in vibration-based piezoelectric energy

harvesting. The methodology applied to develop the folded spring structure for this application is discussed in the following chapter.

2.6   References:

[1]   E. Schroeppel and J. Lin, "Reliability and Clinical Assessment of Pacemaker Power Sources," in *Handbook of Solid State Batteries & Capacitors*, 2 ed, M. Z. A. Munshi, Ed. London: World Scientific Publishing Co, 1999.

[2]   P. Roberts, G. Stanley, and J. M. Morgan, "Abstract 2165: Harvesting the Energy of Cardiac Motion to Power a Pacemaker," *Circulation,* vol. 118, pp. S_679-c-680, October 28, 2008 2008.

[3]   A. M. Barnett, F. A. Domian, B. W. Feycock, D. H. Ford, C. L. Kendall, J. A. Rand, T. R. Ruffins, M. L. Rock, and R. B. Hall, "Development of large area thin crystalline silicon-film solar cells," in *Photovoltaic Specialists Conference, 1988., Conference Record of the Twentieth IEEE*, 1988, pp. 1569-1574 vol.2.

[4]   E. Cantatore and M. Ouwerkerk, "Energy scavenging and power management in networks of autonomous microsensors," *Microelectronics Journal,* vol. 37, pp. 1584-1590, 2006.

[5]   A. G. Dentai, E. C. Burrows, C. R. Giles, C. A. Burrus, and J. C. Centanni, "High-voltage (2.1 V) integrated InGaAs photogenerator," *Electronics Letters,* vol. 33, pp. 718-719, 1997.

[6]   A. G. Dentai, C. R. Giles, E. Burrows, C. A. Burrus, L. Stulz, J. Centanni, J. Hoffman, and B. Moyer, "A long-wavelength 10-V optical-to-electrical InGaAs photogenerator," *Ieee Photonics Technology Letters,* vol. 11, pp. 114-116, Jan 1999.

[7]   C. R. Giles, A. Dentai, C. A. Burrus, L. Kohutich, and J. Centanni, "Microwatt-power InGaAs photogenerator for lightwave networks," *Ieee Photonics Technology Letters,* vol. 9, pp. 666-668, 1997.

[8]   M. Ichiki, H. Furue, T. Kobayashi, Y. Morikawa, K. Nonaka, and R. Maeda, "Photovoltaic properties of ferroelectrics and its applications to optical sensor," Canberra, Australia, 2008, pp. Society of Photo-Optical Instrumentation Engineers (SPIE).

[9]   K. B. Lam, E. A. Johnson, M. Chiao, and L. W. Lin, "A MEMS photosynthetic electrochemical cell powered by subcellular plant photosystems," *Journal of Microelectromechanical Systems,* vol. 15, pp. 1243-1250, Oct 2006.

[10] J. B. Lee, Z. Z. Chen, M. G. Allen, A. Rohatgi, and R. Arya, "A Miniturized High-Voltage Solar-Cell Array as an Electrostatic MEMS Power-Supply. ," *Journal of Microelectromechanical Systems,* vol. 4, pp. 102-108, Sep 1995.

[11] R. Peña, "Photovoltaic converters for optical fibre-based power-by-light systems," Madrid: Universidad Politecnica de Madrid, 2004.

[12] S. Roundy, P. K. Wright, and K. S. J. Pister, "Micro-Electrostatic Vibration-to-Electricity Converters," in *ASME International Mechanical Engineering Congress and Exposition*, 2002.

[13] S. Wojtczuk, T. Parodos, and G. Walker, "P/N In(Al) GaAs multijunction laser power converters," in *Proceedings of the 13th Space Photovoltaic Research and Technology Conference (SPRAT 13)*, Cleveland, OH, United states, 1994, pp. 363-363.

[14] C. L. Bellew, S. Hollar, and K. S. J. Pister, "An SOI process for fabrication of solar cells, transistors and electrostatic actuators," in *TRANSDUCERS, Solid-State Sensors, Actuators and Microsystems, 12th International Conference on, 2003 TRANSDUCERS, Solid-State Sensors, Actuators and Microsystems, 12th International Conference on, 2003 VO - 2*, 2003, pp. 1075-1078 vol.2.

[15] K. Fu, A. J. Knobloch, F. C. Martinez, D. C. Walther, C. Fernandez-Pello, A. P. Pisano, and D. Liepmann, "Design and fabrication of a silicon-based mems rotary engine," in *Proceedings of 2001 ASME International Mechanical Engineering Congress and Exposition* New York, NY, United states, 2001, pp. 875-880.

[16] T. Huesgen, P. Woias, and N. Kockmann, "Design and fabrication of MEMS thermoelectric generators with high temperature efficiency," *Sensors and Actuators, A: Physical,* vol. 145-146, pp. 423-429, 2008.

[17] N. Kockmann, T. Huesgen, and P. Woias, "Microstructured in-plane thermoelectric generators with optimized heat path," in *TRANSDUCERS and EUROSENSORS '07 - 4th International Conference on Solid-State Sensors, Actuators and Microsystems*, Lyon, France, 2007, pp. 133-136.

[18] V. Leonov, P. Fiorini, S. Sedky, T. Torfs, and C. Van Hoof, "Thermoelectric MEMS generators as a power supply for a body area network," in *Digest of Technical Papers - International Conference on Solid State Sensors and Actuators and Microsystems, TRANSDUCERS '05*, Seoul, Korea, Republic of, 2005, pp. 291-294.

[19] A. Mehra, X. Zhang, A. A. Ayon, I. A. Waitz, M. A. Schmidt, and C. M. Spadaccini, "Six-wafer combustion system for a silicon micro gas turbine

engine," *Journal of Microelectromechanical Systems,* vol. 9, pp. 517-527, 2000.

[20]   J. A. Paradiso and T. Starner, "Energy scavenging for mobile and wireless electronics," *Ieee Pervasive Computing,* vol. 4, pp. 18-27, JAN-MAR 2005.

[21]   J. Stevens, "Optimized Thermal Design of Small DT Thermoelectric Generator," in *34th Intersociety Energy Conversion Engineering Congress of the Society of Automotive Engineers*, 1999, pp. 1999-01-2564.

[22]   M. Tecpoyotl-Torres, J. Varona, A. A. Hamoui, J. Escobedo-Alatorre, and J. Sanchez-Mondragon, "Polysilicon thermal micro-actuators for heat scavenging and power conversion," San Diego, CA, United states, 2008, p. The International Society for Optical Engineering (SPIE).

[23]   S. Whalen, M. Thompson, D. Bahr, C. Richards, and R. Richards, "Design, fabrication and testing of the P3 micro heat engine," *Sensors and Actuators, A: Physical,* vol. 104, pp. 290-298, 2003.

[24]   S. Kerzenmacher, J. Ducree, R. Zengerle, and F. von Stetten, "An abiotically catalyzed glucose fuel cell for powering medical implants: Reconstructed manufacturing protocol and analysis of performance," *Journal of Power Sources,* vol. 182, pp. 66-75, 2008.

[25]   M. Kuhn, T. Napporn, M. Meunier, D. Therriault, and S. Vengallatore, "Fabrication and testing of coplanar single-chamber micro solid oxide fuel cells with geometrically complex electrodes," *Journal of Power Sources,* vol. 177, pp. 148-153, 2008.

[26]   N. Mano, F. Mao, and A. Heller, "Characteristics of a Miniature Compartment-less Glucose; O2 Biofuel Cell and Its Operation in a Living Plant," *Journal of the American Chemical Society,* vol. 125, pp. 6588-6594, 2003.

[27]   S. Park and J. M. Vohs, "Direct oxidation of hydrocarbons in a solid-oxide fuel cell. ," *Nature* vol. 404 2000.

[28]   J. R. Rao, "Bioelectrochemistry. I. Biological Redox Reactions," G. Milazzo and M. Black, Eds. New York: Plenum Press, 1983, pp. 283-355.

[29]   S. Aravamudhan, A. R. A. Rahman, and S. Bhansali, "Porous silicon based orientation independent, self-priming micro direct ethanol fuel cell," *Sensors and Actuators, A: Physical,* vol. 123-124, pp. 497-504, 2005.

[30]   J. Cao, Z. Zou, Q. Huang, T. Yuan, Z. Li, B. Xia, and H. Yang, "Planar air-breathing micro-direct methanol fuel cell stacks based on micro-

electronic-mechanical-system technology," *Journal of Power Sources,* vol. 185, pp. 433-438, 2008.

[31] J. P. Esquivel, N. Sabate, J. Santander, N. Torres, and C. Cane, "Fabrication and characterization of a passive silicon-based direct methanol fuel cell," in *Proc. SPIE - Int. Soc. Opt. Eng. (USA)*, USA, 2007, pp. 658903-1.

[32] N. Kuriyama, T. Kubota, D. Okamura, T. Suzuki, and J. Sasahara, "Design and fabrication of MEMS-based monolithic fuel cells," in *TRANSDUCERS and EUROSENSORS '07 - 4th International Conference on Solid-State Sensors, Actuators and Microsystems*, Lyon, France, 2007, pp. 283-286.

[33] S. Motokawa, M. Mohamedi, T. Momma, S. Shoji, and T. Osaka, "MEMS-based design and fabrication of a new concept micro direct methanol fuel cell (Î¼-DMFC)," *Electrochemistry Communications,* vol. 6, pp. 562-565, 2004.

[34] W. Y. Sim, G. Y. Kim, and S. S. Yang, "Fabrication of micro power source (MPS) using a micro direct methanol fuel cell (uDMFC) for the medical application," in *Micro Electro Mechanical Systems, 2001. MEMS 2001. The 14th IEEE International Conference on*, 2001, pp. 341-344.

[35] Z. Yufeng, T. Xiaochuan, Y. Zhenyu, and L. Xiaowei, "Direct methanol fuel cell stack based on MEMS technology," in *Proceedings of SPIE - The International Society for Optical Engineering*, Shenyang, China, 2009.

[36] Y. H. Seo and Y.-H. Cho, "A miniature direct methanol fuel cell using platinum sputtered microcolumn electrodes with limited amount of fuel," in *Proceedings of the IEEE Micro Electro Mechanical Systems (MEMS)*, Kyoto, Japan, 2003, pp. 375-378.

[37] H.-W. Lo and Y.-C. Tai, "Parylene-HT-based electret rotor generator," in *Proceedings of the IEEE International Conference on Micro Electro Mechanical Systems (MEMS)*, Tucson, AZ, United states, 2008, pp. 984-987.

[38] A. M. Paracha, P. Basset, D. Galayko, F. Marty, and T. Bourouina, "A Silicon MEMS DC/DC Converter for Autonomous Vibration-to-Electrical-Energy Scavenger," *Ieee Electron Device Letters,* vol. 30, pp. 481-483, May 2009.

[39] T. Sterken, P. Fiorini, G. Altena, C. Van Hoof, and R. Puere, "Harvesting energy from vibrations by a micromachined electret generator," in *TRANSDUCERS and EUROSENSORS '07 - 4th International Conference on Solid-State Sensors, Actuators and Microsystems*, Lyon, France, 2007, pp. 129-132.

[40]   B. C. Yen and J. H. Lang, "A variable-capacitance vibration-to-electric energy harvester," *IEEE Transactions on Circuits and Systems I: Regular Papers,* vol. 53, pp. 288-295, 2006.

[41]   V. Leonov, P. Fiorini, and C. Van Hoof, "Stabilization of positive charge in SiO2/Si3N 4 electrets," *IEEE Transactions on Dielectrics and Electrical Insulation,* vol. 13, pp. 1049-1056, 2006.

[42]   W. Ma, L. Rufer, Y. Zohar, and M. Wong, "Design and implementation of an integrated floating-gate electrostatic power micro-generator," in *Digest of Technical Papers - International Conference on Solid State Sensors and Actuators and Microsystems, TRANSDUCERS '05*, Seoul, Korea, Republic of, 2005, pp. 299-302.

[43]   W. Ma, R. Q. Zhu, L. Rufer, Y. Zohar, and M. Wong, "An integrated floating-electrode electric microgenerator," *Journal of Microelectromechanical Systems,* vol. 16, pp. 29-37, Feb 2007.

[44]   S. Meninger, J. O. Mur-Miranda, R. Amirtharajah, A. Chandrakasan, and J. H. Lang, "Vibration-to-electric energy conversion," *Very Large Scale Integration (VLSI) Systems, IEEE Transactions on,* vol. 9, pp. 64-76, 2001.

[45]   G. Murillo, G. Abadal, F. Torres, J. L. Lopez, J. Giner, A. Uranga, and N. Barniol, "Harvester-on-chip: Design of a proof of concept prototype," *Microelectronic Engineering,* vol. 86, pp. 1183-1186, 2009.

[46]   A. Nounou and H. F. Ragaie, "A lateral comb-drive structure for energy scavenging," in *Proceedings - 2004 International Conference on Electrical, Electronic and Computer Engineering, ICEEC'04*, Cairo, Egypt, 2004, pp. 553-556.

[47]   K. B. T. Sterken, R. Puers, S. Borghs, "Power Extraction from Ambient Vibration," in *SeSens*, 2002, pp. 680-683.

[48]   S. P. T. Beeby, M.J.; White, N.M; O'Donnel, T.; Saha, C.; Kulkarni, S.; Roy, S., "Micromachined Silicon Generator for Harvesting Power from Vibrations," in *Power MEMS 2004*, Kyoto, Japan, 2004.

[49]   F. Herrault, C.-H. Ji, and M. G. Allen, "Ultraminiaturized high-speed permanent-magnet generators for milliwatt-level power generation," *Journal of Microelectromechanical Systems,* vol. 17, pp. 1376-1387, 2008.

[50]   C. T. Pan and T. T. Wu, "Simulation and fabrication of magnetic rotary microgenerator with multipolar Nd/Fe/B magnet," *Microelectronics Reliability,* vol. 47, pp. 2129-2134, 2007.

[51]   T. Reissman, J. S. Park, and E. Garcia, "Micro-solenoid electromagnetic power harvesting for vibrating systems," San Diego, CA, United states, 2008, p. The International Society for Optical Engineering (SPIE); American Society of Mechanical Engineers.

[52]   C. Serre, A. Perez-Rodriguez, N. Fondevilla, E. Martincic, J. R. Morante, J. Montserrat, and J. Esteve, "Design and implementation of mechanical resonators for optimized inertial electromagnetic microgenerators," in *Proceedings of SPIE - The International Society for Optical Engineering*, Maspalomas, Gran Canaria, Spain, 2007, p. SPIE Europe.

[53]   C. Serre, A. Perez-Rodriguez, N. Fondevilla, J. R. Morante, J. Montserrat, and J. Esteve, "Vibrational energy scavenging with Si technology electromagnetic inertial microgenerators," *Microsystem Technologies,* vol. 13, pp. 1655-1661, 2007.

[54]   R. Amirtharajah and A. P. Chandrakasan, "Self-powered signal processing using vibration-based power generation," *Ieee Journal of Solid-State Circuits,* vol. 33, pp. 687-695, MAY 1998.

[55]   S. P. Beeby, M. J. Tudor, R. N. Torah, S. Roberts, T. O'Donnell, and S. Roy, "Experimental comparison of macro and micro scale electromagnetic vibration powered generators," *Microsystem Technologies,* vol. 13, pp. 1647-1653, 2007.

[56]   C. R. Saha, T. O'Donnell, H. Loder, S. Beeby, and J. Tudor, "Optimization of an electromagnetic energy harvesting device," *IEEE Transactions on Magnetics,* vol. 42, pp. 3509-11, 2006.

[57]   M. S. M. Soliman, E. F. El-Saadany, and R. R. Mansour, "Electromagnetic MEMS Based Micro-Power Generator," in *Industrial Electronics, 2006 IEEE International Symposium on*, 2006, pp. 2747-2753.

[58]   S. P. Beeby, R. N. Torah, M. J. Tudor, P. Glynne-Jones, T. O'Donnell, C. R. Saha, and S. Roy, "A micro electromagnetic generator for vibration energy harvesting," *Journal of Micromechanics and Microengineering,* vol. 17, pp. 1257-1265, 2007.

[59]   P. Glynne-Jones, M. J. Tudor, S. P. Beeby, and N. M. White, "An electromagnetic, vibration-powered generator for intelligent sensor systems," *Sensors and Actuators a-Physical,* vol. 110, pp. 344-349, FEB 1 2004.

[60]   S.-N. Chen, G.-J. Wang, and M.-C. Chien, "Analytical modeling of piezoelectric vibration-induced micro power generator," *Mechatronics,* vol. 16, pp. 379-387, 2006.

[61] R. Elfrink, T. M. Kamel, M. Goedbloed, S. Matova, D. Hohlfeld, Y. Van Andel, and R. Van Schaijk, "Vibration energy harvesting with aluminum nitride-based piezoelectric devices," *Journal of Micromechanics and Microengineering,* vol. 19, 2009.

[62] T. Ishisaka, H. Sato, Y. Akiyama, Y. Furukawa, and K. Morishima, "Bio-actuated power generator using heart muscle cells on a PDMS membrane," in *TRANSDUCERS and EUROSENSORS '07 - 4th International Conference on Solid-State Sensors, Actuators and Microsystems*, Lyon, France, 2007, pp. 903-906.

[63] F. Lu, H. P. Lee, and S. P. Lim, "Modeling and analysis of micro piezoelectric power generators for micro-electromechanical-systems applications," *Smart Materials & Structures,* vol. 13, pp. 57-63, FEB 2004.

[64] C. Mo, L. J. Radziemski, and W. W. Clark, "Performance comparison of implantable piezoelectric energy harvesters," San Diego, CA, United states, 2008, p. The International Society for Optical Engineering (SPIE); American Society of Mechanical Engineers.

[65] M. J. Ramsay and W. W. Clark, "Piezoelectric Energy Harvesting for bio-MEMS Applications," in *SPIE 4332*, 2001, pp. 429-438.

[66] S. Roundy and P. K. Wright, "A piezoelectric vibration based generator for wireless electronics," *Smart Materials and Structures,* vol. 13, pp. 1131-1142, 2004.

[67] T. Starner, "Human-powered wearable computing," *IBM Systems Journal,* vol. 35, pp. 618-629, 1996.

[68] J. Zelenka, *Piezoelectric Resonators and Their Applications*. Amsterdam: Elsevier, 1986.

[69] P. X. Gao, J. Song, J. Liu, and Z. L. Wang, "Nanowire piezoelectric nanogenerators on plastic substrates as flexible power sources for nanodevices," *Advanced Materials,* vol. 19, pp. 67-72, 2007.

[70] Z. Li, G. Zhu, R. Yang, A. C. Wang, and Z. L. Wang, "Muscle-Driven In Vivo Nanogenerator," *Advanced Materials,* vol. 22, pp. 2534-2537, 2010.

[71] S. Xu, Y. Qin, C. Xu, Y. Wei, R. Yang, and Z. L. Wang, "Self-powered nanowire devices," *Nat Nano,* vol. 5, pp. 366-373, 2010.

[72] J. Y. K. Kang, H.J.; Kim J.S; Kim, T.S, "Optimal Design of Piezoelectric Cantilever for Micropower Generator with Microbubble," in *2nd Annual International IEEE-EMBS Special Topic Conference of Microtechnologies in Medicine and Biology*, 2002, pp. 424-427.

[73] Y. Liu, K. Ren, H. F. Hofmann, and Q. Zhang, "Electrostrictive polymers for mechanical energy harvesting," in *Smart Structures and Materials 2004 - Electroactive Polymer Actuators and Devices (EAPAD), Mar 15-18 2004*, San Diego, CA, United Kingdom, 2004, pp. 17-28.

[74] G. W. Taylor, J. R. Burns, S. A. Kammann, W. B. A.-P. Powers, W.B., and T. R. A.-W. Welsh, T.R., "The Energy Harvesting Eel: a small subsurface ocean/river power generator," *Oceanic Engineering, IEEE Journal of,* vol. 26, pp. 539-547, 2001.

[75] W. J. Choi, Y. Jeon, J. H. Jeong, R. Sood, and S. G. Kim, "Energy harvesting MEMS device based on thin film piezoelectric cantilevers," *Journal of Electroceramics,* vol. 17, pp. 543-548, 2006.

[76] R. Duggirala, R. Polcawich, E. Zakar, M. Dubey, H. Li, and A. Lal, "MEMS radioisotope-powered piezoelectric -power generator (RPG)," in *Proceedings of the IEEE International Conference on Micro Electro Mechanical Systems (MEMS)*, Istanbul, Turkey, 2006, pp. 94-97.

[77] H. B. Fang, J. Q. Liu, Z. Y. Xu, L. Dong, L. Wang, D. Chen, B. C. Cai, and Y. Liu, "Fabrication and performance of MEMS-based piezoelectric power generator for vibration energy harvesting," *Microelectronics Journal,* vol. 37, pp. 1280-1284, 2006.

[78] N. M. White, P. Glynne-Jones, and S. P. Beeby, "A novel thick-film piezoelectric micro-generator," *Smart Materials and Structures,* vol. 10, pp. 850-852, 2001.

[79] Y. B. Jeon, R. Sood, J. H. Jeong, and S. G. Kim, "MEMS power generator with transverse mode thin film PZT," *Sensors and Actuators, A: Physical,* vol. 122, pp. 16-22, 2005.

[80] I. Kuehne, D. Marinkovic, G. Eckstein, and H. Seidel, "A new approach for MEMS power generation based on a piezoelectric diaphragm," *Sensors and Actuators, A: Physical,* vol. 142, pp. 292-297, 2008.

[81] B.-S. Lee, S.-C. Lin, and W.-J. Wu, "Comparison of the piezoelectric MEMS generators with interdigital electrodes and laminated electrodes," San Diego, CA, United states, 2008, p. The International Society for Optical Engineering (SPIE); American Society of Mechanical Engineers.

[82] B.-S. Lee, P.-J. Shih, J.-J. He, W.-P. Shih, and W.-J. Wu, "A study of implantable power harvesting transducers," in *Proceedings of SPIE - The International Society for Optical Engineering*, San Diego, CA, United states, 2007, pp. SPIE; American Society of Mechanical Engineers, ASME.

[83]   P.-J. Shih, W.-P. Weng, W.-P. Shih, Y.-C. Tsai, and P.-Z. Chang, "Acoustic polarization for optimized implantable power transimittion," in *Proceedings of the IEEE International Conference on Micro Electro Mechanical Systems (MEMS)*, Kobe, Japan, 2007, pp. 879-882.

[84]   D. L. H. Churchill, M.J; Townsend, C.P.; Arms, S.W;, "Strain Energy Harvesting For Wireless Sensor Networks," in *SPIE*, 2003, pp. 319-327.

[85]   J.-Q. Liu, H.-B. Fang, Z.-Y. Xu, X.-H. Mao, X.-C. Shen, D. Chen, H. Liao, and B.-C. Cai, "A MEMS-based piezoelectric power generator array for vibration energy harvesting," *Microelectronics Journal,* vol. 39, pp. 802-806, 2008.

[86]   D. Shen, J.-H. Park, J. Ajitsaria, S.-Y. Choe, H. C. Wikle, and D.-J. Kim, "The design, fabrication and evaluation of a MEMS PZT cantilever with an integrated Si proof mass for vibration energy harvesting," *Journal of Micromechanics and Microengineering,* vol. 18, 2008.

[87]   S. Kerzenmacher, J. Ducree, R. Zengerle, and F. von Stetten, "Energy harvesting by implantable abiotically catalyzed glucose fuel cells," *Journal of Power Sources,* vol. 182, pp. 1-17, 2008.

[88]   J. Lueke and W. A. Moussa, "MEMS-Based Power Generation Techniques for Implantable Biosensing Applications," *Sensors,* vol. 11, pp. 1433-1460, 2011.

[89]   D. S. L. Cardwell, *Wheels, clocks, and rockets : a history of technology / Donald Cardwell*: New York : W.W. Norton, 2001, c1995., 2001.

[90]   J. W. Gardner, V. K. Varadan, and O. O. Awadelkarim, *Microsensors MEMS and Smart Devices*. Chichester, West Sussex, England: John Wiley & Sons, 2001.

[91]   T. Desai, S. Bhatia, and M. Ferrari, *BioMEMs and Biomedical Nanotechnology: Volume III Therapeutic Micro/Nanotechnology*: Springer, 2006.

[92]   M. J. Madou, *Fundamentals of Microfabrication: The Science of Miniaturization*, Second ed.: CRC Press, 2002.

[93]   M. Klee, R. Eusemann, R. Waser, W. Brand, and H. van Hal, "Processing and electrical properties of Pb (ZrxTi1-x)O3 (x = 0.2-0.75) films. Comparison of metallo-organic decomposition and sol-gel processes," *Journal of Applied Physics,* vol. 72, p. 1566, 1992.

[94]   R. P. Areny and J. G. Webster, *Sensors and Signal Conditioning*. New York: Wiley, 1991.

[95]   A. M. Flynn, L. S. Tavrow, S. F. Bart, R. A. Brooks, D. J. Ehrlich, K. R. Udayakumar, and L. E. Cross, "Piezoelectric Micromotors," *J. Microelectromech. Syst.,* vol. 1, pp. 44-52, 1992.

[96]   A. D. Khazan, *Transducers and Their Elements*. Englewood Cliffs, N.J.: PTR Prentice Hall, 1994.

[97]   B. Marinkovic, T. Kaya, and H. Koser, "Characterization of ferroelectric material properties of multifunctional lead zirconate titanate for energy harvesting sensor nodes," *Journal of Applied Physics,* vol. 109, pp. -.

[98]   C. A. Randall, N. Kim, J.-P. Kucera, W. Cao, and T. R. Shrout, "Intrinsic and Extrinsic Size Effects in Fine-Grained Morphotropic-Phase-Boundary Lead Zirconate Titanate Ceramics," *Journal of the American Ceramic Society,* vol. 81, pp. 677-688, 1998.

3.1   Design Methodology of Fixed-Fixed Folded Spring Harvesters

As discussed in Chapter 2, piezoelectric energy harvesters convert vibration-induced strain to electricity via the piezoelectric effect. Piezoelectric materials have an inherent lack of inversion symmetry, which allows aligned electric dipoles to form within the material [1]. When the crystal structure of the piezoelectric material is strained, the micro-structure of the crystal is distorted. In order to maintain electrical equilibrium within the crystal the electrons become mobile and shift, creating a current [1,2]. This is referred to as the direct piezoelectric effect. The direct piezoelectric effect is mainly used for microgeneration and sensing purposes.

With respect to MEMS-based energy harvesting, there are a variety of methods of producing electricity from vibration, including utilizing piezoelectric beams, fibers, and membranes as discussed in Chapter 2. Piezoelectric-based beam energy harvesters convert the displacement of the beam under vibration into electricity. The most typical configuration of beam based energy harvesting utilizes a cantilever beam and a proof mass. As the structure is subjected to vibration, the strain experienced by the cantilever is applied to the piezoelectric films present on the cantilever, which in turn convert that strain into electricity. This system is shown schematically in Figure 3.1.
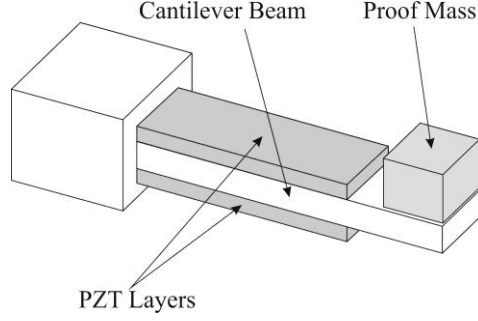
Figure 3.1 – Typical configurations of cantilever-based piezoelectric energy
harvesters [3].

The majority of the research in beam-based piezoelectric energy harvesting focuses on the optimization of the power generation of the harvester. As discussed in Chapter 2, the important design rules of these systems have been postulated by Roundy *et al.* [4-6]. Typically, this framework is used to optimize a specific design of piezoelectric energy harvester. The core design rules postulated by Roundy *et al.* [4-6] state that the output power is maximized when the harvester operates at a low frequency, at or near resonance. For this study, the natural/operational frequency of the harvester will be reduced as much as possible, while maintaining mechanical stability, to maximize the power output. Additionally, the closer the natural frequency of the device is as to the frequency of the input vibrations, the higher the output power will be. For this reason, the operational frequency of the harvesters studied will be kept as close as possible to the natural frequency of the harvester. The frequency dependence of the power output of the harvester can be seen in the analytical formulation shown in equation (1) [4].

$$P = \frac{1}{2R} \times \frac{\left(\frac{2k_{31}t_c}{k_2}\right)^2 \frac{c_p}{\varepsilon} A_{in}^2}{\left[\frac{\omega_n^2}{\omega R C_b} - \omega\left(\frac{1}{R C_b} + 2\xi\omega_n\right)\right]^2 + \left[\omega_n^2\left(1 + k_{31}^2\right) + \frac{2\xi\omega_n}{R C_b} - \omega^2\right]^2} \tag{1}$$

Where R is the load resistance, k_{31} is the piezoelectric coupling coefficient, t_c is the thickness the piezoelectric ceramic, k_2 is a geometric constant that relates

average piezoelectric material strain to the tip deflection, c_p is the elastic constant of the piezoelectric ceramic, ε is the dielectric constant of piezoelectric material, A_{in} is the input vibration amplitude, ω_n is the resonance frequency of the generator, ω is the frequency of driving vibrations, C_b is the capacitance of the piezoelectric bimorph, and ξ is the dimensionless damping ratio which represents the viscous loss from the system [4].

It can be seen from equation (1), in order to provide a high power output, the mechanical behaviour of the harvester is equally important as the electrical behaviour. To further investigate the effects of operational and natural frequency upon the power output of the harvester defined by (1), if all other variables are kept constant, while the operational frequency is varied for a set of natural frequencies, the general behaviour shown in shown in Figure 3.2 is observed.
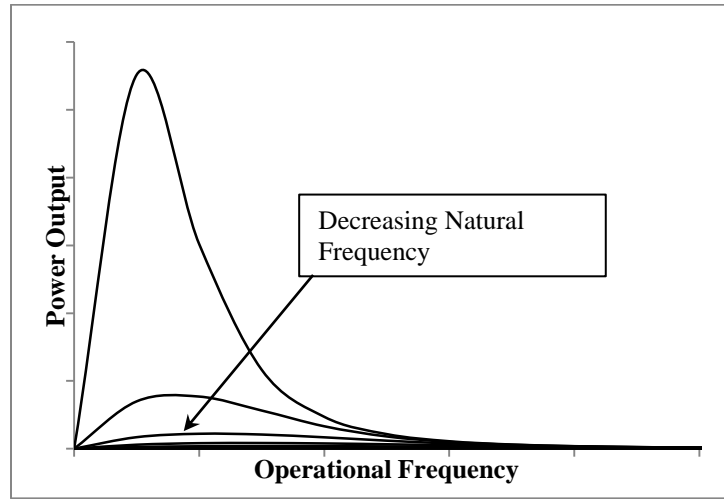
Figure 3.2 - General behaviour of equation (1) varying operational frequency for various natural frequencies, keeping other parameters constant.

As shown in Figure 3.2, the power output is maximum at lowest natural frequency. Additionally, the power output for each specific design of harvester, with a specific natural frequency, is maximized when the operational frequency matches the natural frequency. Therefore, to optimize the power output of the energy harvesters, assuming a matched operational and natural frequency, the highest power output will be achieved at the lowest natural frequency possible.

63

3.1.1   *Motivation for Frequency Optimization of the Energy Harvester*

As seen in equation (1) and Figure 3.2, the natural frequency of the energy harvester has a large effect on the overall power output of the device. The reduction of natural frequency of the harvester is of major importance for energy harvesting from ambient/low frequency vibration. The general scenario of vibrational energy harvesting involves actuation from a base vibration. This poses some interesting challenges in terms of the magnitude and frequency of acceleration load that can be applied to the harvester. The applied load is ultimately limited by the dynamics of the location upon which the harvester is located. This has a significant impact on the overall available energy for a vibration-based harvesting application. Taking into account of the general behavior of piezoelectric energy harvesters as discussed by equation (1), and by examining the case where the natural and operational frequencies are matched, it can be seen in Figure 3.3, that low frequency harvesting is the only real possibility for harvesting meaningful amounts of energy.
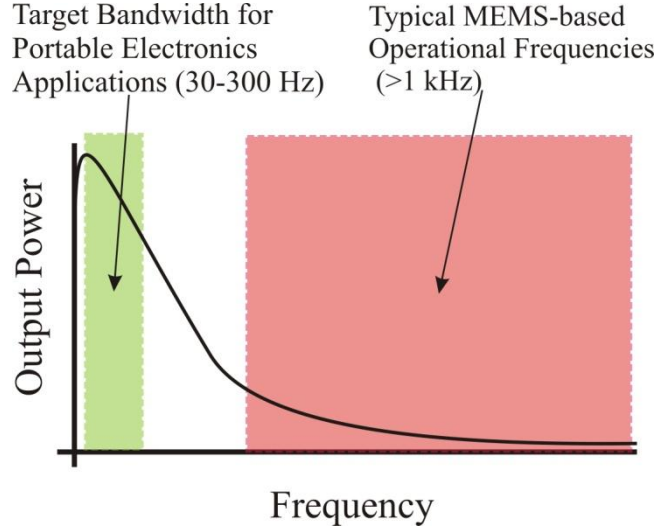
Figure 3.3 – General trend of power output of an energy harvester versus natural frequency/operational frequency.

For the generalized calculation performed above, using equation (1), realistic material property and acceleration values were taken from literature, with the assumption that the operational and natural frequencies were the same. This

simplification demonstrates that the maximum available power to the harvester is seen at low frequency vibrations. It should be noted, however, that for the above trend, this is maximum available power directly from the energy harvester, not taking into account conditioning circuitry concerns. Also, as shown in Figure 3.2, the operational bandwidth general MEMS devices is typically 1 kHz or more, therefore, applying traditional MEMS-based structures for piezoelectric harvesting is not suitable. Additionally, in Figure 3.2, it can be seen that low frequency vibrations, on the order of 30-300 Hz, the frequency range of vibrations typically seen by wireless and portable electronics and the higher output power regime of the energy harvesters coincide. This suggests that if a harvester's natural frequency could be reduced to that range, a reasonable power output could be attained.

The production of a harvester that is sensitive to low frequency ambient vibration represents the largest challenge in piezoelectric energy harvesting. The production of low natural frequency or low-stiffness MEMS devices is very difficult. Mechanically soft structures are hard to microfabricate, can be fragile, and are susceptible to fabrication-induced residual stresses. The following sections will outline the design and methodology that will be used in this research in order to provide a solution to this challenge.

3.2   Methodology

3.2.1   Frequency Optimization Methodology

The frequency response of the beam-based energy harvester can be optimized in two major ways: reducing the mechanical stiffness and adding inertial mass to the system. This can be seen by expressing the dynamics of the piezoelectric energy harvester a linear, one dimensional vibration problem, as shown in Figure 3.4.
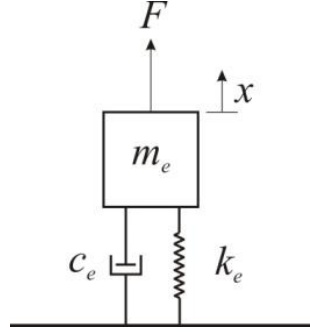
Figure 3.4 – One dimensional mass/spring/damper system.

The piezoelectric energy harvester can be represented (with some assumptions) as a simple linear mass/spring/damper system, with effective masses (m_e), spring stiffnesses (k_e), damping (c_e), displacement (x) with applied forces (F). In the simplification in Figure 3.4, the forces applied to the harvester represent the loading from the ambient vibration and may be time or frequency varying. The effective masses/stiffnesses/damping may be lumped using equations (2) and Figure 3.5 for various geometric configurations.

$$m_{e,cantilever} = M + 0.23m$$
$$k_{e,parallel} = k_1 + k_2 + \ldots + k_n$$
$$k_{e,series} = \frac{1}{k_1} + \frac{1}{k_2} + \ldots + \frac{1}{k_n}$$
$$c_{e,parallel} = c_1 + c_2 + \ldots + c_n$$
$$c_{e,series} = \frac{1}{c_1} + \frac{1}{c_2} + \ldots + \frac{1}{c_n}$$

(2)
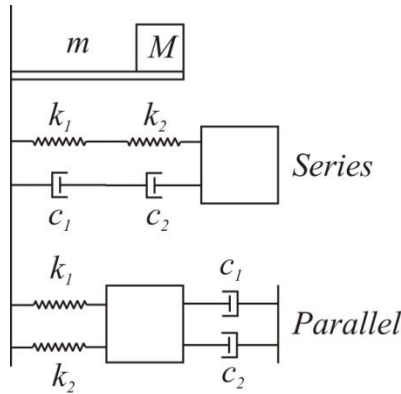
Figure 3.5 – Configurations of lumped systems relative to equation (2).

Where, in equation (2) and Figure 3.5, M is the mass of the suspended masses, m is the mass of the beam, k_n is the stiffness of the nth spring element, and c_n is the damping of the nth damper. As can be seen by equations (2), the proper equation of spring/damper systems must be chosen in order to properly represent the configuration of the system. The equations of motion and equation of natural frequency are shown in equations (3) and (4).

$$F(x) = m_e \ddot{x} + c_e \dot{x} + k_e x \tag{3}$$

$$\omega_n = \sqrt{\frac{k_e}{m_e}} \tag{4}$$

Where all terms in equations (3) and (4) are previously defined. From equation (4), if the stiffness of the harvester is decreased, the natural frequency will be decreased. The same trend will be seen for the increase of mass. Increasing the mass of the system is the preferred method of optimization in literature, and can be accomplished by adding proof or seismic masses to the energy harvesters. This is due to the difficulty of producing low stiffness MEMS structures that are both mechanically stable and do not suffer from residual stress stiffening. As seen in equation 4, increasing mass of the harvester alone cannot truly give a minimized natural frequency. There are several practical limitations that hinder the mass-based frequency optimization of the harvester. The size of the mass that can be added to an energy harvester is limited by practicality. Even with high density masses such as nickel or tungsten, it is typically not possible to microfabricate thick (larger than 1 mm) masses directly on the harvester. Therefore, these masses must be placed via flip chip or by hand to achieve the frequency reduction. Alternatively, as seen in equation (4), the reduction of stiffness can provide an alternate path to natural frequency reduction. Although this method is rarely undertaken in literature, it cannot be ignored in the natural frequency optimization of the energy harvester.

For cantilever based systems, the mechanical stiffness of the energy harvester can be expressed by equation (5) [1]:

$$k = \frac{EWH^3}{4L^3} \tag{5}$$

Where k is the beam stiffness, E is the Young's Modulus, W is the beam width, H is the beam thickness, and L is the length of the cantilever beam. Although the materials used to produce the harvesters are anisotropic, the representation of the Young's Modulus equation (5) is sufficient to illustrate the methodology. The typical methodology of reducing the stiffness of cantilever-based harvesters involves increasing length or decreasing the thickness of the cantilever. When the thickness of the beam is reduced, resulting in a "thin" structure ($H<<W$), the beam curling due to residual stress relaxation of the cantilever can become accentuated with increased length [1]. Even though the residual stress is relieved through the at-rest curling of the beam, this increased curvature will stiffen the system. This stiffness increase will oppose the vibration experienced by the energy harvester, thereby reducing the amplitude of vibration while increasing the natural frequency. This behavior directly opposes any geometry-based optimization of the cantilever-based harvester. Additionally, as will be discussed in the formulation of the complete stiffness of the fixed-fixed folded spring, the axial stress term can become dominant at increased beam length and decreased beam width [1]. In order to overcome this challenge, while reducing the natural frequency of the harvester, a folded spring will be used as the mechanical element of the harvester in this thesis.

3.2.2 Folded Spring Design and Methodology

Folded springs are commonly used in dynamic MEMS devices, such as comb drives and accelerometers, to provide both structural support and required cyclic movement with high accuracy and reliability. This folded spring concept, used in a fixed-fixed configuration, is the basis of the mechanical element that is the core of the stiffness-optimized energy harvester design. By folding the beam, as shown in Figure 3.6, the effective length of the beam exposed to bending is increased [1].
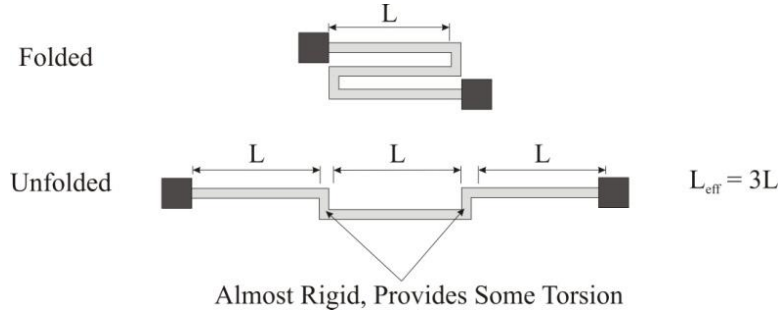
Figure 3.6 - Schematic of the folded spring showing folded and unfolded configurations. By unfolding the spring, the increase in effective bending length can be seen.

The residual stress of a fixed-fixed beam is very influential to the mechanical stiffness. The additional constraint of a second fixed beam end prevents the curling-based stress relaxation seen in cantilevers. Using energy methods, the complete non-linear force/deflection relation of the fixed-fixed beam can be derived, as shown in equation (6), taking into account residual stress effects [1].

$$F = \left\{ \left(\frac{\pi^2}{2} \right) \left[\frac{\sigma W H}{L} \right] + \left(\frac{\pi^4}{6} \right) \left[\frac{E W H^3}{L^3} \right] \right\} x + \left(\frac{\pi^4}{8} \right) \left[\frac{E W H}{L^3} \right] x^3 \qquad (6)$$

Where σ is the residual fabrication-based axial stress and the other terms are previously defined. Each term in x of the above equation specifically defines one component of the overall deflection of the fixed-fixed beam. The linear term in x has two coefficients. The first coefficient deals with the stiffness contribution from the residual axial stress (σ). The second coefficient deals with the small-deflection linear stiffness of the beam with respect to its moment of inertia. In equation (6) above, as L increases, the first term (residual stress term) in the stiffness equation dominates the linear stiffness. The non-linear term in x deals with the stretching of the neutral axis of the fixed-fixed beam [11].

The residual axial stress experienced by thin fixed-fixed beam systems can be overcome by folding the beam. Each individual beam segment is not axially constrained, therefore allowed to expand, contract, and rotate, relieving any beam curvature/residual stresses [7-9]. Therefore, the linear axial stress dependant term

69

of the stiffness is minimized and can be neglected, reducing equation (6) to equation (7).

$$F = \left\{ \left(\frac{\pi^4}{6} \right) \left[\frac{EWH^3}{L^3} \right] \right\} x + \left(\frac{\pi^4}{8} \right) \left[\frac{EWH}{L^3} \right] x^3 \qquad (7)$$

If (7) is examined in detail, varying the effective length of the folded spring through the number of folds, the trends shown in Figure 3.7 are found.
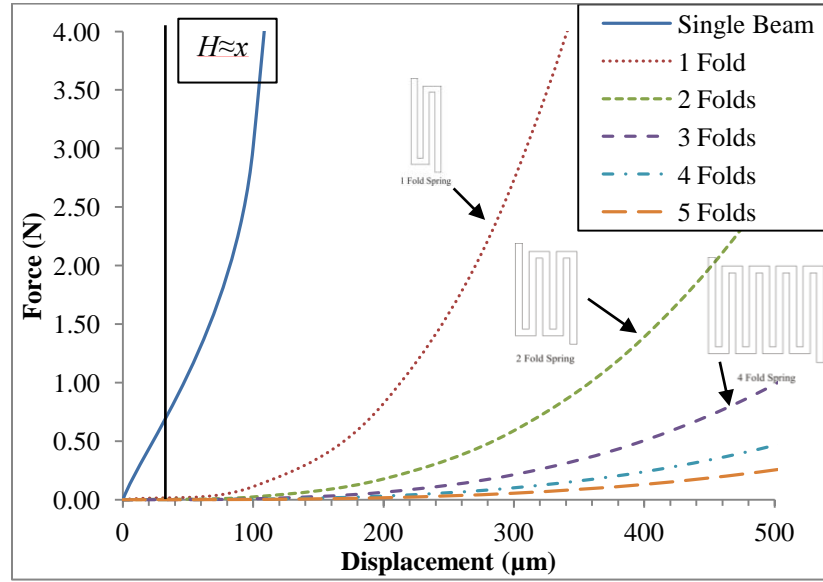
Figure 3.7 - The force versus deflection relations for a sample folded spring with respect to the number of folds comprising the spring. In this case the beam thickness (H) of the folded spring is 30µm.

As shown in Figure 3.7, the stiffness of the folded spring (the slope of the force/displacement relation) exhibits both non-linear and quasi-linear behavior. According to [1], equation (7) will behave linearly when the displacement of the beam is less than or equal to the thickness of the beam, or $H \lesssim x$. This behavior is seen in Figure 3.7 at lower deflections for all number of folds. As the number of folds is increased, this quasi-linear stiffness region expands above the $H \lesssim x$ linearity condition. This suggests that the quasi-linear behavior of the harvester can be extended by using a folded spring. Operating within the linear stiffness region is very important for the energy harvester. As discussed in Chapter 2,

section 2.4, the electrical parameters such as the input impedance of the harvester, are a function of the operational frequency. Since the output power is maximized when operational and natural frequencies match, the electrical properties of the harvester are directly tied to its frequency response. To ensure that maximum power transfer occurs, the load resistance must be matched to the input impedance of the harvester. If the harvester behaves non-linearly and experiences strain stiffening, the natural frequency will wander, causing both a change in input impedance and loss of power output. Conditioning circuitry will be matched according to the input impedance of the harvester; therefore, any stray in natural frequency will cause serious power transfer losses. Therefore, when possible, it is important to operate within the linear regimes to keep power outputs high and electrical properties consistent.

Furthermore, by limiting the input vibration amplitude to enforce the $H \lesssim x$ linearity condition and/or operating within the quasi-linear regime of the mechanical stiffness of a the specific fixed-fixed folded beam, the non-linear stiffness coefficient is eliminated, reducing equation (7) further to equation (8) [1]:

$$k = \frac{\pi^4}{6} \left[\frac{EWH^3}{L^3} \right] \tag{8}$$

If the assumption that the members connecting the individual beam elements, as shown in Figure 3.6, are rigid and only contribute to the stiffness with a negligible amount of torsion [1], the bending stiffness of the folded beam in Figure 3.6 can be expressed by equation (9).

$$k = \frac{\pi^4}{6} \left[\frac{EWH^3}{\left(L_{eff}\right)^3} \right] = \frac{\pi^4}{6} \left[\frac{EWH^3}{\left(3L\right)^3} \right] = \frac{\pi^4}{6} \left[\frac{EWH^3}{\left(nL\right)^3} \right] \tag{9}$$

Where *L,* in this case, is defined in Figure 3.6 and *n* is the number of beam lengths included within the folded beam structure. This simplification composed of the assumptions of residual stress relaxation, operation within the linear range, and

rigid connecting members allows for some interesting observations. The number of folds contained in the folded spring will significantly increase the effective length of the folded spring, decreasing its stiffness. The bending stiffness of the beam should be a major parameter in determining the overall mechanical stiffness of the structure. Additionally, the length of each individual beam segment in the folded spring should have a significant effect on the bending stiffness of the system. A parametric sensitivity study will be undertaken to confirm these observations.

In summary, there are several motivating factors to use a fixed-fixed folded spring as the elastic element of a piezoelectric energy harvester. Generally speaking, cantilever-based systems suffer from scaling problems, similarly to other MEMS systems, where the reduction in the length scale increases the natural frequency of the system. The general solution to this problem is to lengthen and thin the cantilever beam to counteract the increase of the natural frequency. Since the negative effects due to residual stresses in MEMS are length based, this increase in length causes the cantilever to be more susceptible to out of plane curling and stress stiffening. To counteract this phenomenon, the most typical optimization for cantilever based systems is to add relatively large proof masses to drive down the natural frequency. The fixed-fixed folded spring design can provide an alternative to this strategy. Although fixed-fixed beams are much stiffer per unit length than cantilever beams, folding the beam allows for the significant increase of the effective length of the beam, reducing the natural frequency while maintaining the stability and resistance to negative residual stress effects [7-9]. In the folded beam situation, each beam segment is free to expand longitudinally equally, rotate, or displace in any direction to lessen residual stresses [7-9]. This design allows for effectively long beams without the residual stress-based issues that occur in cantilever based systems. Additionally, the folded spring allows the non-linear fixed-fixed beam to behave more linearly, increasing the linear range as the effective bending length increases through additional folds and increased beam length.

3.3   Harvester Design Methodology:

With the methodology discussed above in section 3.2, two classes of folded spring energy harvesters were designed in order to determine the benefit of fixed-fixed folded springs on the dynamics of the energy harvester. The two classes of folded spring energy harvester are shown schematically in Figure 3.8.
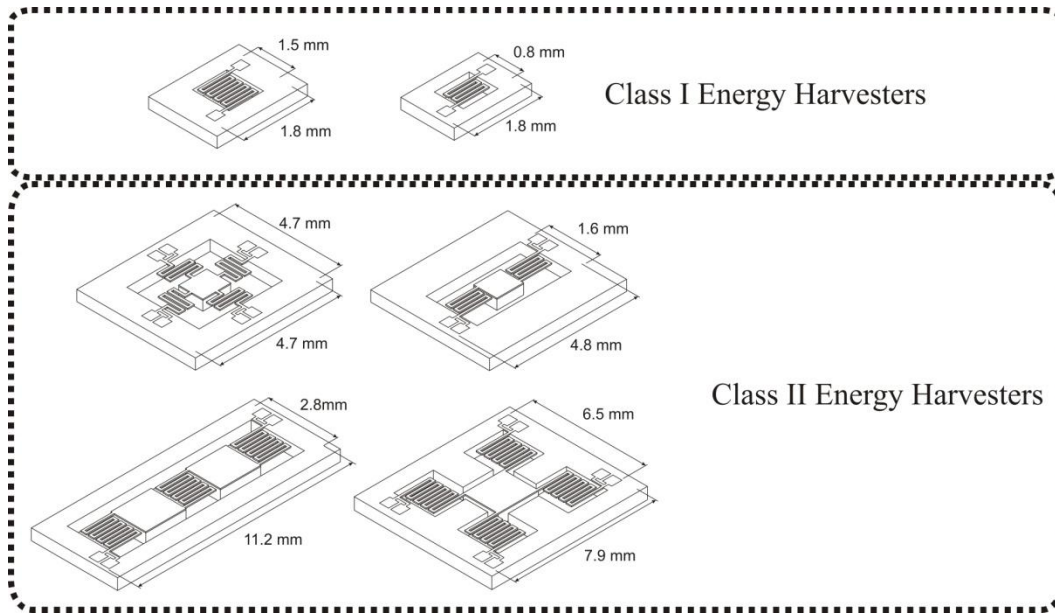
Figure 3.8 – Examples of Energy Harvesters Developed in this Study

The Class I Energy Harvesters, as shown in Figure 3.8, focus upon on the folded springs that have been postulated to be a replacement elastic member for piezoelectric energy harvesters. These proof-of-concept devices allowed for the development of a universal microfabrication process for PZT-based energy harvesters. It is expected that these devices will have a higher natural frequency than the target operational frequency of 30-300 Hz. The major goal of this class of harvester is to confirm the folded spring frequency reduction methodology discussed in this chapter, allowing for subsequent design optimization. Electrical characterization of the Class I Harvesters will be undertaken only to determine if the harvester is converting vibration to electricity.

The Class II Energy Harvesters, as shown in Figure 3.8, included arrays of masses and folded spring energy harvesters to further reduce the natural frequency

and increase power output. The first goal of this class of harvester is to reduce the natural/operational frequency range of the harvesters to that of human motion (30-300 Hz). This will increase the power output of the class of harvester. Additionally, the physical arrangement of the elastic harvesting elements will be studied in order to examine the benefits of parallel and series arrays of harvesting elements. The orientation of the folded spring harvesting elements will be alternated to evaluate the effect on both the mechanical and electrical performance. It is expected that the permutations of spring arrangements and orientation of spring elements will allow for both natural frequency reduction and allow for increased mechanical stability for higher input accelerations. The microfabrication process flow and packaging schemes developed for the Class I Harvesters were used for the Class II Harvesters.

3.3.1 Class I Harvesters

Using the folded spring concept as a basis for design, two separate numerical studies were undertaken in order to understand the design space of the fixed-fixed folded spring and to determine optimized designs given fabrication-based constraints. To save significant computational time and resources, only the structural silicon layer was modeled. It can be shown using by using a composite bending stiffness (product of moment of inertia and Young's Modulus), that the overwhelming thickness of the structural silicon layer (35-40μm) of the energy harvester will dominate the stiffness of the structure versus the thinner layers (500 nm SiO2, 50 nm Titanium, 250 nm Platinum, ~1 um PZT, and 250 nm Platinum). By computing the moment of inertia and the effective bending stiffness with and without the thin layers, it can be seen in Figure 3.9, that the difference in moment and inertia and bending stiffness is negligible.
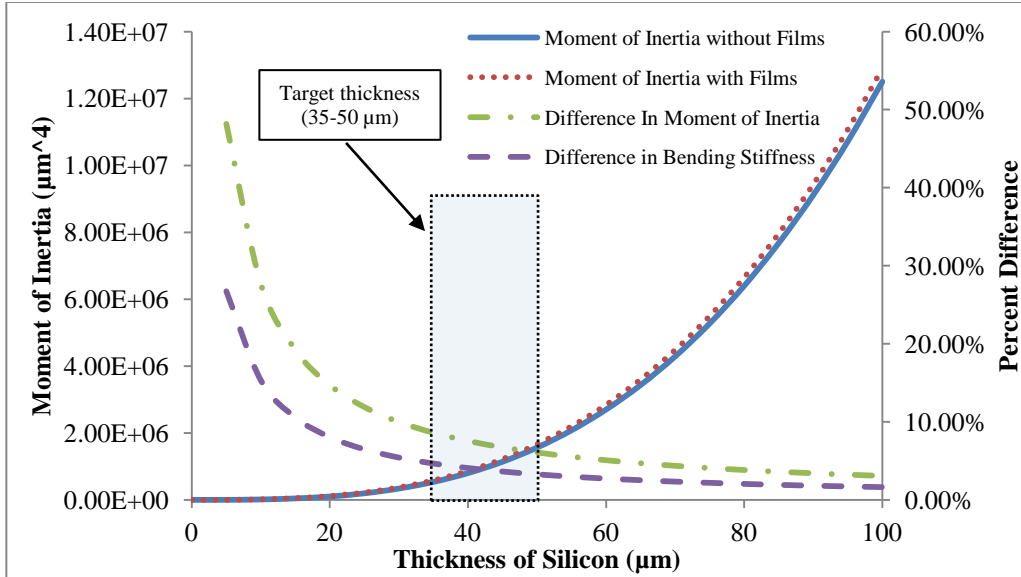
Figure 3.9 – Comparison of keeping/ignoring the thin films in the moment of inertia and bending stiffness of the harvester.

As expected, the addition of the thin films does not add significantly to the overall moment of inertia. Additionally, taking into account the Young's Modulus of each layer in the bending stiffness, it can be seen that the percent difference between keeping and removing the thin layers is small, 3% - 4.68% for the design space of 35-50 µm.

Expanding this comparison to a simulation of the folded spring calculating the natural frequencies of a sample folded spring, with and without the thin layers, it can be seen that the results agree within 2% error for device thicknesses that are expected for the harvester (35-50 µm). This difference is outlined in Table 3.1.

Table 3.1 - The calculated natural frequencies of an example harvester with and without the thin metallic and piezoelectric layers.

	Mode 1 (Hz)	Mode 2 (Hz)	Mode 3 (Hz)	Mode 4 (Hz)	Mode 5 (Hz)
Full Model	6989	7612	13528	14424	19273
No Films	7024	7699	13629	14586	19428
Percentage Difference due to Films	0.50%	1.14%	0.75%	1.12%	0.80%

Although the folded spring examined in Table 3.1 is mechanically stiff, having natural frequencies as high as 6-7 kHz, the difference in stiffness and natural frequency is consistent across the first five modes of the example harvester.

The first numerical study utilized FEA to perform a global sensitivity study on the geometric parameters of the folded spring, in order to confirm the observations made from equation (9). The entire geometry of the folded spring was parameterized into a small number of variables shown in Figure 3.10.
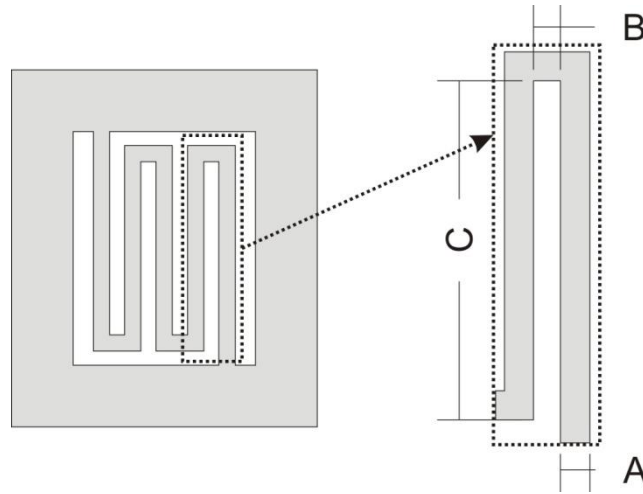
Figure 3.10 – Parameterization of the planar geometry of the folded spring into three variables, the beam width (A), the internal fold gap (B), and the internal beam length (C).

The entire geometry of the folded spring can be defined by four variables: three variables determining the planar geometry and the thickness of the folded spring. The width of the beam is defined by "A", and is kept constant throughout the entire length of the folded beam. The internal fold gap, "B", is the spacing between the beam segments and is kept constant for every fold. The internal length of the beam is defined by parameter "C". By using these variables, the entire planar geometry of the folded spring can be defined and manipulated parametrically.

To perform the sensitivity analysis, a One at A Time (OAT) analysis was utilized. Each parameter of the folded beam, the beam width, gap length, beam

length, and beam thickness, were varied one at a time while the remaining variables were kept constant. The natural frequency of the resulting structure was then calculated by FEA, allowing for the dependence of the natural frequency on each individual variable to be identified. In this analysis, the anisotropic nature of the silicon was taken into account. The model was oriented to allow the material properties to coincide with the intended physical orientation of the devices fabricated. The design range of each parameter is shown in Table 3.2.

Table 3.2 - Parameter ranges for the OAT sensitivity study. Parameters defined in Figure 3.10.

Parameter	Minimum (µm)	Maximum (µm)
Width (A)	100	500
Overlap Gap (B)	5	500
Individual Beam Length (C)	15	2000
Beam Thickness (D)	5	100

The lower bound for each design parameter was based upon what is possible to achieve via microfabrication. Specifically, the width of the folded spring was fixed at 100 µm, the minimum allowable width required by the layered piezoelectric structure. The upper bound for the width and thickness of the beam were chosen in order to attempt to maintain a "thin" cross section. The upper bound for the overlap gap was kept at the same range as the width to prevent bending from taking place in the connecting member. The upper bound for the length of the beam was chosen to be kept within the "MEMS" scale.

The initial case of the global FEA OAT-based sensitivity study was set to half of the upper bound of each of the parameter ranges. A four-fold folded spring was evaluated as the test case. The FEA then swept each parameter, calculating the natural frequency for each combination of parameters. The study produced the relations between natural frequency and the normalized design parameter, as shown in Figure 3.11.
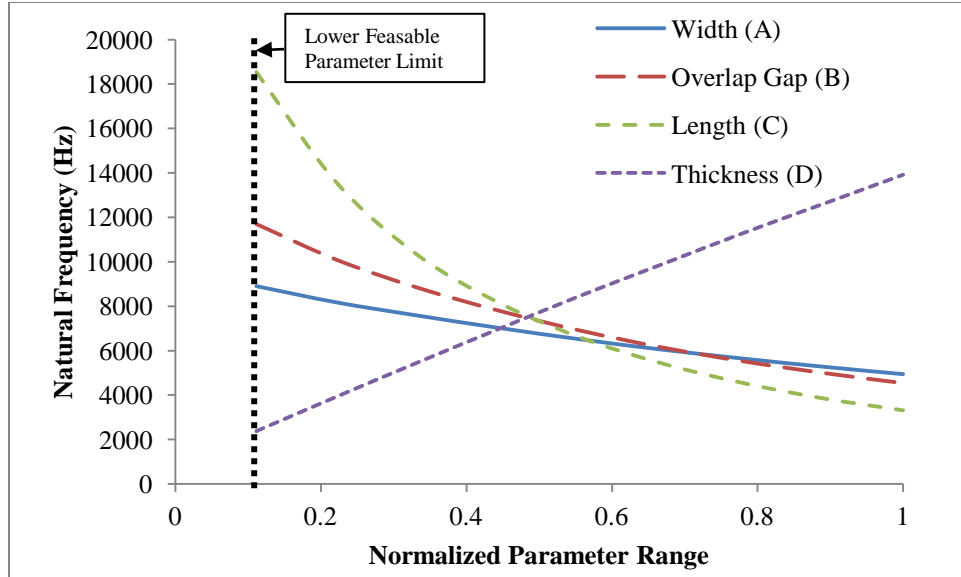
Figure 3.11 – The relations between the natural frequency and the parameter ranges in Table 3.2 as calculated by the OAT-based sensitivity study.

In Figure 3.11, each of the parameters is normalized versus the maximum value in each parameter range, as shown in Table 3.2. The lower feasibility limit for the OAT study is shown in Figure 3.11. Parameter values smaller than the feasibility limit will either violate design intent or result in unfeasible designs.

The OAT-based sensitivity study on the geometric parameters of the folded spring yielded some interesting results. First, the relationship between the natural frequency and each individual design parameter is monotonic, with the optimum value of each parameter occurring at the boundary of the parameter range. This suggests that the lowest natural frequency of the fixed-fixed folded spring will occur with the widest, largest overlap gap, longest, thinnest folded spring possible. This also suggests that the natural frequency reduction of the folded spring is limited by the mechanical stability of the structure produced by microfabrication. To determine the importance of each parameter, each relation was curve fitted using polynomial regression. A derivative of the polynomial fit was then calculated and evaluated at several data points in order to determine an average rate of change for each parameter, as in Table 3.3.

Table 3.3 – Average rates of change for the natural frequency/parameter relations from the OAT sensitivity study.

	Width (A)	Overlap Gap (B)	Length (C)	Thickness (D)
Average Rate of Change	-4649.3	-9357.68	-24526.8	13124

Taking Figure 3.11 and the average rate of change from Table 3.3, the dominance of each parameter can be evaluated. The most dominant parameter, having the highest magnitude change and rate of change is the length of each individual beam segment. The second most dominant parameter is the thickness of the beam, followed by the overlap gap and the width of the beam respectively. The width adds additional mass, however, in comparison to the thickness; it does not greatly affect the stiffness of the folded spring. The overlap gap of the folded spring does not affect the stiffness of the folded spring significantly, since this length of spring will be subject to a small amount of torsion and no appreciable bending. Additionally, increasing the number of folds in the spring, by adding additional beams, decreases the stiffness of the harvester. Table 3.4 summarizes the results of the OAT-based sensitivity study.

Table 3.4 – Summary of the OAT-parametric study of the folded spring.

Dominance	Parameter	Natural Frequency Reduced When Parameter is:
Most	Individual Beam Length (C)	Increased
	Beam Thickness (D)	Decreased
	Overlap Gap (B)	Increased
Least	Beam Width (A)	Increased

With the understanding of the dependence of the natural frequency on each parameter, a second FEA analysis was undertaken to help design some initial folded springs for fabrication. The optimization procedure used a Subproblem Approximation Method [10] to achieve an initial design. The routine initially varies all the design parameters of the folded spring, as defined above in Figure 3.10, randomly to populate the design space. Curve fits are then applied to

determine the relationship between each design variable and the natural frequency. These curve fits are then minimized to the optimum values for each design parameter. The goal of this optimization was to minimize the natural frequency of the energy harvester to the sub-kHz range while maintaining suitable dimensions for microfabrication. To ensure stability and ease of fabrication of the proof of concept prototypes, the overall size the folded spring of the energy harvester was limited to 2 mm x 2 mm, with a minimum beam thickness of 25 μm, and the lower bounds for the other parameters in Table 3.2.

Using this approach, a variety of prototype energy harvesters were designed having numerically optimized natural frequencies ranging from 512-995 Hz (with a device thickness of 25 um). The designs used for mask fabrication varied the parameters "on-plane" with the wafer, including the number of folds, beam widths, lengths, and layer overlap allowance. The structural thickness of the designed folded springs will be defined through the release etches of the fabrication recipe.

In order to help predict the response of each design under actuation, further FEA was undertaken in order to determine the expected mode shapes and reasonable acceleration loads that could be placed on the harvesters. For an example, four-fold, folded spring composed of anisotropic silicon, the simulated frequency response can be seen in Figure 3.12.
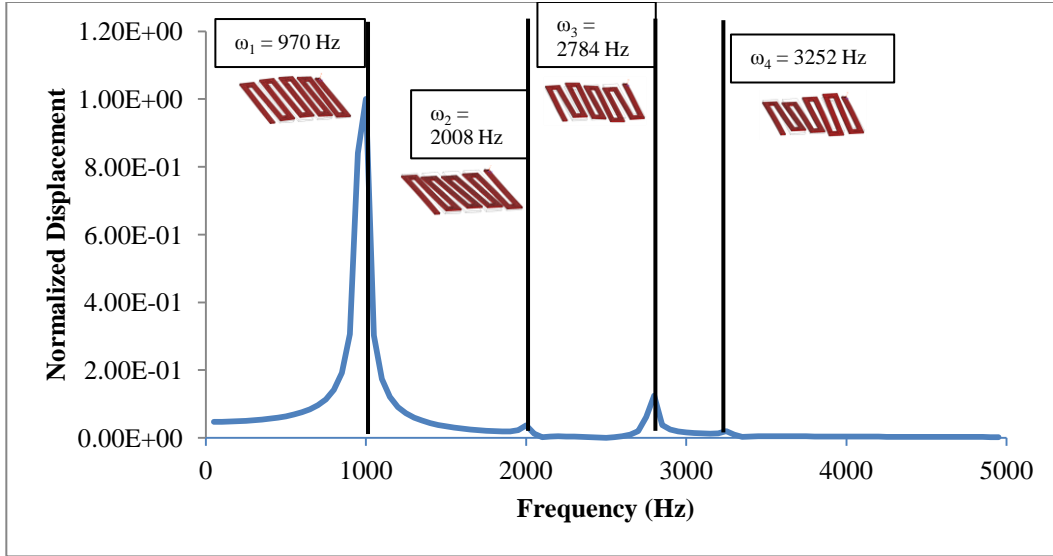
Figure 3.12 – Simulated frequency response of a four-fold folded spring harvester undergoing a sweeping sinusoidal input vibration.

The folded spring was subjected to a 1 μN sinusoidal force, the frequency of which was swept from steady state to 5000 Hz. The magnitude of applied force is typical of what would be applied to the microfabricated harvesters during testing. As seen in Figure 3.12, the first four natural frequencies occur in pairs, the first peak in the pair is more pronounced, followed by a lesser secondary peak, then a drop-off in vibration amplitude. The bandwidth between the odd and even paired resonances is a transition zone between adjacent modes. This transition zone can experience higher than normal amplitude vibrations, and could potentially be used to help broaden the useful actuation bandwidth of the harvester. The relation between the mode shapes can be seen in Figure 3.13.
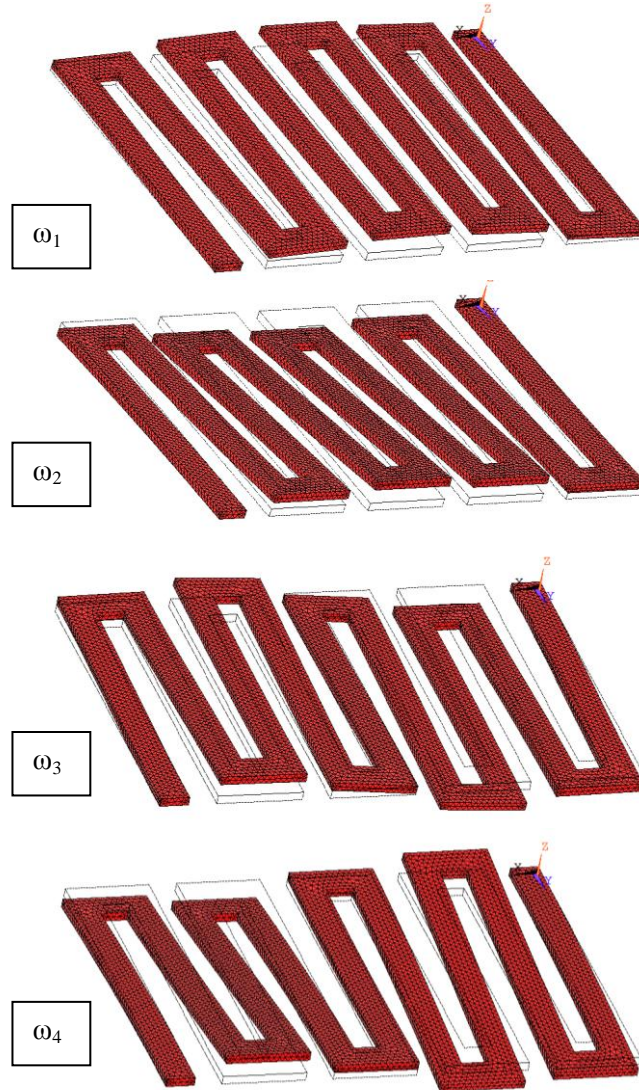
Figure 3.13 – The first four mode shapes of the harvester examined in Figure 3.12.

From Figure 3.13, it can be seen that the modes experienced by the folded spring involve both bending and torsion. The first and third modes act more like a continuous, non-folded fixed fixed beam, with a sinusoidal-based mode shape clearly visible between each beam anchor. The second and fourth modes are a mixture of individual beam segment bending and rotation. Each individual beam segment is experiencing the first bending mode of a fixed-fixed beam, producing a "local" bending mode that resembles a "global" torsional mode. As seen in Figure 3.13 a slight amount of torsion occurs in the connecting members to

82

accommodate the individual movement of each beam segment. No matter the mode experienced by the harvester, the root of the beam will experience bending. The root of the beam in this design is the area upon which the maximum strain, and voltage, will occur during actuation. The internal corners of the folded springs do cause a stress concentration; however, these corners are idealized much sharper than they would be fabricated as. The photolithography and fabrication procedures used would significantly round the corners, mitigating the stress concentration. Therefore, regardless of the mode, there should be increased deflection in the transition bandwidth between the first and second modes in comparison to the frequency range on the opposing skirts of the respective modes. The same behavior is seen in the third and fourth modes of the folded spring harvester. The FEA analysis undertaken on the first class of harvesters will be later used to compare against the experimental measurements for validation.

3.3.2   Class II Harvesters

The second class of energy harvesters examined in this study built upon the characterization of the Class I Harvesters as discussed in Chapter 6. The Class II Harvesters add masses and arrays of harvesting elements to further drive down the natural frequency of the energy harvester and increase the strain on the piezoelectric elements. In this class of energy harvester, there are five major design parameters: the number of folds in the flexible element, the number of masses and flexible elements in the array, the configuration of the flexible elements, the orientation of the flexible elements, and the thickness of the spring elements. A folded spring design is used from the previous work, in a two fold/four fold configuration, as shown in Figure 3.14.

2 Fold Spring   4 Fold Spring
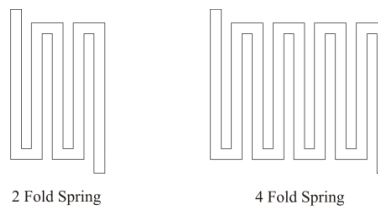
Figure 3.14 - Schematic of a two-fold and four-fold folded spring element.

The masses and springs are arranged in parallel and series configurations to allow for a wider variety of natural frequency ranges. The parallel designs will allow for a good balance between stability and reduction of natural frequency to allow for higher acceleration load applications. The series designs will allow for the further natural frequency reduction through addition of additional masses and spring elements. The additional spring elements in series acted similarly to adding folds to a single folded spring, increasing the effective bending length. Examples of series and parallel are shown in Figure 3.15.
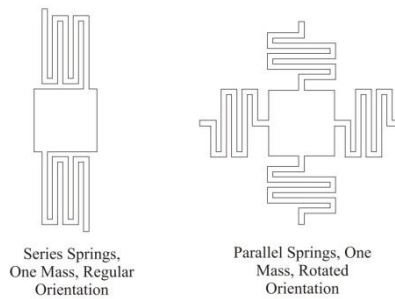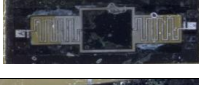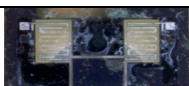
Figure 3.15 **-** Schematic of series and parallel arrangements of folded springs and masses and normal and rotated oriented folded springs.

The orientations of the spring elements were varied in order to take advantage of both out of plane and rotational motion of the proof mass. The first orientation of folded spring, the normal orientation, will allow for the mass to oscillate in an out of the plane of the harvester. The individual beam elements in this orientation will undergo mostly bending in this orientation of the spring element. An example of this spring orientation is seen in the left of Figure 3.15. The second orientation of the folded spring, the rotated orientation, will allow for the masses to mostly rotate, rather than oscillating in and out of plane. The rotation of the mass, in this case, causes the individual beam elements of the folded spring to undergo bending. An example of this spring orientation is seen in the right of Figure 3.15. It was expected that the rotated orientation folded spring harvesters generators will be mechanically stiffer than the normal orientation folded spring bending energy harvesters, allowing for higher amplitude accelerations/larger suspended masses. As with the Class I Harvesters, the thickness of the spring elements will be varied in order to create a wide range of natural frequencies with the same

planar design. The permutations of these parameters will fill the design space, as shown in Table 3.5:

Table 3.5 - The design space of Class II Harvesters varying the number of folds, number of masses, spring configurations, and spring orientations.

Device Design	Number of Folds	Number of Masses	Spring Configuration	Spring Orientation	Schematic of Design
A	2 Folds	1	Series	Normal	
B	2 Folds	1	Series	Rotated	
C	4 Folds	1	Series	Normal	
D	4 Folds	1	Series	Rotated	
E	2 Folds	2	Series	Normal	
F	2 Folds	2	Series	Rotated	
G	4 Folds	2	Series	Normal	
I	2 Folds	2	Parallel	Normal	
J	2 Folds	2	Parallel	Rotated	
K	4 Folds	2	Parallel	Normal	
L	4 Folds	2	Parallel	Rotated	

The Class II harvesters were examined in FEA in order to predict their behavior under actuation. An example of the input code used in the analysis work

can be seen in Appendix A. This allowed for the estimation of natural frequencies and mode shapes which allowed for comparison with experimental results. Additionally, the FEA analysis was helpful to identify reasonable loads and actuation frequencies for testing. Due to the nature of microfabrication, the planar design parameters of the folded spring are fixed through the printing of the lithography mask set, therefore the thickness of the folded springs are the only parameter that can be varied through fabrication. Fortunately, as discussed in the sensitivity study earlier in this chapter, the thickness of the folded spring is second only to the length of each individual beam segment as a critical parameter to define the natural frequency of the folded spring. For this analysis, the thickness of the folded springs was varied from the lowest reasonably achievable device thickness roughly a 1:2 aspect ratio of the beam, from 15-75 μm. The FEA analysis calculated both the natural frequency and mode shapes of each of the designs, using the full three dimensional model composed of anisotropic silicon. The first natural frequency for each of these designs with varying folded beam thickness can be seen in Table 3.6.

Table 3.6 – The first natural frequency (in Hz) of each design of harvesters for varying folded spring thicknesses. Natural frequencies of designs with a 35 μm folded spring thickness are highlighted for mode shape discussions.

Folded Spring Thickness	Natural Frequency (Hz)						
	15 μm	25 μm	35 μm	45 μm	55 μm	65 μm	75 μm
Design A	200.04	422.17	687.82	986.20	1311.32	1656.66	2018.23
Design B	272.67	572.87	931.17	1333.99	1772.47	2239.07	2727.83
Design C	65.47	140.00	230.35	334.00	448.76	573.41	703.02
Design D	65.68	139.91	230.25	333.72	448.26	572.61	704.80
Design E	85.22	180.09	293.70	421.89	561.86	711.60	869.08
Design F	106.04	222.90	361.46	515.91	682.51	857.93	1040.02
Design G	22.39	47.54	77.87	112.32	150.19	190.90	234.01
Design I	291.54	612.60	993.60	1418.92	1878.72	2363.87	2868.47
Design J	383.19	801.71	1297.99	1852.58	2451.92	3085.63	3745.66
Design K	85.51	177.34	286.85	410.29	543.69	685.15	832.03
Design L	98.44	207.09	336.17	481.45	638.68	806.43	980.33

The FEA analysis suggests that the Class II Harvester designs can span a large natural frequency range at each target thickness of folded spring. The thickness of the folded spring, as discussed in Chapter 4, will be defined by a single microfabrication process, therefore all designs of a specific wafer will have similar folded spring thickness. The relation between the natural frequency and thickness of the folded spring will be examined in detail for both simulation and experimental work in Chapter 7.

The identification of the mode shapes of each design of harvester was important for multiple reasons. First, it ensured that the piezoelectric material was being loaded properly in bending throughout the actuation of the harvester. Second, knowing the order of the modes allowed for the visual confirmation of which mode was being actuated experimentally. With the larger devices, it is possible to physically see the harvesters resonate at their mode shapes, as will be discussed in Chapter 7. For illustrative purposes, the mode shapes for each design of Class II Harvester were calculated using FEA at a folded spring thickness of 35 μm. This thickness of folded spring should be easily achievable through microfabrication. To determine the relative dominance/importance of each mode, the frequency response of the harvester was calculated in response to a sinusoidal input vibration applied perpendicular to the plane of the harvester. The frequency is swept from steady state to shortly after the fourth mode as calculated from the modal/eigenvalue FEA analysis. The frequency sweep FEA analysis is analogous to the testing method discussed in Chapter 5, section 5.8.2, used to experimentally determine the frequency response and identify the natural frequencies of the harvesters. Given the structure of the folded spring, the mode shapes for the Class II Harvesters cannot be simply defined. The mode shape for each individual folded spring, as discussed earlier in this chapter, can be a combination of bending, rotation, and/or torsion. With the addition of suspended proof masses, it was found that defining the mode shape of the structure relative to the motion of the proof mass was the most clear definition of the mode shape.

For Design A, the first four mode shapes are shown in Figure 3.16.

Figure 3.16 - First four mode shapes of Design A with folded spring thickness of 35 μm. Mode 1 (Top Left) is an out of plane displacement mode. Mode 2 (Top Right) is a rotational mode. Mode 3 (Bottom Left) is a higher order out of plane displacement mode. Mode 4 (Bottom Right) is a higher order rotation mode.

In first mode shape of Design A, the proof mass displaces in and out of the plane of the folded springs. The second mode of Design A is a rotational mode relative to the proof mass about the longitudinal axis of the harvester. The third mode of Design A is a higher order out of the plane displacement mode, causing rotation about the latitudinal axis of the harvester. The fourth mode of Design A is a higher order rotation-based mode about the longitudinal axis of the proof mass. From the calculated frequency-dependant response of the harvester under a sinusoidal load, as shown in Figure 3.17, it is clear that the first mode of Design A is dominant over the other modes and should be the dominant mode in experimentation.

Figure 3.17 - The calculated frequency response of a Design A harvester with folded spring thickness of 35 μm. The first mode dominates the response of the harvester with a natural frequency of 687 Hz.

Even though the out of plane displacement mode is dominant in the frequency response, the rotational modes, if present, will provide the required bending actuation to achieve the required the 31-mode loading of the piezoelectric layer for voltage generation.

The first four modes for Design B are shown in Figure 3.18.

$\omega_1 = 931$ Hz $\omega_2 = 1107$ Hz

$\omega_3 = 2812$ Hz $\omega_4 = 4992$ Hz
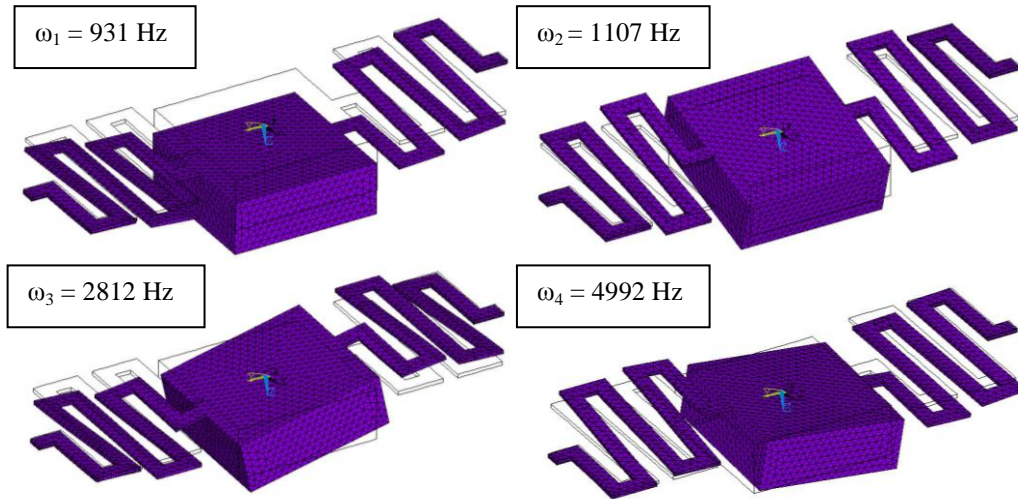
Figure 3.18 - First four mode shapes of Design B with folded spring thickness of 35 μm. Mode 1 (Top Left) is an out of plane displacement mode. Mode 2 (Top Right) is a rotational mode. Mode 3 (Bottom Left) is a higher order out of plane displacement mode. Mode 4 (Bottom Right) is a higher order rotational mode with some lateral translation.

The first mode shape for Design B is a perpendicular displacement mode in and out of the plane of the folded springs. As a system with rotated folded springs, this was not expected. This may be due to the proof mass being concentrated to the longitudinal midline of the harvester, within the span of the folded spring, limiting the amount of rotation that could be developed from the mass. The second mode of Design B is a rotational mode about the longitudinal axis of the proof mass. The third mode of Design B is a higher order bending-based mode causing rotation about the latitudinal axis of the proof mass. The fourth mode of Design B is a higher order rotational mode about the longitudinal axis of the proof mass with some lateral translation of the mass. The frequency response of Design B can be seen in Figure 3.19.

Figure 3.19 - The calculated frequency response of a Design B harvester with folded spring thickness of 35 μm. The first mode dominates the response of the harvester with a natural frequency of 931 Hz.

From the calculated frequency-dependant response of the harvester under a sinusoidal load, as shown in Figure 3.19, it is clear that the first mode of Design B is dominant over the other modes and should be the dominant mode in experimentation. As with Design A, in the unlikely event that other modes other than the first are actuated, bending will be applied to the individual beams of the harvester, providing the required 31-mode actuation for the piezoelectric layer.

The first four modes for Design C are shown in Figure 3.20.
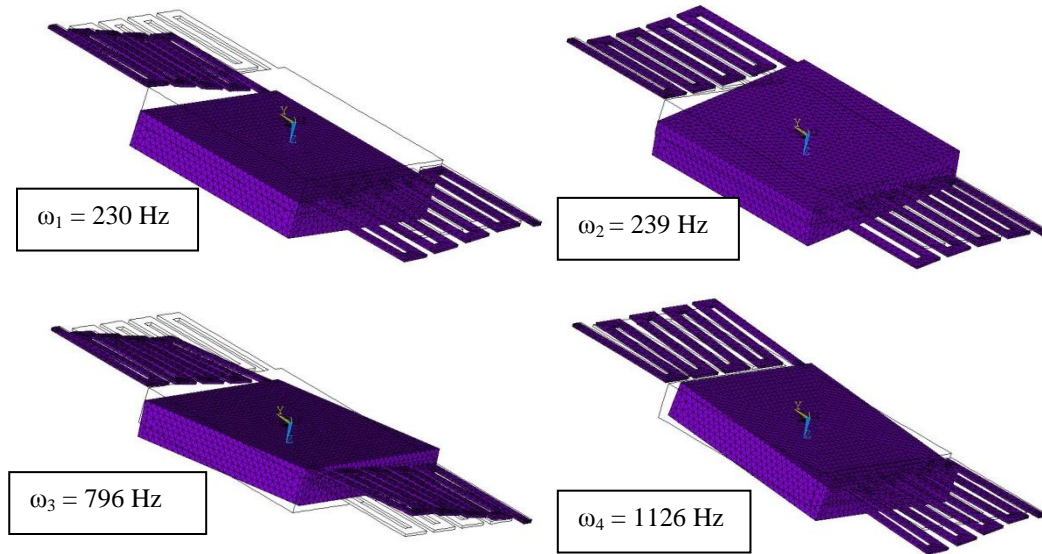
Figure 3.20 - First four mode shapes of Design C with folded spring thickness of 35 μm. Mode 1 (Top Left) is an out of plane displacement mode. Mode 2 (Top Right) is a rotational mode. Mode 3 (Bottom Left) is a higher order out of plane displacement mode. Mode 4 (Bottom Right) is a higher order rotational mode.

The first mode shape for Design C is a perpendicular displacement mode in and out of the plane of the folded springs. The second mode of Design C is a rotational mode about the longitudinal axis of the proof mass. The third mode of Design C is a higher order out of plane displacement mode resulting in a rotation about the latitudinal axis of the proof mass. The fourth mode of Design C is a higher order rotational mode about the longitudinal axis of the proof mass. The simulated frequency response of Design C can be seen in Figure 3.21.

Figure 3.21 - The calculated frequency response of a Design C harvester with folded spring thickness of 35 μm. The first mode dominates the response of the harvester with a natural frequency of 230 Hz.

From the calculated frequency-dependant response of the harvester under a sinusoidal load, as shown in Figure 3.21, it is clear that the first mode of Design C is dominant over the other modes and should be the dominant in experimentation. As with the previous designs, in the unlikely event that other modes other than the first are actuated, bending will be applied to the beams of the harvester, providing the required 31-mode actuation for the piezoelectric layer.

The first four modes for Design D are shown in Figure 3.22.

Figure 3.22 - First four mode shapes of Design D with folded spring thickness of 35 μm. Mode 1 (Top Left) is a rotational mode. Mode 2 (Top Right) is an out of plane displacement mode. Mode 3 (Bottom Left) is a higher order out of plane displacement mode. Mode 4 (Bottom Right) is a higher order rotational mode with some lateral displacement.

The first mode shape for Design D is a rotational mode about the longitudinal axis of the proof mass. The second mode of Design D is perpendicular displacement mode in and out of the plane of the folded springs. The third mode of Design D is a higher order out of plane displacement mode resulting in a rotation about the latitudinal axis of the proof mass. The fourth mode of Design D is a higher order rotational mode about the longitudinal axis of the proof mass with some lateral displacement. This is an interesting mode that was not present in previous designs. A view of this mode from a different orientation is shown in Figure 3.23.

$\omega_4 = 1129$ Hz
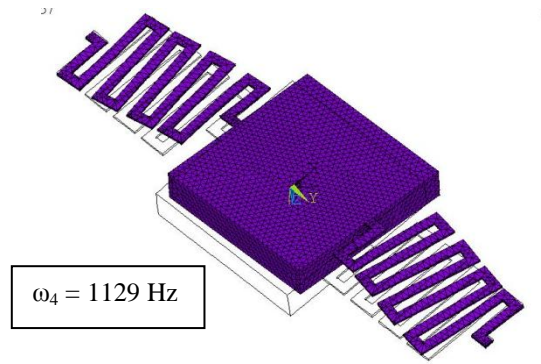
Figure 3.23 - The fourth mode of Design D with a folded spring thickness of 35 μm, showing the lateral displacement that occurs in addition to the higher order rotational mode.

The alternate view of the fourth mode of Design D clearly shows the lateral displacement causing some in-plane lateral bending to the piezoelectric harvesting beams. This bending will not actuate the harvesting elements properly and may cause electrical losses in the system. The calculated frequency response of Design D can be seen in Figure 3.24.

Figure 3.24 - The calculated frequency response of a Design D harvester with folded spring thickness of 35 μm. As shown in the top figure, the first mode dominates the response of the harvester with a natural frequency of 230 Hz. In the bottom figure, the response is zoomed to show the fourth mode at 1129 Hz.

As seen in Figure 3.24, the fourth mode of Design D is more dominant in the overall response than the second and third modes of the design. Additionally, the first mode is much more dominant over the fourth mode by orders of magnitude. Furthermore, the frequency at which the fourth mode may start to manifest in the vibration is far from the optimum operational frequency of this

design; therefore, the fourth mode shape with non-optimal actuation will most likely not affect the operation of this design of harvester. The first, second, and third modes will apply bending to the beams of the harvester, providing the required 31-mode actuation for the piezoelectric layer.

The first four modes for Design E are shown in Figure 3.25.
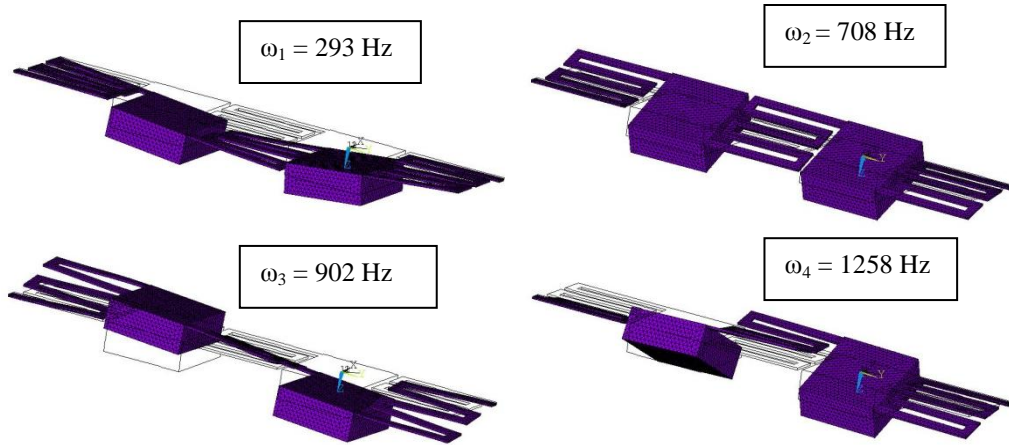
Figure 3.25 - First four mode shapes of Design E with folded spring thickness of 35 μm. Mode 1 (Top Left) is an out of plane displacement mode. Mode 2 (Top Right) is a rotational mode. Mode 3 (Bottom Left) is a higher order out of plane displacement mode. Mode 4 (Bottom Right) is a higher order rotational mode.

The first mode shape for Design E is a perpendicular displacement mode in and out of the plane of the folded springs. The second mode of Design E is a rotational mode about the longitudinal axis of the harvester. The third mode of Design E is a higher order out of plane displacement mode. The fourth mode of Design E is a higher order rotational mode about the longitudinal axis of the harvester. The calculated frequency response of Design E can be seen in Figure 3.26.
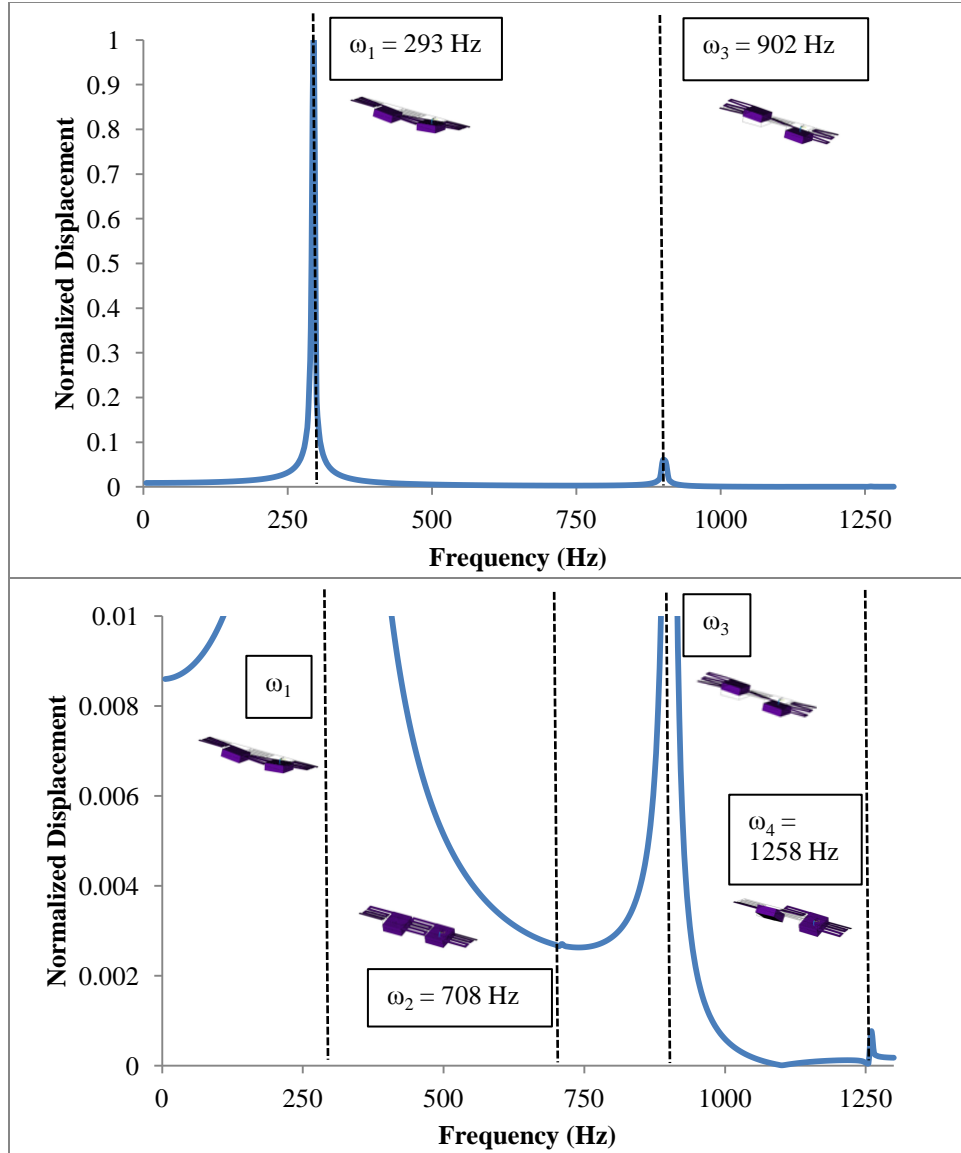
Figure 3.26 - The simulated frequency response of a Design E harvester with folded spring thickness of 35 μm. The top of the figure shows the entire frequency response with the first mode (293 Hz) and third mode (902 Hz). In the bottom figure, the response is zoomed to show the second mode (708 Hz) and fourth mode (1258 Hz).

The top of Figure 3.26 shows the overall frequency response of the harvester in response to a sinusoidal load. From the top of the figure, it is clear that the first mode at 293 Hz will dominate the response of the harvester. The third mode at 902 Hz has some influence, however, the displacement amplitude is

significantly smaller than the first mode and would only manifest if actuated extremely close to that natural frequency. The bottom of Figure 3.26 shows the relative influence of the second mode and fourth mode on the response. The second mode is present, but barely visible at 708 Hz while the fourth mode is present at 1258 Hz. Both of these torsional modes are not influential in the frequency response of the harvester. Even in the unlikely event that the higher order modes are actuated; bending will be applied to the beams of the harvester, providing the required 31-mode actuation for the piezoelectric layer.

The first four modes for Design F are shown in Figure 3.27.
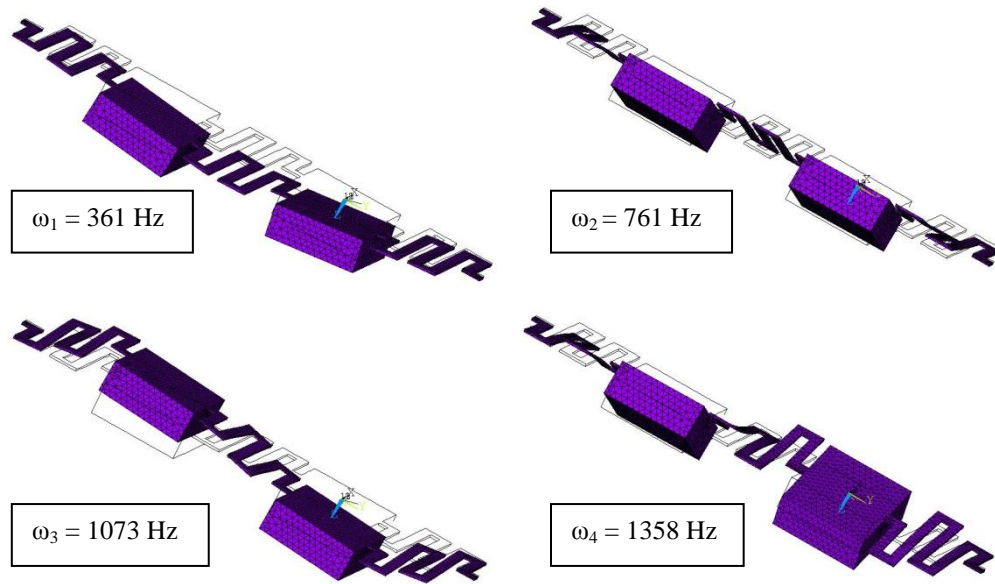
Figure 3.27 - First four mode shapes of Design F with folded spring thickness of 35 μm. Mode 1 (Top Left) is an out of plane displacement mode. Mode 2 (Top Right) is a rotational mode. Mode 3 (Bottom Left) is a higher order out of plane displacement mode. Mode 4 (Bottom Right) is a higher order rotational mode.

As with Design B, the first mode of Design F is an out of plane displacement mode. A rotational mode was expected as the first mode, however, the proof mass is concentrated close to the longitudinal axis of the harvester, therefore, not much rotation of the structure occurred. The second mode of Design F is a rotational mode about the longitudinal axis of the harvester. The third mode

of Design F is a higher order out of plane displacement mode. The fourth mode of Design F is a higher order rotational mode about the longitudinal axis of the harvester. The calculated frequency response of Design F can be seen in Figure 3.28.
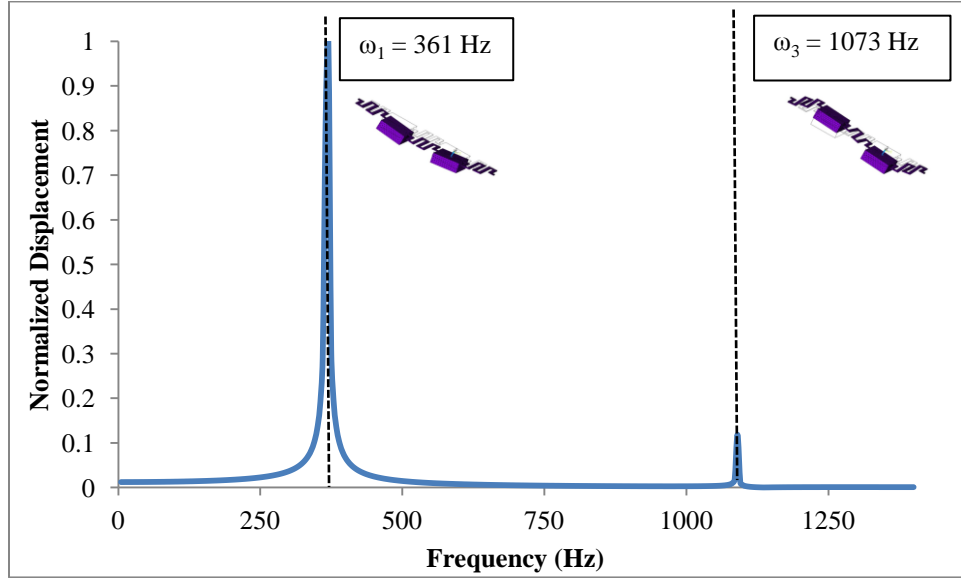
Figure 3.28 - The calculated frequency response of a Design F harvester with folded spring thickness of 35 μm. The first mode dominates the response of the harvester with a natural frequency of 361 Hz. The third mode of the harvester is present at 1073 Hz.

From the calculated frequency-dependant response of the harvester under a sinusoidal load, as shown in Figure 3.28, it is clear that the first mode of Design F is dominant over the other modes and should be the dominant in experimentation. The third mode at 1073 Hz has some influence, however, significantly less than the first mode. The second and fourth modes are present, but are completely negligible in comparison to the other modes. Both of these rotational modes are not influential in the frequency response of the harvester. Even in the unlikely event that modes other than the first are actuated; bending will be applied to the beams of the harvester, providing the required 31-mode actuation for the piezoelectric layer.

The first four modes for Design G are shown in Figure 3.29.

$\omega_1 = 77$ Hz

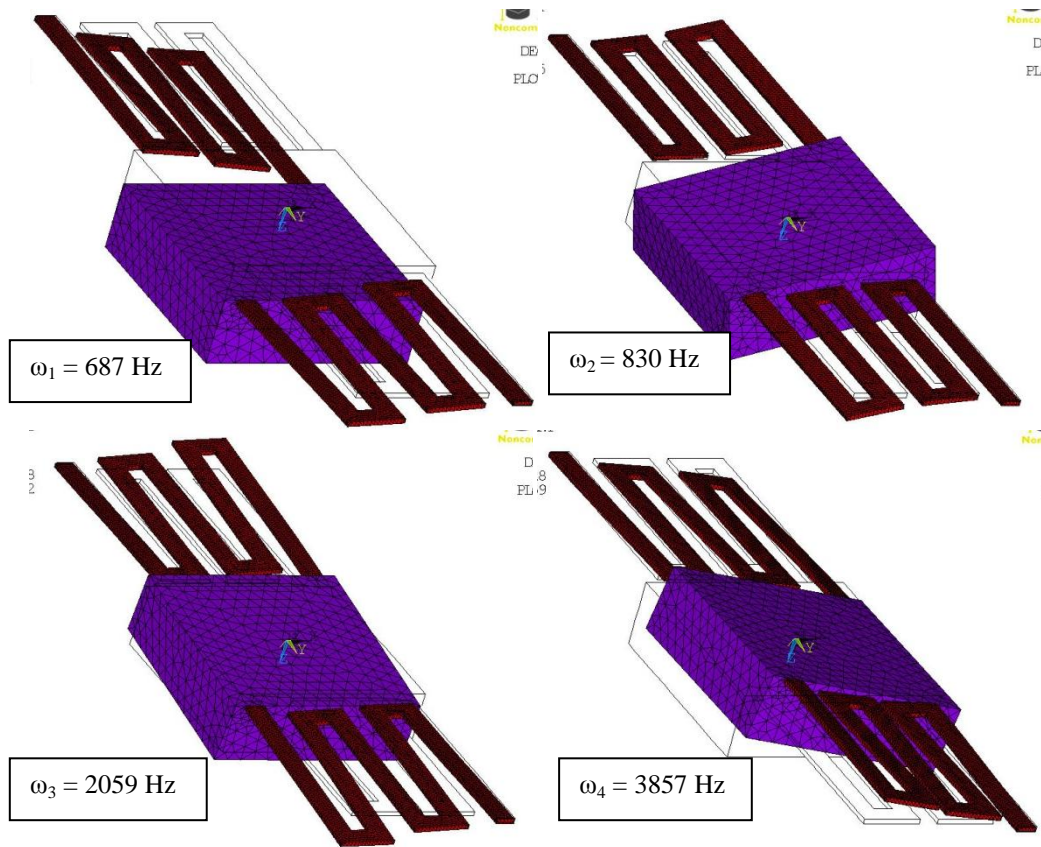$\omega_2 = 158$ Hz

$\omega_3 = 241$ Hz

$\omega_4 = 275$ Hz
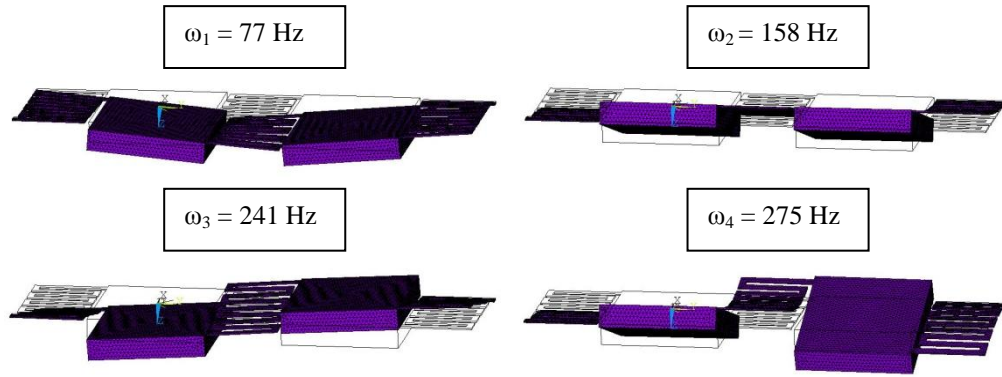
Figure 3.29 - First four mode shapes of Design G with folded spring thickness of 35 μm. Mode 1 (Top Left) is an out of plane displacement mode. Mode 2 (Top Right) is a rotational mode. Mode 3 (Bottom Left) is a higher order out of plane displacement mode. Mode 4 (Bottom Right) is a higher order rotational mode.

The first mode shape for Design G is a perpendicular displacement mode in and out of the plane of the folded springs. The second mode of Design G is a rotational mode about the longitudinal axis of the harvester. The third mode of Design G is a higher order out of plane displacement mode. The fourth mode of Design G is a higher order rotational mode about the longitudinal axis of the harvester. The simulated frequency response of Design G can be seen in Figure 3.30.
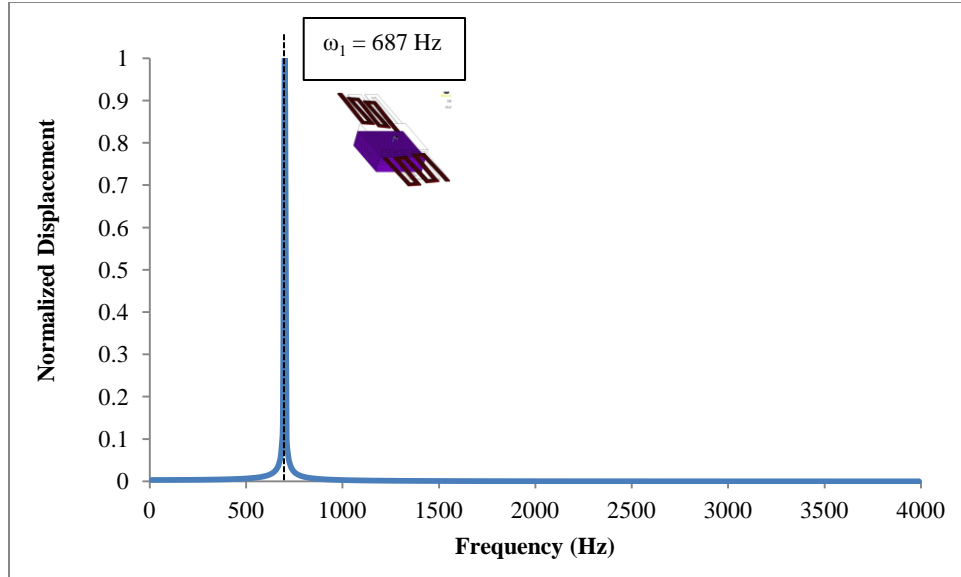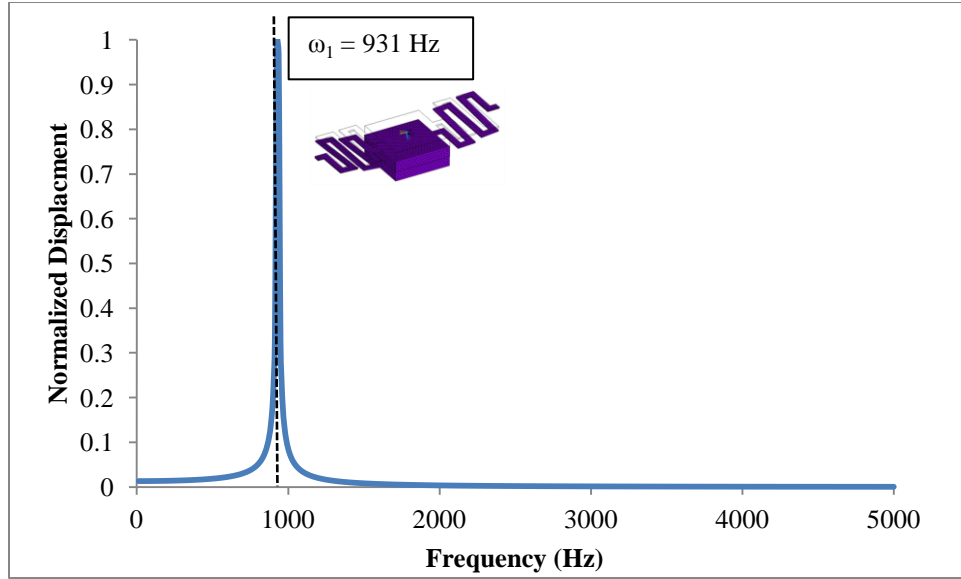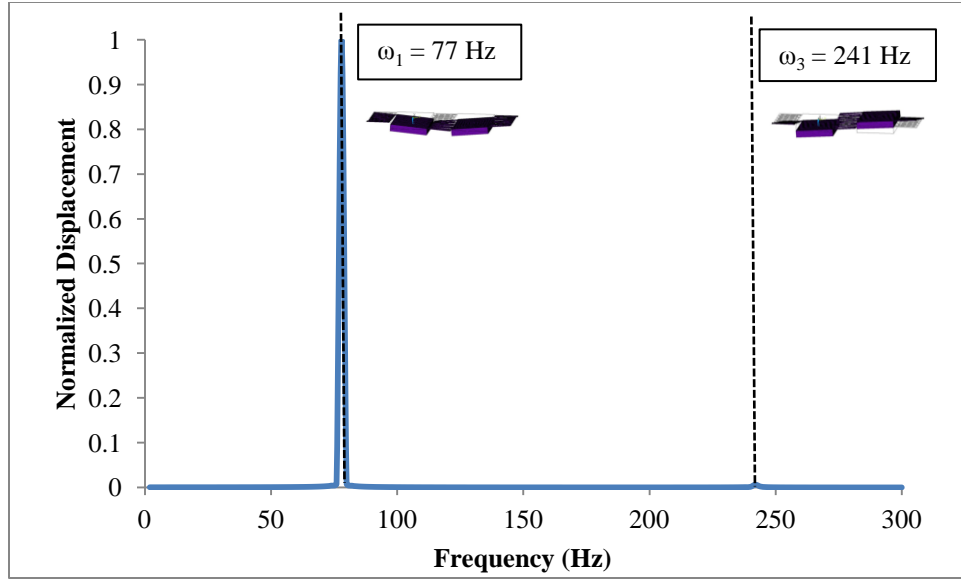
Figure 3.30 - The calculated frequency response of a Design G harvester with folded spring thickness of 35 μm. The first mode dominates the response of the harvester with a natural frequency of 77 Hz. The third mode is the next most dominant at 241 Hz.

As seen in Figure 3.30, the first mode, at 77 Hz, of Design H is highly dominant in the response of the harvester to the driven sinusoidal input. The third mode is the next most dominant mode, significantly less dominant than the first mode. The second and fourth modes are not significant to the response of the harvester under this loading. It is expected that the first mode will be dominant in the response of the harvester during experimentation. In the unlikely event that other modes other than the first are actuated, bending will be applied to the beams of the harvester, providing the required 31-mode actuation for the piezoelectric layer.

The first four modes for Design I are shown in Figure 3.31.
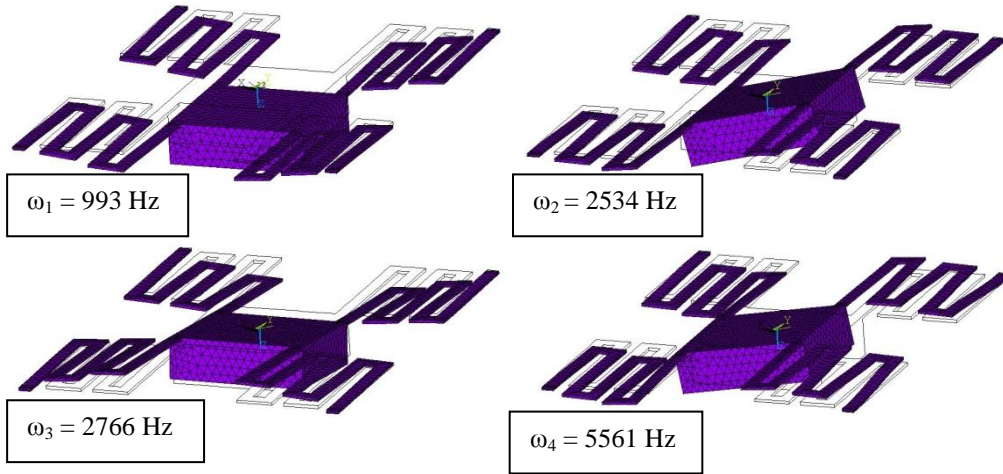
Figure 3.31 - First four mode shapes of Design I with folded spring thickness of 35 μm. Mode 1 (Top Left) is an out of plane displacement mode. Mode 2 (Top Right) is a rotational mode. Mode 3 (Bottom Left) is a rotational mode. Mode 4 (Bottom Right) is a higher order rotational mode with some lateral deflection.

The first mode shape for Design I is a perpendicular displacement mode in and out of the plane of the folded springs. The second mode of Design I is a rotational mode about the longitudinal axis of the device. The third mode of Design I is a rotational mode about the latitudinal axis of the device. The fourth mode of Design I is a higher order rotational mode with some lateral deflection as shown in Figure 3.32.
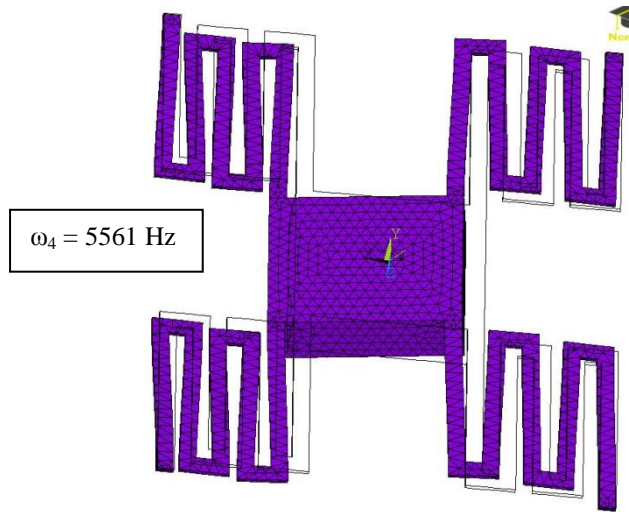
Figure 3.32 - The fourth mode of Design I with a folded spring thickness of 35 μm, showing the lateral displacement that occurs in addition to the rotational mode.

The alternate view of the fourth mode of Design I clearly shows the lateral displacement causing some in-plane lateral bending to the piezoelectric harvesting beams. This bending will not actuate the harvesting elements properly and may cause losses in the system. The calculated frequency response of Design I can be seen in Figure 3.33.
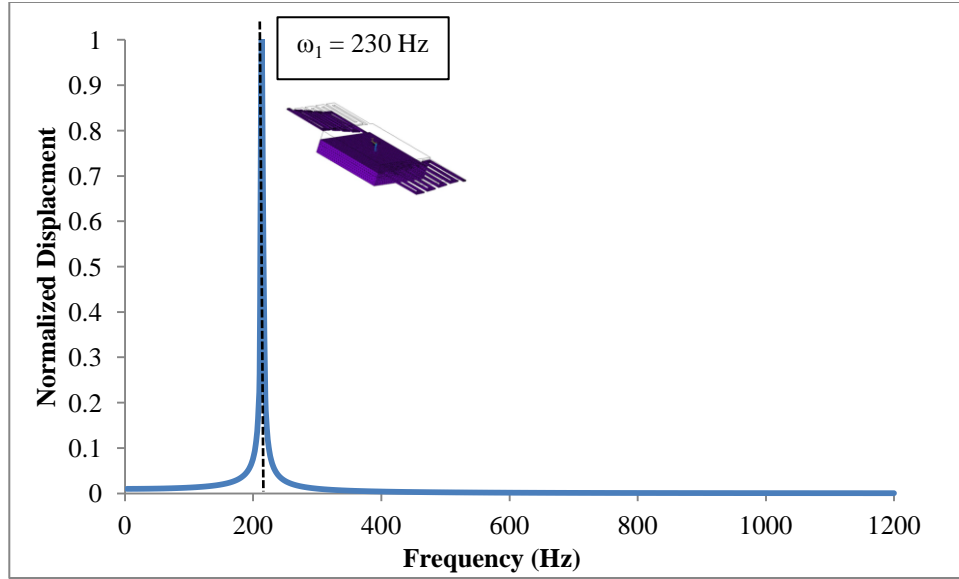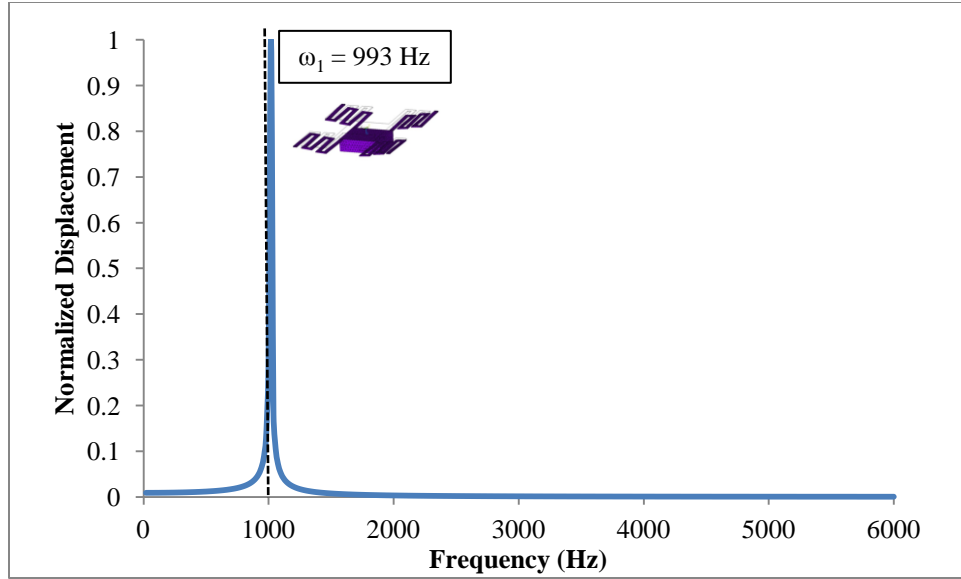
Figure 3.33 - The calculated frequency response of a Design I harvester with folded spring thickness of 35 μm. The first mode dominates the response of the harvester with a natural frequency of 993 Hz.

As shown in Figure 3.33, the first mode dominates the entire frequency response of the harvester under the applied sinusoidal load. Additionally, the fourth mode, the higher order rotational mode with some lateral displacement, predicted at approximately 5561 Hz proved to be negligible. This is a positive result, since the fourth mode is the only mode that does not directly apply the necessary bending to actuate the piezoelectric harvester in the 31-mode.

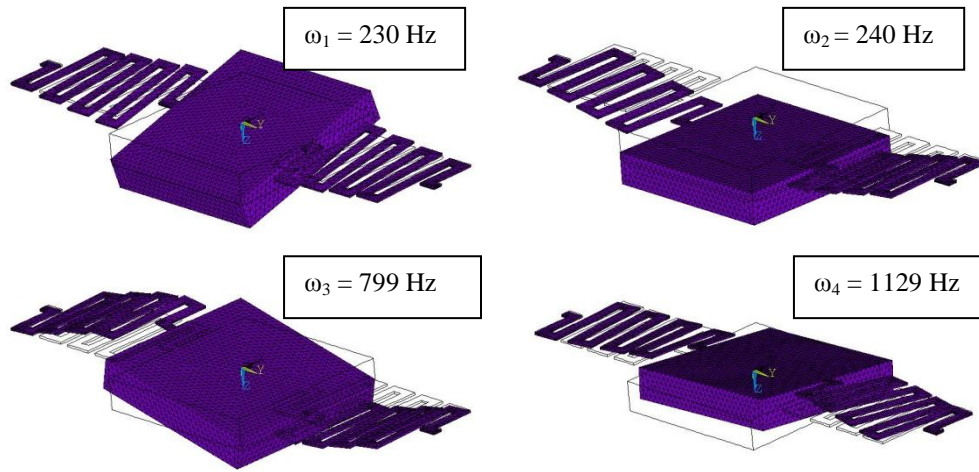The first four modes for Design J are shown in Figure 3.34.
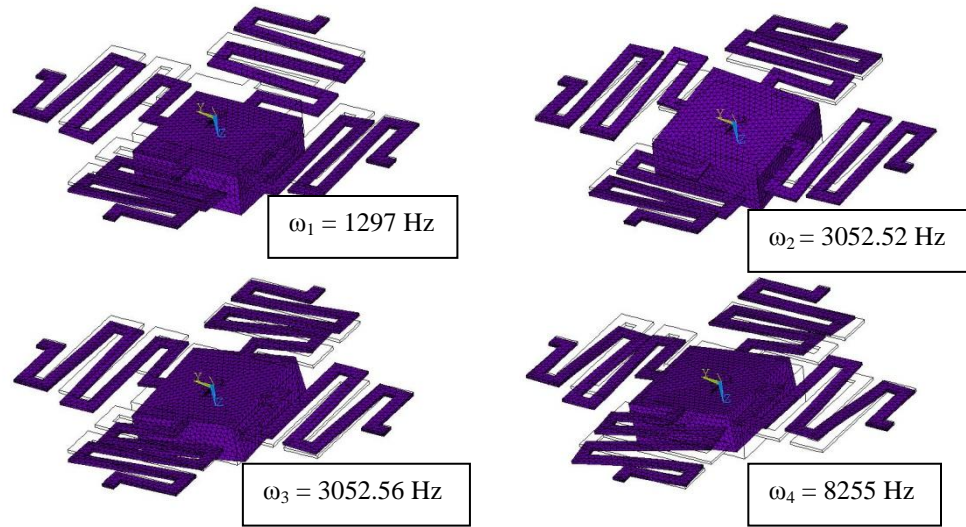
Figure 3.34 - First four mode shapes of Design J with folded spring thickness of 35 μm. Mode 1 (Top Left) is an out of plane displacement mode. Mode 2 (Top Right) is a rotational mode. Mode 3 (Bottom Left) is a rotational mode. Mode 4 (Bottom Right) is a higher order rotational mode with some transverse displacement.

The first mode shape for Design J is a perpendicular displacement mode in and out of the plane of the folded springs. The second and third modes of Design J are rotational modes about longitudinal and transverse axes of the proof mass. These modes occur very close to one another, and simply change the orientation of the rotation experienced by the device. The fourth mode of Design J is a higher order rotational mode about the longitudinal axis of the proof mass with some lateral deflection. The fourth mode of Design J is better illustrated in Figure 3.35.
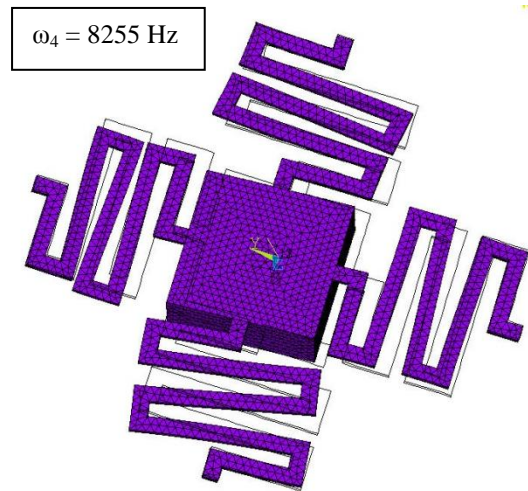
Figure 3.35 - The fourth mode of Design J with a folded spring thickness of 35 μm, showing the lateral displacement that occurs in addition to the rotational mode.

The alternate view of the fourth mode of Design J clearly shows the lateral displacement causing some in-plane lateral bending to the piezoelectric harvesting beams. This bending will not actuate the harvesting elements properly and may cause losses in the system. The calculated frequency response of Design J can be seen in Figure 3.36.
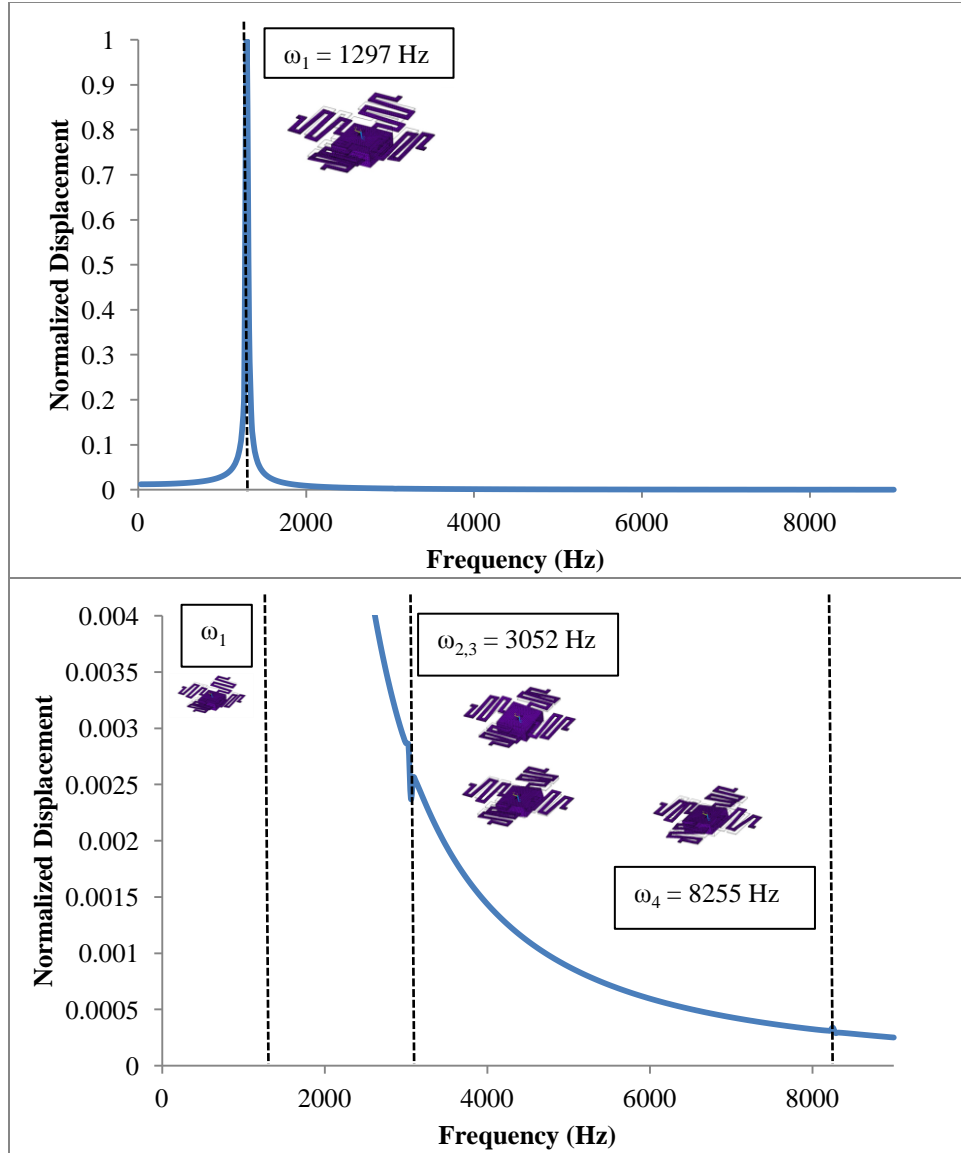
Figure 3.36 - The calculated frequency response of a Design J harvester with folded spring thickness of 35 μm. The top of the figure shows the first mode dominating the response of the harvester with a natural frequency of 1297 Hz. The bottom of the figure shows the other three modes, the second and third modes at approximately 3052 Hz and the fourth at approximately 8255 Hz.

As shown in the top of Figure 3.36, the first mode of Design J completely dominates the frequency response of the harvester. The other three modes are present, as shown in the bottom of Figure 3.36, but are negligible in contribution to the total response of the harvester to the expected loading. This includes the

potentially troublesome fourth mode of this design, which would not provide the necessary bending to the piezoelectric film that would provide the required 31-mode actuation.

The first four modes for Design K are shown in Figure 3.37.
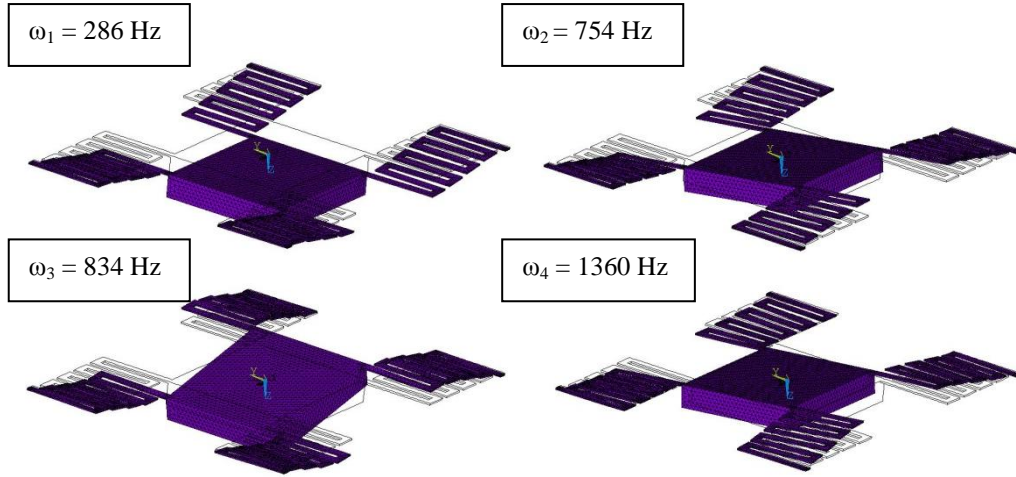
Figure 3.37 - First four mode shapes of Design K with folded spring thickness of 35 μm. Mode 1 (Top Left) is an out of plane displacement mode. Mode 2 (Top Right) is a rotational mode. Mode 3 (Bottom Left) is a rotational mode. Mode 4 (Bottom Right) is a higher order rotational mode with some lateral deflection.

The first mode shape for Design K is a perpendicular displacement mode in and out of the plane of the folded springs. The second mode of Design K is a rotational mode about the latitudinal axis of the proof mass. The third mode of Design K is a rotational mode about the longitudinal axis of the proof mass. The fourth mode of Design K is a higher order rotational mode with some lateral deflection. This fourth mode is better illustrated in Figure 3.38.
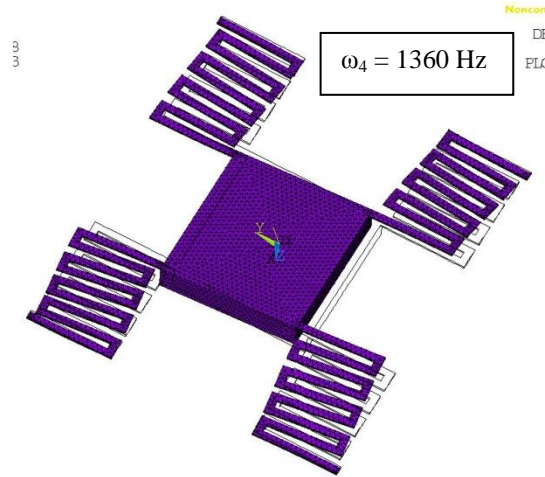
Figure 3.38 - The fourth mode of Design K with a folded spring thickness of 35 μm, showing the lateral displacement that occurs in addition to the rotational mode.

The alternate view of the fourth mode of Design K clearly shows the lateral displacement causing some in plane lateral bending to the piezoelectric harvesting beams. This bending will not actuate the harvesting elements properly and may cause losses in the system. The calculated frequency response of Design K can be seen in Figure 3.39.
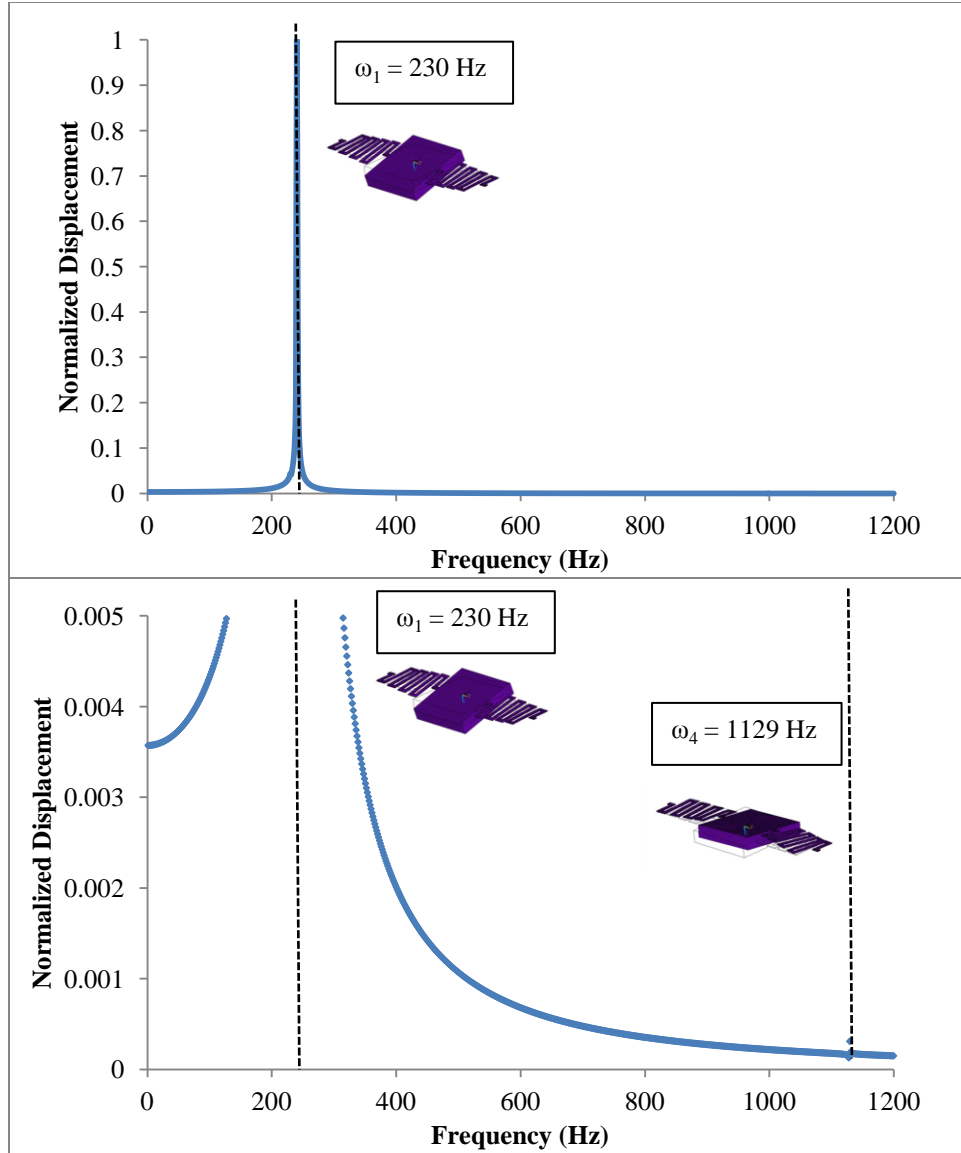
110
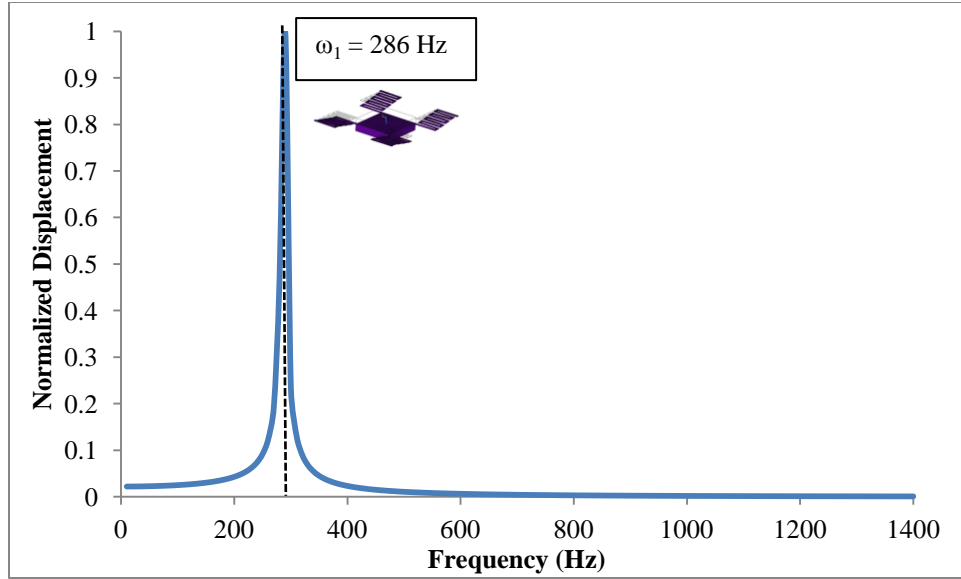
Figure 3.39 - The calculated frequency response of a Design K harvester with folded spring thickness of 35 μm. The first mode dominates the response of the harvester with a natural frequency of 286 Hz.

As shown in Figure 3.39, the frequency response of this specific Design K harvester is dominated by the first mode of the harvester at 286 Hz. The other modes do not significantly affect the response of the harvester with this specific loading. The fourth mode, with some lateral displacement and rotation, does not contribute to the overall response of the harvester. This mode could detract from the required bending that would actuate the 31-mode of the piezoelectric film, required for harvesting.

The first four modes for Design L are shown in Figure 3.40.

ω₁ = 336 Hz   ω₂ = 827.45 Hz

ω₃ = 827.88 Hz   ω₄ = 2092 Hz
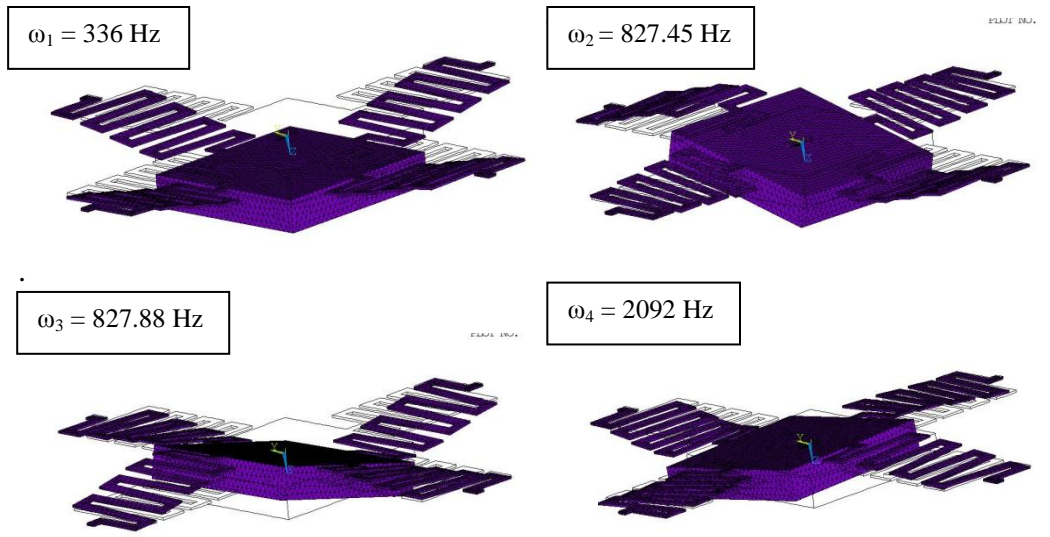
Figure 3.40 - First four mode shapes of Design L with folded spring thickness of 35 μm. Mode 1 (Top Left) is an out of plane displacement mode. Mode 2 (Top Right) is a rotational mode. Mode 3 (Bottom Left) is a rotational mode. Mode 4 (Bottom Right) is a higher order rotational mode with some transverse displacement.

The first mode shape for Design L is a perpendicular displacement mode in and out of the plane of the folded springs. The second and third modes of Design L are rotational modes about longitudinal and latitudinal axes of the proof mass. These modes occur very close to one another, and simply change the orientation of the rotation experienced by the device. The fourth mode of Design L is a higher order rotational mode about the longitudinal axis of the proof mass with some transverse deflection. The fourth mode of Design L is better illustrated in Figure 3.41.
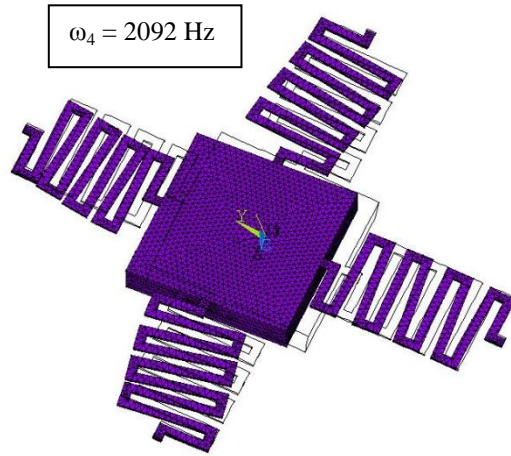
Figure 3.41 - The fourth mode of Design L with a folded spring thickness of 35 μm, showing the lateral displacement that occurs in addition to the rotational mode.

The alternate view of the fourth mode of Design L clearly shows the lateral displacement causing some in-plane lateral bending to the piezoelectric harvesting beams. This bending will not actuate the harvesting elements properly and may cause losses in the system. The calculated frequency response of Design L can be seen in Figure 3.42.
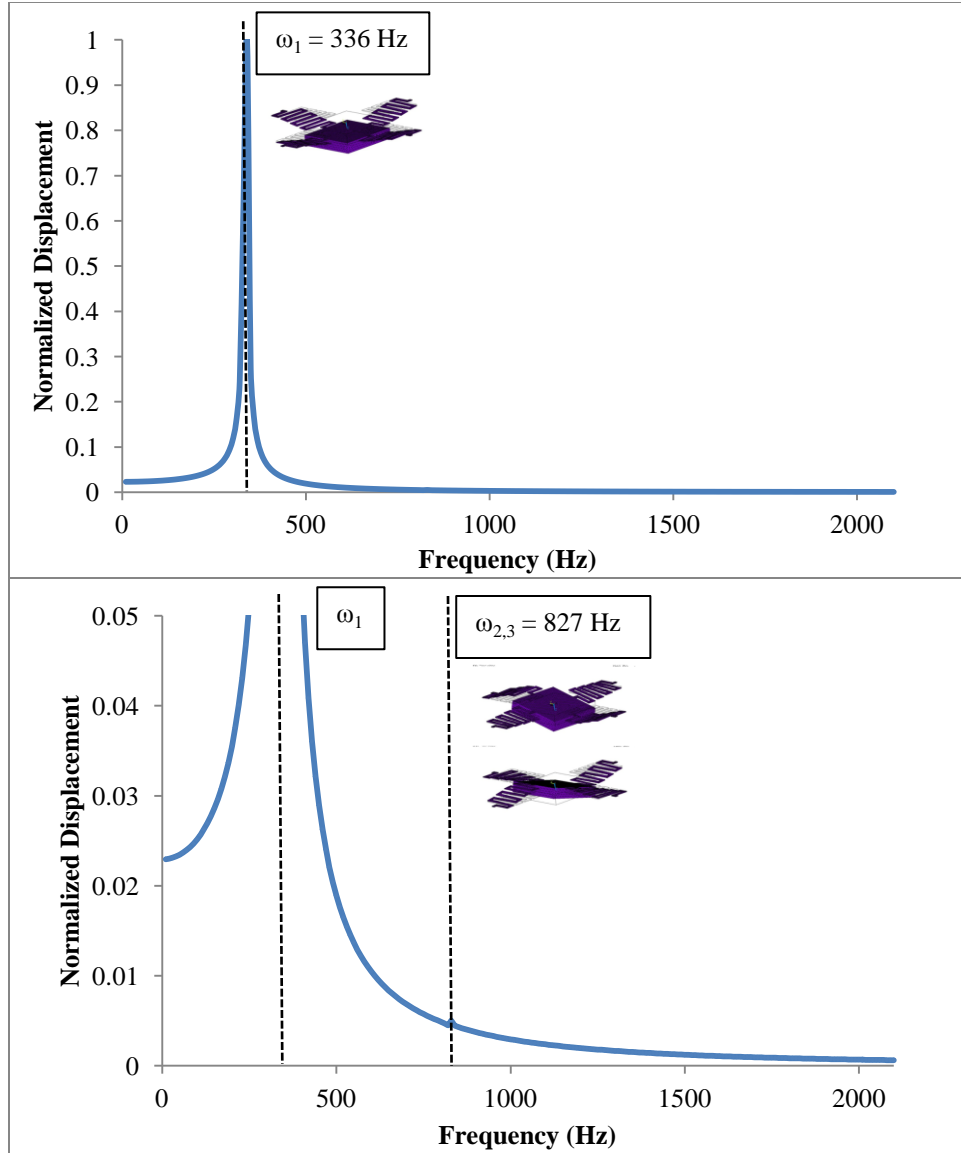
Figure 3.42 **-** The calculated frequency response of a Design L harvester with folded spring thickness of 35 µm. The top of the figure shows that the first mode dominates the response of the harvester with a natural frequency of 336 Hz. The bottom of the figure shows the second and third modes at 827 Hz.

As shown in the top of Figure 3.42, the first mode of Design L completely dominates the frequency response of the harvester under this loading. The second and third modes are present, as shown in the bottom of Figure 3.42, but are negligible in contribution to the total response of the harvester to the expected

loading. The fourth mode is not visible in the frequency response; therefore losses from this non-bending mode will not affect the required 31-mode actuation.

With the modes and frequency response of each design calculated, it will be possible to compare the simulation results with the experimental work in order to verify the overall methodology and assumptions made. Additionally, predicting the behavior of the harvesters under the expected loading of the testing setup will aid in the development of the experimental methodology.

3.4   Summary

As discussed in this chapter, the methodology undertaken to reduce the frequency of the energy harvesters is to apply a fixed-fixed folded spring to allow for frequency reduction. This structure allows for the increase of effective length of the beam, while reducing the negative effects of microfabrication-based residual stresses on the stiffness of the harvester. The folded spring structure was parametrically analyzed, showing that the length of the beam segments in the fold and the thickness of the folded spring are the most critical parameters in the mechanical stiffness of the structure. With this knowledge, a wide range of Class I Harvesters were designed, with natural frequencies ranging from 512-995 Hz, to allow for initial characterization and development of microfabrication processes. Through the characterization of these devices, the methodology was evolved into arrays of folded spring harvesters and proof masses. The Class II Harvesters additionally vary the orientation of the folded springs and relative arrangement of springs and masses to broaden the design space for a wide range of natural frequencies. The Class II Harvesters were numerically examined in detail to determine the expected behavior of each design of harvester to the test loading that will be used in vibration-based characterization. For each design, the natural frequencies, the mode shapes and relative dominance of each mode were calculated to gain an understanding of the expected experimental behavior of the harvesters. This will allow for both verification of the simulation and design methodology, as well as a prediction of expected results to aid in characterization.

To characterize the harvesters, a microfabrication process must be developed, as discussed in the next chapter.

3.5   References:

[1]   S. Senturia, *Microsystem Design*, First ed. Boston: Kluwer Academic Publishers, 2001.

[2]   M. J. Madou, *Fundamentals of Microfabrication: The Science of Miniaturization*, Second ed.: CRC Press, 2002.

[3]   J. Lueke and W. A. Moussa, "MEMS-Based Power Generation Techniques for Implantable Biosensing Applications," *Sensors,* vol. 11, pp. 1433-1460, 2011.

[4]   S. Roundy, E. S. Leland, J. Baker, E. Carleton, E. Reilly, E. Lai, B. Otis, J. M. Rabaey, P. K. Wright, and V. Sundararajan, "Improving power output for vibration-based energy scavengers," *Ieee Pervasive Computing,* vol. 4, pp. 28-36, 2005.

[5]   S. Roundy and P. K. Wright, "A piezoelectric vibration based generator for wireless electronics," *Smart Materials and Structures,* vol. 13, pp. 1131-1142, 2004.

[6]   S. Roundy, P. K. Wright, and K. S. J. Pister, "Micro-Electrostatic Vibration-to-Electricity Converters," in *ASME International Mechanical Engineering Congress and Exposition*, 2002.

[7]   K. B. Lee, "Statics," in *Principles of Microelectromechanical Systems*: John Wiley & Sons, Inc., pp. 64-143.

[8]   K. B. Lee, "Static Behavior of Microstructures," in *Principles of Microelectromechanical Systems*: John Wiley & Sons, Inc., pp. 144-234.

[9]   K. B. Lee, "Dynamics," in *Principles of Microelectromechanical Systems*: John Wiley & Sons, Inc., pp. 235-324.

[10]   "Advanced Analysis Techniques Guide," in *ANSYS Mechanical Advanced APDL Help File* ANSYS Inc., Release 13.

4.1   Introduction

With the thorough investigation of the design parameters and development of prototype designs of two classes of harvesters in Chapter 3, a microfabrication process flow was required to microfabricate sample harvesters for testing. This chapter discusses the development of the microfabrication process flow and the required core microfabrication processes. This includes the design of the piezoelectric stack required for adhesion and charge collection, the development of specific patterning techniques for the materials required, and the development and testing of the microfabrication process as a whole.

4.2   General Fabrication-based Design

4.2.1   Piezoelectric Stack Design

To accommodate the PZT film, the energy harvester requires a variety of different materials and micromachining processes for adhesion and electrical isolation. For most applications, the PZT film is deposited in the configuration shown in Figure 4.1 [1].

Figure 4.1 - The general piezoelectric stack required for PZT deposition [1].

The general PZT-based stack includes a number of materials, each

required to perform a specific task. First, an electrical isolation and diffusion barrier is required to prevent both current and dopant leakage into the silicon substrate. Typically, a silicon oxide layer is deposited on a silicon substrate to perform this task, either thermally grown or deposited via chemical vapor deposition (CVD). Adhesion layers are then required to allow the PZT to adhere to the bulk wafer. The adhesion layers function as the lower electrode in the 31-mode arrangement of the piezoelectric material. In literature, as seen in Figure 4.1, titanium and platinum are the most typical materials used. Next, the PZT is deposited onto the adhesion layer. To complete the stack, an upper electrode, typically platinum, is deposited. The following sections will further discuss the requirement of each specific film in the piezoelectric stack.

4.2.1.1 Isolation Layer

The entire piezoelectric stack must be electrically insulated from the rest of the wafer to prevent electron leakage into the silicon substrate. The materials deposited through the fabrication of the piezoelectric stack may diffuse into the silicon at high temperature, therefore, a diffusion barrier is required. The most typical isolation layers used for MEMS-based applications are silicon oxide and silicon nitride [2-5]. Of these two materials, silicon oxide is the preferred choice for energy harvesters, due to lower residual stresses in comparison to similar thickness nitride layers [6]. The deposition of the silicon oxide can be achieved by wet or dry thermal oxidation, plasma enhanced chemical vapor deposition (PECVD) or low pressure CVD (LPCVD). Typically, dry oxidation will provide a denser silicon oxide film with better insulating properties than wet oxidation. Additionally, the silicon dioxide is required as an adhesion layer for the titanium-based bottom electrode layer.

4.2.1.2 Bottom Electrode

The structure of 31-mode piezoelectric harvesters requires a bottom and a top electrode to capture the voltage produced through application of strain. In literature, several materials have been used for a bottom electrode for this application. Platinum is typically chosen as the bottom electrode [7-11] with a

thin titanium-based adhesion layer. Diffused titanium from this layer can aid in the formation of the perovskite structure of the PZT during crystallization. The titanium acts as a nucleation site for the formation of PTO ($PbTiO_3$), which then is converted to PZT at higher temperatures [12,13]. Using these layers, in this order, allows for better microstructure and electrical properties in the PZT film [14,15]. In general, for sensing and actuation applications, the adhesion of the PZT film is of the utmost importance. In this study, both titanium and titanium tungsten were used as the bottom electrode, as will be discussed throughout this chapter.

4.2.1.3 <u>Top Electrode</u>

A number of materials and techniques have been used to deposit and pattern the required top electrode. For PZT-based harvesters, many possibilities are available including aluminum [3,16,17], platinum [10,15] or gold [7]. Platinum is the preferred choice as the top electrode for harvesters due to its chemical stability, conductive properties, and insensitivity to thermal processing [18]. The top electrode may be deposited through either sputtering or evaporation techniques, and patterned in a variety of ways, such as etching [19] and lift-off [7,9]. In this thesis, the platinum top electrode will be patterned by lift-off rather than a wet etch technique. The undercut of the required wet etch may etch or damage the PZT and underlying layers; therefore, lift-off is preferred [20]. The specific piezoelectric stack to be used in this study is shown in Figure 4.2.
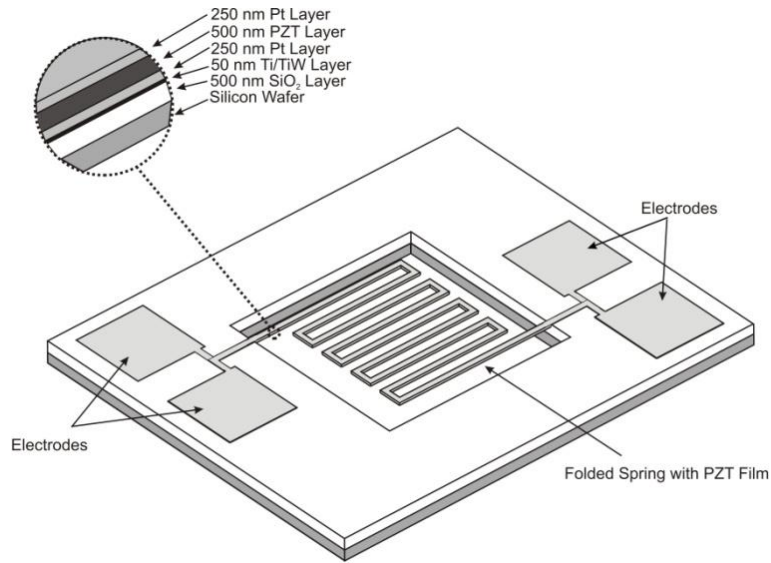
Figure 4.2 – Cross section of Class I Harvesters, showing chosen materials and resulting stepped cross sectional profile.

In addition to the layered structure, a stepped cross sectional profile buffers against alignment and microfabrication errors. In order to prevent electrical shorting, each additional layer deposited on the piezoelectric stack will be 10-15 μm narrower (depending on location) to allow for alignment errors. This produces a stepped or "pyramid"-like profile, preventing unwanted overlapping and short circuiting of electrode layers. The alignment of each of these layers in microfabrication through photolithography is a manual operation, limited to the resolution of the optical systems available for alignment.

4.2.2 PZT Layer

A variety of deposition methods have been reported in literature to deposit the required PZT layer for the folded spring energy harvester. These methods include sputtering [13,21-27], Metal Oxide Chemical Vapor Deposition (MOCVD) [28,29], and sol-gel deposition [30-38]. In addition to the deposition methods, a variety of PZT materials with specific material properties are available. The main variation in the composition of the available materials is the differing mass fraction of zirconium and titanium in the PZT compound ($PbZr_xTi_.$

$_x$O$_3$) [30-34]. This variation allows for the tuning of material properties, as will be discussed in the following sections.

4.2.2.1   PZT Sputtering

Sputtering is a well-known and reliable method of PZT deposition. It is a more mature deposition technology, where commercial-based concerns, such as uniformity and high throughput are very important [23]. During sputtering, a solid mass of the desired sputtering material is etched in a vacuum chamber using a high energy plasma. The etched material is then deposited uniformly on all surfaces in the vacuum chamber, coating the device wafers. The general advantages of sputtering PZT, with respect to the other deposition technologies, include uniformity in film thickness, mechanical, and ferroelectric properties [13,23,25-27,39]. The main limitation of sputtering PZT is the total film thickness that can be achieved. As PZT is sputtered, the wafer must be cooled throughout the process to maintain a high quality film. Lead is the most volatile compound found in PZT [13]; therefore, the wafer must be cooled in order to prevent the lead from locally evaporating or re-sputtering from the PZT film. The loss of lead from the PZT film will cause local non-uniformities in ferroelectric and mechanical properties [23]. This suggests that low temperature deposition of the PZT film will create much more uniform ferroelectric and dielectric properties, improving device reliability and operation. According to Suu *et al.* [23], the fraction of lead remaining in the deposited film is greatly dependant on wafer temperature during deposition. Once the substrate temperature increases above 50°C [23], lead begins to evaporate from the PZT film. This suggests that substrate cooling is required to help maintain the quality and uniformity of the PZT film throughout deposition. In addition to temperature concerns, physical differences between the substrate holder, sputtering shields, sputtering target surface and the plasma shape in the chamber may promote the lead to resputter off the target substrate [13].

Multi-target reactive sputtering, as discussed by Suchaneck *et al.* [24], may also be performed to deposit the PZT layer. In this method, multiple targets

consisting of the constituent elemental species (lead, zirconium and titanium) are used rather than a single PZT target. In this study, ZrO_2 was used as a buffer/adhesion layer, rather than platinum and titanium [24]. To form the PZT film, the individual compounds are etched off each target and accelerated towards the target wafer's surface. The compounds then combine at the wafer surface to form the PZT film on the wafer. In comparison to the single target method used previously, the reactive sputtering technique can allow for the direct manipulation of the constituent mass fractions for different material properties [24]. This method may allow for detailed tuning of the material properties, however, the overall film quality may be greater with a single PZT sputtering target.

Another method of PZT sputtering utilizes a pulsed laser as the excitation mechanism for sputtering instead of plasma from a RF Magnetron [25]. The substrate was kept at 650ºC, to induce crystallization during deposition [25]. Although the substrate temperature may be higher than some other sputtering methods, the laser removes some of the concerns with plasma shape and intensity that can be experienced during sputtering.

4.2.2.2 Metal Organic Vapor Deposition

Metal Organic Vapor Deposition (MOCVD) is a promising deposition technology, since the film uniformity, composition control, and step coverage offered by the process is suitable to many IC and semiconductor applications, as discussed by Li *et al.* [28]. In comparison to regular CVD, MOCVD of PZT requires the use of liquid reagents that are vaporized prior to injection into the reaction chamber. Each of the reagents is dissolved in a solvent comprised of tetrahydrofuran, isopropanol, and tetraglyme, in a 8:2:1 ratio, and then pumped into a vaporizer at flow rates of 0.1 - 0.5 ml/min [28]. Once vaporized, the vapors are injected into the reactor via an argon flow, heated to 220 - 250ºC [28,29]. The vapors react on the wafer's surface to create the solid PZT film. Excess gasses and by-products of the reaction are exhausted from the reaction chamber.

The deposition of PZT, following this procedure, can be undertaken in two

ways. The first method involves depositing the entire desired thickness of PZT film in one step, crystallizing the film during the deposition or after the deposition with an additional anneal [28]. The second method involves a two step deposition process. The first step in this method is to deposit a thin nucleation layer of PZT at low temperature. The remainder of the film thickness is deposited in the second step, at the crystallization temperature, to encourage grain growth and proper crystallization [28]. Higher polarization, smaller coercive field, order of magnitudes less leakage current, and a much smoother surface make the two step deposition more attractive for semiconductor applications [28].

In addition to producing films with desirable properties, it is possible to produce a PZT film with good step coverage via MOCVD. Funakubo *et al.* [29] examine this property of MOCVD. The deposition equipment, chemicals, and conditions are very similar to [28] for this MOCVD method. When building a the three-dimensional capacitor, Funakubo *et al*. [29] use a ruthenium (Ru) electrode instead of platinum as the electrode layers in the piezoelectric sandwich structure. To evaluate the step coverage of the MOCVD PZT film, trenched SiO_2/TiAIN/Ti/SiO_2/Si was used as the target substrate of the MOCVD. At 540ºC and 670 Pa, a near conformal step coverage was attained [29]. This suggests that step coverage of the MOCVD PZT is suitable for use in innovative, non-planar topographies. In addition, this gives PZT as much flexibility in deposition as other well known and commonly used materials in both semiconductor and MEMS applications.

4.2.2.3   Sol-Gel PZT Deposition

Sol-Gel deposition, regardless of material deposited, follows a very specific set of processing steps. First, a uniform layer of precursor solution is and spun onto the target wafer. Once the wafer has been well coated, the wafer is baked in order to evaporate the solvent present in the precursor solution. Once the film is dried, the wafer is subjected to a crystallization process, typically an anneal, to produce the required crystal structure of the material deposited. Although the general sol-gel deposition process is relatively simple, the variation in materials

and processing steps can be large, adding complexity and variability to the deposition. Thick films (above 1 μm) are possible using sol-gel deposition through multiple consecutive deposition steps.

In general terms, PZT sol-gel is a colloidal suspension of a crystalline $PbZr_xTi_{1-x}O_3$ powder that has been synthesized via chemical means [30-34]. Specific precursor solutions have been developed to tune the material properties of the film through the control of relative amounts of zirconium and titanium in the PZT powder. There are many methods of synthesis, requiring various process steps and initial ingredients. For example, Jacob *et al.* [30] react lead acetate $(CH_3COO)_2Pb \cdot Pb(OH)_2$, titanium tetrabutoxide $Ti(O^nBu)_4$ and zirconium acetylacetonate $Zr(CH_3COCHCOCH_3)_4$, to create a $PbZr_{0.55}Ti_{0.45}O_3$ powder. Lashgari and Westin [31] used lead nitrate dissolved in triethelene glycol, zirconium methoxy ethanolate, and titanium methoxy ethanolate to synthesize a $PbZr_{0.53}Ti_{0.47}O_3$ based precursor. Caruso *et al.* [32] produce a $PbZr_{0.5}Ti_{0.5}O_3$ powder from reacting lead acetate trihydrate $(Pb(O_2C_2H_3)_2 \cdot 3H_2O)$, titanium ethoxide $(C_2H_5O)_4Ti)$ and zirconium n-propoxide $(Zr(O(CH_2)_2CH_3)_4)$. As can be seen from these example PZT sol-gel precursors, great variety and flexibility is available. This allows for the selection or synthesis a particular PZT sol-gel precursor for a specific chosen set of dielectric or mechanical material properties.

The majority of research of PZT Sol-gel based sensors and actuators use commercially available sol-gel precursors [40,41]. Work by Wu *et al.* [35] into the long term stability of these sol-gel precursors has proven that stored sol-gels will give films with similar ferroelectric properties upwards of twelve months after synthesis. Proper storage, such as refrigeration and packaging under Argon will further increase the shelf-life of a sol-gel precursor [35].

The deposition of PZT sol-gel closely resembles the deposition of standard photoresist. In order to evenly spread the sol-gel precursor, a wafer spinner must be used. The speed and duration of spread and spin cycles will depend on the viscosity of the specific sol-gel precursor used. Spreads of a few hundreds of RPM for 5-10 s and spins of 2000-3000 RPM for 30 s [31,33] are typical

parameters for the spread/spinning of sol-gel precursors. Next, the wafer must be baked to solidify the deposited film. For thick films, greater than 1 μm, multiple deposition steps will be needed in order to build up enough PZT thickness [31]. Regardless of how many layers are deposited, a baking step is necessary after each deposition to drive off solvents and to make a solid base for the following deposition [31]. For the bake, the wafer may be heated on a hot plate [33] or undergo a low temperature rapid thermal anneal [31]. Usually the bake temperature is much less than the crystallization temperature, in the realm of 150-300°C [31,33]. For the majority of sol-gel deposition methods, the preferred crystallization step is an anneal at the crystallization temperature required by the specific PZT sol-gel precursor. The crystallization temperatures will vary according to the approximate value of x in $PbZr_xTi_{1-x}O_3$. In general, as the fraction of zirconium increases, in relation to the fraction of titanium, the crystallization temperature required for perovskite formation increases. For example, for x ≈ 0.5, perovskite crystal structures from at 550°C [32]; for x ≈ 0.53, 600°C was required [34]; and for x ≈ 0.55, 650°C was required [33]. It is of utmost importance that the film is subjected to the correct temperature anneal, otherwise the film will not exhibit the piezoelectric effect or material properties correctly. Additionally, the anneal step can be undertaken in multiple atmospheres or by rapid thermal annealing [30-34].

There are alternate methods of PZT crystallization, such as microwave-induced crystallization, as discussed by Wang *et al.* [37]. Wang deposited a x ≈ 0.52 $PbZr_xTi_{1-x}O_3$ film by spinning a pre-manufactured PZT precursor onto $Pt/Ti/SiO_2/Si$ wafer at 2600 rpm for 20s and then 4000 rpm for 40s [37]. The film was then baked on a hotplate at 120°C for 2 minutes to remove the solvent. In addition, the wafer was then pyrolyzed at 400°C for 5 minutes [37]. In order to build up a PZT film thickness of 1 μm, the deposition process described above was repeated five times [37]. The wafer was then exposed to microwave irradiation at 2.5 kW in air, from a multimode millimeter-wave heating system operating at 28 GHz, for approximately 4.5 minutes [37]. By preparing the PZT film in this manner, Wang *et al.* were able to produce a fully functional PZT film

of reasonable thickness at a crystallization temperature of only 480°C [37]. This method of crystallization may be more suitable to device applications where there is a "thermal budget" associated with the device to prevent unwanted diffusion of dopants or thermal damage to previously existing structures.

The nature of the spin coated, PZT sol-gel material leaves it susceptible to uneven surface morphologies, localized pin-holes, and cracking. If these pin-holes and cracks are not filled with additional PZT material, they have the potential to cause short circuits when the top electrode is deposited. A variety of methods have been reported to overcome the pin-hole defects of the sol-gel deposited PZT [42-46]. Dauchy *et al.* [43] have shown that lead diffusing from the PZT sol-gel layer cause pin-holes in the sol-gel deposited film. Multiple alternating layers of deposited sol-gel precursor and a PZT-based slurry were found to produce a continuous layer of PZT [43]. Additionally, multiple repeated layers of sol-gel were seen to fix voids and pin-holes, as shown by Okamura *et al*. [44]. Wang [46] and Bathusrt [42] have explored ink jet printing-based deposition of PZT sol-gel to overcome issues with pin holes and cracks.

4.2.3   Summary of Deposition Techniques

Sputtering is a well known and mature deposition technology capable of depositing thin film PZT. Through the multiple methods of sputtering, material composition and uniformity can be controlled, producing a high quality film. However, the loss of lead in the sputtering process is a large concern reducing the film quality. The resputtering of lead in a multi-user sputtering system would contaminate other user's processes. In industry, PZT sputtering is typically undertaken with dedicated equipment, to limit the potential for cross contamination of lead from PZT to other materials.

Metal Oxide Chemical Vapor Deposition (MOCVD) is comparable to sputtering of PZT, allowing for improvements in film properties. Through MOCVD, it is possible to attain improved polarization, smaller coercive field, order of magnitudes less leakage current, and a much smoother film surface.

These improvements cause MOCVD to be very appealing for use in semiconductor and integrated circuit applications. The major benefit to using MOCVD is the excellent, near-conformal, step coverage that can be attained especially in high aspect ratio applications. This is certainly important for adventurous topologies of non-planar PZT films. In addition, this allows PZT to be as versatile in deposition as other more common and well used materials in micro and nanofabrication.

PZT sol-gel deposition is a diverse and versatile deposition technology. The wide variety of precursor solutions and resulting material properties make sol-gel deposition attractive for any application of PZT - actuation, sensing, or capacitance. The scalability of the sol-gel deposition allows for a variety of film thicknesses through repeated depositions. Thick film deposition ($> 1 \mu m$) is easily attainable, which is preferable for sensing, actuation, and energy harvesting applications. Sol-gel deposition does not require expensive equipment to perform effectively, making it attractive for research and development. A resist spinner, a hot plate, and a furnace are the bare minimums required in order to be able to deposit sol-gel effectively. Sol-gel is also the method of choice for "shared" micro and nanofabrication facilities, due to the small possibility of lead cross-contamination in fabrication tools. For the research and development of sensors and actuators, the repeatability and uniformity of the films deposited by sol-gel deposition is adequate. However, for material science research, semiconductor applications, and integrated circuit applications, sputtering and MOCVD will be superior in terms of film quality and uniformity.

The general parameters of each deposition technique for PZT are summarized in Table 4.1.

Table 4.1 - Specifications of different PZT deposition techniques [47].

PZT Deposition Technique	Specifications
Sputtering	• Good for very thin layers (maximum thickness is ~1 µm). • Smooth, uniform films are achievable. • Potential cross contamination risk.
Sol-gel Technique	• Thicker films (above 1 µm) are achievable. • Deposition can result in pin-holes; requiring extra processing to resolve. • Requires multiple baking/thermal processes to build thickness. • Low risk of contamination.
MOCVD	• Suitable step coverage for 3D applications. • Good composition control. • IC and semiconductor compatible. • Very specialized equipment and materials required. • More of industrial/production process rather than research.

Although other deposition methods could provide more uniformity and better control over the material properties, Sol-gel deposition was chosen as the PZT deposition method for the microfabrication of the harvesters in this thesis. The customizability and increased thickness of the PZT film is desirable. Additionally, multiple deposition cycles that are required to build up sufficient PZT thickness will fill any potential pin-holes that may occur. The practical constraints of equipment availability and cross contamination played a large role in this methodology. PZT-based sputtering was not available at the University of Alberta Nanofab, therefore, PZT sol-gel deposition was developed through this research. Sol-gel lends itself very well to short batch, research driven microfabrication, with limited requirements for equipment and materials. The sputtering and MOCVD methods are more suited to batch fabrication of commercial products, due to the possibility of contamination and cost of equipment.

4.2.4   Patterning of the PZT Film

There are three methods available to pattern the PZT film: dry plasma

etching, lift-off, and wet etching. Dry plasma etching typically requires a Reactive Ion Etching (RIE) or combined plasma/chemical gas technique to remove the PZT film. The plasma-based dry techniques are combinations of mechanical and chemical etches. Argon ions are accelerated by the plasma into the surface of the target wafer to mechanically etch the wafer. At the same time, a mix of gasses is flowed through the reaction chamber to chemically etch the surface of the wafer [48-51]. This method is preferred in literature to other patterning methods, for both general materials and PZT, due to the increased accuracy and anisotropy that can be achieved [48-51]. However, this process is the exact inverse of the sputtering process used to deposit thin films; therefore, the possibility of cross contamination of lead is a significant drawback for this process. Some attempts have been made to reduce the lead-based contamination issues [52,53] in order to allow for more universal application of dry etching of PZT.

A lift off technique can also be used to pattern the PZT layer. In this technique, a layer of sacrificial material is used to prevent the adhesion of the PZT film in unwanted areas. When the photoresist is removed after the deposition of the PZT, the unadhered PZT is removed leaving the desired pattern. Procedurally, this lift-off is not different than lift-off procedures for other materials; however, an additional challenge exists with using lift-off with sol-gel PZT deposition. A thermal budget is imposed on the sol-gel deposition process to ensure the survival of sacrificial lift-off materials [54]. This places a temperature limit on the annealing/crystallization procedures when the sacrificial photoresist is present, requiring intermediate lower temperature anneals to solidify the PZT sol-gel material prior to lift-off. If the photoresist is heated too much, it will ash and permanently adhere to the wafer. This causes both the pattern to be lost and the wafer to be irrecoverable.

Wet etching of PZT is possible using chemistries based on combinations of buffered hydrofluoric acid and hydrochloric acids [55]. The main challenges of this wet etch technique include the potential undercut of the PZT layer during the etch and the selectivity of the etchants to other materials present in the device. For

example, the large concentration of hydrofluoric acid (HF) would preferentially etch silicon oxide and titanium layers, significantly damaging the harvesters. A number of techniques have been presented to minimize the undercut and to control the selectivity of the etch [9,56-58]. These techniques will be applied to the wet etch chosen for this microfabrication flow, as will be discussed in section 4.3.7.

4.3 PZT-based Energy Harvester Microfabrication Flow

4.3.1 Process Flow Introduction

The process flow used to microfabricate the energy harvesters has undergone several complete iterations of development to produce functioning harvesters. The iterative nature of this development was required in order to diagnose and troubleshoot fabrication processes throughout the project. From this work, a microfabrication process flow was developed with multiple options for the lower electrode and PZT deposition and patterning, resulting in a Report of Invention with the University of Alberta. In Figure 4.3, the entire fabrication flow is shown, with the most optimum/successful path of the fabrication flow highlighted.

Piezoelectric Energy Harvester Fabrication Process Flow

A. Initial Conditions — <100> Silicon Wafer with SiO₂ Grown

B. Platinum Lift-off
- Photolithography to Prepare for Titanium/Titanium Tungsten/Platinum Lift Off
- Titanium/Titanium Tungsten and Platinum Sputtering
- Lift Off to Pattern Platinum/Titanium/Titanium Tungsten

C. Platinum Wet Etch
- Titanium and Platinum Sputtering
- Photolithography and Aqua Regia Etch to Remove Platinum/Titanium

D. Silicon Oxide Etch — Photolithography and BOE Etch to Remove Excess SiO₂

E. PZT Lift-off
- Photolithography and PZT Sol-Gel Deposition
- Patterning of PZT Thin Film via Lift-Off
- Photolithography and Sputtering of Upper Platinum Layer
- Patterning of Upper Platinum via Lift-Off

F. PZT Wet Etch
- PZT Sol-gel Deposition
- Photolithography for PZT Wet Etch
- PZT Wet Etch (Note Residues on Silicon)
- Photolithography and Sputtering of Upper Platinum Layer
- Patterning of Upper Platinum via Lift-Off
- Photolithography for PZT Residue Removal
- PZT Residue Removal (PZT Wet Etch and BOE)

G. Definition and Release of the Harvesters
- Photolithography and Front Side DRIE to Define Energy Harvester Shape
- Adhesion of Carrier Wafer on Front Side of Device Wafer, Photolithography and Back Side DRIE to Define Folded Spring Thickness
- Removal of Photoresist/Carrier Wafer in Acetone Bath, Completed Energy Harvester

Advanced MEMS/NEMS Multiphysics — Design Lab

Figure 4.3 – Prototype Energy Harvester Microfabrication Process Flow

The entire microfabrication process flow has been qualified extensively producing prototype energy harvesters. Over the development of the fabrication process flow, there have been a number of iterations and changes to the fabrication flow according to various challenges encountered. Each step of the

fabrication process will be discussed in detail, with challenges encountered and overcome discussed when appropriate in the following sections.

This fabrication flow is capable of producing piezoelectric energy harvesters of the same cross section (Pt/PZT/Pt stack) of any configuration and beam thickness. Therefore, the fabrication flow can be adapted as a general fabrication procedure for a number of PZT-based energy harvesting designs. In the following discussion of the fabrication flow, each section of the fabrication flow shown in Figure 4.3 will be referenced and discussed in detail.

4.3.2 *Wafer Preparation and Initial Conditions*

As shown in Figure 4.3 in "A. Initial Conditions", the fabrication process starts with wafer preparation. Double side polished prime <100> silicon wafers are preferred for this process flow. In later fabrication steps, the double sided polish wafers are useful for a more accurate backside pattern alignment. The rough surface of the backside of a single side polished wafer will scatter some of the infrared light used in backside photolithography. Therefore, the use of a single side polished wafer may add additional alignment error to the final dry etch process.

The thickness and uniformity of the wafer chosen for this process will have several implications. First, the thickness will directly define the volume of the proof masses used in the Class II Harvesters. This will directly influence the natural frequency of the harvesters produced. Second, the uniformity in thickness will define the variability in the volume of the proof masses. Additionally, the uniformity will have a significant effect on the etch uniformity in the definition of the folded springs. Therefore, the wafer thickness uniformity will directly affect the variability in natural frequency of the produced harvesters. For this process, it is important to have wafers with as uniform thickness as possible.

The wafers should be cleaned in a "Piranha" solution to remove all organics before growth of silicon oxide. The Piranha cleaning solution is a 3:1 mixture of sulphuric acid and hydrogen peroxide. This solution is required to

remove all organic materials from the wafers, to ensure that the various patterning and deposition processes are not adversely affected by residual organics in any way. Foreign material will prevent the adhesion of thin films and may mask various etch processes, preventing accurate fabrication of the harvesters.

Silicon oxide was chosen as the isolation and diffusion barrier for the energy harvester. Additionally, the silicon dioxide is required as an adhesion layer for the titanium-based layer of the piezoelectric stack. Titanium will only adhere to surfaces that have an abundance of free oxygen for the free electrons of titanium to bind to. A dense, dry silicon oxide is preferred over a wet oxide due to better insulation and diffusion barrier characteristics. The dry oxide is grown in an annealing furnace under a nitrogen/oxygen environment, where water vapor is not present. Wet silicon oxide is grown in an annealing furnace where steam is present. This allows for an increased growth rate of silicon oxide, producing a thicker, but less dense silicon oxide film. For this fabrication flow, dry oxide would be preferred; however, only wet oxidation was available. For this procedure, the wafer was wet oxidized at 1000ºC for 100 minutes in a steam atmosphere to grow approximately 500 nm of SiO_2 on the surface of the silicon wafer.

4.3.3   Lower Electrode Deposition

The lower electrode of the energy harvester has been deposited in two different methods in this microfabrication flow, depending upon the materials deposited. The first method used in this research, as shown in "C. Platinum Wet Etch" in Figure 4.3, patterned the titanium/platinum layers via an aqua regia wet etch. Later in the research, due to the use of a different adhesion material, a lift-off procedure was used to pattern the lower electrode, as shown in "B. Platinum Lift-Off" in Figure 4.3.

4.3.3.1   Platinum/Titanium Wet Etch

Section "C. Platinum Wet Etch" in the microfabrication process flow in Figure 4.3 outlines the wet etch based patterning of the metallic

electrode/adhesion layers of the energy harvester. For this case, platinum and titanium are the only allowable metallic layers for this process. The aqua regia etch is an isotropic wet etch that can pattern both metal layers simultaneously. Specialized etching equipment is required to increase the etch rate of the process while handling the chlorine exhaust and etch waste in a safe manner.

4.3.3.1.1 Metallization

The platinum and titanium electrodes were deposited via RF Magnatron Sputtering using an argon plasma. Both metals were deposited sequentially in one deposition step. First, the titanium was deposited at a base pressure of $7x10-6$ Torr, with sputtering power of 300 W. A $50 - 60$ nm thick layer of titanium was deposited at approximately 8 nm/min. Directly following the deposition of the titanium, the platinum was deposited at the same base pressure with a deposition power of 75 W, producing a deposition rate of approximately 3.8 nm/min. The deposited thickness of the platinum was varied from 200 to 250 nm over the research. The thickness of the platinum layer was varied in an attempt to fix various PZT-based adhesion issues encountered in later fabrication. The sputtering of these two materials is performed sequentially under the same pump down to prevent any potential oxidation or contamination between layers.

4.3.3.1.2 Aqua Regia Etch

The aqua regia etch will pattern both the platinum and titanium layers in one etch step. The photoresist required to mask this etch is AZ 506. For this specific etch, the AZ 506 is deposited with a spread cycle of 500 RPM for 10 seconds, spin cycle of 4000 RPM for 40 seconds, with a soft bake of 115ºC for 90 seconds on a vacuum hotplate. The photoresist requires a 15 minute rehydration in order to promote proper exposure and resistance to etchants. The photoresist is patterned using an optical mask aligner, exposing the photoresist to be removed for approximately 3 seconds. The exposed photoresist is then developed in 354 developer for approximately 45 seconds, until the red streaks from the dissolving photoresist disappear. This procedure produces a photoresist thickness of approximately 1.2-1.5 µm. The photoresist is then hard baked at 115ºC for 15

minutes on a hot plate in order to maximize the resist's resilience to the aqua regia etch.

Platinum is a very robust and is etch-resistant material. Aqua regia, a 3:1 ratio of hydrochloric and nitric acids, is one of the few wet etchants capable of etching platinum. An experimental setup was developed to allow for the control of the etch process, including solution temperature, agitation, removal of the by-product chlorine gas, and the aspiration of the waste solution. The experimental setup can be seen in Figure 4.4.

Figure 4.4 – Aqua Regia Etch System (ARES) developed in order to perform the etch process.

The entire apparatus is housed within a glove box to keep the process in a controlled volume to add an additional layer of protection for the user. The setup contains a self contained reaction chamber, covered by a vented bell jar, allowing for controlled exhaust of the by-product chlorine gas. The exhaust from the reaction chamber is drawn, via suction, from the reaction chamber and bubbled through a gas wash bottle. This allows for the dissolving of the chlorine gas into the wash bottle, creating a weak hydrochloric acid solution which can be easily disposed of. In addition, the clear reaction chamber allows the etch to be easily monitored. Since parameters such as temperature, agitation, age of solution, and relative volume of reactants all effect the etch rate, visual monitoring is required to determine the "stop point" of the etch. A detailed explanation of the Aqua Regia Etch System (ARES) and the operation of the system are discussed in Appendix B.

The aqua regia solution used in this process is a 3:1 solution of hydrochloric and nitric acids with a total volume of approximately 160 mL. The solution should be aged and heated at approximately 75°C for 10 minutes. Without the aging, the etch rate of the solution will be slowed. The use of the ARES system to control the parameters of the etch allowed for the increase of the etch rate of aqua regia from 3 nm/min reported in literature [59] to approximately 12–15 nm/min. The solution must be continually agitated for the duration of the process. Although the etch rate is fairly consistent with an aged solution, it must be monitored visibly for a noticeable color change as the silicon dioxide layer becomes visible. The surface of the wafer will turn from metallic grey to an emerald green to show the 500 nm SiO_2 layer, signifying the end of the etch. If the Aqua Regia solution is not aged properly before etching, over etching and pattern damage will occur.

4.3.3.2   Lower Electrode Lift Off

Section "B. Platinum Lift-Off" in Figure 4.3 outlines an alternative to the aqua regia etch which has been used to overcome two particular challenges that arose through the development of the microfabrication process flow. The first challenge was the uneven etching that occurred due to the interaction of the increased etch rate of the aqua regia etch and the non-uniformity of the sputtering processes. Typically, the isotropy of the aqua regia wet etch is not a drawback, however, when coupled with the non-uniformity of titanium/platinum sputtering, on the order of a few tens of nanometers across the wafer, the situation seen in Figure 4.5 can arise.
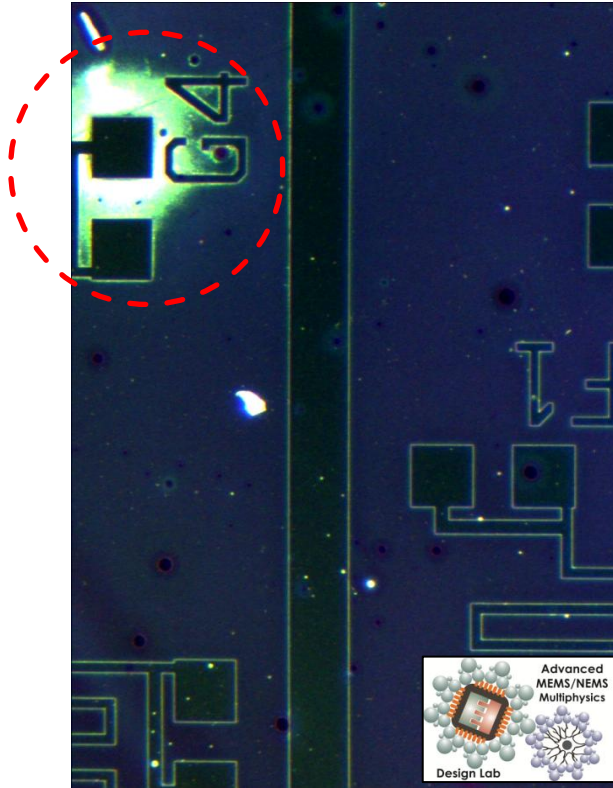
Figure 4.5 – Platinum and titanium films etched by aqua regia. Residual titanium from underetching is highlighted.

Due to the nonuniformity in the deposition, it is possible to have areas of completely etched and under etched film on the same wafer. The residual titanium shown surrounding the electrode pad in Figure 4.5, in later steps involving a Buffered Oxide Etch (BOE), would be instantly etched, lifting off the platinum layer above. The etch rate of titanium in BOE is extremely high [59], therefore any exposure to the BOE etchant in any subsequent step would cause the behavior shown in Figure 4.6.
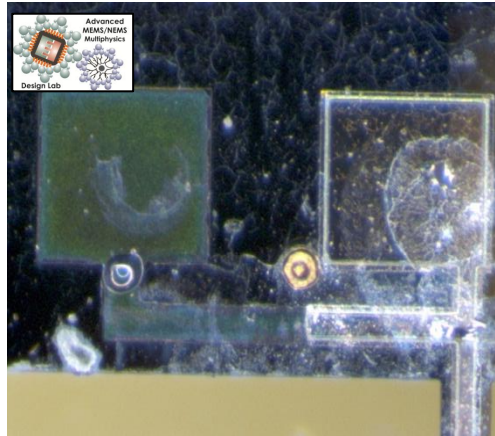
Figure 4.6 – Resulting lift off of the electrodes due to the residual titanium residue. The visible green silicon oxide remaining shows the complete removal of the titanium/platinum electrode.

As shown in Figure 4.6, the residual titanium that extends beyond the boundaries of the pad allows for the complete undercutting of the titanium layer. This can be clearly seen in Figure 4.6, where the lower electrode pad (on the left) has been completely removed, leaving the green silicon oxide layer behind To salvage the devices damaged in this manner, the packaging scheme had to be altered, which will be discussed in Chapter 5.

The second challenge that prompted the use of a lift-off procedure was the poor adhesion of the PZT layer. Although the PZT deposition is farther downstream in the process flow, the adhesion of the bottom electrodes is critical for the adhesion of the PZT. As will be discussed in the PZT deposition section, titanium tungsten was chosen as an alternative adhesion layer instead of titanium as a solution to film peeling due to titanium migration. According to literature, titanium tungsten has a slightly higher etch rate in aqua regia as platinum, 3.9 nm/min versus 3.5 nm/min respectively [59]. Therefore, with the increased etch rates achieved with the aqua regia etch process developed in this research, the possibility of not being able to accurately control the patterning of the titanium tungsten was too great. It was likely that any sputtering uniformity issues would be exacerbated by the faster etch rate of titanium tungsten in aqua regia,

magnifying the existing over/under etch issue. For this reason, the patterning of titanium tungsten was chosen to be completed by lift off only.

4.3.3.2.1 Photolithography for Lift off

The first step in this option of the process flow involves depositing a photoresist to serve as the sacrificial layer in the lift off procedure. The goal of this sacrificial layer is to prevent the adhesion of the sputtered metal to the wafer. After the metal is deposited, the photoresist is dissolved, and the unwanted material is removed from the wafer, as shown in Figure 4.7.
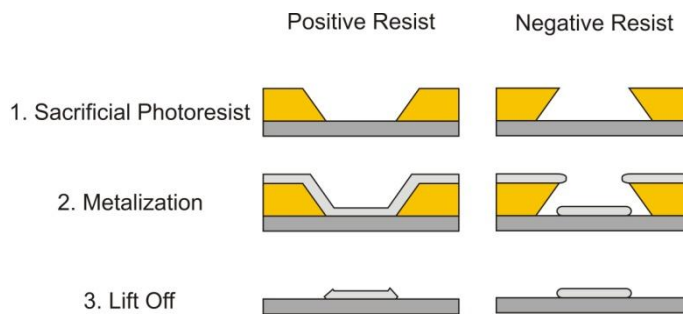
Figure 4.7 – A schematic outlining the stages of the lift off process with both positive and negative photoresists. Sidewall angles are exaggerated for illustration.

In the initial iterations of the lift off procedures used in this fabrication process, a positive photoresist was used. Typically, "positive" and "negative" refer to the response of the photoresist to the UV light used in exposure. A positive photoresist will be removed in the areas where the resist is exposed to UV light. A negative photoresist will crosslink where exposed to UV light. The areas not exposed to UV light will be removed during development. For the lift off application, the polarity is not specifically important – the cross sectional profile of the resultant photoresist pattern is important. When a positive photoresist is used for lift-off, the cross sectional profile that is achieved is shown above in Figure 4.7. Although the sidewall angle is not as exaggerated as shown in Figure 4.7, the sidewalls will be coated with the sputtered metal, creating a continuous metal film. This becomes a significant issue during lift-off. In order to

complete the lift off procedure with a positive photoresist, ultrasonic cleaning and other harsh means are required to remove the unwanted metal. The ultrasonic cleaning may lead to redeposition of metal particles creating short circuits and uneven topologies on the surface of the wafer, causing additional fabrication issues for the subsequent fabrication steps.

For this lift off procedure, a negative photoresist, AZ 5214, was used in order to perform the lift off. This resist can achieve an undercut sidewall profile, as shown in Figure 4.7, which is beneficial for lift-off. This cross section causes the sputtered metal to be physically patterned by the overcut photoresist profile. When exposed to acetone or similar solvents, the removal of the sacrificial material takes place very quickly and cleanly.

The AZ 5214 resist is spread on the wafer at 500 RPM for 10 seconds and then spun at 4000 RPM for 50 seconds. The photoresist is baked on a vacuum hotplate at 90ºC for 40 seconds. It is critical to allow the photoresist to rehydrate after the baking step for 20 minutes, otherwise, the photoresist will not switch polarity correctly or react properly to the UV exposure light. Next, the photoresist is exposed with ultraviolet light for 4.5 seconds to transfer the desired pattern to the wafer. The photoresist is then baked again on a vacuum hotplate at 110ºC. This baking step converts the photoresist from a positive photoresist to a negative photoresist. Again, the photoresist needs to be rehydrated for 20 minutes for proper operation. The entire wafer is then flood exposed to UV light to expose the previously masked photoresist. The resist is then developed in MF 319 for approximately 25-30 seconds. This procedure allows for a negative photoresist of approximately 1.5 μm thick with an undercut cross section, suitable for lift off.

4.3.3.2.2 Metallization

The lift-off process can be used to pattern any suitable lower electrode metal. With this procedure, platinum, titanium, and titanium tungsten have been patterned for use as a lower electrode for the harvesters. The parameters for depositing titanium and platinum are no different than previously discussed for

lower electrode deposition section. Titanium tungsten is deposited through RF Magnitron sputtering as well, at a deposition base pressure of 7x10-6 Torr with a deposition power of 275 W. These parameters give a deposition rate of approximately 5.4 nm/min for titanium tungsten. As with the titanium layer previously used, the target film thickness is 50 nm. When titanium tungsten was used as the adhesion layer, it simply replaced the titanium in the order of deposited metals.

4.3.3.2.3 Lift-Off of Lower Electrode Metal

To lift off the lower metal electrodes, the entire wafer must be immersed in a solvent that removes the sacrificial material. For the initial work with positive photoresists, a long and tedious release procedure was required. In order to allow the acetone to infiltrate the thin metallic layer to dissolve the photoresist, the wafer was soaked for at least 12 hours. To remove the unadhered metal, the wafer was ultrasonically cleaned. This caused the remaining metal to peel/break away from the pattern, creating the rough edge conditions shown in Figure 4.7. The negative photoresist (AZ 5214) discussed above did not allow for the conformal coating of the sidewalls of the resist, therefore, the acetone easily penetrates into the photoresist allowing the lift off to occur quickly. The wafers were soaked in acetone for several hours, inverted, so that the dissolved material would fall away from the wafer. This allowed for the acetone to dissolve all the photoresist easily, allowing for the non-adhered film to be washed away with a spray of acetone. The use of a negative photoresist greatly improved the edge conditions and accuracy of the lift-off procedure, as shown in Figure 4.7.

4.3.4   Patterning of Silicon Dioxide

As shown in Section "D. Silicon Oxide Etch" in Figure 4.3, regardless of method used to deposit and pattern the lower electrode of the harvester, the underlying silicon oxide layer was patterned next. The silicon oxide is patterned with a AZ 504 photoresist. The AZ 504 is spread on the wafer at 500 RPM for 10 seconds, spun at 4000 RPM for 40 seconds, and then soft baked of 115ºC for 90 seconds on the vacuum hotplate. A rehydration of 15 minutes is required to ensure

proper exposure of the resist. The pattern is then transferred by optical mask aligner with a UV exposure of approximately 3 seconds. The photoresist is then developed in 354 developer, for approximately 45 seconds or until the red streaks from the dissolving photoresist disappear. The silicon oxide is wet etched using a standard recipe with a pre-mixed Buffered Oxide Etch (BOE). The typical etch rate of this specific BOE etchant is 35-50 nm/minute, requiring approximately 10-14 minutes to etch the 500 nm of SiO_2. The BOE solution is typically reused many times, with the etch rate degrading over time with multiple uses.

4.3.5 *Deposition and Patterning of PZT and Upper Electrode*

As shown in Figure 4.3, two separate methods were developed to deposit and pattern the PZT and upper electrodes. Each method uses a different PZT sol-gel precursor, thereby requiring different deposition and annealing parameters. The first method used in the initial stages of the fabrication process, as shown as Section "E. PZT lift-off" in Figure 4.3, utilized a lift-off to pattern the PZT film. This method worked well to develop the understanding of the PZT film deposition procedure; however, there were significant issues with the specific PZT material. When it was apparent that better material properties and coverage/thickness were available with a different PZT sol-gel precursor, a second deposition/patterning technique was developed for the new PZT material. This procedure is shown as "F. PZT Wet Etch" in Figure 4.3. The second PZT material had a much higher yield of electrically functioning harvesters. In both methods, the deposition and patterning of the upper electrode are completed through a lift-off procedure.

4.3.6 *Lift off of PZT and Upper Electrode*

Section "E. PZT Lift-off" in the microfabrication process flow in Figure 4.3 outlines the lift-off based deposition process developed to deposit the PZT film. Due to the anneal/bake requirements of the PZT and the thermal budget of the sacrificial photoresist, the lift-off and deposition must occur simultaneously. After the lift off and deposition, the platinum top electrode is deposited via another lift off process.

4.3.6.1.1 Lift off Patterning of the PZT film.

To pattern the first PZT material used in the research, from Alfa Aesar, the deposition and lift-off must occur in tandem. A sacrificial layer of photoresist is deposited and patterned to prevent the PZT film from adhering to the wafer in areas that the PZT film is not required. As with the other initially developed lift-off procedures, a positive photoresist was used as the sacrificial material. After the photoresist is patterned, the PZT sol-gel then spun on to the wafer. Approximately 5 mL of the PZT sol-gel precursor is spread on the wafer at 250 RPM for 20 seconds, and then spun at 1000 RPM for 30 seconds. Once the spinning of the PZT precursor is complete, the wafer must be baked to drive the solvent from the PZT film. The baking step must be ramped to 100ºC in order to prevent film cracking through thermal shock. The film is baked at 100ºC for 15 minutes to evaporate the sol-gel precursor solvent. When the baking is complete, a partial anneal is required in order to solidify the film sufficiently to allow for lift off to occur. As with the other thermal processing step, it must be ramped in order to prevent thermal damage. The anneal is ramped to 150ºC and held for 15 minutes. After the partial anneal was complete, the temperature was ramped down to ambient.

As with other lift off processes, the wafer was immersed in acetone to remove the sacrificial photoresist. The critical difference with this lift-off process is the length of time the PZT film can be exposed to acetone. The PZT sol-gel film is partially soluble in acetone; therefore, it was necessary to limit the total exposure. The optimum lift off occurred with a 5 minute soak in acetone, followed by a 2 minute, mid power, ultrasonic bath. After the excess PZT material was removed, the wafer was annealed to crystallize the PZT film. To prevent cracking from thermal shock, the crystallization anneal was also ramped to the required 475ºC. The PZT film was annealed for one hour, and then ramped down to ambient over several hours. If the annealing furnace was opened prematurely, the thermal shock of the ambient air rushing into the furnace would damage the PZT film.

This method of PZT deposition was capable of producing films as thick as 3 μm, with some uniformity and coverage issues, as shown in Figures 4.8 and 4.9.
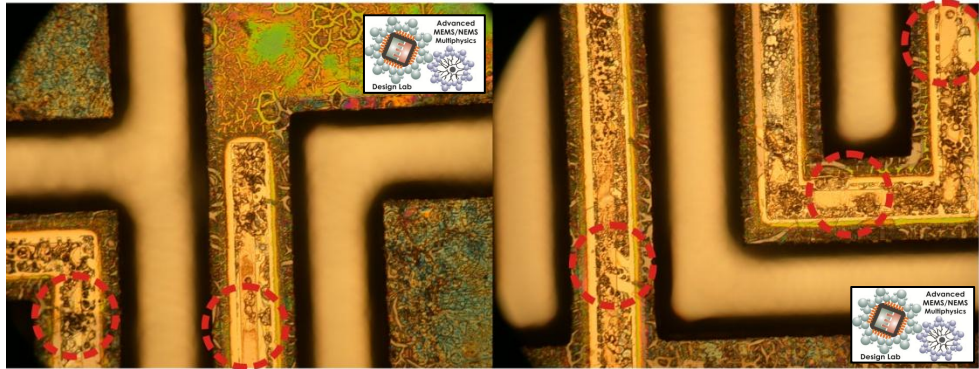
Figure 4.8 – Examples of poor quality PZT film patterned by the lift off procedure. Circled areas denote short circuits.
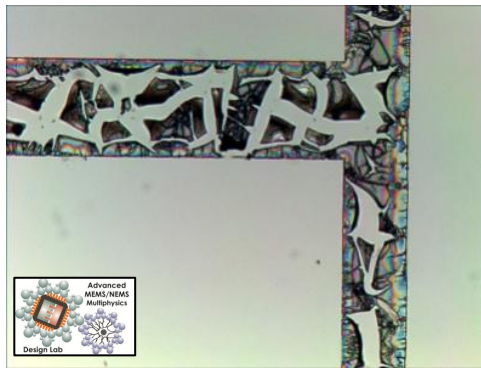
Figure 4.9 – An example of voids created through the loss of PZT precursor solution during the PZT lift-off process.

During the lift-off, it was found that the semi-solid PZT film would locally dissolve from the wafer when exposed to acetone. This caused a net volume loss, which ultimately led to a contraction of the PZT film during annealing, causing the voids and cracks that are seen in both Figure 4.8 and 4.9. To fill these voids, an additional layer of PZT is required. This required the repetition of the entire PZT lift-off process.

4.3.6.1.2 Lift-off of Upper Platinum Electrode

The upper platinum electrode required to complete the piezoelectric stack was deposited and patterned using the same procedure as "B. Platinum Lift-Off"

in Figure 4.3 and section 4.3.3.2. Approximately 250 nm of platinum was deposited by this method in order to complete the piezoelectric stack.

4.3.7 PZT Wet-Etch and Lift-off of Upper Electrode

Section "F. PZT Wet Etch" in the microfabrication process flow in Figure 4.3 outlines the wet etch-based procedure used to deposit and pattern the second PZT material used in this research. The second PZT material, from Mitsubishi Materials Corporation, required a crystallization temperature of 700ºC. Therefore, the lift-off process that was developed in the previous section would not be suitable for patterning. Although the first PZT material could achieve continuous, thick, PZT films, the overall yield of functioning devices was very poor. The new PZT material had better coverage and uniformity than the previous PZT material. To pattern the second PZT material, a wet etch was selected from literature and then adapted for use in our fabrication facility.

4.3.7.1 PZT Sol-gel Deposition (Mitsubishi Materials Corporation):

The second PZT sol-gel deposition procedure was similar to the previous deposition procedure, with some minor precursor-based changes. In this case, a repeated spin-bake process was required to build up the thickness of the film. The PZT sol-gel was spun on the wafer at 500 RPM for 5 seconds and then spread on the wafer at 3000 RPM for 30 seconds. This PZT material did not require the ramped bake as the previous PZT material; therefore the thermal steps took much less time to accomplish. Once the PZT sol-gel was spun, the film was baked on a hot plate at approximately 350ºC to solidify the film. At this point, this spin-bake process must be repeated three times to build up 0.24 μm of PZT, in steps of 0.08 μm. Once the spin-bake cycle was completed, the film was annealed to crystallize the PZT film. The anneal takes place at 700ºC for 15 minutes, with no ramp up or ramp down required. Once annealing is complete, the entire deposition process can be repeated in order to add additional PZT thickness in steps of 0.24 μm. In this work, PZT thicknesses of up to 0.96 μm have been achieved.

The PZT material was characterized with X-Ray Diffraction (XRD) to ensure that the material was crystallizing properly with this fabrication process, as shown in Figure 4.10.
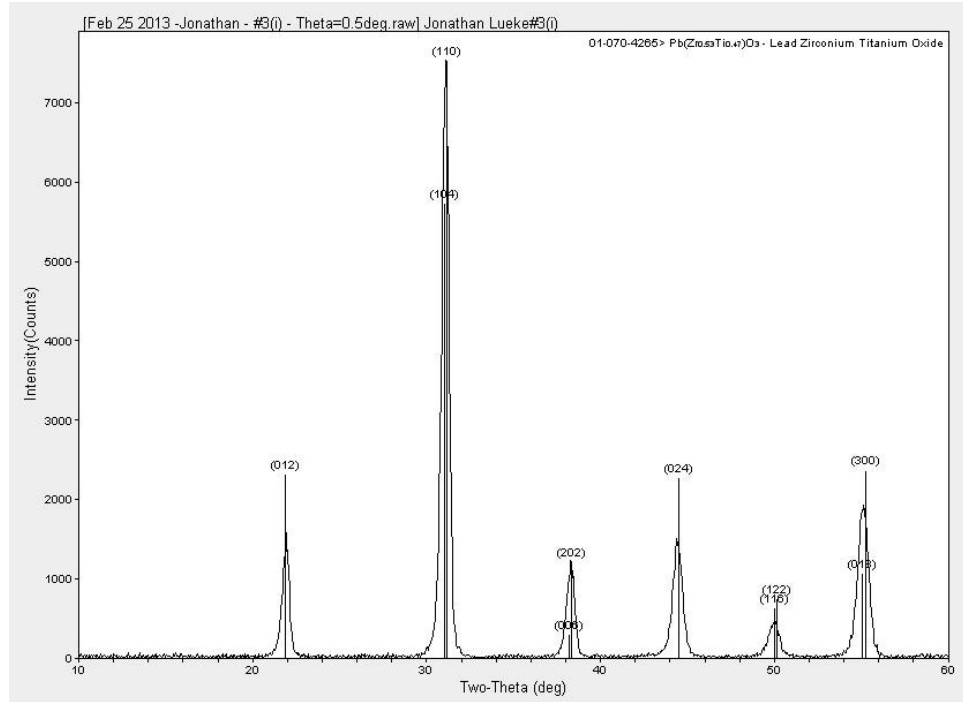
Figure 4.10 – XRD of the Mitsubishi Materials PZT material. This XRD is for a sample of 0.24 μm. The peaks of the measured intensity match the vertical lines of expected peaks (with plane identifiers in parenthesis) confirming the PZT material is present and crystallized properly.

The measured reflected intensity peaks from the XRD analysis of the fabricated PZT are shown in Figure 4.10. The expected peaks of the PZT material standard are shown as vertical lines with parenthesis defining each crystal plane. The measured intensity peaks follow the expected peaks for the PZT material; therefore, the PZT deposited is crystallized properly.

In addition to the proper crystallization, it should be noted that the PZT deposited required a different adhesion layer to allow for multiple layers of PZT to be deposited. The anneal required for crystallization occurs at the same temperature titanium based silicides begin to form at the silicon oxide/titanium

interface [60]. Therefore, as the wafer is annealed, titanium migrates from the titanium layer into the silicon oxide, reducing the thickness of the titanium layer. Given enough time in the annealing furnace, the titanium layer is completely removed, causing the PZT to peel off the wafer due to residual stresses and poor adhesion between the remaining platinum and silicon oxide. Titanium tungsten was used as a replacement material. The larger tungsten atoms act as a diffusion barrier, not allowing the titanium to freely migrate out of the film during the anneal. This prevents most of the titanium loss, maintaining the thickness and adhesion of the films. This allowed for the deposition of continuous PZT films, without major cracks/voids, through multiple applications of the PZT sol-gel. On areas of exposed silicon and silicon oxide, the PZT film tended to crack and produce discontinuous films. Ultimately, this is more of a cosmetic problem and does not cause any performance-related issues. An example of an annealed PZT film using this process can be seen in Figure 4.11.
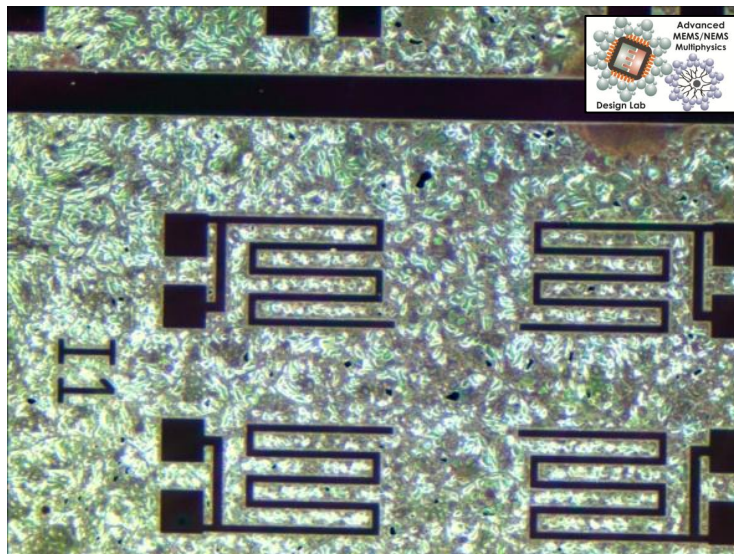
Figure 4.11 – Correctly formed PZT thin film, continuous on the exposed platinum, cracked/discontinuous on the exposed silicon/silicon oxide.

4.3.7.2   Photolithography and PZT Wet Etch

As was discussed previously, lift-off of this specific PZT material was not possible. Additionally, due to cross contamination concerns, dry plasma etching

147

of PZT was not available. Therefore, a wet etch technique was chosen from literature, and adapted for use in our fabrication facility [58].

In this etch step a thick photoresist, AZ 4620, was selected to protect the metal electrodes of the harvester. A specific recipe for AZ 4620 was developed for this microfabrication process that allows for deposition of approximately 12 μm thick layer with no pinholes or voids. The photoresist is spun on the wafer at 500 RPM for 10 seconds and spread at 2000 RPM for 25 seconds. The photoresist is then baked on a vacuum hot plate at 100ºC for 150 seconds. Due to the thickness of the photoresist, the rehydration, exposure, and development steps all require additional time in comparison to the previous resists used. For the AZ 4620, the rehydration period is increased to 24 hours in a moist environment. To expose the entire thickness of the photoresist, the exposure time must be increased to 12 seconds. The UV exposure of the photoresist may be divided into thirds to prevent localized heating of the photoresist. To develop the photoresist, the resist must be immersed in AZ 400K developer for approximately 1 minute and 20 seconds. The development of the photoresist is critical and must be visually inspected prior to processing. Residual photoresist, even very thin layers, can significantly inhibit many etch processes masking areas that are meant to be etched.

Once the wafer is patterned with AZ 4620, the PZT film can be wet etched. The wet etch adapted from literature is composed of three separate wet etches [58]. First, the PZT is etched in a solution of $1BOE:2HCl:4NH_4Cl:4H_2O$ to convert the open PZT material to a white residue of PbClF [58]. In comparison to other available PZT wet etch procedures, the addition of the ammonium chloride (NH_4Cl) salt helps reduce the problematic undercut caused by the BOE etch, slowing the etch rate slightly, minimizing the lateral etch [58]. Second, the PbClF residue is etched with a solution of $2HNO_3:1H_2O$ producing a residue of water soluble $PbCl_2$ [58]. Lastly, a prolonged soak in deionized water is used to remove the water soluble $PbCl_2$. This etch process is specifically meant to etch the PZT that is present on the platinum electrodes only – not the poor quality film on

deposited on the exposed silicon and silicon oxide. The progression of the etch and examples of residues left by this process are shown in Figure 4.12.
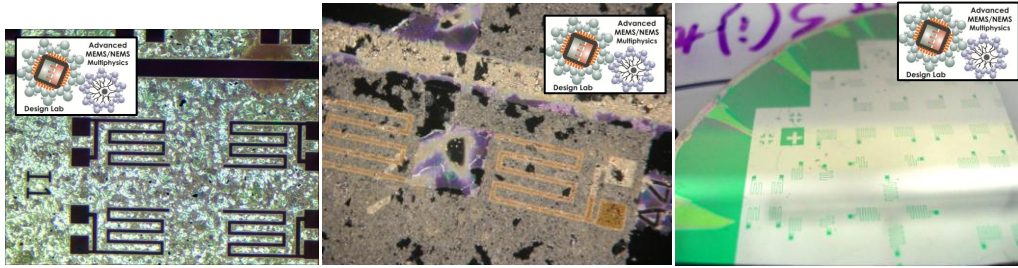
Figure 4.12 – The PZT film during the etch process. Left shows the unetched PZT film. Middle shows the intermediate residue left after the second etch process. Right shows the completed etch. PZT deposited on platinum appears dark green.

The PZT wet etch process is very capable of producing clean and accurate patterns on platinum films, as shown by the right figure in Figure 4.12. However, on silicon and silicon oxide, PZT residues require an additional etch step for removal. To meet the requirements of the fabrication facility, the residual PZT film must be removed in order to prevent cross contamination of etch equipment in the subsequent deep silicon etches of the microfabrication process. Therefore, a second PZT wet etch, followed by a prolonged BOE etch, using the previous parameters, were required to remove the residual PZT film. As shown in Figure 4.13, the etch area for this process is far from the piezoelectric stack (distinguishable by the metallic silver and multiple layers).
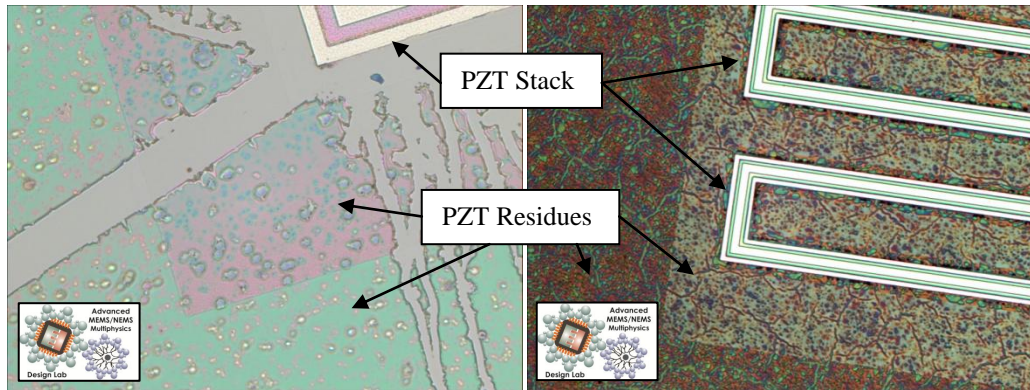
Figure 4.13 – Mid-process photos of the second PZT etch needed to remove the residual PZT film from the silicon/silicon oxide. In both photos, a color change in the PZT residual film denotes a height change from etching.

The photos in Figure 4.13 were taken at an intermediate point in the development of this "clean up" etch while determining the etch rate and required additional processing required to complete the etch. Since PZT is semi-transparent, optically behaving like silicon oxide having different colors at different thicknesses, the difference in thickness can be easily observed in Figure 4.13.

4.3.8   *Definition and Release of the Harvesters*

As shown as Section "G. Definition and Release of the Harvesters" in Figure 4.3, two sequential deep reactive ion etches (DRIE) were required to define the geometry of the folded springs and release the harvesters. DRIE is based upon the Bosch Etch Process [61], where a number of shallow isentropic plasma etches are used in sequence, with a passivation step, to create a deep anisotropic etch with near vertical side walls. The process uniformity of the DRIE process coupled with the thickness variation of the silicon wafer selected for fabrication can cause a significant challenge to the uniformity and accuracy of the etch depth. The DRIE non-uniformity is a function of the overall depth, therefore the total error in uniformity and etch depth increases cumulatively with etch depth [41,61-64]. This variability ultimately causes individual devices, of the same design, on the same wafer to have differing natural frequencies. There have been

150

some attempts to tune the parameters of the DRIE/ICPRIE process, such as RF power, chemistries used in the etch, cooling backpressure, dummy structures, and so on, to achieve a more consistent and accurate etch [41,61-65].

The methodology used to define the planar geometry and release the energy harvesters is based upon overlapping the etched volumes created from two sequential etch steps, as shown in Figure 4.14.
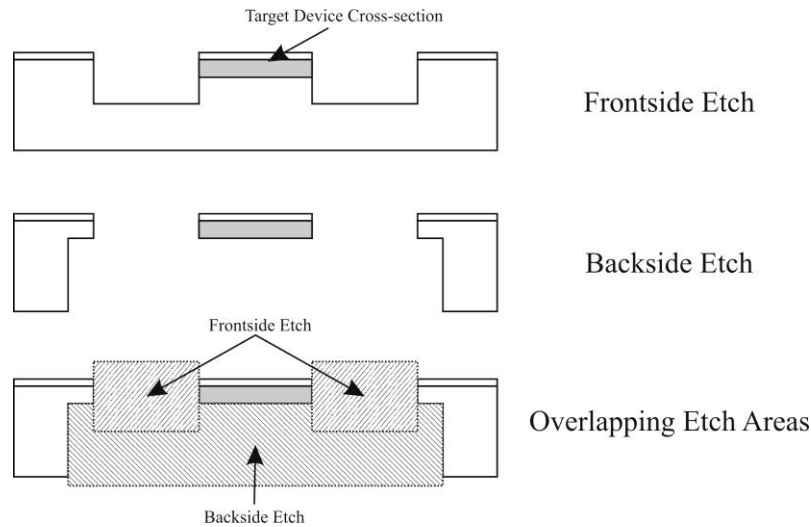
Figure 4.14 – Overlapping Etch Areas Providing Released Devices [47]

The two-step methodology begins with a fairly deep front side DRIE (at least 100 µm) to define the planar geometry, followed by a deep backside DRIE to define the thickness of the folded springs. The depth of the front side etch is significantly larger than the desired thickness of the energy harvester to ensure that the folded springs of the harvester have as vertical sidewalls as possible. The deep backside DRIE then completes the near-rectangular cross section of the folded silicon beam.

The methodology used to release the energy harvesters through the combination of etch steps adds a major wafer handling challenge. Since deep wells are etched through the wafer in the final etch process, the device wafer becomes progressively more delicate. Typically, the DRIE process requires the wafer to be gas cooled to maintain a constant etch rate. The slight pressure

differential between the near-vacuum required for the plasma and the few millitorr of helium required to cool the wafer will cause the increasingly delicate wafer to burst during the final stages of the etch process. If the wafer survives the final DRIE etch, the weakened wafer can spontaneously cleave along etched areas and/or major crystallographic planes. Due to this problem, it was necessary to stabilize the device wafer with a carrier wafer previous to the final etch step. Additionally, the use of a carrier wafer allowed for the exploitation of this behavior to cleave the completed harvesters along trenches etched into the backside of the wafer. After the backside etch is completed, the wafer is then immersed in acetone to release the carrier wafer. The completed devices can then be separated through cleaving along the etched trenches for packaging and testing.

4.3.8.1   Frontside Etch Photolithography

To define the planar geometry of the harvester, the wafer is etched from the device side using a mask of one layer of AZ 4620 photoresist. The deposition parameters of the photoresist are the same as previously described, however, the photoresist is overexposed and overdeveloped on purpose by 10%. This ensures that the photoresist is completely exposed and developed. A partially masked DRIE can cause a significant problem, as will be explained in the next section. Once the wafer is patterned with AZ 4620, it was hard baked at 115ºC for 15 minutes to strengthen the photoresist. By hard baking, the resilience of the photoresist to DRIE etching is increased, increasing the possible etch depth that can be achieved by upwards of 2:1 before the photoresist is completely removed by the DRIE.

4.3.8.2   DRIE the Wafer to Etch Frontside Features.

After the lithography and hard bake are completed, a 30 second BOE dip is required to remove the native oxide on the wafer. During any deep etch process, any particles, remnant photoresist, or residual native silicon oxide left on the incident surface of the intended etch area will mask the DRIE etch locally, resulting in a pillar-like morphology [41], resembling grass made of silicon, as shown in Figure 4.15.
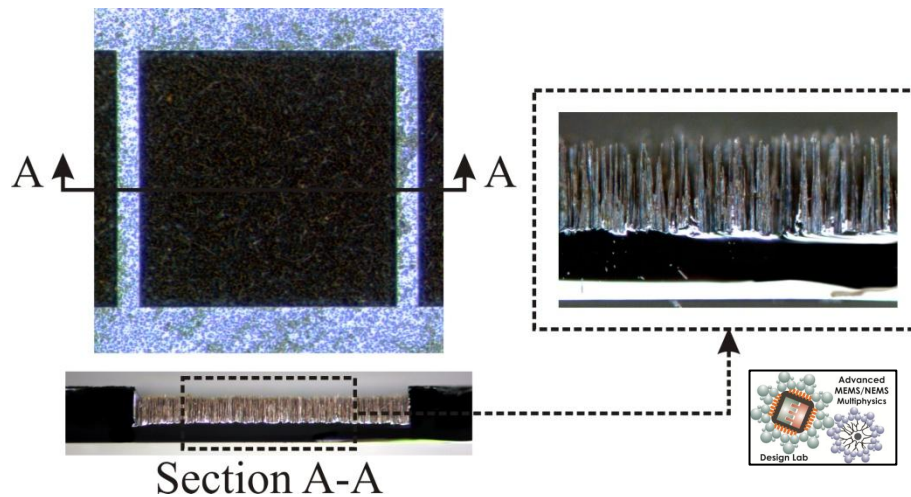
Figure 4.15 – Silicon grass encountered in this fabrication process, preventing the expected etch depth of the DRIE process from being achieved [47].

As the etch process continues post initial grass formation, the "side wall"/passivation area of the DRIE process increases significantly, eventually preventing vertical etching, resulting in shallower than intended etches. This phenomenon can be prevented with good clean room practices, complete removal of photoresist from the intended etch areas and a BOE Dip previous to the DRIE process to remove native oxide.

A STS ICP-DRIE is used to etch the frontside features of the energy harvesters. The ICP-DRIE is a commercially available dry plasma etch system that uses a variety of pre-programmed standard recipes with various mixtures of etchant gas, cycle times, temperatures, reactant gas pressures, and cooling backpressures to achieve specific etch parameters such as depth, uniformity, repeatability, and sidewall profile. The typical DRIE recipe will have a known etch rate per cycle, therefore, the number of cycles defined by the user will determine the etch depth. For both DRIE etch steps required for the release of the harvesters, the DEEP_ETCH recipe from the STS ICP-RIE located at the University of Alberta Nanofab will be used. This program is specifically designed to have a high silicon etch rate and a very low AZ 4620 etch rate. The etch rate for this recipe is reported to be approximately 1.5 µm/cycle for a standard test pattern. Since the etch rate is dependent on the open surface area available to the etch

process, a different etch rate will be experienced for the pattern used in this fabrication process. In this research, the etch rate was measured to be closer to 1.2211 µm/cycle. The target etch depth for this etch step was approximately 100 µm, regardless of target thickness of the spring elements of the harvesters. This is to allow the spring elements to have as rectangular of a cross section as possible, not suffering from the local isotropy of the DRIE process.

4.3.8.3 Pattern Backside DRIE and Application of Carrier Wafer

For the final etch step, two layers of AZ 4620 photoresist are required to mask the deep etch required for release of the harvesters. This etch step occurs from the back side of the wafer. The first layer of AZ 4620 is deposited as previously discussed. After the first 24 hour rehydration, a second layer of AZ 4620 is deposited directly on top of the first, following the same procedure. Again, the photoresist must be rehydrated for 24 hours. The alignment for this photolithography step is more complicated than previous, aligning the desired pattern on the back of the wafer to the existing metal features on the front of the wafer. An infrared thru wafer mask aligner is required is required to align the mask to the pattern. The silicon wafer is transparent to infrared, allowing for the alignment of patterns on opposite sides of the wafer. As with the previous use of AZ 4620, the UV exposure for each layer of resist is approximately 12 seconds, for a total exposure of 24 seconds. Given the features of this pattern are on the order of a few millimeters, alignment errors of 20-25 µm are not significant. Therefore, it is advisable to overexpose the photoresist significantly to ensure that silicon grass does not form. A safety factor of 30% was used to ensure that the photoresist was sufficiently exposed. As with the other photolithography steps involving AZ 4620, the pattern was developed in AZ 400 K developer. The required time of 1 minute, 20 seconds per layer of photoresist was modified with the same 30% safety factor to 3 minutes, 30 seconds to prevent silicon grass.

After the lithography was complete, the carrier wafer was adhered to the device side of the wafer before hard baking the photoresist. Three techniques are

available to affix the carrier wafer to the device wafer, as summarized in Table 4.2.

Table 4.2 – Methods to adhere a carrier wafer to a device wafer [47].

Adhesive Used	Methodology	Separation Method
Photoresist	Spin-coat AZ506, Apply light pressure, bake	Soak in acetone
Crystalbond Adhesive	Apply to wafer at >66°C	Soak in hot water
Double Sided Tape	Apply tape between carrier and device wafer.	Heat on hotplate at 120°C until to release tape

The first method involves using a medium thickness photoresist, such as AZ 506 (~2 μm) as an adhesive. This involves spinning the photoresist with the previous recipe and immediately affixing the carrier wafer to the device wafer, wet photoresist surface of the carrier wafer to the device surface of the device wafer, with light pressure. The wafers are then baked to bond the device and carrier wafer together. Once the required backside etch is complete, wafers can be separated by an acetone soak. The second method to affix a carrier and device wafers involves using Crystalbond adhesive. This semi-permanent adhesive can be applied by hand to a silicon wafer heated above 66^0C. It should be noted that no Crystalbond adhesive should be exposed on the etch surface after adhesion. If the Crystalbond adhesive is exposed to the RIE, it can reflow and redeposit, masking etch areas and causing non-uniformities. Once the etching is complete, the wafers adhered by Crystalbond can be easily separated by soaking both wafers in hot water. Lastly, thermally activated double side tape can be used to affix the device and carrier wafers together. When heat is applied to this tape, the tack on one side of the tape degrades. Therefore, it is important that the "permanent" side of the tape is adhered to the carrier wafer, not the device wafer. Once the etching (or any other) process is finished, the wafers can be separated through heating the wafers at 120^0C for a few minutes. The thermally active side of the tape will separate from the device wafer. Patience is required for this release step, since forcing the wafers apart will damage the released structures

The deciding factor of using a particular method of carrier wafer with the DRIE process used in this research was the heat transfer from the carrier wafer, through the adhesive, to the etched wafer [66]. As the wafer is etched, both the mechanical etching and the plasma heat the top surface of the wafer. Silicon, having a high thermal conductivity, transfers the heat almost instantaneously. In typical situations, the backcooling of the DRIE process is tuned to offset the heating of the etch such that the photoresist mask does not exceed its maximum temperature. If the resist is heated above its maximum temperature, the resist will degrade, either reflowing, losing the pattern of the mask completely, or irreversibly adhering to the surface of the wafer. This typically causes poor quality etching, non-uniformities, etch artifacts, global wafer thinning, and limited etch depth. The adhesive must be able to transfer heat sufficiently to prevent the degradation of the photoresist. The double sided tape performs the worst of all the methods tested in this research. The tape itself is limited in area and did not conduct heat sufficiently, leading to burnt photoresist. The Crystalbond adhesive was suitable for the heat conduction, however, the through-wafer holes produced by this etch process caused the Crystalbond adhesive to reflow and inhibit the etch process. The photoresist-based method performed suitably in both adhesion and heat transfer, therefore, it will be used as the main method of adhering a carrier wafer in this fabrication process.

In this process, the carrier wafer was adhered to the device wafer using a layer of AZ 506 photoresist, using the previously discussed recipe for this resist. While still wet, the carrier wafer was placed wet-side up on a clean room wipe on a flat surface. The device wafer was then adhered, device surface down, onto the carrier wafer with light pressure. The wafer is then hard baked at 100ºC for 15 minutes both to adhere the wafers together and hard bake the AZ 4620. The addition of a carrier wafer allows for the addition of cleaving lines to the pattern of the backside etch. This allows for efficient and safe separation of devices after fabrication is complete.

4.3.8.4   <u>Backside DRIE to Release Devices</u>

This etch process is very similar to the first DRIE etch process undertaken in the release procedure. A BOE dip is required, as previous, to ensure that native oxide is not present in the etch windows. The DRIE etch is completed with the STS ICP-DRIE, using the DEEP_ETCH recipe. In this case, the depth of the etch is directly calculated from the target spring thickness, the thickness of the device wafer used, and the uniformity of thickness of the device wafer. With the desired etch depth, the number of cycles required in the backside etch step could be calculated using the measured the etch rate of 1.2211 μm/cycle. Although the etch rate data was time consuming to collect, it was necessary for accurate definition of the folded spring thickness for expanding the natural frequency range of the harvesters. To limit the heating of the photoresist, it was chosen to limit the maximum amount of DRIE cycles of any one etch step to 160 cycles. If the entire etch procedure required 375 cycles to accomplish the required depth, every 160 cycles, the wafer would be removed from the etch system for inspection and depth measurement. The measurement of the etch depth was non-trivial and non-intuitive. Although there were a variety of tools available to measure the step height created through the DRIE, such as the Alpha Step Profilometer and Anvil Micrometer, interpreting the measurement was non-obvious. Although the starting photoresist thickness was known, the DRIE process progressively etches the photoresist. Therefore, in order to estimate the depth of etch, the etch rate of the photoresist in this etch process must be known. Although it was not always possible to determine an accurate etch depth with the presence of the photoresist, it was necessary to take a variety of measurements across the wafer during the intermediate steps to ensure that the DRIE process was etching uniformly. The etch rate data was checked with SEM measurements after the devices were separated and tested. Once the etch was completed through multiple etch steps of 160 DRIE cycles, the carrier wafer could be removed and devices separated.

4.3.9   Cleaving

The last step in the microfabrication process involves the removal of the carrier wafer and the cleaving of the device wafer into individual harvesters. To

remove the carrier wafer, both wafers are immersed in acetone and soaked for at least 24 hours. The immersion in acetone completely dissolves all photoresist present. Additionally, the low surface tension of the acetone prevents any mechanical damage during the separation of the wafers. Active MEMS devices can be severely damaged through stiction [41]. As water evaporates from the MEMS device, the surface tension of the droplet may be the largest force applied to the device due to scaling. If two surfaces are brought close enough together through the evaporation, they will bond to one another due to van der Waals forces [41]. Separating the wafers in a low surface tension liquid, such as acetone, prevents stiction from occurring. Once the wafers are separated, the device wafer must be removed from the acetone bath and placed in a deionized water bath. The bottom of the bath should be lined with cleanroom wipes in order to provide a semi-flexible surface for cleaving. The cleaving must take place under water so that the energy released by the cleaving is damped sufficiently to prevent device damage. Once the wafer is submerged, the wafer is cleaved into sequentially smaller pieces until each harvester is separated. Light pressure applied by a sharp object will provide sufficient force to cleave the wafer along the etched cleaving trenches. This cleaving procedure was the precursor to the work undertaken in [67].

4.4 Summary

The microfabrication process flow discussed in this chapter is capable of producing any design of piezoelectric harvester using a typical cross sectional arrangement required by PZT. In order to facilitate the microfabrication of the harvesters, multiple microfabrication processes were developed. An Aqua Regia Etch System was developed in order to pattern the required lower platinum and titanium electrodes in a controlled manner. Additionally, multiple methods of deposition and patterning of the PZT film were developed. Two different PZT materials were deposited by the sol-gel process. The first material required a simultaneous deposition and lift-off to pattern the PZT film. The second material was not suitable for lift-off, therefore, a wet etch was adapted to allow for

accurate patterning of the PZT. Due to the two-step DRIE release procedure, a carrier wafer was required in order to stabilize the wafer. The addition of the carrier wafer was used to allow for the devices to be separated by cleaving, reducing the possibility of damage from vibrations induced through dicing. The most successful arrangement of microfabrication processes, shown as in Figure 4.3 with dashed red lines, was capable of producing PZT-based harvesters with PZT thickness of up to 0.96 μm. A Report of Invention was filed based upon this microfabrication flow. This process flow, combined with the methodology outlined in Chapter 3, resulted in a US Patent Application (Serial No. 14/032,018). To package and test the harvesters produced by this microfabrication flow, the packaging and testing methodologies discussed in Chapter 5 are required.

4.5   References:

[1]   J. Lueke and W. A. Moussa, "MEMS-Based Power Generation Techniques for Implantable Biosensing Applications," *Sensors,* vol. 11, pp. 1433-1460, 2011.

[2]   R. Elfrink, T. M. Kamel, M. Goedbloed, S. Matova, D. Hohlfeld, Y. Van Andel, and R. Van Schaijk, "Vibration energy harvesting with aluminum nitride-based piezoelectric devices," *Journal of Micromechanics and Microengineering,* vol. 19, 2009.

[3]   T. Pedersen, C. C. Hindrichsen, E. V. Thomsen, K. Hansen, and R. Lou-Moller, "Investigation of top/bottom electrode and diffusion barrier layer for PZT thick film MEMS sensors," in *Proceedings of IEEE Sensors*, Atlanta, GA, 2007, pp. 756-759.

[4]   P. Wang, K. Tanaka, S. Sugiyama, X. Dai, X. Zhao, and J. Liu, "A micro electromagnetic low level vibration energy harvester based on MEMS technology," *Microsystem Technologies,* vol. 15, pp. 941-951, 2009.

[5]   Y. Yee, H. J. Nam, S. H. Lee, J. U. Bu, and J. W. Lee, "PZT actuated micromirror for fine-tracking mechanism of high-density optical data storage," *Sensors and Actuators, A: Physical,* vol. 89, pp. 166-173, 2001.

[6]   J. Laconte, D. Flandre, and J. P. Raskin, "Micromachined thin-film sensors for SOI-CMOS co-integration," *2006 XIII,* p. 292, 2006.

[7]   J. Baborowski, "Microfabrication of piezoelectric MEMS," *Journal of Electroceramics,* vol. 12, pp. 33-51, 2004.

[8]   S. P. Beeby, N. J. Grabham, and N. M. White, "Microprocessor implemented self-validation of thick-film PZT/silicon accelerometer," *Sensors and Actuators, A: Physical,* vol. 92, pp. 168-174, 2001.

[9]   S. Ezhilvalavan, Z. Zhang, J. Loh, and J. Y. Ying, "Microfabrication of PZT force sensors for minimally invasive surgical tools," *Journal of Physics: Conference Series,* vol. 34, pp. 979-984, 2006.

[10]   J. H. Lee, K. S. Hwang, and T. S. Kim, "The Microscopic Origin of Residual Stress for Flat Self-Actuating Piezoelectric Cantilevers," *Nanoscale Research Letters,* vol. 6, pp. 1-6.

[11]   W. Liu, J. Ko, and W. Zhu, "Device patterning of PZT/Pt/Ti/thin films on SiO2/Si3N4 membrane by a chemical wet etching approach," *Journal of Materials Science Letters,* vol. 19, pp. 2263-2265, 2000.

[12]   K. Aoki, Y. Fukuda, K. Numata, and A. Nishimura, "Electrical comparison of sol-gel derived lead-zirconate-titanate capacitors with Ir and Pt electrodes," *Proceedings of the 12th Meeting on Ferroelectric Materials and Their Applications (FMA-12), May 24-27 1995 Japanese Journal of Applied Physics, Part 1: Regular Papers & Short Notes & Review Papers,* vol. 34, pp. 5250-5253, 1995.

[13]   K. Yamakawa, O. Arisumi, K. Okuwada, K. Tsutsumi, and T. Katata, "Development of stable PZT sputtering process using ex-situ crystallization and PZT/Pt interface control technique," *IEEE International Symposium on Applications of Ferroelectrics,* pp. 159-162, 24 August 1998 through 27 August 1998 1998.

[14]   R. Tian-Ling, Z. Lin-Tao, L. Li-Tian, and L. Zhi-Jian, "Electrical properties of a silicon-based PT/PZT/PT sandwich structure," *Ferroelectrics,* vol. 259, pp. 311-316, 12 December 2002 through 15 December 2002 2001.

[15]   J. Wang, L. Zhang, X. Yao, and J. Li, "Characterization of PZT/PT multilayer thin film by sol-gel," *Ceramics International,* vol. 30, pp. 1517-1520, 7 December 2003 through 11 December 2003 2004.

[16]   D. A. Barrow, T. E. Petroff, R. P. Tandon, and M. Sayer, "Characterization of thick lead zirconate titanate films fabricated using a new sol gel based process," *Journal of Applied Physics,* vol. 81, pp. 876-881, 1997.

[17]   S. P. Beeby, A. Blackburn, and N. M. White, "Silicon micromachining processes combined with thick-film printed lead zirconate titanate actuators for microelectromechanical systems," *Materials Letters,* vol. 40, pp. 187-191, 1999.

[18]   A. Kumar, M. R. Alam, A. Mangiaracina, and M. Shamsuzzoha, "Synthesis of the PZT films deposited on Pt-coated (100) Si substrates for nonvolatile memory applications," *Journal of Electronic Materials,* vol. 26, pp. 1331-1334, 1997.

[19]   G. Piazza, P. J. Stephanou, and A. P. Pisano, "Piezoelectric aluminum nitride vibrating contour-mode MEMS resonators," *Journal of Microelectromechanical Systems,* vol. 15, pp. 1406-1418, 2006.

[20]   S. Kimura, S. Tomioka, S. Iizumi, K. Tsujimoto, T. Sugou, and Y. Nishioka, "Improved performances of acoustic energy harvester fabricated using sol/gel lead zirconate titanate thin film," *Japanese Journal of Applied Physics,* vol. 50.

[21]   K. Suu, A. Osawa, N. Tani, M. Ishikawa, K. Nakamura, T. Ozawa, K. Sameshima, A. Kamisawa, and H. Takasu, "Lead content control of PLZT thin films prepared by RF magnetron sputtering," *Proceedings of the 1996 8th International Symposium on Integrated Ferroelectrics. Part 1 (of 3), Mar 18-20 1996 Integrated Ferroelectrics,* vol. 14, pp. 59-68, 1997.

[22]   K. Suu, A. Osawa, Y. Nishioka, and N. Tani, "Stability control of composition of RF-sputtered Pb(Zr, Ti)O3 ferroelectric thin film," *Japanese Journal of Applied Physics, Part 1: Regular Papers & Short Notes & Review Papers,* vol. 36, pp. 5789-5792, 1997.

[23]   K. Suu, T. Masuda, Y. Nishioka, and N. Tani, "Process stability control of Pb(Zr,Ti)O3 ferroelectric thin film sputtering for FRAM application," *Proceedings of the 1998 11th IEEE International Symposium on Applications of Ferroelectrics (ISAF-XI), Aug 24-Aug 27 1998 IEEE International Symposium on Applications of Ferroelectrics,* pp. 19-22 BN - 0-7803-4959-8, 1998.

[24]   G. Suchaneck, V. S. Vidyarthi, M. Reibold, A. Deyneka, L. Jastrabik, G. Gerlach, and J. Hartung, "Large area deposition of Pb(Zr,Ti)O-3 thin films for piezoelectric MEMS devices," *Journal of Electroceramics,* vol. 20, pp. 17-20, FEB 2008.

[25]   Z. Y. Yang, Y. C. Zhou, X. J. Zheng, Z. Yan, and G. Bignall, "Determination of residual stress in PZT thin film prepared by pulsed laser deposition," *Journal of Materials Science Letters,* vol. 21, pp. 1541-1544, OCT 1 2002.

[26]   K. Suu, A. Osawa, N. Tani, M. Ishikawa, K. Nakamura, T. Ozawa, K. Sameshima, A. Kamisawa, and H. Takasu, "Preparation of (Pb, La)(Zr, Ti)O3 ferroelectric films by RF sputtering on large substrate," *Japanese Journal of Applied Physics, Part 1: Regular Papers and Short Notes and Review Papers,* vol. 35, pp. 4967-4971, 1996.

[27]   T. Masuda, Y. Miyaguchi, M. Tanimura, Y. Nishioka, K. Suu, and N. Tani, "Development of PZT sputtering method for mass-production," *Applied Surface Science,* vol. 169-170, pp. 539-543, 2001.

[28]   T. K. Li, P. Zawadzki, and R. A. Stall, "Microstructure and properties of PbZr1-xTixO3 thin films made by one and two step metalorganic chemical vapor deposition," *Integrated Ferroelectrics,* vol. 18, pp. 155-169, 1997.

[29]   H. Funakubo, A. Nagai, J. Minamidate, J. M. Koo, S. P. Kim, and Y. Park, "Trial for making three dimensional PZT capacitor for high density ferroelectric random access memory," *Integrated Ferroelectrics,* vol. 81, pp. 219-226, 2006.

[30]   K. S. Jacob, N. R. Panicker, I. P. Selvam, and V. Kumar, "Sol-Gel Synthesis of Nanocrystalline PZT Using a Novel System," *Journal of Sol-Gel Science and Technology,* vol. 28, pp. 289-295, 2003/11// 2003.

[31]   K. Lashgari and G. Westin, "Preparation of PZT Film and Powder by Sol-Gel Technique Using Ti- and Zr-Alkoxides and a Novel Pb-Precursor; Pb(NO3)2 1.5EO3," *Journal of Sol-Gel Science and Technology,* vol. 13, pp. 865-868, 1998/01// 1998.

[32]   R. Caruso, O. de Sanctis, A. Frattini, C. Steren, and R. Gil, "Synthesis of precursors for chemical solution deposition of PZT thin films," *Surface and Coatings Technology,* vol. 122, pp. 44-50, 1999/12/1 1999.

[33]   N. Ozer and T. Sands, "Preparation and Optical Characterization of Sol-Gel Deposited Pb(Zr0.45Ti0.55)O3 Films," *Journal of Sol-Gel Science and Technology,* vol. 19, pp. 157-162, 2000/12// 2000.

[34]   P. Lobmann, S. Seifert, S. Merklein, and D. Sporn, "Lead Zirconate-Titanate Films Prepared from Soluble Powders," *Journal of Sol-Gel Science and Technology,* vol. 13, pp. 827-831, 1998/01// 1998.

[35]   A. Wu, I. M. M. Salvado, P. M. Vilarinho, J. o. L. Baptista, and A. J. D. Silvestre, "Lead Zirconate Titanate Stable Stock Solution: Characterization and Applications," *Journal of Sol-Gel Science and Technology,* vol. 19, pp. 671-676, 2000/12// 2000.

[36]   K. Maki, N. Soyama, K. Nagamine, S. Mori, and K. Ogi, "Low-temperature crystallization of sol-gel derived Pb(Zr-0.4,Ti-0.6)O-3 thin films," *Japanese Journal of Applied Physics Part 1-Regular Papers Short Notes & Review Papers,* vol. 40, pp. 5533-5538, SEP 2001.

[37]   Z. J. Wang, H. Kokawa, H. Takizawa, M. Ichiki, and R. Maeda, "Low-temperature growth of high-quality lead zirconate titanate thin films by 28 GHz microwave irradiation," *Applied Physics Letters,* vol. 86, pp. -, MAY 23 2005.

[38]   H. C. Pan, C. C. Chou, and H. L. Tsai, "Low-temperature processing of sol-gel derived La0.5Sr0.5MnO3 buffer electrode and PbZr0.52Ti0.48O3 films using CO2 laser annealing," *Applied Physics Letters,* vol. 83, pp. 3156-3158, OCT 13 2003.

[39]   K. Suu, A. Osawa, N. Tani, M. Ishikawa, K. Nakamura, T. Ozawa, K. Sameshima, A. Kamisawa, and H. Takasu, "Lead content control of PLZT thin films prepared by RF magnetron sputtering," *Integrated Ferroelectrics,* vol. 14, pp. 59-68, 1997.

[40]   J. W. Gardner, V. K. Varadan, and O. O. Awadelkarim, *Microsensors MEMS and Smart Devices*. Chichester, West Sussex, England: John Wiley & Sons, 2001.

[41]   M. J. Madou, *Fundamentals of Microfabrication: The Science of Miniaturization*, Second ed.: CRC Press, 2002.

[42]   S. P. Bathurst and S. G. Kim, "Designing direct printing process for improved piezoelectric micro-devices," *CIRP Annals - Manufacturing Technology,* vol. 58, pp. 193-196, 2009.

[43]   F. Dauchy and R. A. Dorey, "Patterned crack-free PZT thick films for micro-electromechanical system applications," *International Journal of Advanced Manufacturing Technology,* vol. 33, pp. 86-94, 2007.

[44]   S. Okamura and T. Shiosaki, "Properties of micropatterned ferroelectric thin films fabricated by electron beam exposed chemical solution deposition process," *Ferroelectrics,* vol. 232, pp. 15-24, 1999.

[45]   T. Uchida and T. Kikuchi, "Effect of surface modification of titanium substrate by anodic oxidation on hydrothermally synthesized PZT poly-crystalline film," in *Proceedings - IEEE Ultrasonics Symposium*, Beijing, 2008, pp. 2122-2125.

[46] D. Wang, M. J. Edirisinghe, and R. A. Dorey, "Formation of PZT crack-free thick films by electrohydrodynamic atomization deposition," *Journal of the European Ceramic Society,* vol. 28, pp. 2739-2745, 2008.

[47] M. Rezaei, J. Lueke, D. Raboud, and W. Moussa, "Challenges in fabrication and testing of piezoelectric MEMS with a particular focus on energy harvesters," *Microsystem Technologies,* pp. 1-25, 2013.

[48] G. Suchaneck, R. Tews, and G. Gerlach, "A model for reactive ion etching of PZT thin films," *Surface and Coatings Technology,* vol. 116-119, pp. 456-460, 1999.

[49] T. A. Tang, Z. Chen, N. Li, and S. X. Zou, "Reactive ion etching of sol-gel derived PZT thin film and Pt/Ti bottom electrode for FRAM," *Ferroelectrics,* vol. 232, pp. 47-52, 1999.

[50] S. Wang, X. Li, K. Wakabayashi, and M. Esashi, "Deep reactive ion etching of lead zirconate titanate using sulfur hexafluoride gas," *Journal of the American Ceramic Society,* vol. 82, pp. 1339-1341, 1999.

[51] R. J. Zeto, B. J. Rod, M. Dubey, M. H. Ervin, R. C. Piekarz, S. Trolier-McKinstry, T. Su, and J. F. Shepard, "High-resolution dry etch patterning of PZT for piezoelectric MEMS devices," *IEEE International Symposium on Applications of Ferroelectrics,* pp. 89-92, 24 August 1998 through 27 August 1998.

[52] F. Chen, R. Schafranek, W. Wu, and A. Klein, "Formation and modification of Schottky barriers at the PZT/Pt interface," *Journal of Physics D: Applied Physics,* vol. 42, 2009.

[53] H. W. Jiang, P. Kirby, and Q. Zhang, "Fabrication of PZT actuated cantilevers on silicon-on-insulator wafers for a RF microswitch," *Micromach Microfabr Process Technol, VIII, San Jose California, USA,* vol. 2003, pp. 165-173, 2003.

[54] X. Y. Wang, C. Y. Lee, C. J. Peng, P. Y. Chen, and P. Z. Chang, "A micrometer scale and low temperature PZT thick film MEMS process utilizing an aerosol deposition method," *Sensors and Actuators, A: Physical,* vol. 143, pp. 469-474, 2008.

[55] T. H. Yeh, M. B. Suresh, J. N. Shen, J. C. Yu, and C. C. Chou, "Chemical reactions during wet-etching process of LSMO/PZT/LSMO-structured device fabrication," *Ferroelectrics,* vol. 380, pp. 97-101, 2 August 2008 through 6 August 2008 2009.

[56] S. Ezhilvalavan and V. D. Samper, "Ferroelectric properties of wet-chemical patterned Pb Zr0.52 Ti0.48 O3 films," *Applied Physics Letters,* vol. 86, pp. 1-3, 2005.

[57] R. A. Miller and J. J. Bernstein, "A novel wet etch for patterning lead zirconate-titanate (PZT) thin-films," *Integrated Ferroelectrics,* vol. 29, pp. 225-231, 2000.

[58] K. Zheng, J. Lu, and J. Chu, "A novel wet etching process of Pb(Zr,Ti)O3 thin films for applications in microelectromechanical system," *Japanese Journal of Applied Physics, Part 1: Regular Papers and Short Notes and Review Papers,* vol. 43, pp. 3934-3937, 2004.

[59] K. R. Williams, K. Gupta, and M. Wasilik, "Etch rates for micromachining processing - Part II," *Journal of Microelectromechanical Systems,* vol. 12, pp. 761-778, 2003.

[60] M. Ohring, "Chapter 11 - Interdiffusion, reactions, and transformations in thin films," in *Materials Science of Thin Films (Second Edition)* San Diego: Academic Press, 2002, pp. 641-710.

[61] F. Laermer and A. Schilp, "Method of anisotropically etching silicon," *Method of Anisotropically Etching Silicon,* 1996.

[62] S. Jensen, J. M. Jensen, U. J. Quaade, and O. Hansen, "Uniformity-improving dummy structures for Deep Reactive Ion Etching (DRIE) processes," in *Progress in Biomedical Optics and Imaging - Proceedings of SPIE*, San Jose, CA, 2005, pp. 39-46.

[63] H. Sun, T. Hill, M. Schmidt, and D. Boning, "Characterization and modeling of wafer and die level uniformity in deep reactive ion etching (DRIE)," *Mat Res Soc Symp Proc,* vol. 782, pp. A1021-A1026, 2004.

[64] S. Senturia, *Microsystem Design*, First ed. Boston: Kluwer Academic Publishers, 2001.

[65] H. Zhu, J. Miao, B. Chen, Z. Wang, and W. Zhu, "Membrane microcantilever arrays fabrication with PZT thin films for nanorange movement," *Microsystem Technologies,* vol. 11, pp. 1121-1126, 2005.

[66] U. Sokmen, A. Stranz, S. Fandling, H. H. Wehmann, V. Bandalo, A. Bora, M. Tornow, A. Waag, and E. Peiner, "Capabilities of ICP-RIE cryogenic dry etching of silicon: Review of exemplary microstructures," *Journal of Micromechanics and Microengineering,* vol. 19, 2009.

[67]   M. Rezaei, Lueke, J., Sameoto, D., Raboud, D., Moussa, A., "A New Approach to Cleave MEMS Devices from Silicon Substrates," *Journal of Mechanics Engineering and Automation,* vol. 3, pp. 731-738, 2013.

5.1   Introduction

There are many packaging schemes reported in literature for MEMS-based devices. Unfortunately, there are limited complete packaging solutions for vibration-based energy harvesting. The energy harvesters were characterized under a base excitation; therefore, it was not possible to directly probe the energy harvesters in a typical probing station. The entire harvester would move in and out of the contact with the electrical probes, thereby preventing the continual capture of the output electrical signal. Typical packaging schemes for MEMS-based devices need to be adapted to suit the specific needs of piezoelectric energy harvesters. This inherently causes a variety of challenges for the development of a suitable packaging scheme. The packaging scheme must allow for unhindered movement of the harvester to prevent damage and electrical losses. Additionally, suitable electrical connections must be made to the harvester to capture the voltage created through the vibration of the structure. Finally, the package must allow for protection from the external environment and integration into larger electronic systems. The following sections will discuss these challenges and the packaging methodologies that were developed to package the harvesters produced in this research. In addition, the testing and characterization methodologies that were developed to evaluate the microfabrication, frequency response, and electrical response of the harvesters will be discussed as well.

5.2   Dicing/Cleaving

Energy harvesters typically operate under a base vibration; therefore, complete packaging is required for testing and integration. To be packaged effectively, individual harvesters must be separated from the device wafer. The

most common method of separating MEMS devices, dicing, is not well suited for this application. Dicing the wafer could adversely affect the overall yield of the harvesters by damaging the flexible released structures. In the dicing process, a high speed rotary diamond blade, lubricated by a water jet, is used to cut the wafer into smaller sections. Both the vibration caused by the cut and the force of the water jet can cause serious damage to the individual energy harvesters during dicing.

Cleaving, as discussed in Chapter 4, can be used as an alternative for dicing to separate individual energy harvesters [1-5]. For this specific application, the use of a carrier wafer in the final DRIE etch step in the microfabrication process shown in Figure 4.3, allowed for the addition of deep cleaving trenches to the final backside etch pattern. These trenches, as shown in Figure 5.1, followed major crystallographic planes of the silicon and were etched to the same thickness as the folded springs.

Figure 5.1 – Cleaving trenches and backside wells etched on the backside of a testing wafer.

Once the device wafer is removed from the carrier wafer, only gentle pressure is required to separate individual devices. Using the methodology discussed in section 4.3.9 of Chapter 4, it was possible to separate the devices easily without damaging the released energy harvesters.

5.3 Packaging Materials and Mechanical Packaging

A variety of packaging options are available to both protect the energy harvesters and provide suitable mechanical and electrical connections. These include printed circuit boards (PCB), flexible printed circuit boards (FPCB) and typical electronic packages such as Dual In-line Packages (DIP) or Ceramic Pin Grid Array (CPGA). PCB and FPCB based packaging schemes can be custom designed for specific applications to allow direct integration of the energy harvesters into larger electronics systems. Flexible PCB's are particularly useful for "size critical" applications, where the flexibility of the circuit board can be used to provide electrical connections while minimizing space. Typically, FPCB are fabricated from layers of Kapton film and gold or aluminum traces. The FPCB tend to be highly biocompatible. Printed circuit boards are composed of multiple layers of rigid fiberglass and copper or gold traces. PCB is a well known and mature method of integrating electronic circuits. The customizability and availability of PCB makes it attractive for research-based applications. Electronic packages are also applicable for packaging for energy harvesters. The DIP/CPGA has a standard electronic footprint; therefore, integration into existing electronic systems is expedited. Additionally, with a suitable cover plate or cap, these packages help to protect the energy harvester from the external environment. Hermetic/vacuum packaging can also be introduced to eliminate damping from the system, increasing the overall energy production of the harvester. For the initial stages of testing and characterization, F/PCB will be used due to the flexibility in application, size, and cost. Later in the development and testing, DIP/CPGA-type packages may be used to provide a more refined packaging method.

To bond the energy harvester to the circuit board, a variety of adhesives are available, such as non-conductive epoxy, conductive epoxy, and cyanoacrylate glue [5,6]. Specifically for energy harvesters, care must be taken in the mechanical packaging to ensure that the motion of the energy harvester is unhindered. This ensures that the energy harvester will not crash against the

circuit board during operation, preventing harvesting losses and potential damage. In the developed packaging methodology, two methods were developed to provide sufficient travel to the proof mass, depending upon the type of PCB available, as shown in Figure 5.2.
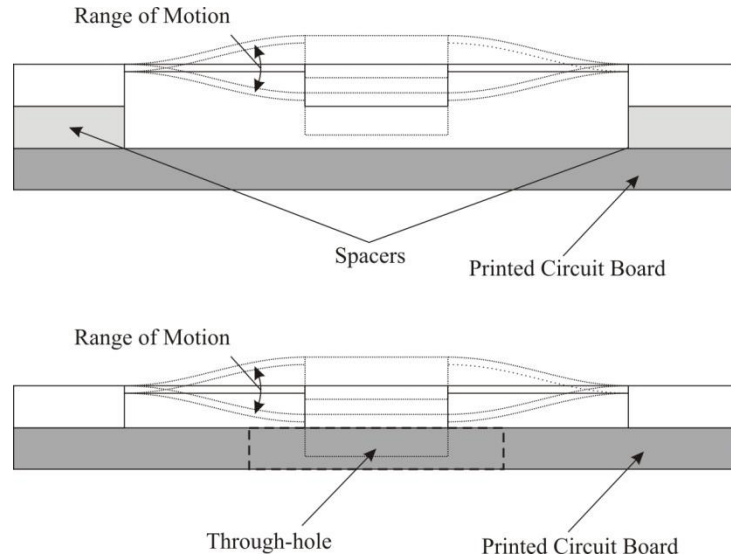
Figure 5.2 – Bonding schematic of an energy harvester using spacers (top) and a through-hole (bottom) to allow for sufficient vibration space [5].

The first method, as shown in Figure 5.2, involves using mechanical spacers to provide the necessary travel for the proof mass. This is accomplished by gluing the spacers to the harvester by hand, then gluing the harvester to the circuit board. This approach was preferred for the harvesters packaged onto FPCB. The second method, as shown in Figure 5.2, involved designing the PCB with a through-hole specifically placed to allow the mass to freely travel. This allowed the energy harvester to be directly glued to the PCB without the use of spacers.

5.4 Wire Bonding

The electrical connections for piezoelectric energy harvesters are typically made through wire bonding [7]. Wire bonding uses a very fine wire (on the order of 25 µm) and specialized bonding tool to make very small electrical connections.

The wire is ultrasonically welded to the target pads with very high accuracy. There are two types of wire bonds that can be used to make electrical connections: wedge-wedge and ball-wedge bonds as shown in Figure 5.3.

(a)   (b)
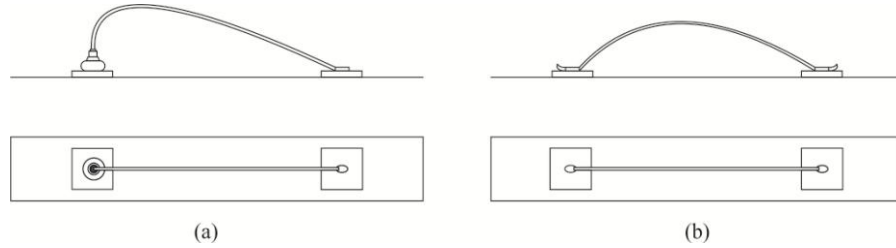
Figure 5.3 – Examples of wire bonds that can be used to provide electrical connections to the energy harvester. (a) shows a ball-wedge bond, (b) shows a wedge-wedge bond [5].

Wedge-wedge wire bonds, as shown in the right of Figure 5.3, ultrasonically bond the wire to the pads on the start and the end of the bond. When material compatibility between the PCB pad and wire is high, the wedge-wedge bond is suitable [6]. Ball-wedge wire bonds, as shown in the left of Figure 5.3, start with a ball bond and end with a wedge bond. The ball bond uses a semi-molten ball of the wire material to improve adhesion. This ball is ultrasonically welded to the contact pad instead of a wedge. The adhesion of this first bond is improved due to the additional surface area and solidification of the semi-molten ball on the target pad. The second bond in the ball-wedge wire bond is wedge bond, the same bond used in a wedge-wedge wire bond.

When material compatibility, bond adhesion and bond direction are a challenge, ball-wedge bonding is a more suitable choice. For example, for energy harvesters using platinum for electrode layers, the ball-wedge bond is more suitable to overcome the difficult adhesion to platinum. Additionally, the pad conditions of the package must be taken into account. If FPCB is used, it must be immobilized to prevent internal damping of the flexible polymer from decreasing the effectiveness of the ultrasonic bonding [6]. Ball-wedge bonding can provide more flexibility in overcoming this challenge. Less mechanically flexible

packaging options, such as PCB or typical electronics packages, do not suffer from the material damping issues. Also, ball-wedge bonding provides additional flexibility by allowing bonding at low ultrasonic bonding power, overcoming material compatibility issues such as fragile/rough structures, including the Pt/PZT/Pt layers produced in the research. The use of a ball bond allows for the decrease of applied ultrasonic energy to the Pt/PZT/Pt stack, decreasing the potential delamination of electrodes.

Generally, achieving good bond quality and adhesion is the major challenge in wire bonding of energy harvesters. This can be significantly improved by tuning the bonding parameters to suit the electrode materials. These parameters include the bonding ultrasonic power, ultrasonic time, diameter of ball bond, and applied force [6]. Tuning these parameters for specific pad materials and conditions allows for the reliable and consistent bonding.

5.5   Flip-chip Bonding

Flip-chip bonding is a low volume, 3D vertical integration scheme that allows for direct connection between PCB and device pads. This packaging scheme can be used to create a small footprint packaged devices with high precision, allowing for flexibility in design. In this case, the energy harvester is inverted and picked up by a vacuum tip on a pivoting arm as shown schematically in Figure 5.4.
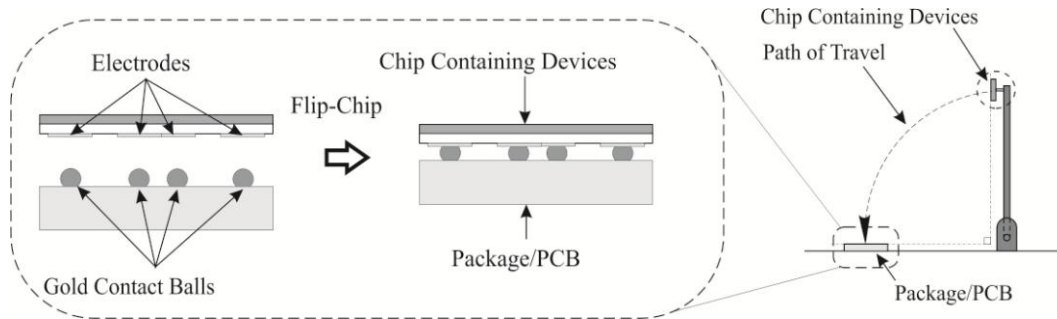
Figure 5.4 – Schematic of flip-chip bonding process [5].

The arm of the flip-chip bonder is designed such that the surfaces to be bonded, from both package and device, will maintain planarity with each other throughout the bonding process. The package is then placed in the apparatus, and a camera/prism system is used to align the pads of both the chip and the package. There are a variety of methods available to create the electrical and mechanical bonds required. Compression-based, thermal-based, ultrasonic-based, or any combination of these methods can be used to achieve a bond with conductive epoxy, non-conductive epoxy, conductive films (anisotropic and isotropic) and stud/solder bumps [6]. Typically, conductive epoxy/film is used for compression and thermal based schemes. In the case of anisotropic conductive film, the compression will create the conductive path necessary to complete the electrical circuit. Solder based reflow techniques using solder bumps can also be used for thermal or compression based bonding. Ultrasonic-based flip-chip bonding is typically accomplished using either gold or solder stud bumps. An example of this bond is shown in Figure 5.5.

173
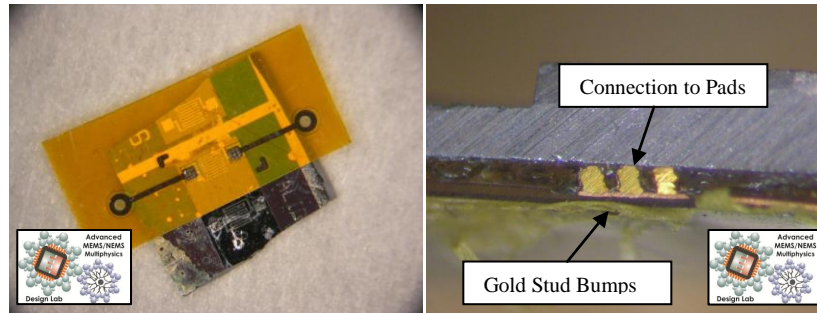
Figure 5.5 – Test energy harvester flip-chipped onto a FPCB using ultrasonic compressive bond with gold stud bumps [5].

A non-conductive epoxy is used to backfill the bond to ensure mechanical adhesion. As with wire bonding, the majority of challenges involved with flip-chip bonding involve determining the proper bonding parameters for each required bond. A thermocompressive bond, using an anisotropic conductive film will have completely different parameters than an ultrasonic bond using gold stud bumps. Tuning of these bonding procedures will ultimately increase yield and bond strength. In regards to energy harvesting, flip-chip packaging can be used to overcome a variety of packaging challenges, such as adapting the energy harvester into a specific space-critical application with high precision. Flip-chip packaging equipment has the ability to place delicate components with 5 μm accuracy on any flat surface. This additional handling ability, coupled with the variety of bonding schemes discussed above can be used to pick, place, and package the energy harvester onto/into a variety of different situations. However, when flip-chip bonding released structures, great care must be taken to both immobilize the device and prevent direct loads from being applied to the released structure. If the vacuum required to keep the chip on the pivot arm is directly applied to the harvester, it may damage the device. It is possible to overcome this challenge with a custom designed vacuum head to allow for the mounting of the energy harvester while avoiding applying vacuum at critical areas.

Furthermore, flip-chip bonding can allow advanced packaging schemes, such as Through Silicon Vias (TSV), to be adapted to allow for quick, consistent,

and space efficient packaging [8]. TSV are vias etched through the wafer that are consequently filled with a conductive material to provide a vertical electrical contact to the opposite side of the chip. This may allow for the placement of the harvester directly upon a specific package using a flip-chip technique without needing to invert the device. The flip chipping method of integration can provide very reliable bonds, however, for large scale testing/integration applications, it is more suitable to use wire bonding.

5.6   Packaging Methodology for the Energy Harvesters:

Taking the above methods into account, a packaging methodology was devised in order to allow for the full characterization of the harvesters. It was chosen to package the harvester onto flexible and regular printed circuit boards (FPCB/PCB) to enable *in-situ* characterization. To mechanically integrate the piezoelectric energy harvester into the F/PCB, the energy harvester is adhered to the F/PCB using cyanoacrylate glue. The cyanoacrylate glue is biocompatible, and strongly adheres the silicon base of the energy harvester to the F/PCB. Spacers were used in order to allow for free movement of the proof masses of the harvesters, as shown in Figure 5.2. In the case of FPCB, additional steps to stabilize the FPCB for testing to prevent delamination of the energy harvester or any wire bonds. As seen in Figure 5.6, solid PCB's were also designed and fabricated to package individual harvesters.
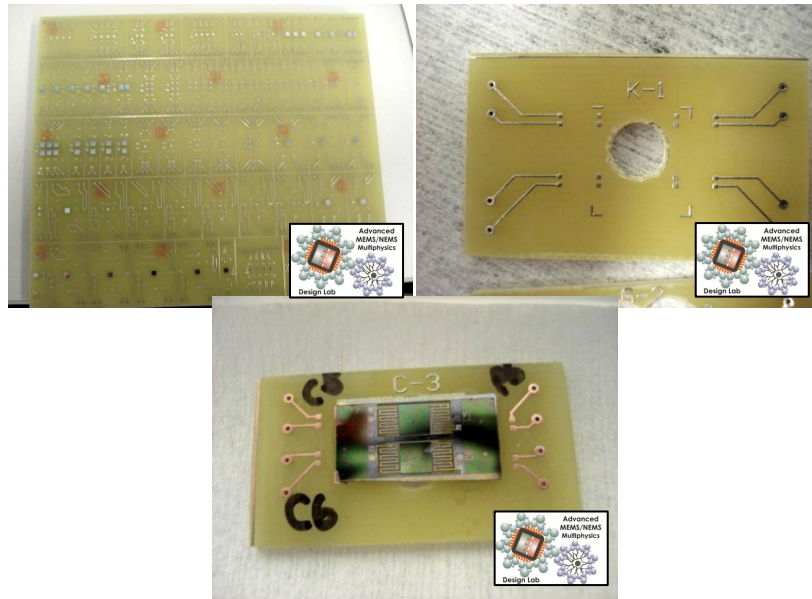
Figure 5.6 - Solid PCBs developed for harvester packaging. (Top Left) full sheet of Solid PCB. (Top Right) separated and prepared individual PCBs. (Bottom) a mechanically packaged harvester on an individual PCB.

The prepared PCB allowed for the direct mounting of a harvester chip with cyanoacrylate glue, without spacers, reducing the required handling and potential for damage. The majority of harvesters in this study were packaged using solid PCB. The designed PCBs are single layer fibreglass, with a single top layer of copper/solder paste traces. As shown in Figure 5.6, the PCBs are ordered in a large sheet, and then are broken down into individual PCBs designed for each individual cleaved harvester chip. To allow for free vibration and to increase yield of the mechanical packaging, a hole is punched in the PCB where the proof mass of the harvester is expected to be located. The solder paste layer is removed from the PCB in order to wire bond directly onto the copper trace. This is a well-known and reliable bond used by multiple users in our laboratory. Wire bonding onto the solder paste is unreliable and could permanently plug the capillary used in the ball-wedge wire bonding. This method of packaging has been proven in this study not to add a parasitic capacitance that would restrict energy harvesting.

After the harvester was adhered to the PCB, the electrical connections from the harvester to the PCB were provided by ball-wedge gold wire bonds. The connections to the outside world were provided by wires soldered to the PCB. The wire bonding was accomplished by using a West Bond 747677E wire bonder, using 25 μm gold wires. This scheme proved to be more consistent and less time consuming than the flip chip bonding.

Two separate wire bonds were developed in this research in order to successfully bond to the two pad types that are present in the energy harvesters. The first pad, comprised of just the lower platinum electrode, was the simpler of the two required wire bonds. Platinum is a much more difficult material to wire bond to than aluminum or gold. Typically, one would match the bonding wire to the pad material; however, this was not practical with platinum. The solution involved increasing the ultrasonic energy applied to the bond to adhere the gold wire. The wire bonder was set to an ultrasonic power of 1.5 W and an ultrasonic time of 250 ns. In comparison, the manufacturer standard gold pad bonding procedure applies an ultrasonic power of 0.6 W for 30 ns. This additional bond energy, when coupled with the "ball-end" of the ball-wedge bond, allowed for the successful bonding to this harvester pad type. The second type of electrode pad present in the harvester presented a unique challenge in the wire bonding process. From the initial development of this bond, it was clear that the PZT was strongly adhered to the lower platinum electrode. However, the adhesion of the upper platinum electrode to the PZT was not as strong. The increased power required to bond the wire to the pad would routinely delaminate the top electrode from the PZT, causing the platinum film to peel off the harvester as the wire was spooled to make the subsequent bond. In order to complete this bond, it was necessary to reverse the bond order. With ball-wedge wire bonding, typically, the ball, or start of the bond is reserved for the pad that is more difficult to bond to. In this case, it was advantageous to use the wedge-end of the bond on the platinum/PZT/platinum stack. The heating applied to the bonding capillary was increased, in order to make the gold wire more malleable during bonding.

177

Typically, the heat applied to the capillary would be minimized, since the increased malleability of the wire would lead to a greater chance of plugging the bonding capillary. However, the softer wire allowed for the ultrasonic energy applied in the final bond to be decreased significantly to 0.3 W for 30 ns. This allowed for the wedge bond on the top platinum electrode to be completed with minimum ultrasonic energy applied. The gold wire is brought into contact with the pad, with the small amount of ultrasonic power applied essentially smearing the wire onto the pad, without delaminating the upper electrode film. Examples of these wire bonds can be seen in close up in Figure 5.7.
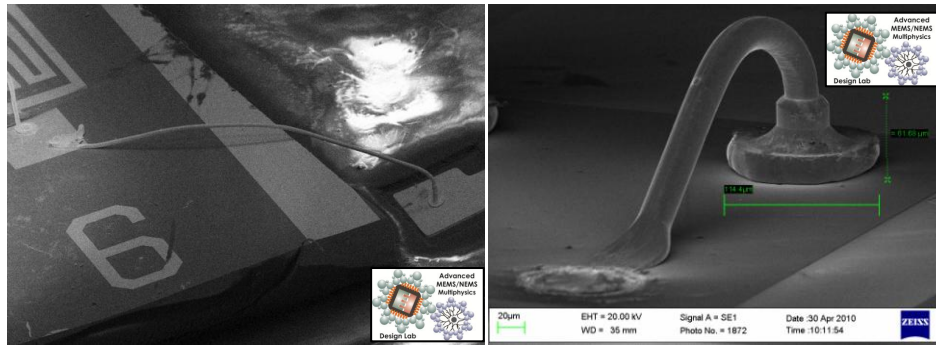
Figure 5.7 – Scanning Electrode Microscope images of sample wire bonds used to package the energy harvesters [5].

This method of packaging developed for the energy harvesters has been proven not to add a parasitic capacitance that would reduce electrical output. Examples of packaged harvesters can be seen in Figure 5.8.
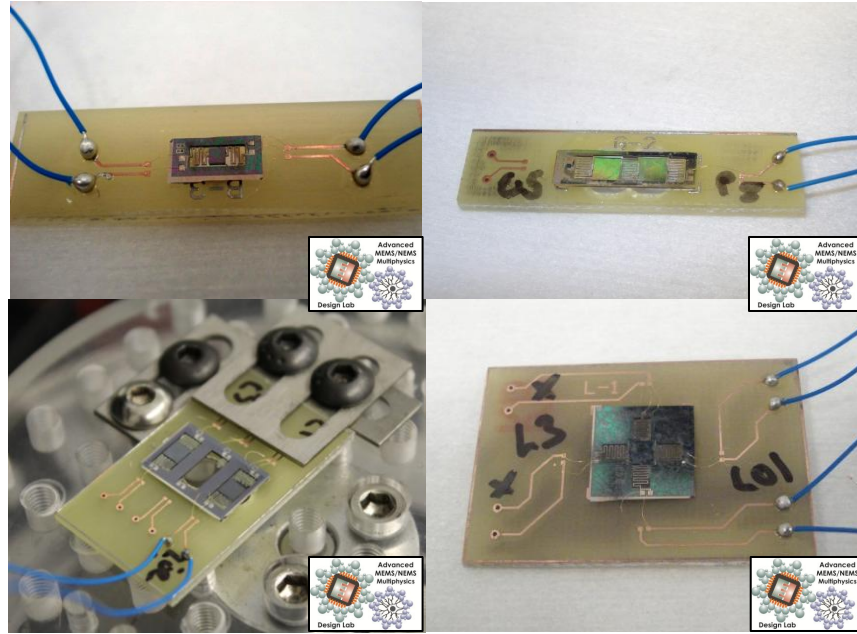
Figure 5.8 – Several examples of fully packaged Class II Harvesters ready for testing.

The wire bonding scheme developed in this work also allowed for the reclamation of the harvesters that were damaged through overetching issues encountered in the development of the microfabrication process, as discussed in Chapter 4, section 4.3.3.2. The overetch due to residual titanium completely removed the platinum lower electrodes of many of the harvesters, leaving only the platinum/PZT/platinum stack electrode. To gain access to both electrodes, the upper platinum electrode and PZT material was carefully removed by hand. This allowed for access to both electrodes for wire bonding, as shown in Figure 5.9.
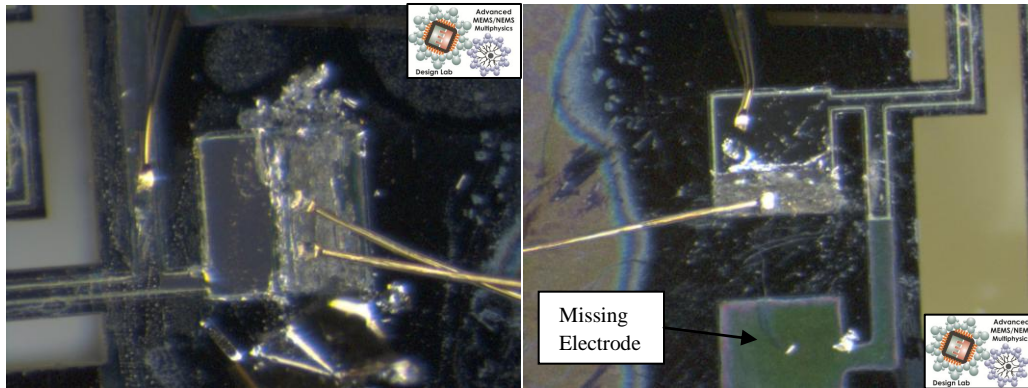
Figure 5.9 – Examples of removing platinum and PZT from the remaining electrode of a damaged harvester to allow for packaging.

The remaining electrode pad area is sufficiently large enough to gain access to both upper and lower electrode layers. The wire bonding procedures were not altered once access to both pads was achieved. As can be seen in the left of Figure 5.9, each wire bond does not require a large area to make a connection, capable of bonding directly to the upper electrode of the PZT stack away from the electrode pad itself. The ability to salvage damaged harvesters further demonstrates the robustness of this packaging scheme.

5.7 Conditioning Circuitry for the Energy Harvesters

The energy harvesters require conditioning circuitry for measurement, characterization, and to rectify the AC signal produced into DC signal for use in electronics. In this research, three types of conditioning circuits were developed. The first conditioning circuit allowed for the amplification of the electrical output of the Class I and early Class II Harvesters, by a known gain, to confirm the harvesters were converting vibration to electricity. The second allowed for the characterization of the optimum load resistance and measurement of output power for functioning harvesters. The third conditioning circuit was designed to convert the output AC signal produced by the harvester into a DC signal for storage and use in electronics.

5.7.1 Amplification Circuitry

Early in the development of the energy harvesters, the output signal from the harvesters was very low and required amplification to have enough resolution to be measured. The output signals were not large enough to distinguish the expected signal from the 60 Hz noise floor of the AC signal that was measured. Therefore, a simple operational amplifier circuit was used to amplify the signal from the harvester, as shown in Figure 5.10.
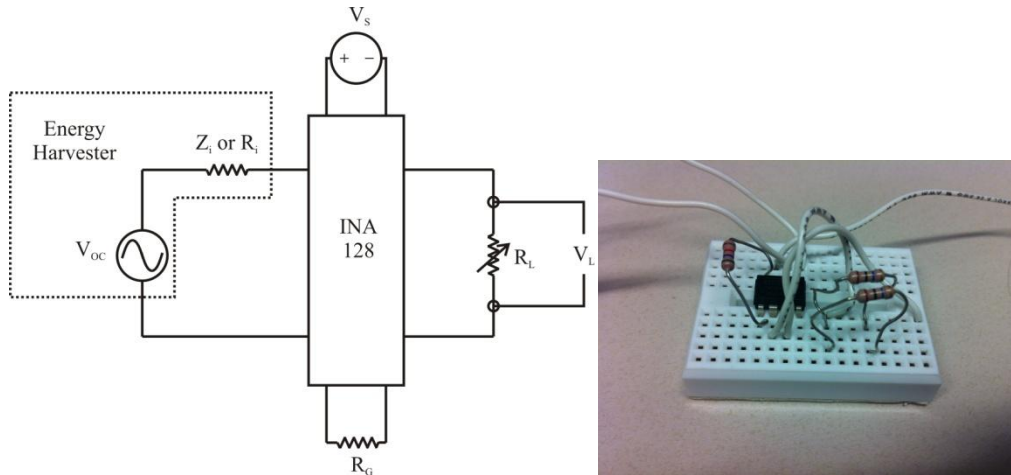
Figure 5.10 – Amplification circuitry developed to aid in detecting harvested electricity. (Left) The circuit diagram of the amplification circuit. (Right) The circuit built on breadboard using the discrete components.

The circuit shown in Figure 5.10 uses a Texas Instruments INA128P operational amplifier. This amplifier will amplify the signal at a known gain, defined by the gain resistance (R_G), which can be tuned as required. A DC voltage source is required in order to power the operational amplifier (V_s). The signal from the energy harvester is amplified by the gain and then applied across a variable load resistor (R_L) in order to measure the output voltage across a load (V_L). To preserve the magnitude of the output signal, the gain can be extracted after measurement to give the true output, minimizing the effect of the imposed noise on the system. This circuit was used solely to confirm that the harvesters were operational early in the fabrication and testing process while various PZT and fabrication challenges were causing significant electrical losses.

5.7.2 Measurement Circuitry

In order to measure the output power of the harvester, a simple circuit was required in order to determine the optimum load resistance and the voltage across that resistance. For maximum power transfer, the internal, or input resistance of the voltage source must match the load resistance [9]. The simple circuit designed to accomplish both these tasks is shown in Figure 5.11.
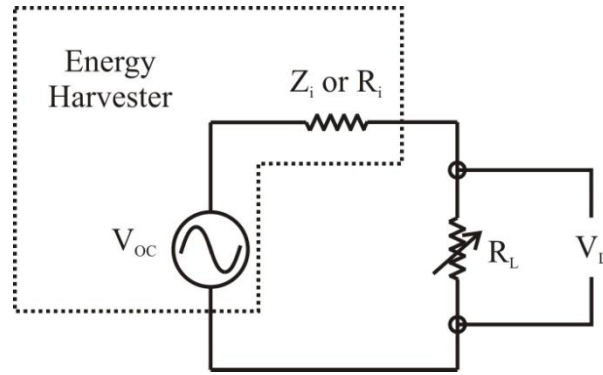
Figure 5.11 – Measurement circuitry consisting of the energy harvester and a variable load resistor.

As can be seen in Figure 5.11, the energy harvester can be idealized as an AC voltage source and a resistor symbolizing the real component of the internal impedance of the harvester (Z_i or R_i). As discussed in Chapter 2, section 2.4, the internal impedance of the harvester is a function of the operational frequency of the harvester and the capacitance formed across the deposited PZT material. The load resistance (R_L), as shown in Figure 5.11, supplied by a variable resistor, can be varied to capture the output voltage of the circuit in response to a varying load resistance. When the load resistance matches the input resistance of the harvester, the harvester should be transferring maximum output power to the circuit. This circuit was used to confirm the operation of the harvesters and to determine the maximum output power available from the harvester.

5.7.3 Rectification Circuitry

To extract the power from the harvester for use in electronics, a conditioning circuit must be used to convert the AC signal produced by the harvesters into a usable DC signal. The basic form of the conditioning circuitry required is shown in Figure 5.12:
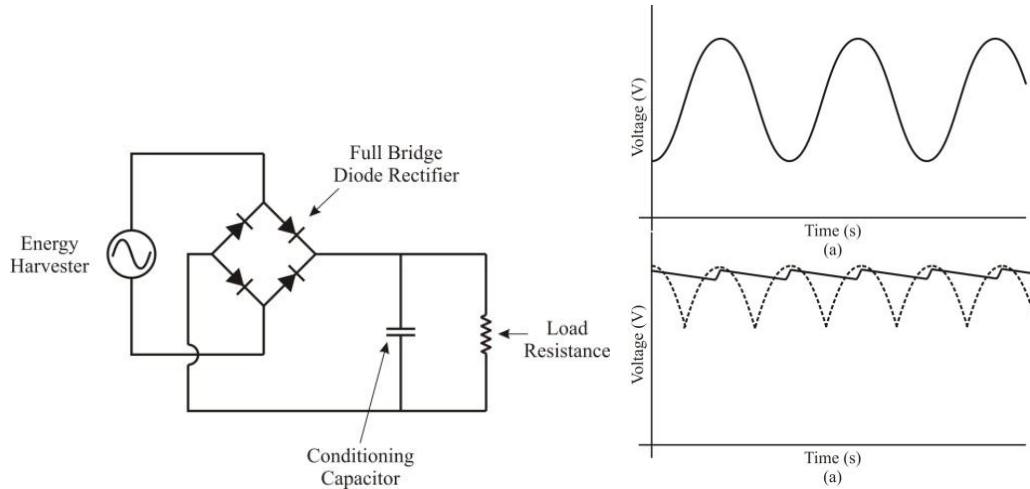
Figure 5.12 – Basic Form of rectification circuitry [5] and resultant waveforms produced from the circuit.

The output voltage of the harvester should follow the input vibration, which will cause opposing phases of voltage in the output signal, as shown in the right of Figure 5.12. The full bridge rectifier, as shown in the left Figure 5.12, will convert the two-phase AC signal produced by the harvester (positive and negative voltage signals) into a single phase signal. This prevents signal cancellation from the production of equal and opposite voltages produced in the harvester (or an array of harvesters). The dotted signal shown in the right of Figure 5.12 is an example the rectified signal. A conditioning capacitor is charged during the high voltage peaks, and then acts as a source in the signal troughs, to condition the overall signal (shown as the solid rectified signal in Figure 5.12). The resulting signal is a DC voltage with a small AC ripple signal superimposed on the DC voltage. The amplitude of the ripple is defined by the chosen capacitor. This signal can now be used to charge a battery or storage system, given that the voltage provided is above the required threshold voltage to charge the battery. The

conditioning circuitry can be expanded to take advantage of the multiple harvesting elements present in the Class II Harvesters. The individual harvesting elements can be paired in series to increase the voltage output, as shown in Figure 5.13.
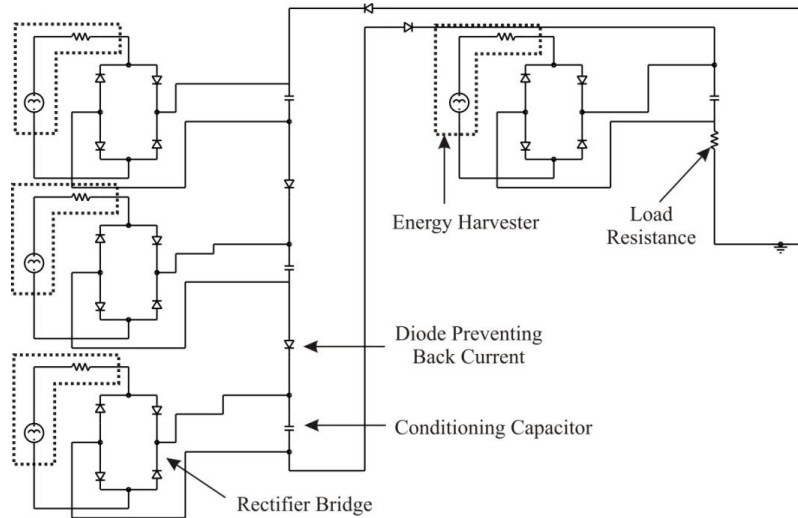
Figure 5.13 - Schematic energy harvesting conditioning circuits in series.

To illustrate the effect of this circuit on the output of the energy harvester, an analysis was undertaken in PSpice to calculate the potential power output of a sample energy harvesting system in this configuration. As can be seen in Figure 5.13, each harvesting circuit has an extra diode to prevent current backflow. Additionally, capacitors are used in each harvesting unit to store charge and condition the rectified AC signal into a quasi-DC signal. As shown in Figure 5.14, the effect of one conditioning circuit on the sample output voltage of one harvesting element of the harvester can be seen.
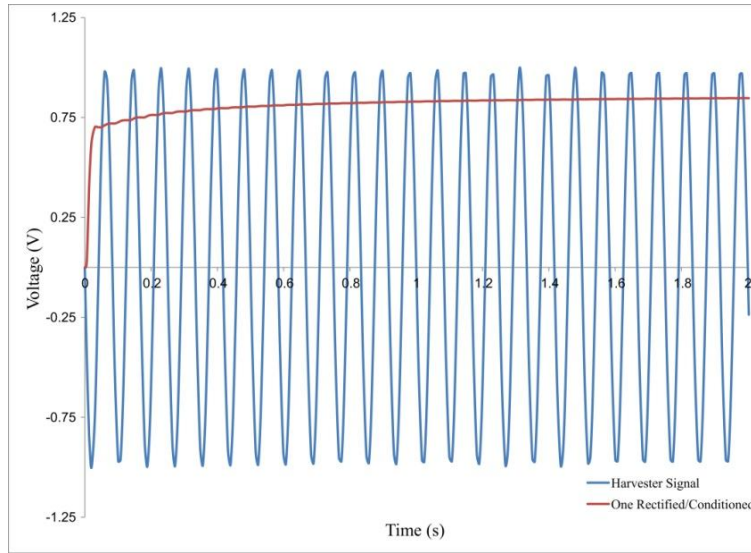
Figure 5.14 – Sample voltage output of a single harvester (Rectified and Non-rectified)

If the rectified signal of each harvesting element is then arrayed in series, the overall output voltage created through this system is shown in Figure 5.15.
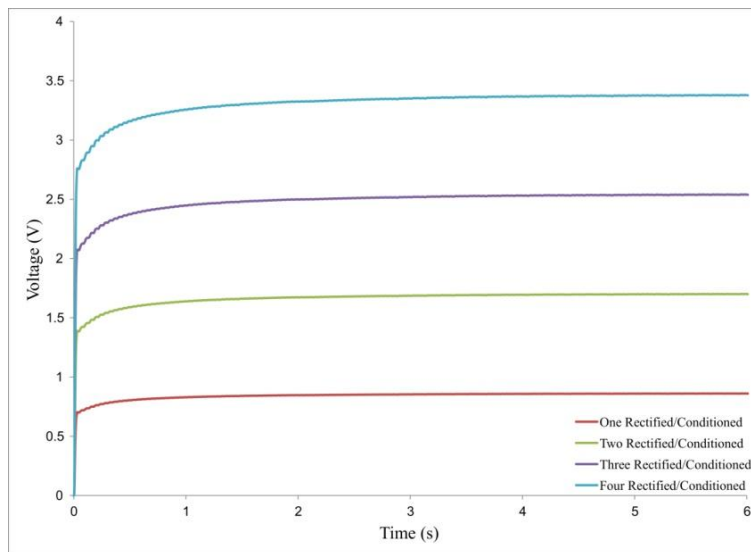
Figure 5.15 – Harvesting system output voltage with harvesters arrayed in series.

Additionally, the current in the whole system is shown in Figure 5.16 with an average current of approximately 300 nA, when subject to steady state operation.
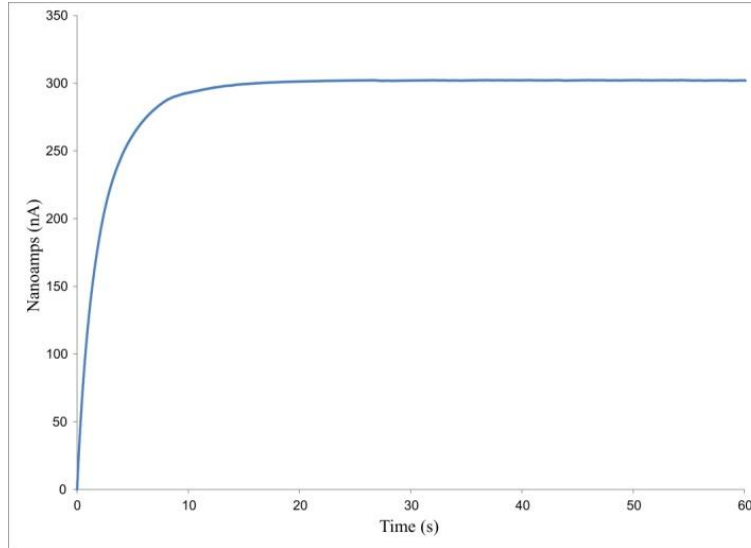
Figure 5.16 - Time history current output of the conditioning circuit

This analysis demonstrates that a conditioning circuit could be used to allow the energy harvesters to drive an *in-situ* application, either augmenting an existing battery source or directly powering electronics. The conditioning circuit could be altered to emphasize either voltage output (as discussed above) or current output (a parallel arrangement of harvesters). Additionally, a half-bridge or "voltage doubler" based conditioning circuit could be used to accomplish the same rectifying effect, with less diode drop-based electrical losses.

5.8   Characterization and Testing Methodology

The general characterization and testing methodology used in evaluating both classes of harvesters produced in this thesis is shown in Figure 5.17.
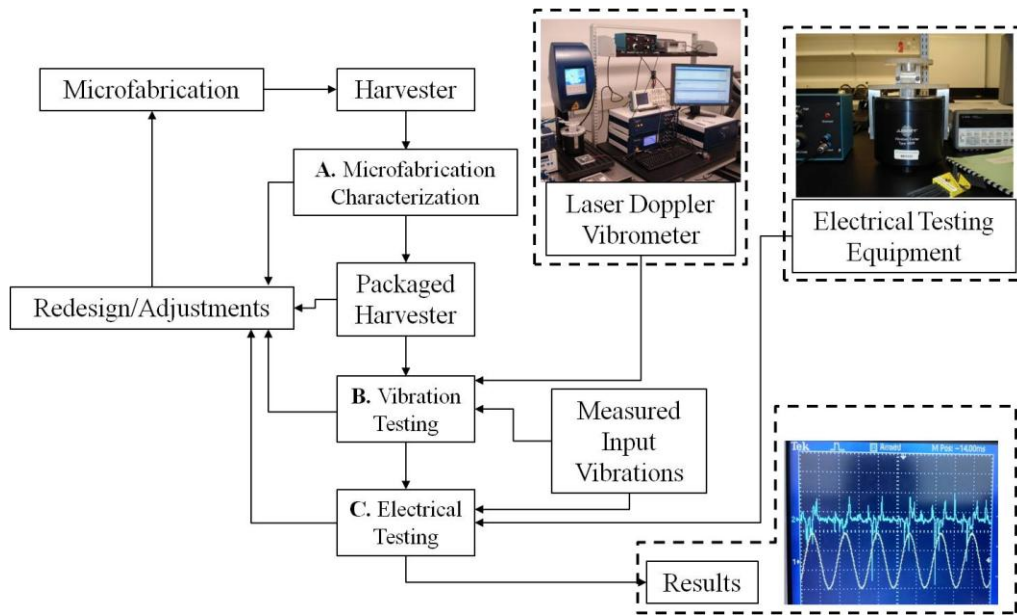
Figure 5.17 – A schematic outlining the characterization and testing methodology. The testing and characterization provides a feedback loop to the microfabrication process to diagnose and correct device-based problems.

The harvesters are initially characterized to evaluate the performance of the individual microfabrication processes. Once the fabrication process flow was sufficiently refined, the harvesters could be then packaged to provide the necessary electrical connections for testing equipment. Once suitably packaged, the frequency response of the harvester is measured using a Laser Doppler Vibrometer (LDV). Finally, the electrical performance of the harvester is tested by applying a known vibration and measuring the electrical output of the harvester using one of the conditioning circuits. As seen in Figure 5.17, the results of the testing and characterization, positive or negative, are used to revise the designs and microfabrication processes to improve the microfabrication and device performance.

5.8.1   *Microfabrication Characterization:*

The initial characterization of the harvesters focused on evaluating the effectiveness of the microfabrication processes required to produce the energy harvesters. The microfabrication recipe was validated and tested to ensure that the recipe was producing operational piezoelectric energy harvesters. Thickness measurements and surface profiles were taken by optical profilometry, physical profilometry and scanning electron microscopy in order to ensure proper film thicknesses, continuous films, and that electrical shorting was not occurring. The sol-gel PZT film was characterized with X-Ray Diffraction (XRD) to ensure that the proper crystal structure is attained. Characterization of the microfabrication processes to diagnose microfabrication difficulties throughout the development of the microfabrication recipe has been essential in fabrication development. The major results in the microfabrication characterization are discussed throughout Chapter 4 in the appropriate section for each microfabrication process.

5.8.2 Vibration Testing

The vibration testing of the piezoelectric energy harvester focused on capturing the response of the harvester in response to a base excitation. This involved applying a base excitation to the harvester with a mechanical shaker and recording the resulting vibration with a LDV. The vibration rig is comprised of a Brule and Bajer single axis electromagnetic shaker with a custom-built vibration platform, an arbitrary function generator and an amplifier to provide a suitable input signal to the shaker, as shown in Figure 5.18.
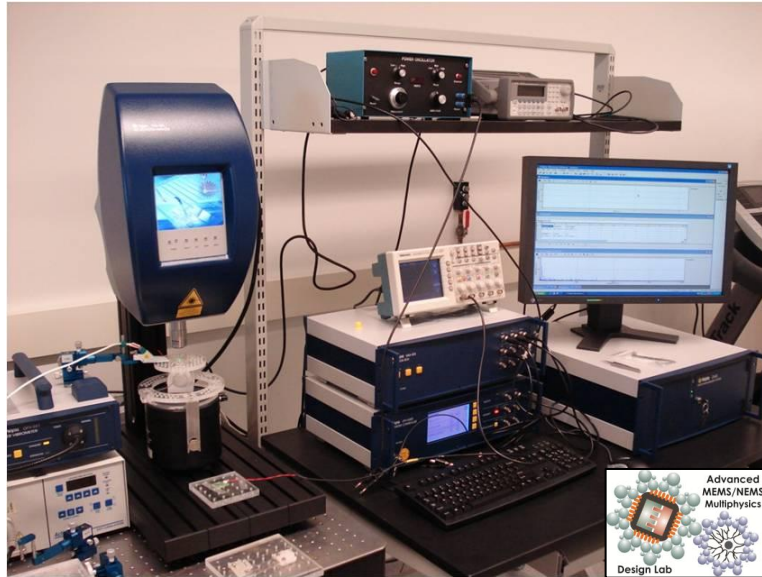
Figure 5.18 – Laser Doppler Vibrometer experimental setup.

The vibration experimental setup can impart known vibrations to an integrated energy harvester on a known loading axis. The input vibration can be varied in amplitude (up to 12mm displacement), frequency (0-5kHz), and application direction ($\theta = 0 - 45°$ off vertical axis). The function generator can apply any manner of vibration signal to the vibration rig, including user generated acceleration signals. This experimental vibration setup is used both for the vibration and electrical characterization of the energy harvester, allowing for full characterization.

In order to measure the frequency response of the energy harvester, one may apply either pseudo random noise or a harmonic frequency sweep as an input vibration signal. The applied pseudo random vibration will cause the harvester to resonate at its natural frequency. The harmonic frequency sweep will cause the energy harvester to resonate as the frequency of the applied vibration nears the natural frequency of the energy harvester. The LDV is used to directly measure the out of plane velocity of the energy harvester. The laser beam of the LDV is focused on the point of interest on the energy harvester. The Doppler shift of the reflected laser light is measured, allowing for real time measurement of the out of

plane velocity of the harvester. This process is shown schematically in Figure 5.19.
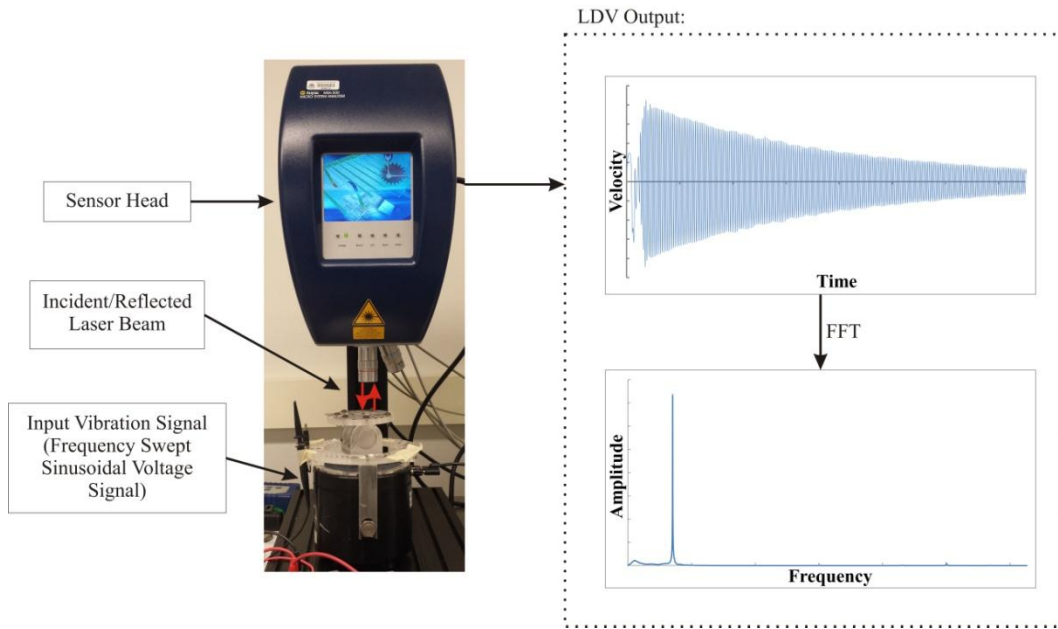
Figure 5.19 – Schematic of the Laser Doppler Vibrometer measurement scheme.

The velocity profile of the harvester is recorded in the time domain, in response to the input vibration applied to the harvester. The velocity profile can be integrated after the measurement or in real time to determine the displacement profile of the harvester in the time domain [10]. Typically, the velocity profiles are more accurate and are less sensitive to errors and integration drift. The Fast Fourier Transform (FFT), of either the velocity or displacement profile, will give the frequency response of the harvester, allowing for identification of the natural frequencies of the energy harvester.

The complete frequency response of the device, in this case, under a base excitation, will be a superposition of the dynamics of the harvester and shaker system. To determine the frequency spectrum of the harvester from alone, two separate measurements are required: the response of the device (point of interest) and the response of the base of the device (a reference point of no "device" displacement expected). To isolate the response of the device, the frequency

spectrum of the harvester is normalized by the frequency spectrum of the base of the harvester [10]. The effect of the normalization is shown in Figure 5.20.
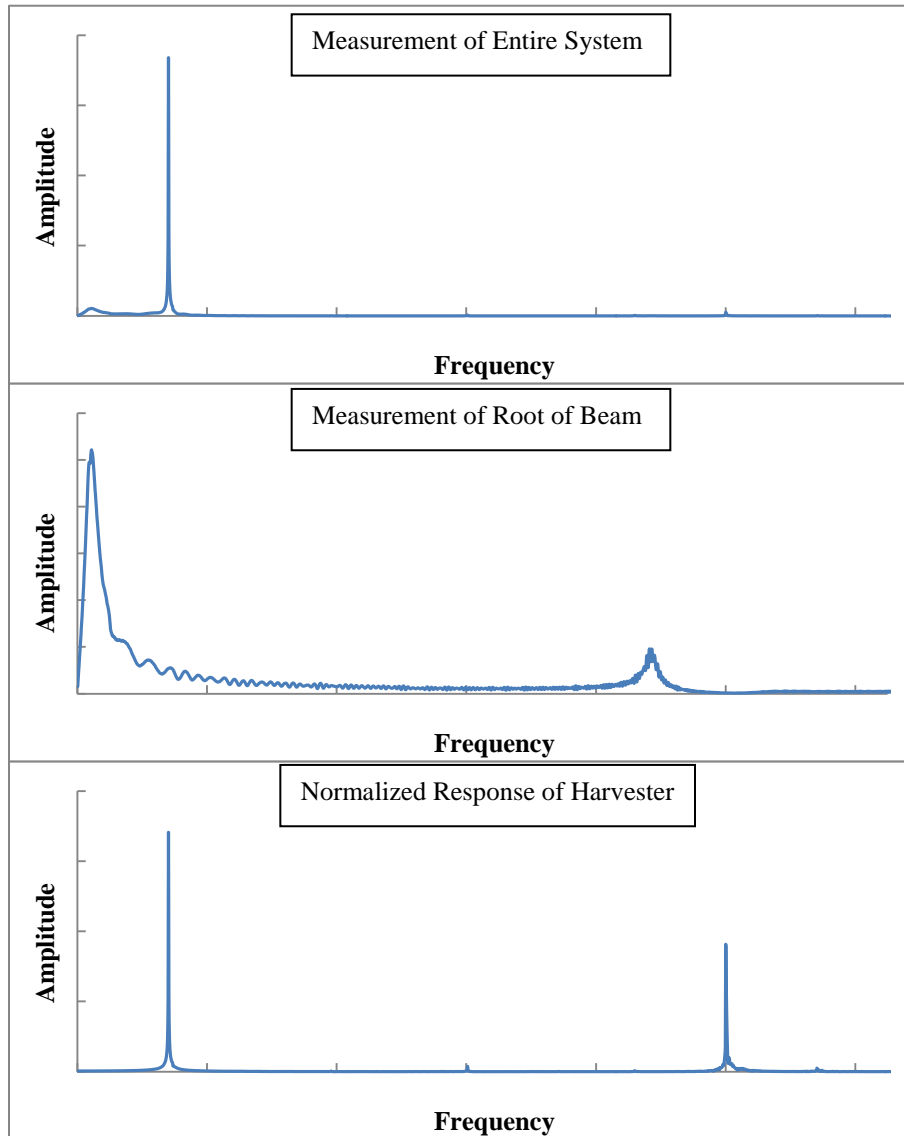
Figure 5.20 – (Top) An experimental frequency response of a Class II Harvester at the point of interest, including the base and shaker dynamics. (Middle) The frequency response of the root of the harvester beam. (Bottom) The normalized frequency response of the harvester after the base and shaker dynamics are removed.

Through this normalization step, the entire dynamics of the base of the energy harvester (noise, vibrations of the base of the device, dynamics of the shaker, etc.) are removed. Although this process is very useful in removing the unwanted dynamics from the system, it can distort the relative magnitudes of the displacement when the vibrations of the harvester and the base of the harvester are of the similar magnitudes. Therefore, it is only relevant for determining the existence of modes or natural frequencies, rather than the absolute magnitudes of the vibration at the natural frequencies.

5.8.3 Electrical Testing

The electrical testing of the energy harvester included several sequential stages, such as checking harvesters for electrical short circuits, measuring the capacitance of the harvester to calculate the input impedance, determining the optimum load resistance of the harvester, and finally measuring the maximum output power to a specific known input acceleration.

The first stage of electrical testing involved evaluating the harvesters for short circuits with a multimeter. A shorted harvester would not produce an output signal, since any voltage across the thickness of the film would be instantly equalized via the short circuit. This was typically caused by pinholes and non-continuous PZT films allowing the upper and lower electrodes to contact. Shorted harvesters are typically non-recoverable and will only provide data for vibration-based analysis.

The next stage of electrical testing involved the calculation of the input impedance of the harvesters through a capacitance measurement. The piezoelectric stack in this device produces a capacitor, with PZT as the dielectric material. The capacitance of non-shorted harvesters were measured, at rest, by multimeter. Next, the input impedance of the harvester was calculated from the measured capacitance and the measured natural frequency of the harvester. This allows for the calculation of the impedance at the intended operational frequency

of the system. The calculated input impedance was used to compare against the optimum load resistance measured in the next phase of electrical characterization.

In order to match conditioning circuitry and confirm the operation of the harvester, the optimum load resistance must be determined for each harvester. For this test, low amplitude vibrations were applied to the harvester at (or as near as possible to) its natural frequency. Using the measurement circuitry discussed in section 5.7.2 to vary the load resistance, it was possible to determine the optimum load resistance that allows maximum power transfer. According to the maximum power transfer theorem, input impedance and the optimum load resistance should be equal to allow for maximum power transfer [9]. This behavior is shown in Figure 5.21, showing the typical relation of the power output and load resistance peaking at the optimum load resistance.
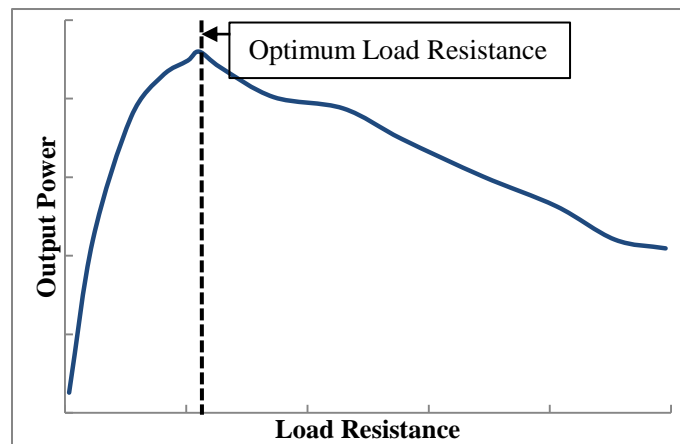
Figure 5.21 – Typical power output versus load resistance characteristic curve for piezoelectric harvesters developed in this thesis.

Once the harvester was confirmed to be operational, the acceleration applied to the harvester was increased in order to evaluate the maximum harvesting potential of the design.

5.9   Summary

A complete packaging methodology was developed for the harvesters to overcome challenges involved in testing MEMS devices actuated under a base vibration. The packaging methodology was adapted from various available packaging techniques to allow the direct probing of the microfabricated energy harvesters. The movement of the energy harvester is not hindered in any way. Multiple wire bonding methodologies were developed to allow bonding to both platinum and PZT-stack electrodes. The flexibility of the packaging scheme allowed for the reclamation of several overetched energy harvesters.

Several conditioning circuits were developed to allow for the characterization of the electrical characteristics of the energy harvesters. This included an amplification circuit, which allowed for the direct measurement of initial energy harvesters with low power output. The measurement circuit developed allowed for identification of the optimum load resistance and the maximum power that could be transferred from the harvester. Several rectification conditioning circuits were postulated that could be used to convert the AC signal produced by the harvester into a DC signal usable by common electronics.

A complete testing and characterization methodology was discussed, including microfabrication, vibration-based, and electrical-based characterization. The characterization of the microfabrication process and performance of individual processes allowed for the diagnosis and troubleshooting of the harvester fabrication. The vibration-based characterization, with the use of a mechanical shaker system and Laser Doppler Vibrometer, allowed for the capture of the velocity profile and frequency response of the harvester in real time. The electrical characterization allowed for the capture of the electrical characteristics of the harvester, including input impedance, optimum load resistance and maximum power transfer.

5.10 References

[1]   A. D. Oliver, T. A. Wallner, R. Tandon, K. Nieman, and P. L. Bergstrom, "Diamond scribing and breaking of silicon for MEMS die separation," *Journal of Micromechanics and Microengineering,* vol. 18, 2008.

[2]   T. Overstolz, P. A. Clerc, W. Noell, M. Zickar, and N. F. De Rooij, "A clean wafer-scale chip-release process without dicing based on vapor phase etching," in *Proceedings of the IEEE International Conference on Micro Electro Mechanical Systems (MEMS)*, Maastricht, 2004, pp. 717-720.

[3]   I. Sari, I. Zeimpekis, and M. Kraft, "A dicing free SOI process for MEMS devices," *Microelectronic Engineering,* vol. 95, pp. 121-129.

[4]   M. Rezaei, Lueke, J., Sameoto, D., Raboud, D., Moussa, A., "A New Approach to Cleave MEMS Devices from Silicon Substrates," *Journal of Mechanics Engineering and Automation,* vol. 3, pp. 731-738, 2013.

[5]   M. Rezaei, J. Lueke, D. Raboud, and W. Moussa, "Challenges in fabrication and testing of piezoelectric MEMS with a particular focus on energy harvesters," *Microsystem Technologies,* pp. 1-25, 2013.

[6]   D. Benfield, J. Lueke, and W. A. Moussa, "MEMS packaging using flexible printed circuit boards," *CMC Packaging Application Note*.

[7]   J. Q. Liu, H. B. Fang, Z. Y. Xu, X. H. Mao, X. C. Shen, D. Chen, H. Liao, and B. C. Cai, "A MEMS-based piezoelectric power generator array for vibration energy harvesting," *Microelectronics Journal,* vol. 39, pp. 802-806, 2008.

[8]   D. Benfield, E. Lou, and W. A. Moussa, "A packaging solution utilizing adhesive-filled TSVs and flip-chip methods," *Journal of Micromechanics and Microengineering,* vol. 22, p. 065009.

[9]   J. D. Irwin and C.-H. Wu, *Basic engineering circuit analysis (6th ed.)*: Prentice-Hall, Inc., 1999.

[10]   O. Ozdoganlar, B. Hansche, and T. Carne, "Experimental modal analysis for microelectromechanical systems," *Experimental Mechanics,* vol. 45, pp. 498-506, 2005.

6.1   Introduction

With the microfabrication process outlined in Chapter 4 and the packaging and testing methodologies outlined in Chapter 5, the Class I Harvesters were fabricated, packaged, and tested. An example of the fully packaged Class I Harvesters is shown in Figure 6.1.
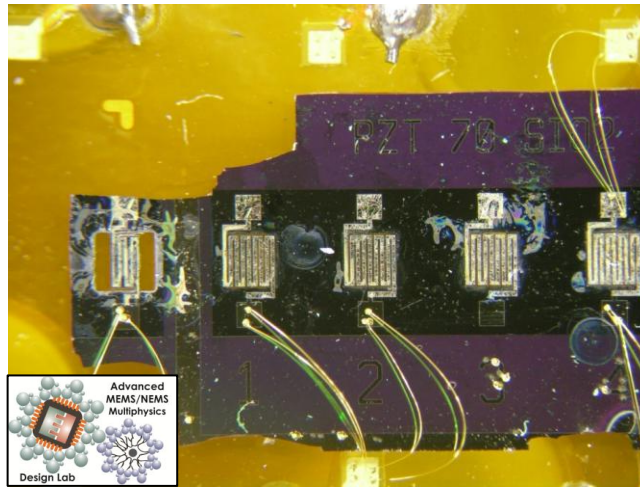
Figure 6.1 - Fully packaged Class I Harvesters on Flexible Printed Circuit Board (FPCB)

6.2   Microfabrication Characterization

Throughout the development of the microfabrication process in Chapter 4, the processes used to fabricate the Class I Harvesters were characterized in order to overcome fabrication-based challenges. Every process outlined in Figure 4.3 was initially developed with the Class I Harvester design. As seen throughout Chapter 4, the microfabrication procedures were characterized with a variety of fabrication-based measurement and inspection equipment to ensure proper film thickness, photoresist development, film composition (XRD), and etch depths.

The characterization allowed for identification of the proper procedure and required parameters to deposit a continuous PZT film, diagnosing adhesion and overetching problems, and determining the effects of non-geometric fabrication-constrained parameters. These non-geometric parameters included maximum allowable processing temperatures for specific materials, material incompatibility, and required buffer spacing for alignment error. Additionally, the microfabrication characterization allowed for the diagnosis of issues related to the aqua regia etch and PZT deposition/lift-off procedures, as discussed at length in Chapter 4. For example, many surface profile measurements of aqua regia trial etches were taken with optical profilometry, as shown in Figure 6.2, to calculate the 12-15 nm/min etch rate achieved with the Aqua Regia Etch System.
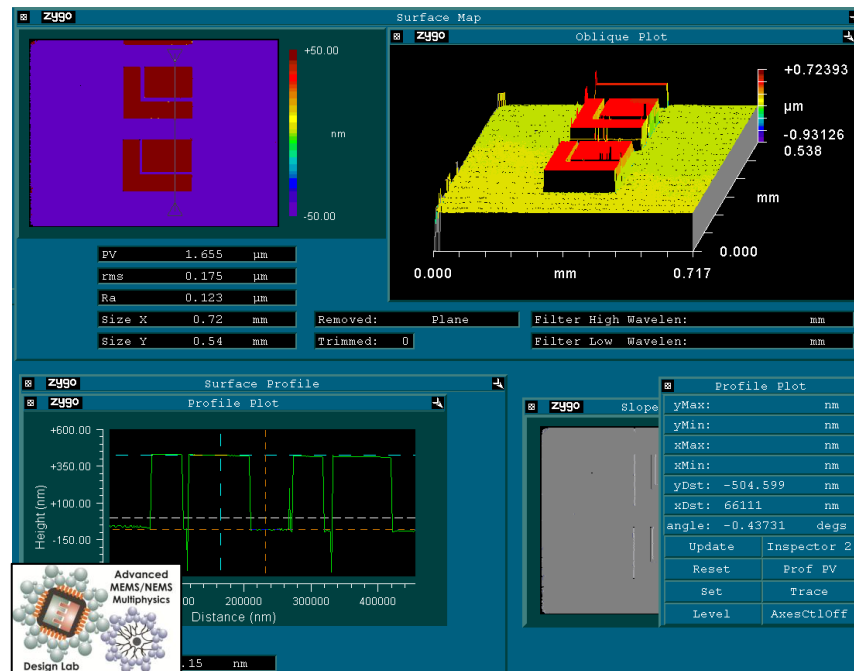
Figure 6.2 – A sample profile measurement of a test pattern etched into platinum and titanium films.

As will be shown in the vibration characterization of the Class I Harvester, the microfabrication characterization allowed for the identification of sources of error directly related to the microfabrication processes.

6.3   Vibration Characterization

The Class I Harvesters were tested according to the vibration characterization methodology described in Chapter 5. An example of the frequency response behavior of an example four-fold harvester is shown in Figure 6.3.
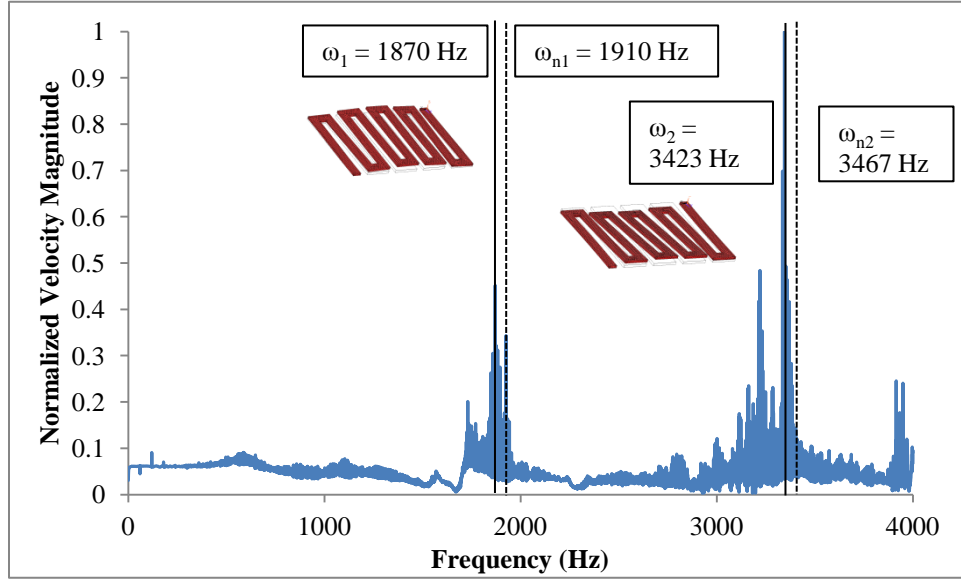
Figure 6.3 - Experimental frequency response of an example Class I Harvester. Experimentally measured natural frequencies of $\omega_1 = 1870$ Hz and $\omega_2 = 3423$ Hz. Design natural frequencies of $\omega_{n1} = 1910$ Hz and $\omega_{n2} = 3467$ Hz.

The frequency-based behaviour of the sample harvester shown in Figure 6.2 was typical for Class I Harvesters. As shown Figure 6.2, the measured natural frequency of the harvester, captured at 1870 Hz was close to the simulated design natural frequency of 1910 Hz. Although the second measured natural frequency at 3423 Hz appears to be the dominant frequency of the system due to a higher normalized velocity magnitude, the normalization required to remove the base dynamics of the testing equipment distorted the magnitudes of the resonant peaks. For the majority of Class I Harvesters, the magnitude of the velocity response of the device was on the same order of magnitude as the base/background dynamics, therefore, the normalization was distorted. Additionally, the low quality factor of

the folded spring harvester without masses contributed to the overall poor and jagged frequency response. This was one of the major motivations of adding masses to the system to increase the resolution of this measurement, as shown from the experimental measurement of a Class II Harvester shown in Figure 5.20.

The experimental and calculated natural frequency for the Class I Harvester shown in Figure 6.3 agree within approximately 40 Hz, or ~2%. There are several factors contributing to the offset between the design and measured natural frequencies in Figure 6.3. The silicon wafer used to fabricate the Class I Harvesters had a thickness variation of approximately 5% (on 500 μm). This thickness variation, when compounded with the uniformity of the DRIE etch process used to define the folded spring, typically caused a 3.25 – 5.45 μm standard deviation of the thickness of the folded springs (refer to Table 7.1, Chapter 7). This effect can be seen in the rippling of the undersides of the folded beams shown in Figure 6.4.
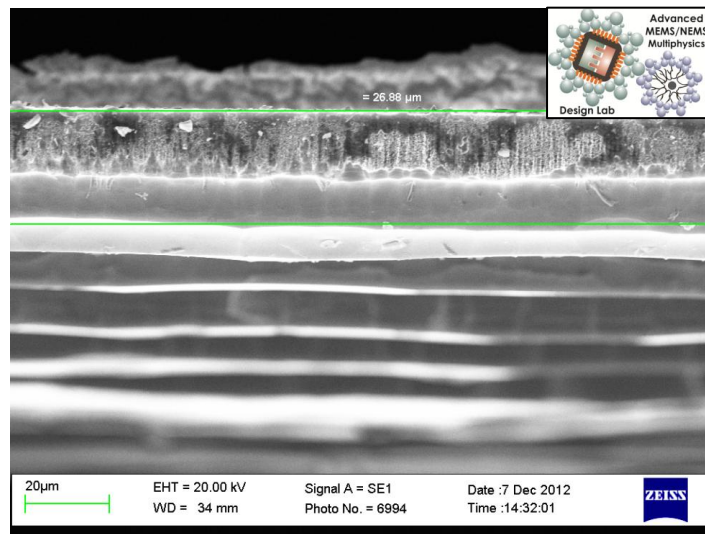
Figure 6.4 – SEM image illustrating the variability in thickness due to etch and wafer uniformity.

The etch processes used to define the cross section of the folded spring also did not produce a truly rectangular cross sectioned beam. As can be seen in

Figure 6.5, the DRIE processes used to define the cross section of the harvester can degrade the design intent of the devices.
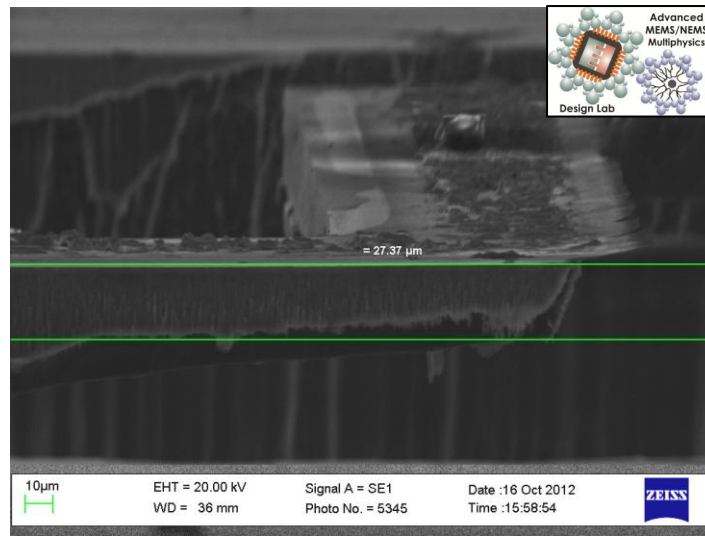
Figure 6.5 – SEM image of the corner of the folded spring, illustrating the thickness and cross section of the folded spring.

The isentropic nature of the DRIE etch caused difficulty in achieving a rectangular cross section for the folded springs. As the DRIE etch depth increases, the isotropy of the repeated cyclic etch causes the sidewalls of the etch well to be progressively more etched. This causes the sidewalls of the harvester to be scalloped, as shown in Figure 6.6, eventually leading to sloped sidewalls.
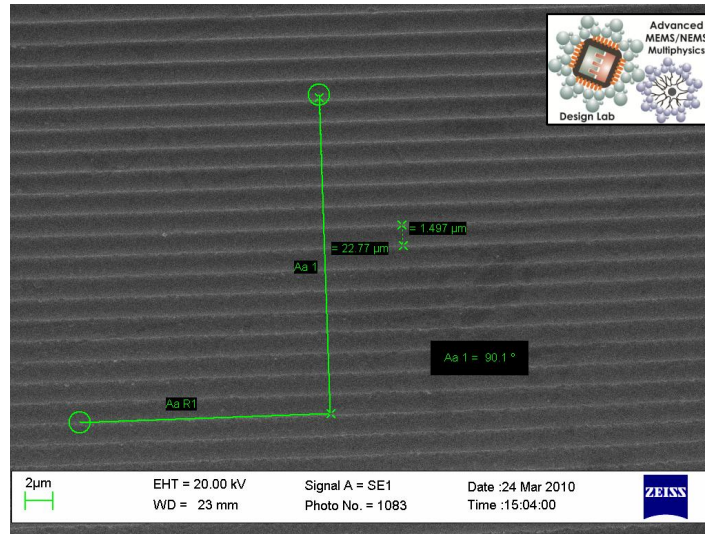
Figure 6.6 – Scalloped sidewalls of the folded spring beams due to the DRIE process.

This behavior reduces the mass and stiffness of the folded springs slightly and was an additional source of natural frequency variability. The undercut of the sidewalls of the harvester imposes a trapezoidal cross section onto the harvester, reducing the moment of inertia and stiffness of the harvester. Using the moment of inertia of a trapezoidal cross section and equation (8) of Chapter 3, the effect of this undercut on the cross section can be seen in Figure 6.7.
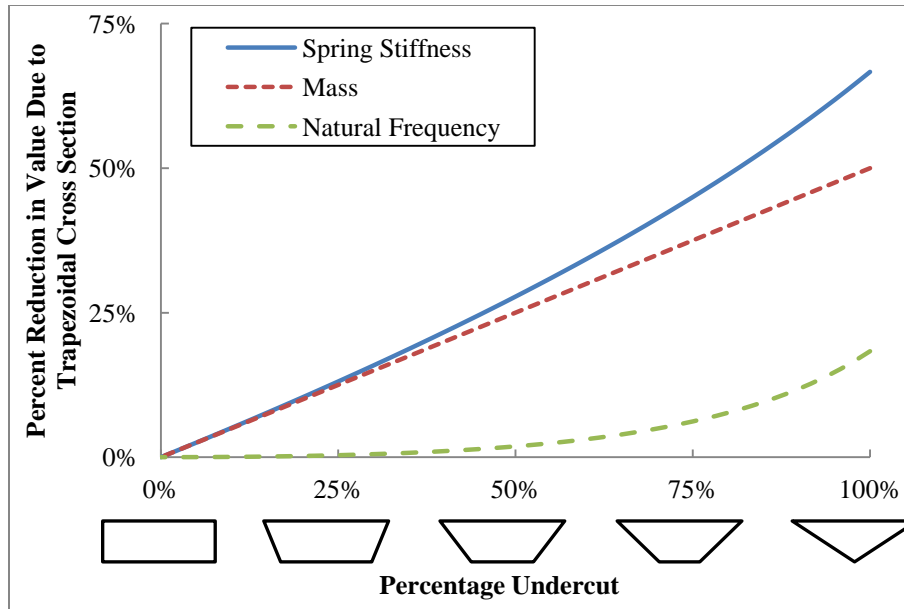
Figure 6.7 – The effect of the undercut from the DRIE process on the spring stiffness, mass and natural frequency of the energy harvester.

The undercut of the beam occurs symmetrically, from both sides of the beam, therefore it is reasonable to use a symmetric trapezoid for the calculation in Figure 6.7. As can be seen in Figure 6.7, the loss of stiffness behaves non-linearly as the cross section transitions from rectangular to triangular. At the absolute extreme, this behavior can cause upwards of 66.6% stiffness loss at a complete undercut. The mass loss of the harvester due to undercut is linear according to the loss of cross sectional area. At the absolute extreme, up to 50% of the beam mass could be lost by the undercut. Interestingly, the overall change in natural frequency due to the undercutting, as seen in Figure 6.7, is fairly small until the undercut becomes more pronounced, at around 50% undercut. At this point, the stiffness loss due to undercut becomes non-linear, and begins to steadily increase the rate of stiffness loss. Depending on the depth of etches undertaken in the two-step release for a specific harvester, this microfabrication-based deviation from the design intent could account for a significant portion of offset error between the calculated and measured natural frequencies.

The harvester did not exhibit any of the symptoms of residual stress-based beam curling. As shown in Figure 6.8, the beams do not curl out of plane, suggesting that the folded beams are insensitive to the negative stiffening effects of microfabrication-based residual stresses.

Figure 6.8 - SEMS/Pictures of the Class I Harvester, showing the lack of residual stress-based beam curling.

The characterized Class I Harvesters have validated the initial simulation work. The measured and calculated natural frequencies agree, for the example in Figure 6.3 by ~2%, with the major sources of error identified and quantified. Additionally, the characterization has suggested that the methodology to lower the natural frequency of the harvester using folded springs is valid and warrants additional exploration with Class II Harvesters.

6.4   Electrical Characterization

Due to the scope and yield of the Class I Harvesters, a partial electrical characterization was undertaken, using the methodology discussed in Chapter 5. The yield problems of the PZT film used initially in the microfabrication process flow made it difficult to produce a sufficient number of harvesters to perform suitable testing. Additionally, the results of the vibration characterization

suggested that a structural redesign was required in order to improve the displacement of the harvesters through the addition of a proof mass. Therefore, the main goal of the electrical characterization was to confirm that the Class I Harvesters were capable of converting strain to voltage.

A small number of Class I Harvesters were electrically characterized using a sinusoidal input acceleration signal of 17.6 m/s^2 at a frequency of 12 Hz. This harsh loading was required in order to provide sufficient displacement to the harvester to produce a measurable signal. In comparison, the Class II Harvesters are easily actuated by acceleration loads of much lower than 1 m/s^2. Even with this harsh loading, an amplification conditioning circuit, as discussed in Chapter 5, was required in order to provide sufficient signal resolution in order to discern the output voltage produced across the load resistor. With this circuit, it was possible to capture an output signal from the functioning Class I Harvesters, with a maximum instantaneous power output of approximately 10.90 nW. A typical output signal from these harvesters under the harsh loading is shown in Figure 6.9.
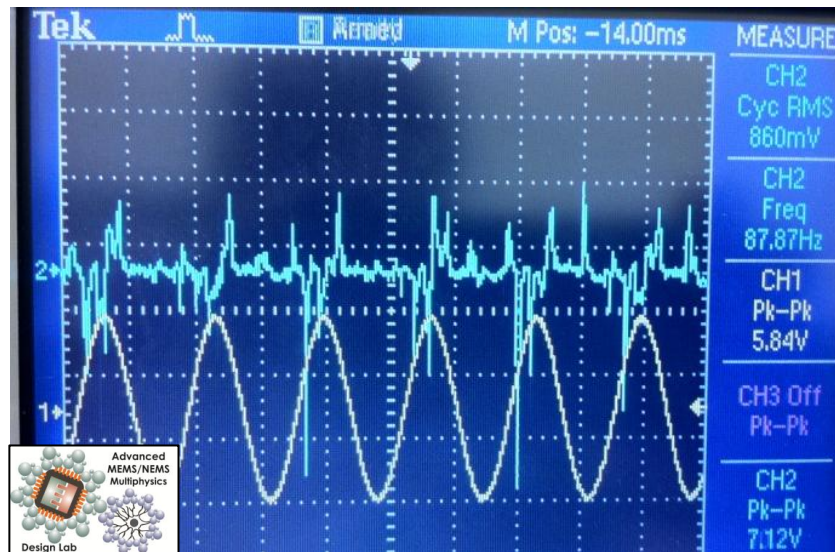
Figure 6.9 - The amplified output signal of the Class I Harvester (blue/upper signal) in response to the input signal into the vibration testing system (yellow/bottom signal).

As can be seen in Figure 6.9, the output signal produced by the Class I Harvester is typically very choppy, due to driving the system far from its natural frequency. This caused the RMS power of the system to be almost nil. However, the harvester does produce a somewhat repetitive signal under sinusoidal actuation.

As this was the initial attempt of adapting a folded spring to a piezoelectric energy harvesting application, the presence of a measurable output signal was the major achievement that allowed for the more complex designs of the Class II Harvesters to be pursued.

6.5   Summary

The microfabrication characterization, mostly occurring during the development of the microfabrication process flow developed in Chapter 4, allowed for the diagnosis and troubleshooting of various fabrication-based problems. The frequency response of the harvesters agreed with the calculated response from the design phase of the harvester. The small deviation between the measured and calculated natural frequencies can be attributed to the variation in material properties from silicon wafer to wafer, the variation in thickness of the wafer affecting the accuracy of the release etch, and the undercut of the sidewalls of the harvester creating a trapezoidal cross section. From Figure 6.7, it can be seen that the total effect of the undercut transitioning the rectangular cross section to a triangular one is small, as long as the mass and stiffness reduction is consistent. Once the stiffness reduction begins to act non-linearly due to the undercut, the reduction in natural frequency begins to increase significantly. This behaviour discovered through the characterization of the Class I Harvester will significantly aid in the characterization of the Class II Harvesters.

Generally, the vibrational testing of the Class I Harvesters verified the modeling of the folded spring. Design modifications are required in order to help improve the quality of frequency response measurements. The harvesters must have a higher vibration amplitude in order to improve the quality of the filtered

measurements. The addition of a proof mass in the Class II Harvester designs will aid in improving the quality of these measurements. The vibration-based characterization suggested that the methodology of folding the spring to reduce the natural frequency is valid, suitable for further extension into more complex devices.

The presence of a measurable output signal allowed for the extension of the design to the Class II Harvesters. It was clear that the lack of a proof mass in the design of the energy harvester significantly limited the vibration amplitude, natural frequency reduction, and output power. The electrical output will not improve unless a sufficient displacement can be generated from the vibration applied to strain the piezoelectric element of the harvester.

The Class II Harvesters will include masses to further reduce the natural frequency of the harvester to the target bandwidth of 30-300 Hz, with increased deflection and output power. The effects of adding a proof mass and using more complicated arrays of folded spring elements will be explored in Chapter 7.

7.1   Introduction

The Class II Harvesters are an evolution of the folded spring harvester design examined in Chapter 6. From the characterization of the previous designs, it was required to add proof masses and use arrays of folded springs to increase the displacement of the harvester and further reduce that natural frequency of the system. The improved designs will be evaluated in detail in this chapter.

The released Class II Harvesters did not exhibit any symptoms of fabrication-based residual stresses, such as beam curling, mass rotation, or distortion of the harvester design at rest, confirming the intended residual stress relaxation of the folded spring-based design.

7.2   Vibration Testing of Class II Harvesters

7.2.1   Mode Shape Verification

The Class II Harvesters had their frequency response characterized using the LDV and the testing methodology outlined in Chapter 5. Multiple examples of fully packaged Class II Harvesters are seen throughout Chapter 5, and in Figure 7.1.
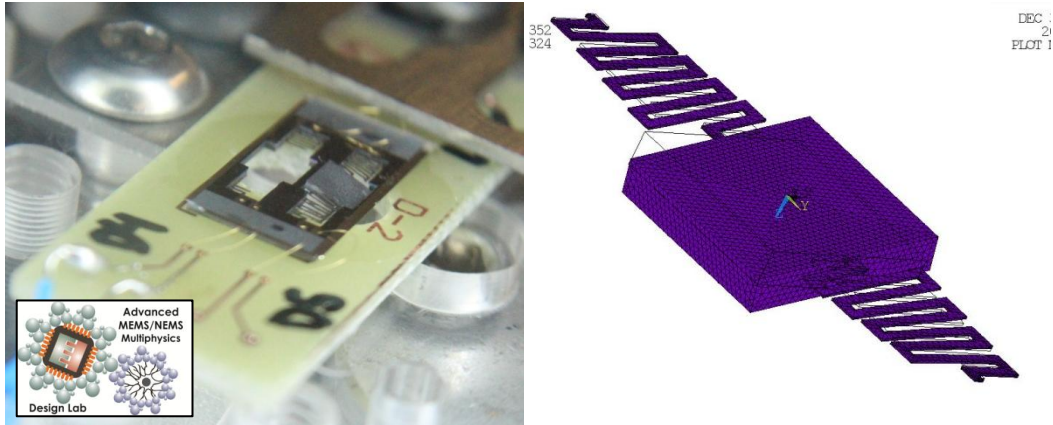
Figure 7.1 – (Left) A fully packaged Class II Design D harvester oscillating at its first mode shape. (Right) The calculated first mode shape for Design D.

From the initial vibrational characterization, the Class II Harvesters exhibited expected mode shapes, as seen from the Design D harvester oscillating at the predicted mode shape at its first natural frequency, as shown in Figure 7.1. This qualitative result validates the simulation of the expected mode shapes.

7.2.2 *Vibration Characterization of Natural Frequency versus Folded Spring Thickness*

To validate the simulation work, the assumptions made in the design of the harvesters, and methodology of applying the folded spring to the energy harvester, the effect of the thickness of the folded springs of the Class II Harvesters was experimentally examined. As discussed in Chapter 2, the folded spring thickness is the most critical design parameter that can be manipulated during microfabrication. The length of the individual beam segments is forced to be constant due to the photolithography masks required for microfabrication. The thickness of the fabricated devices from each wafer was measured by Scanning Electron Microscopy (SEM). The thickness measurements from test structures and harvesters broken through packaging and release processes were used to determine the folded spring thickness expected from each wafer. Examples of the SEM measurements taken can be seen in Figure 7.2.
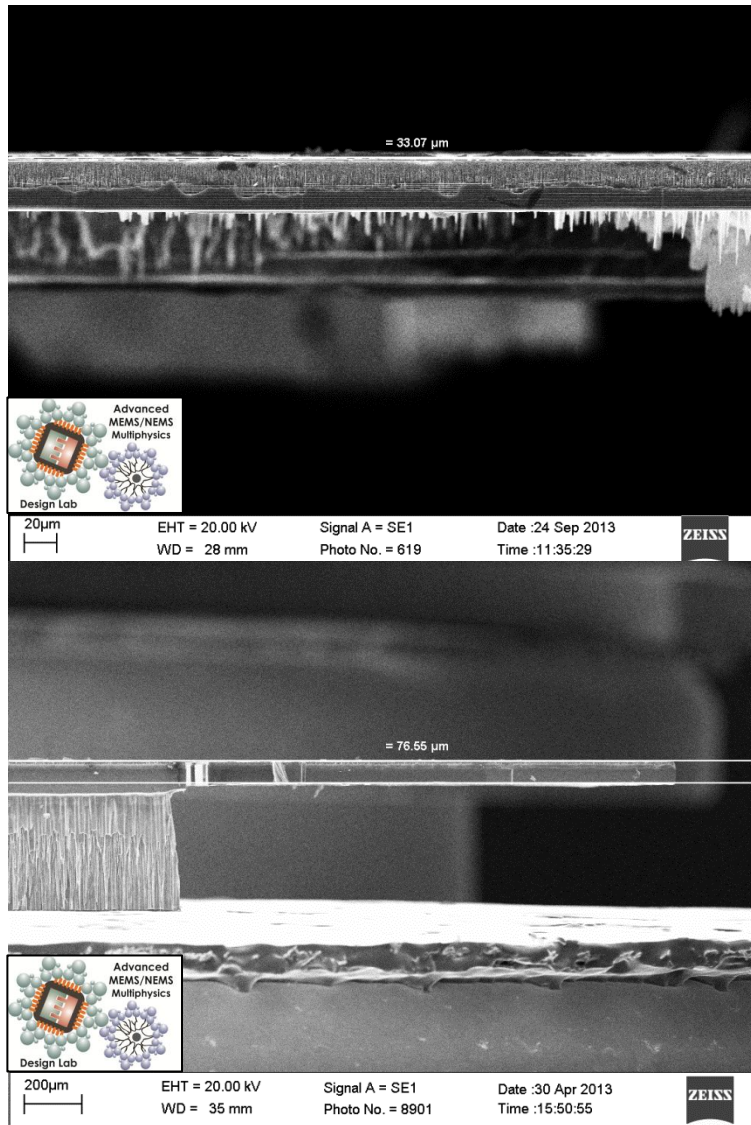
Figure 7.2 – Examples of thickness measurements taken via SEM to determine the thickness of the folded springs of the energy harvester. Measurements from wafers MS2LO2 (top) and MS2P6 (bottom).

The wafers produced in this research had average folded spring thicknesses varying from 19.85 to 118.65 μm, as shown in Table 7.1.

Table 7.1 – Folded spring thickness for each wafer of Class II Harvesters.

Wafer of Class II Harvesters	Average Folded Spring Thickness (µm)	Folded Spring Thickness Standard Deviation (µm)
MS2P1	55.04	3.25
MS2P2	55.04	3.25
MS2P3	25.26	3.27
MS2P4	19.85	4.15
MS2P5	65.68	3.54
MS2P6	76.60	3.48
MS2P7	42.84	3.18
MS2P8	31.69	4.32
MS2P9	39.50	3.78
MS2LO1	118.65	5.45
MS2LO2	38.16	3.65

As discussed in Chapter 4 and Chapter 6, there are many factors that affect the thickness of the folded springs, including the depth of backside etch, the starting thickness of the wafer, and the variation in both the etch and wafer thickness. To gain a firm understanding of the etch rate of the DRIE process to accurately define the spring thickness, the target spring thickness of several of the initial wafers were specifically chosen. With sufficient data, it was possible to determine that the average etch rate for the specific etch process was approximately 1.2211 µm/cycle, allowing for the spring thickness of the remaining wafers to be chosen with some accuracy.

MS2P1 and MS2P2 were etched using the same parameters, one after the other, during the same session on the ICPRIE; therefore they have the same thickness and standard deviation of thicknesses. Additionally, the backside DRIE processing of wafer MS2LO1 failed due to the wafer cracking during a final etch step. This prevented the full etch depth from being reached, resulting in very thick folded springs. These devices did not follow the design intent of thin folded

springs, having aspect ratios of nearly 1:1. Therefore, the natural frequency measurements from that wafer were not included in the following analysis.

The standard deviation of the measured spring thickness appears to be fairly large in comparison to the measured thickness. For example, the standard deviation of 4.15 μm for MS2P4 is large compared the average thickness of 19.85 μm. This is due to the variation of the thickness being directly related to the variability of the etch depth of the process, rather than the remaining thickness. The depth of the etch undertaken on MS2P4 was approximately 480 μm, therefore the standard deviation of 4.15 μm on that value is more reasonable.

The frequency response of the Class II Harvesters was characterized using the LDV and the previously discussed methodology in Chapter 5. In the following figures, the simulated and experimentally measured natural frequencies for a variety of harvester designs will be compared. For each figure, the simulated range of natural frequencies includes an upper and lower bound of natural frequencies based on the variation of proof mass due to wafer thickness variation (510 μm ± 15 μm). The expected natural frequency from the harvester examined should occur within the simulation range created by these bounds. Additionally, it was not possible to directly correlate the natural frequency measured from a specific harvester to its specific folded beam thickness. To directly measure the thickness of the folded spring of the specific harvester, the device would have to be broken to allow for a SEM image to be taken perpendicular to the thickness of the spring. Since this was not feasible, the average and standard deviation of the thickness of the folded springs produced from each wafer, along with the corresponding natural frequency measurements for each design set from a specific wafer, were used to show the most probable region where the measurements would be expected. For the discussions below, this area will be referred to as the "error area" of each design. In cases of only one surviving harvester per design/wafer, a single point with error bars representing the standard deviation of folded spring thickness is shown.

The comparison of the calculated and experimental results for Design A can be seen in Figure 7.3.

Figure 7.3 – Comparison of natural frequency versus folded spring thickness for both simulations and experiments for Design A.

As shown in Figure 7.3, Design A spanned natural frequencies from 277.86 to 2327.20 Hz. The correlation between the experimental and simulated natural frequencies of the Design A harvester agreed well for most of the range of spring thickness examined. The range of experimentally measured points fell within the expected natural frequency range for most of the spring thickness domain. The Design A harvesters from thicker folded spring wafers, such as MS2P6, seemed to have more variability in natural frequency, causing the overall trend of experimental measurements to deviate from the simulated expected range at higher folded spring thickness. Taking into account the increased variability of the results from MS2P6, the correlation of the experimental and simulated results suggest that the simulation and design methodology are validated for this design.

Design B, as shown in Figure 7.4, is of similar scale to Design A, however, utilizes rotated folded springs.

Figure 7.4 - Comparison of natural frequency versus folded spring thickness for both simulations and experiments for Design B.

Design B spanned natural frequencies from 319.63 to 2544.8 Hz. As expected, the design with the rotated folded springs (Design B) was slightly stiffer than the normal orientation folded springs (Design A). The polynomial fit of the experimental measurements follows the same general trend of the simulation. The individual frequency measurements from each wafer are a bit more scattered in proximity to the polynomial fit, producing a lower coefficient of determination. Although the data points are a bit more scattered than in Design A, the all of the error areas from each wafer, except MS2P8, are in close proximity, with some bias offset, to the expected results from simulation. Given the variability of the frequency response results from the polynomial fit, potentially from sources of fabrication-based variation, as discussed in Chapter 6, section 6.3, the general

trend of the polynomial fit suggests agreement between the simulation and experimental results of this design.

The comparison of natural frequency to spring thickness of Design C can be seen in Figure 7.5.

Figure 7.5 - Comparison of natural frequency versus folded spring thickness for both simulations and experiments for Design C.

As shown in Figure 7.5, Design C spanned natural frequencies from 137.29 to 587.25 Hz over the range of tested wafers. It is clear that the larger mass and additional folds applied to Design C, in comparison to Design A, additionally reduced the natural frequency with a small increase in footprint. Only one harvester from MS2P3, with folded spring thickness of 25.26 μm survived packaging and testing. The samples from MS2P4, with beam thicknesses of 19.85 μm, were not mechanically stable for Design C. From Figure 7.5, it can be seen that the clusters of data from each wafer correlate fairly well to the polynomial fit.

Additionally, the polynomial fit follows the same general trend as the simulated response of the design with a bias error. The general trend of the fit, when coupled with the correlation of the data points, suggests that there is a common trend between the experimental and simulated results. The bias offset error of this specific design of harvester is comparatively the largest of all designs.

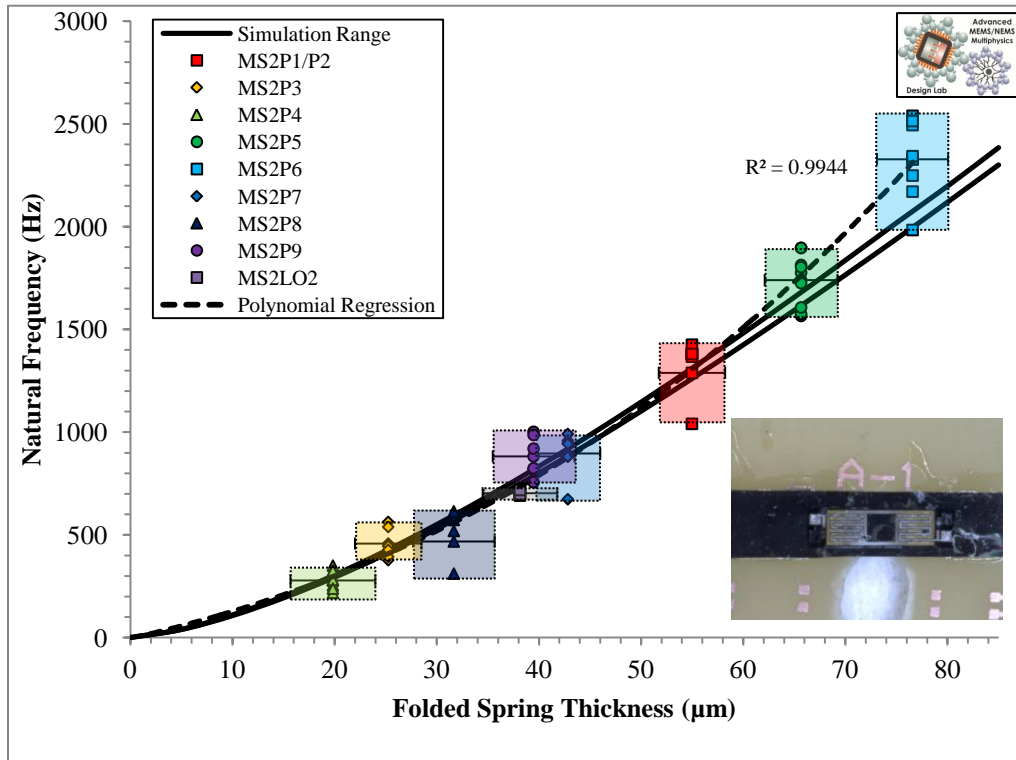The comparison of natural frequency to spring thickness of Design D can be seen in Figure 7.6.

Figure 7.6 - Comparison of natural frequency versus folded spring thickness for both simulations and experiments for Design D.

As shown in Figure 7.6, Design D spanned natural frequencies from 118.13 to 660.47 Hz over the range of tested wafers. It is clear that the larger mass and additional folds applied to Design D, in comparison to Design B, additionally reduced the natural frequency with a small increase in footprint. The samples from MS2P4, with beam thicknesses of 19.85 μm, were not mechanically stable

for Design D. With stiffer rotated folded springs, Design D was capable of producing devices from MS2P3, allowing for the natural frequency span of this design to be slightly larger than Design C. This suggests that the rotated folded springs may allow for a targeted balance between stability and natural frequency reduction. From Figure 7.6, it can be seen that the clusters of data from each wafer correlate fairly well to the polynomial fit. The polynomial fit follows the same general trend as the simulated response of the design with a bias error, as was the case with Design C. The general trend of the fit, when coupled with the correlation of the data points, suggests that there is a common trend between the experimental and simulated results.

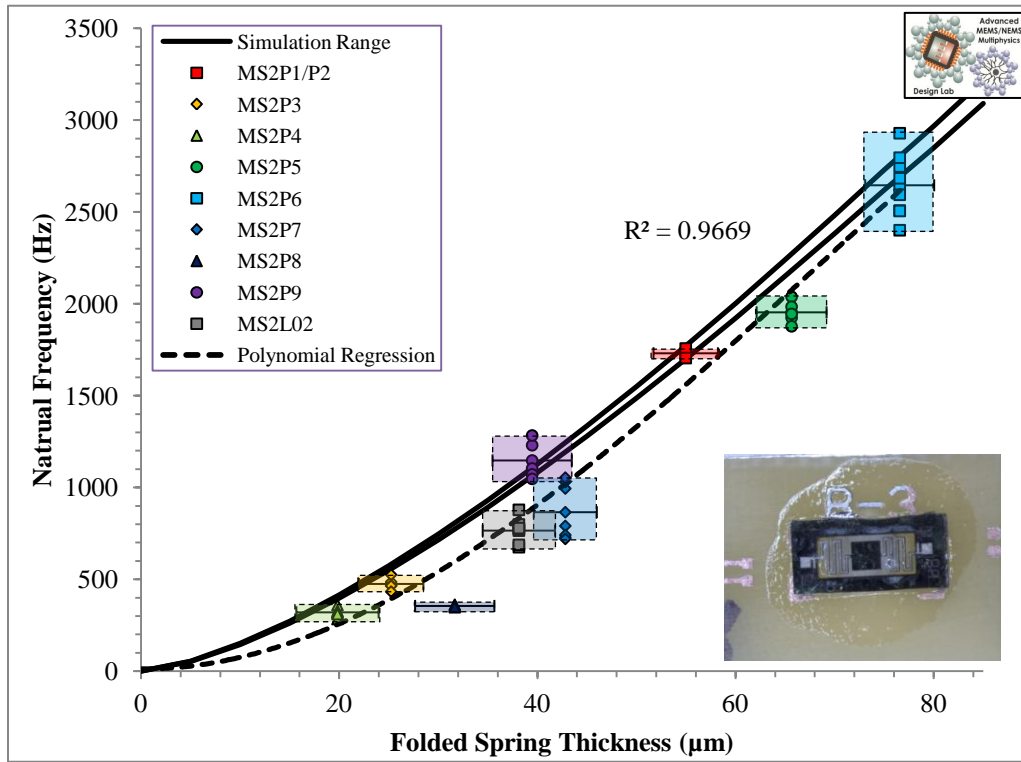The comparison of natural frequency to spring thickness of Design E can be seen in Figure 7.7.

Figure 7.7 - Comparison of natural frequency versus folded spring thickness for both simulations and experiments for Design E.

As shown in Figure 7.7, Design E spanned natural frequencies from 95.00 to 856.63 Hz over the fabricated wafers. Design E further extended Design A by adding an additional mass and spring element in series. The additional folded spring element in series cumulatively added to the effective bending length of the structure, driving the natural frequency range of the design downward significantly. The stability limit due to thickness was not reached with these expanded designs, as was seen with Designs C and D, therefore, it may be possible to further reduce the thickness of the folded springs in these devices to further drive down the natural frequency. The experimental data agreed fairly well with the simulation results. Error areas from all wafers overlapped the simulation range of natural frequencies expected. The polynomial fit had a strong correlation to the experimental data and showed the same general trend as the simulations with a small bias offset. These factors suggest that the simulation and experimental work agree for this design of harvester.

The comparison of natural frequency to spring thickness of Design F can be seen in Figure 7.8.
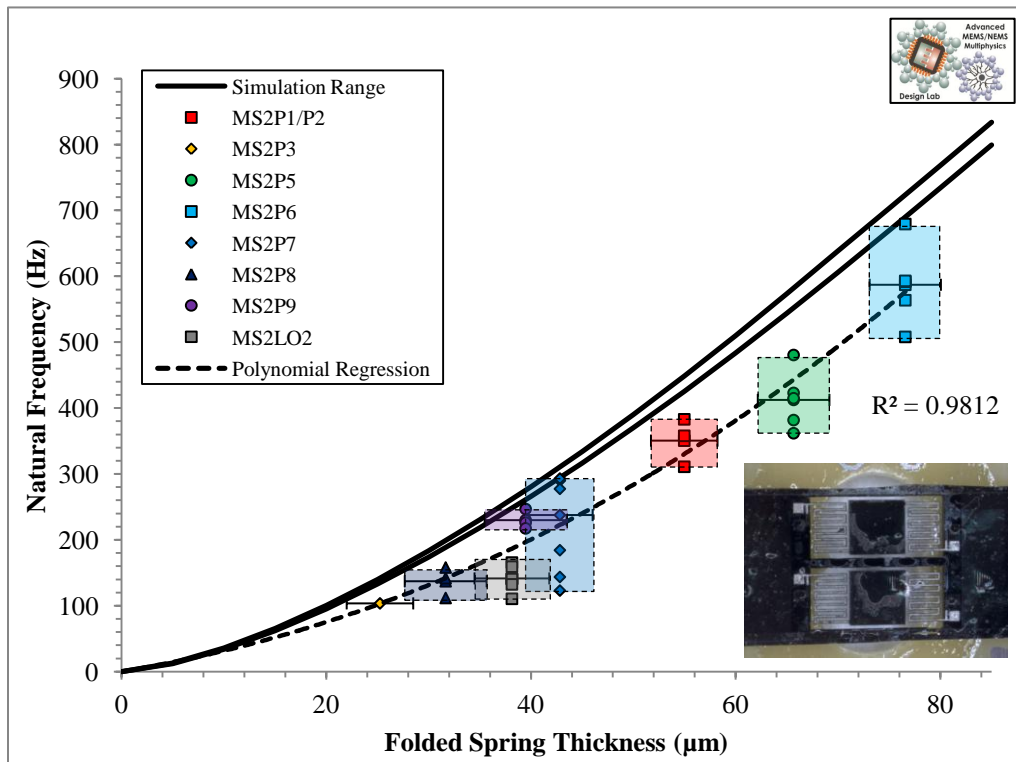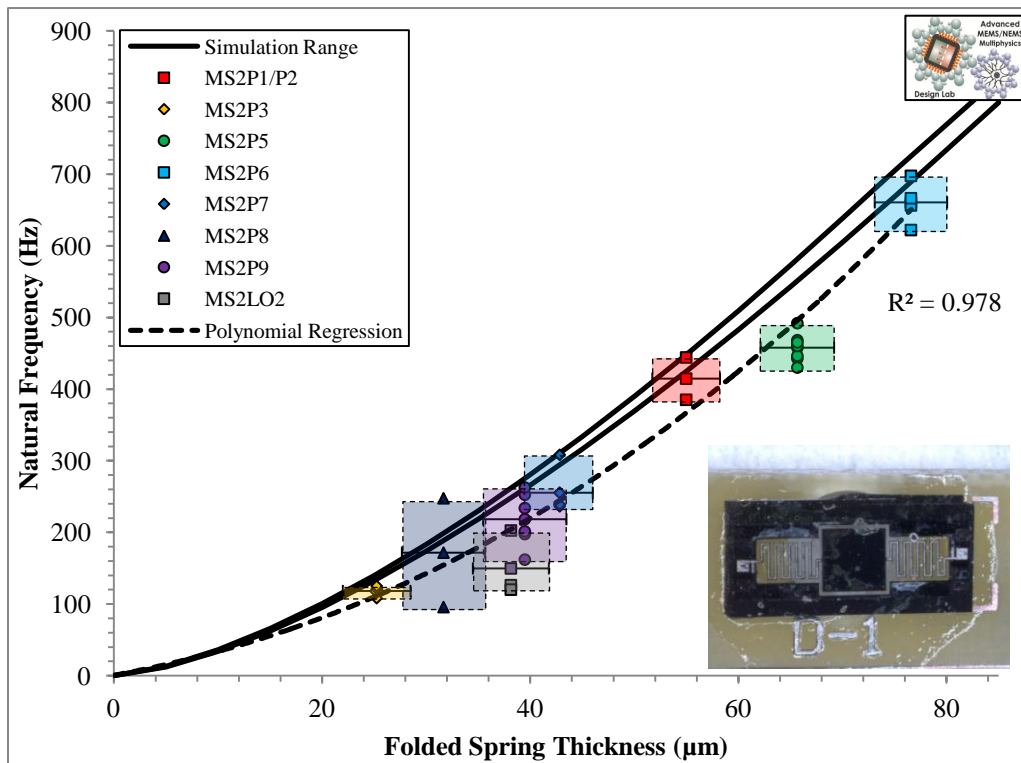
Figure 7.8 - Comparison of natural frequency versus folded spring thickness for both simulations and experiments for Design F.

As shown in Figure 7.8, Design F spanned natural frequencies from 119.58 to 999.27 Hz over the range of folded spring thicknesses produced. This design built upon Design B by adding an additional mass and spring element in series. The additional folded spring element in series cumulatively added to the effective bending length of the structure, driving the natural frequency range of this design downwards significantly. As with Design E, the stability limit due to thickness was not reached with these expanded designs, therefore, it may be possible to further reduce the thickness of the folded springs in these devices to further drive down the natural frequency. Similarly to Design E, there is a strong correlation of the experimental data to the simulated range of natural frequencies expected for all groups of Design F harvesters, except those from MS2LO2. The harvesters from MS2LO2 were the only data group not to have its error area overlap the expected range of natural frequencies. Additionally, the average natural frequency of MS2LO2 deviates the farthest from the polynomial fit used

218

to determine the trend of the experimental data. For all designs tested, MS2LO2 consistently had a lower average natural frequency than the polynomial fit and the simulated range of natural frequency. It is most likely that the starting wafer thickness of MS2LO2 is slightly larger than the other wafers used in this study, and therefore has heavier proof masses, causing the consistent, lower than expected behavior. Taking the behavior of MS2LO2 into account, the strong correlation of both the polynomial fit and the experimental data to the simulated range of expected natural frequencies suggests that the experimental work and simulation agree for this design of harvester.

The comparison of natural frequency to spring thickness of Design G can be seen in Figure 7.9.

Figure 7.9 - Comparison of natural frequency versus folded spring thickness for both simulations and experiments for Design G.

As shown in Figure 7.9, Design G was capable of spanning natural frequencies from 45.21 to 207.88 Hz for the harvesters produced. Design G had the lowest mechanical stiffness of all designs in the study and therefore had the

219

lowest natural frequency range. As with the other less mechanically stiff designs, the maximum frequency reduction was limited by the mechanical stability of the fabricated harvesters. As with Design C, Design G did not have any functioning devices from MS2P3 or MS2P4. This was expected, since the evolution from Design C to Design G was the addition of an additional mass and spring element, thereby producing a heavier and less stiff structure. The data captured from the tested harvesters correlated fairly well with the polynomial fit, however, as with Designs C and D, a bias error occurred. As with the other designs, the harvesters produced with Design G yielded lower natural frequencies than expected by the simulations. Only MS2P7 and MS2P9 had error areas overlapping the simulated expected natural frequency range. All other data points suggested that the simulation predicted too high of a natural frequency. The general trend of the fit, when coupled with the correlation of the data points, suggests that there is a common trend between the experimental and simulated results.

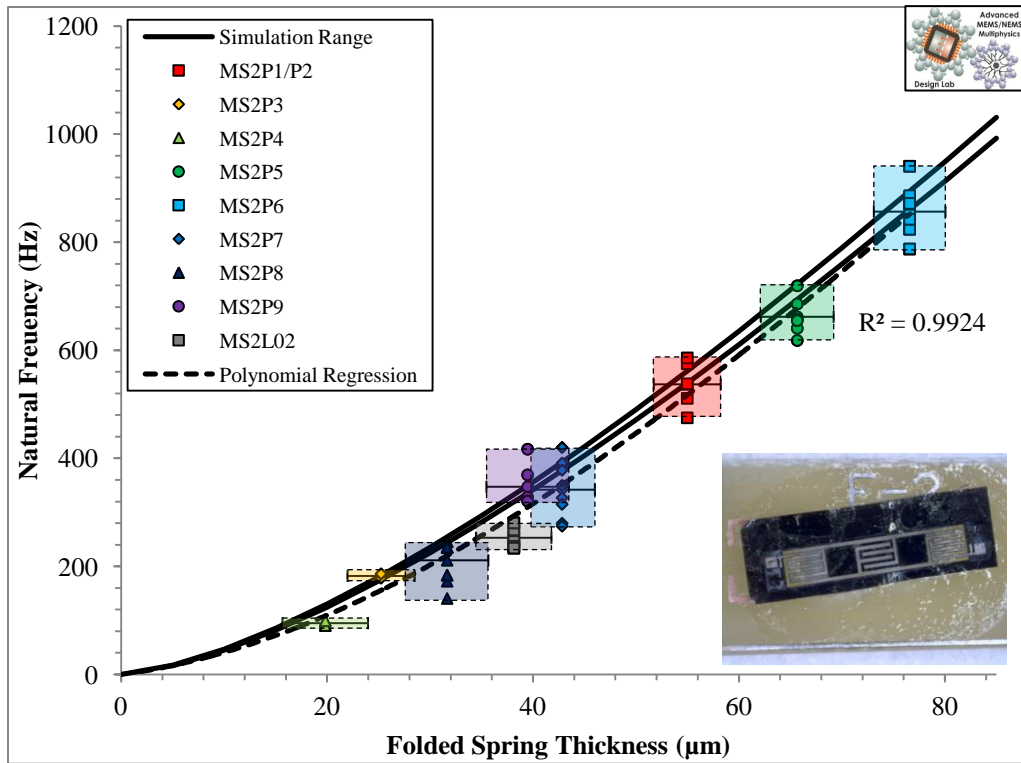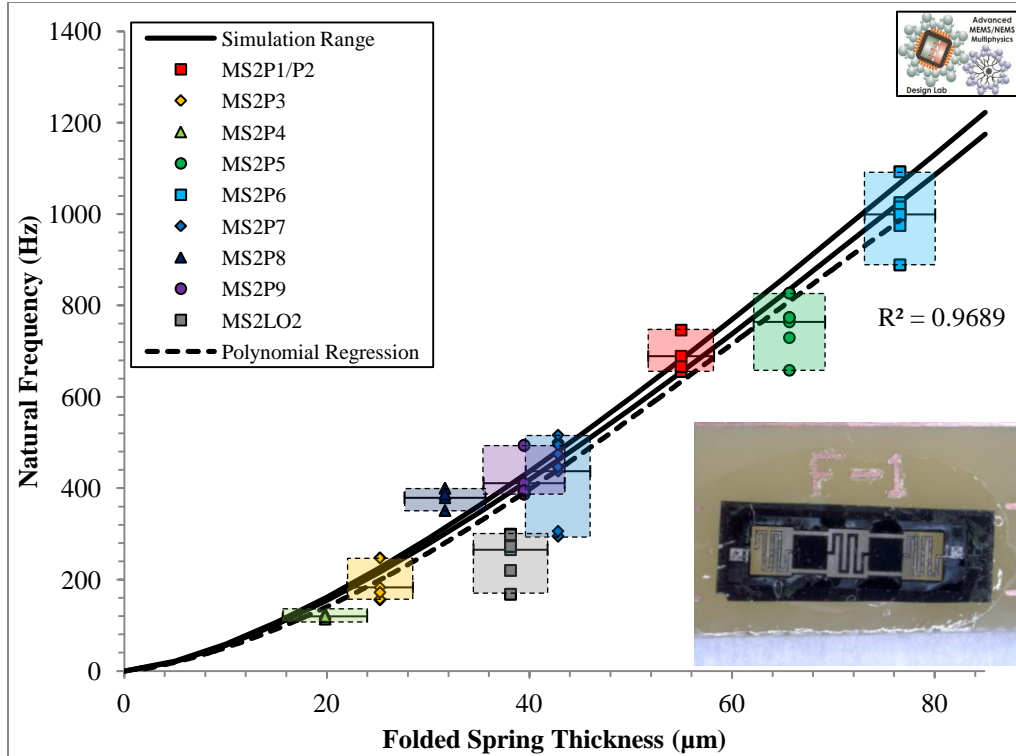The comparison of natural frequency to spring thickness of Design I can be seen in Figure 7.10.

Figure 7.10 - Comparison of natural frequency versus folded spring thickness for both simulations and experiments for Design I.

As shown in Figure 7.10, Design I spanned natural frequencies from 420.47 to 3131.90 Hz for the range of fabricated harvesters. As can be seen in the figure, the experimental data points agree well to the simulated range of expected natural frequencies. The error areas of every design of harvesters overlap the range of expected natural frequencies. Additionally, the polynomial fit of the experimental data agrees well with the simulated range of expected natural frequencies. As previously experienced, the harvesters from MS2P6 had a very large variation in natural frequency measured. As with Design A, this behavior was contained to that specific wafer of devices, therefore, it is most likely an isolated fabrication-based problem. The strong agreement of the data to the simulated range of expected natural frequencies suggests that the simulation work is valid for this design.

The comparison of natural frequency to spring thickness of Design J can be seen in Figure 7.11.

Figure 7.11 - Comparison of natural frequency versus folded spring thickness for both simulations and experiments for Design J.

As shown in Figure 7.11, Design J spanned natural frequencies from 336.04 to 3667.20 Hz for the folded spring thicknesses of harvesters fabricated. Design I and Design J were parallel configurations of springs and a single mass that produced a large, mechanically stable, range of natural frequencies over the range of achieved thicknesses. As expected, the rotational folded spring orientation in Design J was slightly more mechanically stiff, resulting in higher comparative natural frequencies. As seen in the Figure 7.11, the experimental data and the simulated range of expected natural frequencies correlate, with error areas overlapping the simulation range. However, the polynomial fit of the data suggests that a bias error exists between the experimental data and the simulation, with the simulation overestimating the experimental natural frequency. The

general trend of the fit, when coupled with the correlation of the data points, suggests that there is a common trend between the experimental and simulated results.

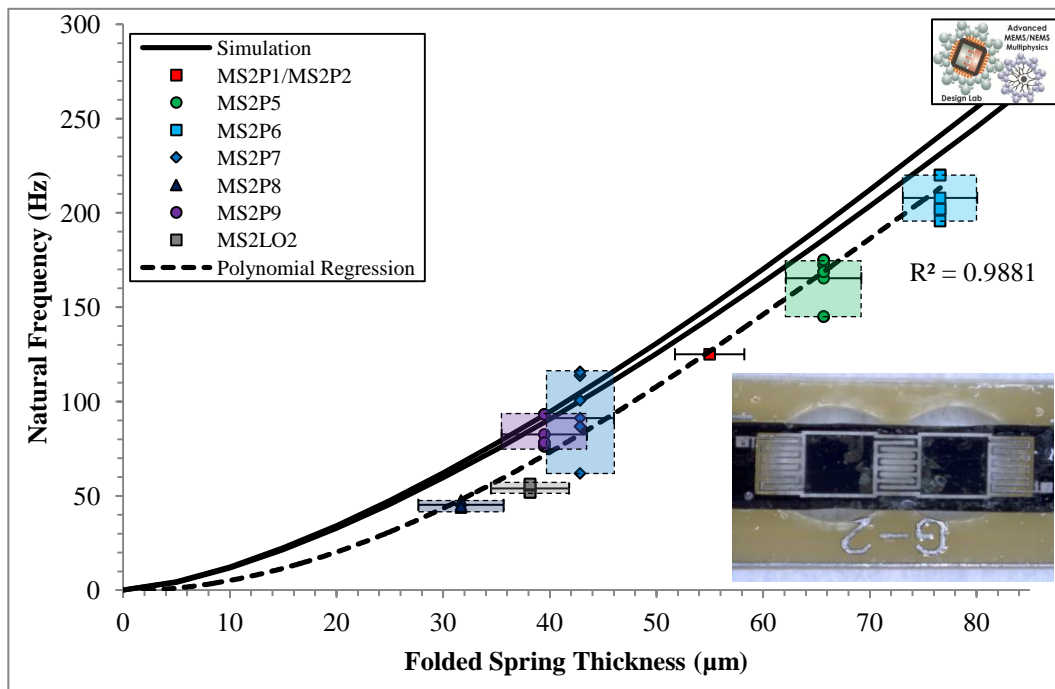The comparison of natural frequency to spring thickness of Design K can be seen in Figure 7.12.

Figure 7.12 - Comparison of natural frequency versus folded spring thickness for both simulations and experiments for Design K.

As shown in Figure 7.12, Design K spanned natural frequencies from 80.63 to 832.50 Hz for the harvesters tested in this study. This design scaled up Design I by adding additional mass volume and folds to the folded springs. This drove down the natural frequency range in comparison to the smaller footprint design. The experimental data has some correlation to the simulated range of natural frequency, with overlapping error areas for most of the wafers tested. As with other designs, the harvesters from MS2P6 have a large variability in natural

frequency. The high variability in the harvesters produced from MS2P6 is confined to that wafer of devices. Additionally, this variability causes the polynomial fit of the data to be somewhat distorted at near the MS2P6 data set. At lower thicknesses, it can be seen that the polynomial fit of the data exhibits a bias offset to the simulated range of natural frequencies. Although the error areas of many of the sets of harvesters correlate to the expected natural frequency range from simulation, the bias error in the experimental trend suggests a correlation in experimental and simulated trends only.

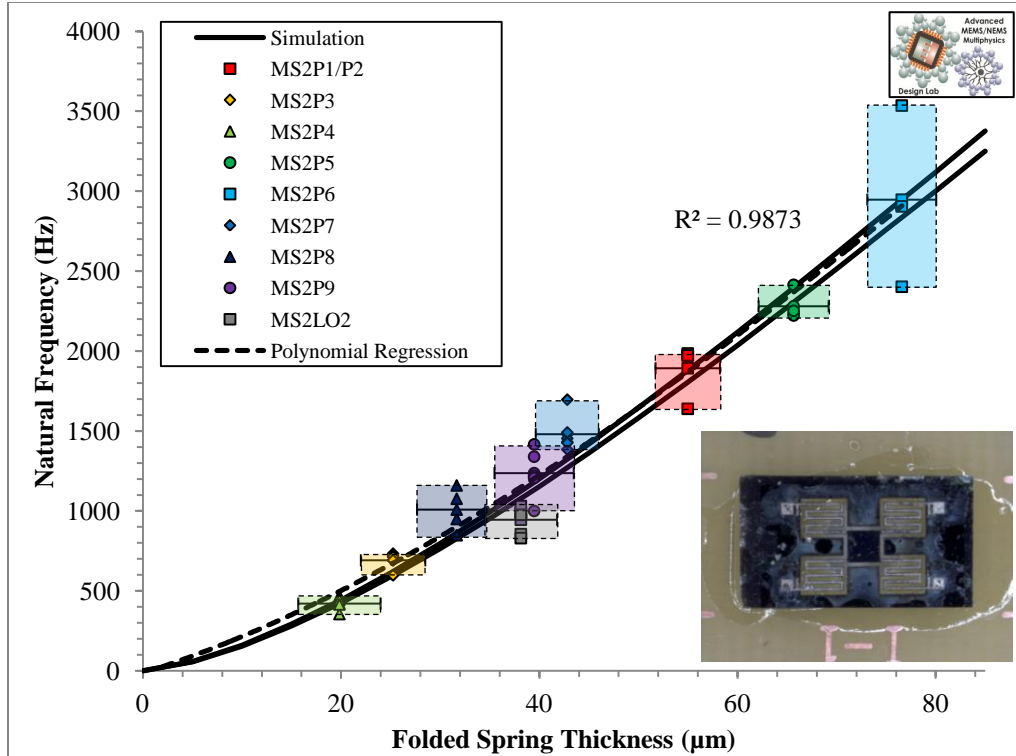The comparison of natural frequency to spring thickness of Design L can be seen in Figure 7.13.
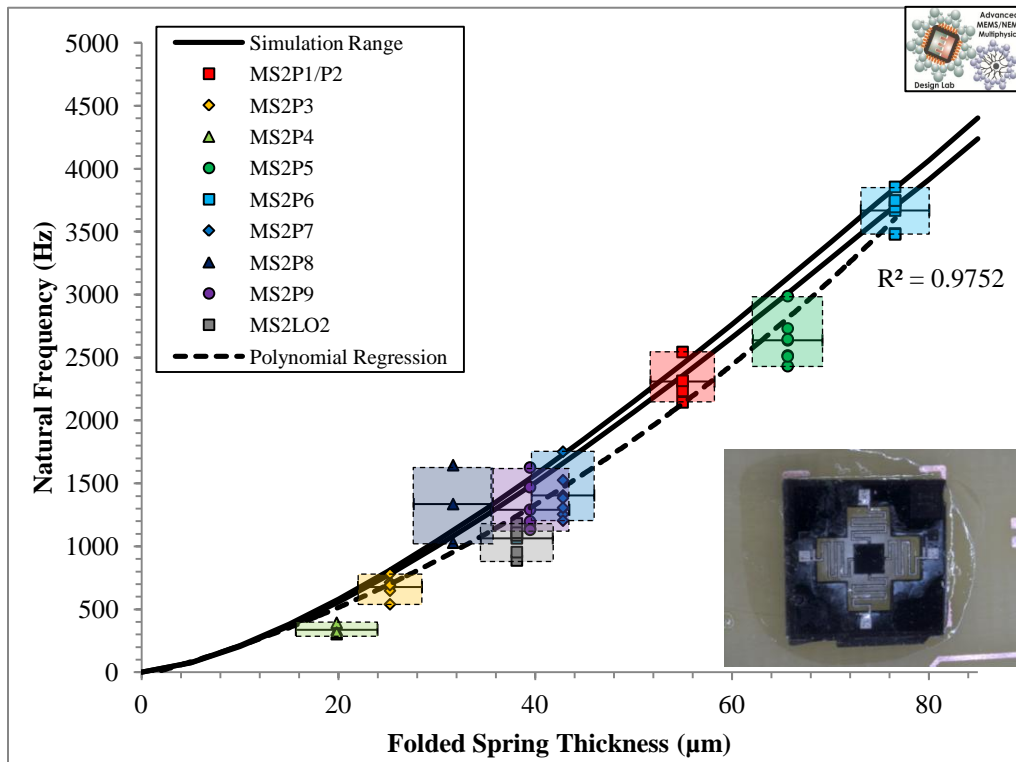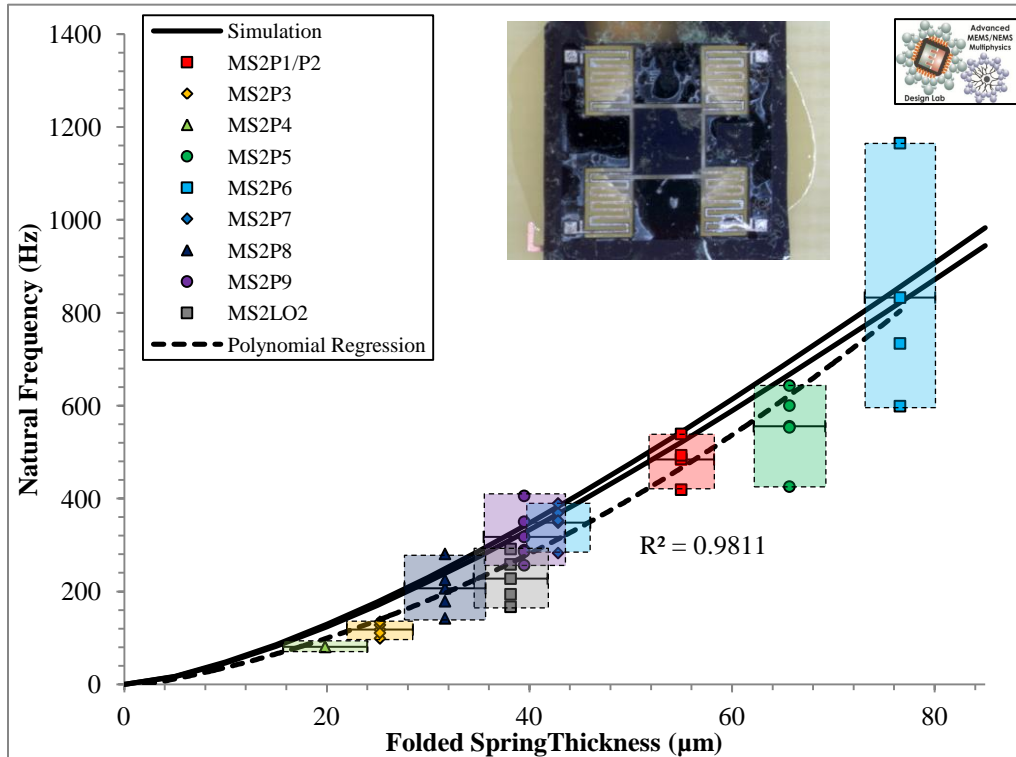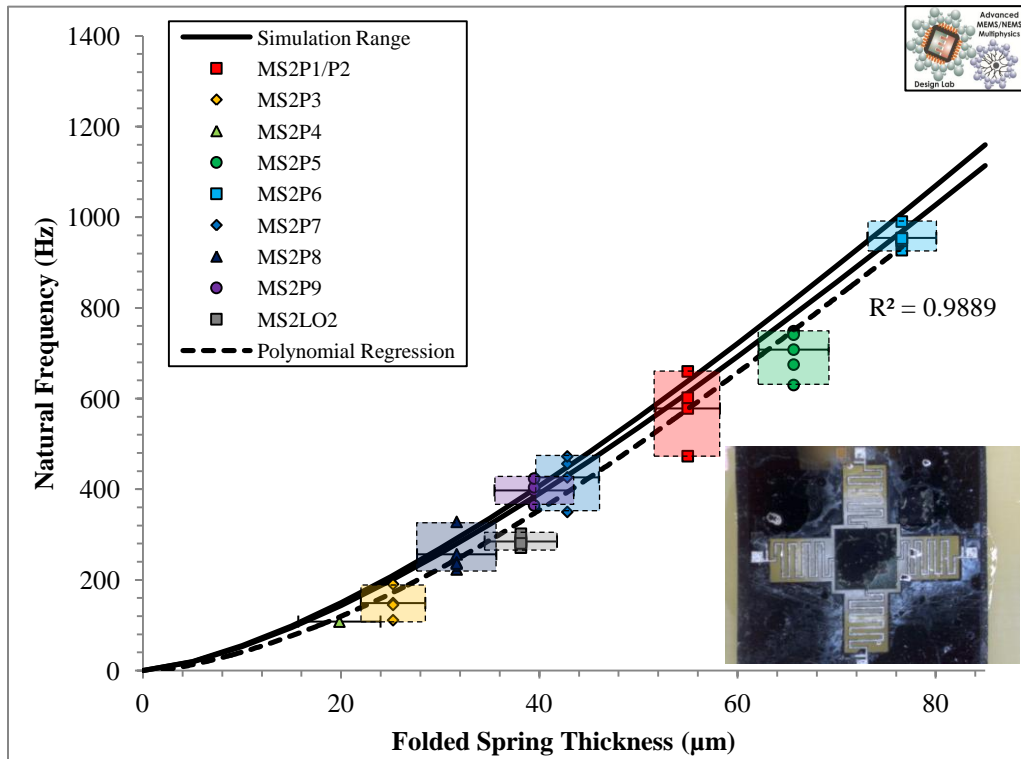

Figure 7.13 - Comparison of natural frequency versus folded spring thickness for both simulations and experiments for Design L.

As shown in Figure 13, Design L spanned natural frequencies from 108.13 to 954.50 Hz for the range of harvesters produced. These designs scaled up Design J by adding additional mass volume and folds to the folded springs. This

drove down the natural frequency range in comparison to the smaller footprint design. The experimental data points correlate with the simulation range, with overlapping error areas with all designs of harvester, except MS2LO2. As with other designs, MS2LO2 has a lower average natural frequency than both the polynomial fit and the simulated range of natural frequency. The polynomial fit correlates well with the experimental data, however, has a bias offset to the simulated data. Although the experimental data points correlate to the expected simulation range, the bias error suggests a similar trend only.

The bias error between the simulated and measured natural frequencies encountered over the various designs of harvesters was not contained to a specific subset of designs - it occurred, to some degree with every design. It was more prevalent with Designs C, D, G, J, K, and L; therefore, it cannot be linked to a specific spring orientation or arrangement of harvester. Nor can it be linked to a specific general size of harvester – Design J is comparatively small to some of the designs affected. According to Dixit *et. al.* [1], the local etch rate of a DRIE process is dependent on the available surface area. Areas of larger open surface area will etch faster than smaller open surface areas. Designs C, D, G, J, K, and L have the largest open surface area backside wells of all the designs produced in this study. This suggests that these devices will be comparatively thinner than the average thickness measured from the devices on the same wafer. This overestimation of the true thickness of the harvesters for this design would cause the bias error seen in the comparisons. Therefore, the designs affected by the area-dependant etch variation, having suitable experimental trend behavior matching the simulation trends with a bias offset also verify the simulation and design work.

The correlation of the simulation and experimental results suggests that the effect of the microfabrication residual stresses on the stiffness of the harvesters was small and that the linear approximation of the folded spring stiffness made in Chapter 3 by equation (9) is valid. This will allow for certainty in matching the frequency and input impedance/load resistance requirements of

specific applications, moving forward with new designs and optimization of these more complex systems.

In general, it was seen that the normal orientation folded springs are less mechanically stiff than the rotated folded springs. The proof mass placement in the studied designs suits normal orientation springs, since a higher degree of bending can be applied to the individual beam elements with the same loading. It was found that the arrangement of the centrally aligned rotated folded springs and masses did not allow for a significant amount of rotation of the proof mass, causing a lower degree of bending to be applied to the individual beam elements in the rotated folded springs. The bending could be enhanced for the rotated folded springs by offsetting the centroid of the proof masses from the midline of the folded springs.

As expected, the designs with the four-fold springs had much lower natural frequencies, than the two-fold systems. This was due to the larger effective length of the beam. The series systems have much lower natural frequencies the parallel systems, however, tend to be more fragile. The additional effective beam length that can be accomplished through series systems is limited by mechanical stability of the harvester design. Beyond manipulating the design and creating a new mask set, manipulating the thickness of these devices will have the greatest impact on their natural frequency. Both the footprint and device thickness can be chosen to optimize the mechanical performance of the harvester to a specific target application. If there are few constraints on the footprint of the intended harvester, a series-based harvester utilizing more than one mass (Designs E, F, and G) could be used to fill this role with a large device thickness. This would allow the device to be actuated at the appropriate frequency, while being mechanically robust and reliable. An example of this type of methodology in this work would be Design G, where the footprint of the overall device is large; however, it is able to achieve significantly lower natural frequencies while at relatively higher thicknesses. If the available footprint of the harvester is limited, then the overall thickness of the device would need to be reduced to allow

sufficient frequency reduction. In this case, either a single mass series-based design (Designs A, B, C, or D) or a parallel-based system (Designs J-L) would be the most appropriate. The thinning of the devices for these designs has less of an adverse effect on the mechanical robustness of these harvesters, allowing for target natural frequencies to be achieved in a smaller footprint.

As can be seen from Figures 7.3-7.13, the achievable natural frequency range of each design of the harvester was highly dependent on the folded spring thickness. The entire design space of the Class II Harvesters was able to cover a wide range of operational frequencies, from 45.21 Hz with Design G of MS2P8 to 3667.20 Hz with Design J of MS2P6, using the same mask set by simply varying the device thickness. When the entire design space is compared with the target natural frequency range of 30-300 Hz to harvest low frequency vibration, it was found, as seen in Figure 7.14, that most of the designs were capable of satisfying this requirement.
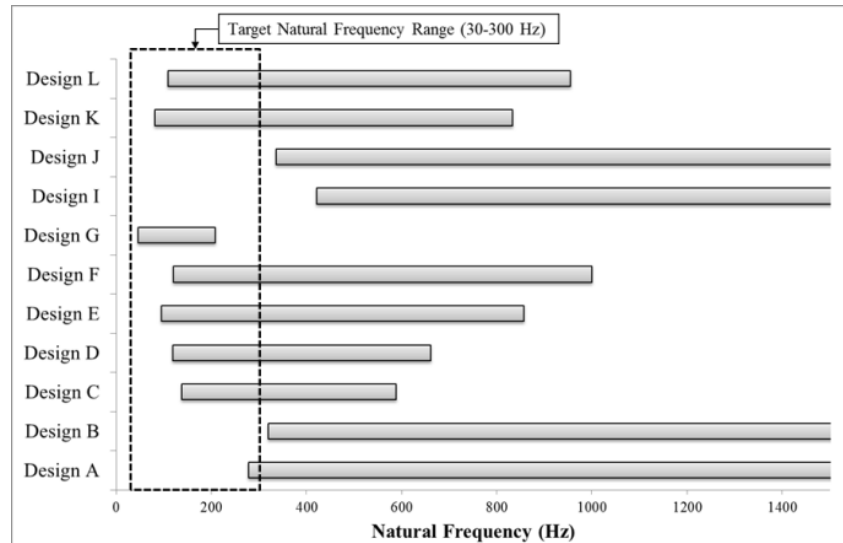
Figure 7.14 - Natural frequency ranges of all designs compared to the target frequency range of 30-300 Hz. All designs except Designs B, I, and J are capable of meeting this requirement in this work.

227

As seen in Figure 7.14, the only designs that were not capable of meeting the goal natural frequency range are Designs B, I, and J. Design A was only partially capable of meeting the 300 Hz requirement, while the rest of the designs were capable of meeting the majority of the target frequency range. These designs would be able to meet this target frequency range easily at a reduced spring thickness. This further suggests that the examined designs of folded spring harvesters are capable of harvesting low frequency vibrations.

The range of natural frequencies that can be achieved by these designs are very large, therefore a variety of device thickness, natural frequency, and design combinations can be used to accommodate various vibration conditions and size constraints.

7.3   Electrical Results

The first step of the electrical characterization of the Class II Harvesters was testing the harvesters for short circuits and measuring the capacitance of the energy harvesters. The capacitance of each harvester element was based upon the active surface area of the PZT layer, the thickness of the PZT layer, and the thickness-dependant dielectric properties of the PZT material used [2]. Four harvester element footprints were used throughout the eleven designs; therefore, similar capacitances will occur across different designs of the harvester, given a consistent PZT thickness, as shown in Table 7.2.

Table 7.2 - Summary of measured capacitances for each design of Class II Harvesters for a PZT thickness of 0.24 μm

Design	Average Capacitance (nF)	Standard Deviation (nF)
A/E/I	14.825	0.78876
B/F/J	14	0.640312
C/G/K	19.88	1.298846
D/L	18.2	1.284523

To ensure that the harvester is converting vibration to electricity, the input impedance of each harvester was calculated using the capacitance measurement

taken at rest and the natural/operational frequency of each harvester. This calculated input impedance was then compared with the optimum load resistance attained in later measurements.

The electrically operational harvesters were tested in detail to verify vibration-to-electricity conversion. As discussed in the testing methodology in Chapter 5, the devices were actuated in the linear regime by a low amplitude vibration at their natural frequency to optimize power output. The load resistance and sinusoidal vibration amplitude applied to the harvester were varied to determine the optimum load resistance for maximum power transfer. The typical electrical behavior of the harvesters in response to a varying load resistance can be seen in Figures 7.15-7.18.
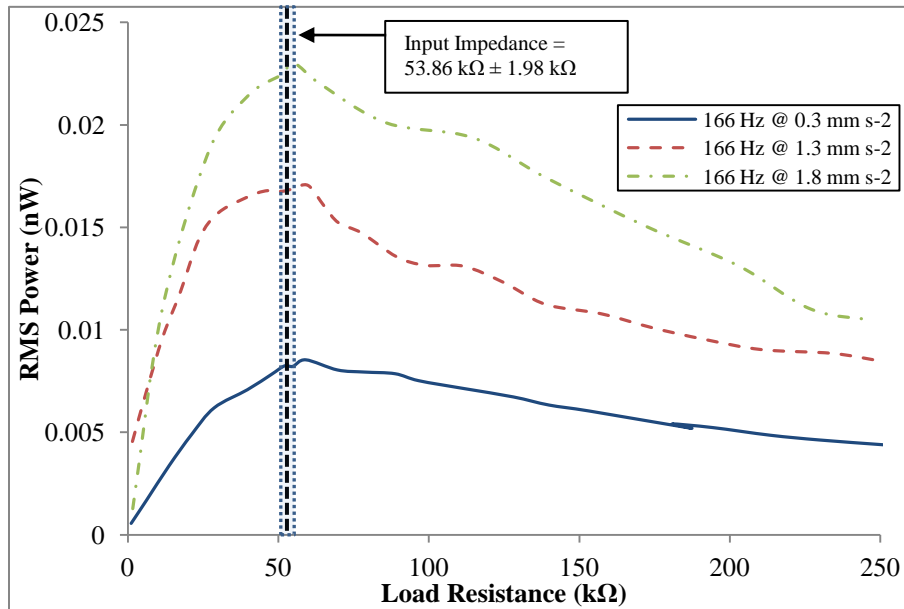
Figure 7.15 – Root Mean Squared (RMS) power measured over a known load resistance for Device C1 (MS2L02) for varying sinusoidal accelerations applied at the measured natural frequency. The input impedance is noted in the figure.
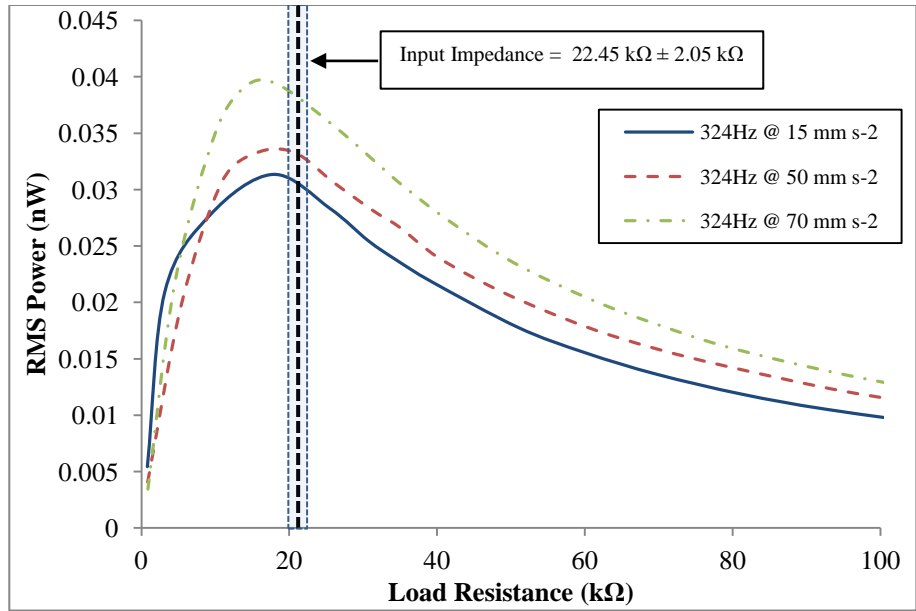
Figure 7.16 - Root Mean Squared (RMS) power measured over a known load resistance for Device L1 (MS2L02) for varying sinusoidal accelerations applied at the measured natural frequency. The input impedance is noted in the figure.
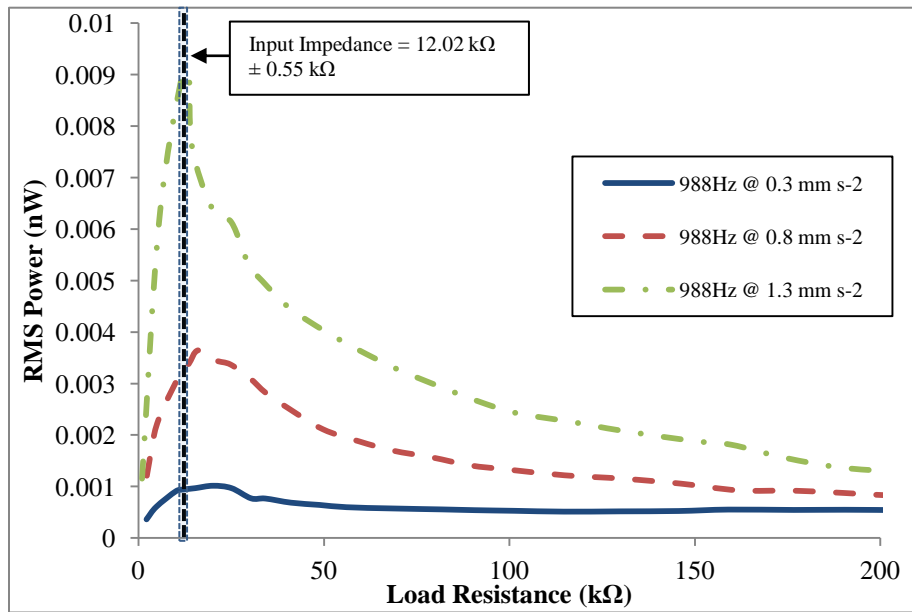
Figure 7.17 - Root Mean Squared (RMS) power measured over a known load resistance for Device I2 (MS2L02) for varying sinusoidal accelerations applied at the measured natural frequency. The input impedance is noted in the figure.
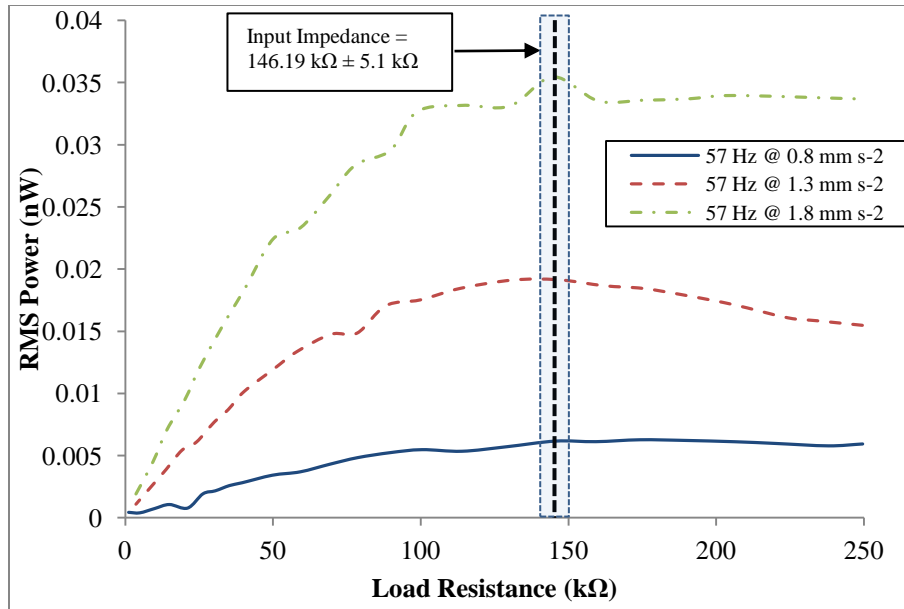
Figure 7.18 - Root Mean Squared (RMS) power measured over a known load resistance for Device K2 (MS2L02). The input impedance is noted in the figure. Device K2 had a lower than expected natural frequency due to a broken folded spring.

By measuring the root mean squared voltage across the load resistance, it was possible to capture the root mean squared power output the harvester produced as the load resistance was varied, as seen in Figures 7.15 to 7.18. As expected, for the four example harvesters examined above, the optimum load resistance for maximum power output was consistent for each individual harvester as the applied acceleration was increased. In the experiments, the input vibrations applied to the harvesters were specifically chosen to be very low, in the "sub-g" range, from 0.3-70 mm/s^2 to ensure that the operation of the harvester stays within the quasi-linear range. If the harvester behaved non-linearly, the input impedance of the harvester would have matched the natural frequency shift due to the non-linear stiffening of the harvester. The amplitude stiffening would have caused the natural frequency of the harvester to increase; therefore the peaks of the Figures 7.15-7.18 would have not been nested, and would have tended forward to higher optimum load resistance as the amplitude of the input vibration increased.

231

Additionally, as expected, the output power increased as the acceleration applied to the harvester was increased.

When the optimum load resistances were compared to the input impedance calculated from the capacitance measurements in previous testing, it was seen that the input impedances and optimum load resistances were well correlated. The input impedance and optimum load resistance, as shown in Figures 7.15 to 7.18 coincided at 53.86 kΩ for Device C1, 22.45 kΩ for Device L1, 12.02 kΩ for Device I2, and 146.19 kΩ for Device K2 This correlation of the input impedance the energy harvester and the optimum load resistance of the conditioning circuit suggests that the harvesters are converting vibration to electricity in a predictable manner as designed.

Once it was confirmed that the harvesters were operating correctly, the input acceleration near resonance was increased significantly up to 9.81 m/s^2. Measurements were then taken using the appropriate optimum load resistance to determine a maximum power transfer possible from the harvesters. For this experiment, a sinusoidal acceleration was applied to the harvester at a suitably chosen acceleration for the harvester design. Figure 7.19 shows common examples of the output waveform:
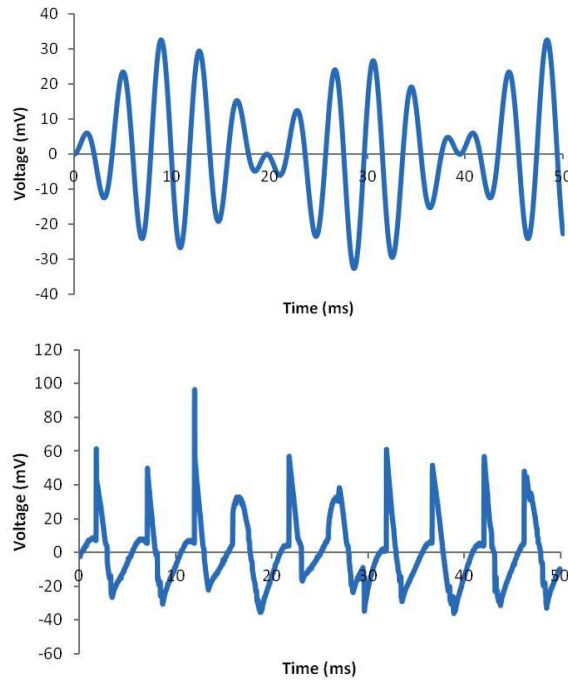
Figure 7.19 - Common Output Waveforms, (Top) Amplitude Modulated Output,
(Bottom) Sawtooth-like Voltage Output

In Figure 7.19, it can be seen that external electrical factors are important in the measurement of the output signal. The top of Figure 7.19 shows an amplitude modulated signal, suggesting that the oscilloscope used in measurement may have been loading the harvester. Additionally, the bottom of Figure 7.19 shows that there may have been some capacitive influence on the output of the harvester, creating the spikes shown.

A sample of power output measurements for single harvesting elements of each harvester (each folded spring is a separate harvesting element) are summarized in Table 7.3, showing the natural frequency at which the harvester was excited, the input impedance, the measured RMS voltage across the load resistance, and the calculated RMS current and RMS power produced by the harvester.

Table 7.3 - Summary of measured RMS voltages, calculated RMS current and calculated RMS power for single harvesting elements of sample energy harvesters with PZT layer thickness of 0.24μm.

Wafer	Device	Natural Frequency (Hz)	Input Impedance (Ω)	RMS Voltage (mV)	RMS Current (μA)	RMS Power (nW)
MS2P9	F4	395.00	28780.28	62.0	2.15	135.79
MS2P9	C2	226.25	35384.67	153.0	4.32	690.50
MS2P9	C3	217.50	36808.19	82.5	2.24	186.44
MS2P9	B1	1229.40	9246.95	52.5	5.68	309.99
MS2P9	B2	1103.20	10304.76	48.5	4.71	233.73
MS2P8	A9	311.25	34491.82	38.5	1.12	45.07
MS2P8	C4	111.88	71556.86	82.5	1.15	95.90

As seen in Table 7.3, the harvesters are able to produce a reasonable power output near resonance. The best power output achieved in this study was with Device C2 from wafer MS2P9. This device was capable of producing approximately 690.50 nW of power at a RMS voltage of 153.0 mV and RMS current of 4.32 μA across the optimum load resistance, while operating at its natural frequency of 226.25 Hz at a 9.81 m/s^2 acceleration. Although this power output is not as high as some comparable devices in literature, the power output for the thickness of PZT film used in these harvesters (0.24 μm) was reasonable, producing a comparable energy density of approximately 54 μW/cm^2. There were some titanium-based adhesion challenges encountered were encountered in producing PZT films thicker than 0.24 μm, which necessitated the use of a titanium tungsten adhesion film. PZT films as thick as 0.96 μm have been produced in microfabrication tests, however, have not yet been applied to the folded spring harvesters. The increased PZT thickness will result in an increase of power output, according to equation (1) of Chapter 3. Taking into account the effect of the increased PZT thickness, the resulting power output can be estimated. Based on the result in table 7.3, if Device C2 had a PZT thickness of 0.96 μm, its natural frequency would remain unchanged, the input impedance would increase to 100.85 kΩ, the output RMS voltage would increase to 527.77 mV, the output RMS current would increase to 5.23 μA, and the output power would increase to 2.76 μW. As can be seen by this estimation, the increase in

output voltage far outweighs the increase in output current for the increase in PZT thickness. This is due to the increase in input impedance due to the change in relative permittivity in response to the PZT thickness. In addition, as discussed in Chapter 5, by electrically arraying the harvesting elements of the Class II Harvester designs, it will be possible to additionally increase the overall power output of the harvester.

7.4   Summary

The full characterization of the Class II Harvesters yielded several important results. First, the released Class II Harvesters did not exhibit any symptoms of fabrication-based residual stress stiffening, such as beam curling, mass rotation, or distortion of the harvester design at rest, confirming the residual stress relaxation of the folded spring-based design.

As it was seen in this chapter, the numerical studies used to predict the behavior of the harvesters were validated by the vibration-based characterization over a wide range of spring thickness for each design. The calculated mode shapes were qualitatively verified by the initial vibrational characterization. The trends experimental natural frequency data from the entire range of folded spring thicknesses followed the simulated range of expected natural frequencies well. In several designs of harvester, an open etch area-based etch rate deviation caused for some variation in fabricated thickness from design to design on the same wafer. This bias error caused the experimental trend to be offset from the simulated natural frequency/folded spring thickness trends. This variation was not tied to a specific design of harvester, however the open etch area used to define the depth of etch from the backside of the wafer. This effect was seen especially in Designs C, D, G, J, K, and L having the largest open surface area backside wells. Taking this variation into account, it can be seen that the simulation, given the proper folded spring thickness, is capable of predicting the behavior and natural frequency of the folded spring energy harvester. The frequency-based

simulation undertaken to understand and predict the frequency behavior of the folded spring energy harvesters is valid.

With stiffer rotated folded springs, Design D was capable of producing devices from MS2P3, allowing for the natural frequency span of this design to be slightly larger than Design C. This suggests that the rotated folded springs may allow for a targeted balance between stability and natural frequency reduction. The validation of the simulated results suggests that the assumptions made about the behavior of the folded spring structure of these energy harvesters are valid as well.

The majority of Class II Harvesters were capable of reaching the natural frequency goal of 30-300 Hz. Designs B, I, and J. Design A were only partially capable of meeting the 300 Hz requirement. However, these designs do not reach a critical thickness where the harvester becomes unstable, therefore, these designs would be able to meet this target frequency range easily at a reduced spring thickness.

It was shown that the harvesters are capable of converting the vibration applied to the harvester into electricity. By matching input impedance of the harvester at rest and optimum load resistance under an acceleration load, it is clear that the harvester is converting strain to electricity. The maximum power output achieved was approximately 690.50 nW of power at a RMS voltage of 153.0 mV and RMS current of 4.32 μA, while operating at its natural frequency of 226.25 Hz at a 9.81 m/s^2 acceleration. With increased PZT thickness, the power generated from each individual harvesting element will be increased. It is expected that with increased PZT thickness and arranging the individual harvesting elements in an array to maximize the power output, that the overall power output of the harvesters examined in this thesis will increase to levels suitable for *in-situ* harvesting applications.

7.5   References

[1]   P. Dixit and J. Miao, "Effect of SF 6 flow rate on the etched surface profile and bottom grass formation in deep reactive ion etching process," *Journal of Physics: Conference Series,* vol. 34, p. 577, 2006.

[2]   B. Marinkovic, T. Kaya, and H. Koser, "Characterization of ferroelectric material properties of multifunctional lead zirconate titanate for energy harvesting sensor nodes," *Journal of Applied Physics,* vol. 109, pp. -.

8.1   Conclusions

In this thesis, a folded spring-based piezoelectric energy harvester was presented as an alternative to the traditional cantilever-based configuration of piezoelectric harvesters to reduce the natural/operational frequency for low frequency applications.

Piezoelectric energy harvesting is a very flexible and robust method of generating electricity on a micro-scale. Devices centered on piezoelectric generation are highly customizable, and can be designed for many applications. The majority of the research into piezoelectric energy harvesters centers on optimizing the performance of the generator through manipulation of the frequency spectrum of the device. The research presented in this thesis focused on the further natural frequency reduction of the harvester by reducing the mechanical stiffness of the energy harvester. A fixed-fixed folded spring was postulated as an alternative structural element for vibration-based piezoelectric energy harvesting to achieve the desired natural frequency reduction.

A design methodology was developed in order to apply the fixed-fixed folded spring structural element to the piezoelectric harvester. The folded spring structure allows for the increase of effective length of the beam, while reducing the detrimental stiffening effects of microfabrication-based residual stresses. The folded spring structure was parametrically analyzed, showing that the length of the beam segments in the fold and the thickness of the folded spring are the most critical parameters in the mechanical stiffness of the structure. To test these hypotheses, two classes of harvesters were designed. The Class I Harvesters, consisting of a single fixed-fixed folded spring, were designed with natural frequencies ranging from 512-995 Hz, to allow for initial characterization and development of microfabrication processes. The primary goals of the Class I

Harvesters were to develop the required microfabrication process flow to fabricate PZT-based harvesters and an initial characterization of the folded spring methodology. Through the characterization of the Class I Harvesters, the design methodology was evolved to include arrays of folded spring harvesters and proof masses. The Class II Harvesters vary the number of folds in the spring, the orientation of the spring elements, the arrangements of springs and masses, and the thickness of the folded springs to broaden the design space for a wider range of natural frequencies. The Class II Harvesters were numerically examined in detail to determine the expected behavior of each design of harvester to the test loading that will be used in vibration-based characterization.

To experimentally characterize the energy harvesters, a microfabrication process flow was developed capable of producing any design of piezoelectric harvester using the same materials and cross section. The microfabrication process flow discussed in this thesis is capable of producing any design of piezoelectric harvester using a typical cross sectional arrangement required by PZT. In order to facilitate the microfabrication of the harvesters, multiple microfabrication processes were developed. An Aqua Regia Etch System was developed in order facilitate patterning of the required lower platinum and titanium electrodes in a controlled manner. Additionally, multiple methods of deposition and patterning of the PZT film were developed. Two different PZT materials were deposited by the sol-gel process. The first material required a simultaneous deposition and lift-off to pattern the PZT film. The second material was not suitable for lift-off, therefore, a wet etch was adapted to allow for accurate patterning of the PZT. The most successful arrangement of microfabrication processes was capable of producing PZT-based harvesters with PZT thickness of up to 0.96 μm. A Report of Invention was filed based upon this microfabrication flow. This process flow, combined with the methodology outlined in Chapter 3, resulted in a US Patent Application (Serial No. 14/032,018).

A complete packaging methodology was developed for the harvesters to overcome challenges involved in testing MEMS devices actuated under a base vibration. The packaging methodology was adapted from various available packaging techniques to allow the direct probing of the microfabricated energy harvesters under experiment. The packaging scheme consisted of custom printed circuit boards and wire bonds to provide the needed mechanical support and electrical connections. Multiple wire bonding methodologies were developed to allow bonding to both platinum and PZT-stack electrodes. The flexibility of the packaging scheme allowed for the reclamation of several overetched energy harvesters. The developed packaging methodology allows for complete packaging of the harvesters without adding any detrimental parasitic capacitance effects.

A complete testing and characterization methodology was developed, including microfabrication, vibration-based, and electrical-based characterization. The characterization of the microfabrication process and performance of individual processes allowed for the diagnosis and troubleshooting of the harvester fabrication process flow. The vibration-based characterization, with the use of a mechanical shaker system and Laser Doppler Vibrometer, allowed for the capture of the velocity profile and frequency response of the harvester in real time. The electrical characterization allowed for the capture of the electrical characteristics of the harvester, including input resistance, optimum load resistance and maximum power transfer.

The vibrational testing of the Class I Harvester verified the initial design methodology of the folded spring based harvester design. The frequency response of the harvesters agreed with the calculated response from the design phase of the harvester. The small deviation between the measured and calculated natural frequencies can be attributed to the variation in material properties from silicon wafer to wafer, the variation in thickness of the wafer affecting the accuracy of the release etch, and the undercut of the sidewalls of the harvester creating a trapezoidal cross section. Once the stiffness reduction begins to act non-linearly due to the undercut, the reduction in natural frequency begins to increase

significantly. Design modifications were required in order to improve the quality of frequency response measurements of the Class I Harvesters. A higher vibration amplitude was required in order to improve both the quality of the frequency response measurements and the magnitude of the electrical measurements. The addition of a proof mass and additional folded spring elements in the Class II Harvesters aided in overcoming these challenges. The presence of a measurable output signal allowed for the extension of the design to the Class II Harvesters. It was clear that the lack of a proof mass in the design of the energy harvester significantly limited the vibration amplitude, natural frequency reduction, and output power.

The full characterization of the Class II Harvesters yielded several important results. First, the released Class II Harvesters did not exhibit any symptoms of fabrication-based residual stress stiffening, such as beam curling, mass rotation, or distortion of the harvester design at rest, confirming the residual stress relaxation of the folded spring-based design.

The numerical studies used to predict the behavior of the harvesters were validated by the vibration-based characterization over a wide range of spring thickness for each design. The calculated mode shapes were qualitatively verified by the initial vibrational characterization. The trends experimental natural frequency data from the entire range of folded spring thicknesses followed the simulated range of expected natural frequencies well. In several designs of harvester, an open etch area-based etch rate deviation caused for some variation in fabricated thickness from design to design on the same wafer. This bias error caused the experimental trend to be offset from the simulated natural frequency/folded spring thickness trends. This variation was not tied to a specific design of harvester, however the open etch area used to define the depth of etch from the backside of the wafer. This effect was seen especially in the harvester designs with large open surface area backside wells. Taking this variation into account, it can be seen that the simulation, given the proper folded spring thickness, is capable of predicting the behavior and natural frequency of the

folded spring energy harvester. The frequency-based simulation undertaken to understand and predict the frequency behavior of the folded spring energy harvesters is valid. The validation of the simulated results suggests that the assumptions made about the behavior of the folded spring structure used in the design methodology of the energy harvesters is valid as well.

With stiffer rotated folded springs, Design D was capable of producing devices from MS2P3, allowing for the natural frequency span of this design to be slightly larger than Design C. This suggests that the rotated folded springs allow for a targeted balance between stability and natural frequency reduction.

The majority of Class II Harvesters were capable of reaching the natural frequency goal of 30-300 Hz. Three of the eleven designs were only partially capable of meeting the 300 Hz requirement. However, these designs do not reach a critical thickness where the harvester becomes unstable, therefore, these designs would be able to meet this target frequency range easily at a reduced spring thickness.

It was shown that the Class II Harvesters are capable of converting the vibration applied to the harvester into electricity. During experimentation, the measured input impedance of the harvester at rest and optimum load resistance applied by the conditioning circuit coincided for the operational, non-shorted energy harvesters. From this observation, it is clear that the harvester is converting strain to electricity. The maximum power output achieved was approximately 690.50 nW of power at a RMS voltage of 153.0 mV and RMS current of 4.32 μA, while operating at its natural frequency of 226.25 Hz at a 9.81 m/s^2 acceleration, with a PZT film of 0.24 μm thickness. Although this power output is not as high as some comparable devices in literature, the power output for the thickness of PZT film used in these harvesters (0.24 μm) was reasonable, producing a comparable energy density of approximately 54 μW/cm^2. With increased PZT thickness, the power generated per harvester will be increased. Additionally, by arranging the individual harvesting elements in an array to

maximize the power output, the overall power output of the harvesters examined in this thesis will increase to levels suitable for *in-situ* harvesting applications.

In summary, this thesis has a number of research contributions and novelties to the field of MEMS-based piezoelectric energy harvesting including the following:

- Using a fixed-fixed folded spring as the mechanical element of the energy harvester. This allows for a reduction of natural frequency of the harvester without the residual stress stiffening issues encountered in natural frequency reduction of cantilever-based systems. This contribution resulted in a journal publication (**Lueke**, Rezaei, Moussa. In review. *Journal of Micromechanics and Microengineering*), several presentations, and a US Patent Application (Serial No. 14/032,018).

- The important design parameters of the fixed-fixed folded spring geometry were identified. The individual length of the folded beam segments that experience bending and the thickness of the folded spring were the most critical parameters. Optimizing these parameters allows for the stiffness of the harvester to be decreased in the folded spring configuration, without residual stresses counteracting the stiffness optimization. This contribution resulted in a journal publication (**Lueke**, Rezaei, Moussa. In review. *Journal of Micromechanics and Microengineering*).

- The optimization of the fixed-fixed folded spring increased the linear stiffness range of the harvester, allowing for predictable dynamics during operation. This contribution resulted in a journal publication (**Lueke**, Rezaei, Moussa. In review. *Journal of Micromechanics and Microengineering*).

- The use of arrays of folded springs in parallel and series configurations allows for balancing of natural frequency and mechanical stability, in order for the energy harvester to be optimized to a variety of applications. This contribution resulted in a journal publication (**Lueke**, Rezaei, Moussa. In review. *Journal of Micromechanics and Microengineering*).

- A robust and universal silicon-based microfabrication procedure was developed. The fabrication flow is capable of fabricating harvesters of any planar design, with or without seismic masses, with multiple piezoelectric materials and related electrode materials. This contribution resulted in four journal publications (**Lueke**, Rezaei, Moussa. In review (2013). *Journal of Micromechanics and Microengineering;* **Lueke**, Rezaei, Moussa. In review (2014). *Journal of Micromechanics and Microengineering;* Rezaei, **Lueke**, Moussa. *Microsystem Technologies,* 2013, 1-25; Rezaei, **Lueke**, Moussa. *Journal of Mechanics Engineering and Automation,* 2013, 3 731-738) and a US Patent Application (Serial No. 14/032,018).

- A research-grade Aqua Regia Etch process and the required equipment were developed to allow for an Aqua Regia etch to pattern platinum for microfabrication purposes. This contribution resulted in a Report of Invention with the University of Alberta.

- A general research-based packaging scheme was developed for energy harvesters that could be adapted to a variety of platinum/PZT/platinum stacked piezoelectric energy harvesters. The packaging scheme does not add any parasitic capacitance or loss effects that would reduce the effectiveness of the harvester. This contribution resulted in three journal publications (**Lueke**, Rezaei, Moussa. In review (2013). *Journal of Micromechanics and Microengineering;* **Lueke**, Rezaei, Moussa. In review (2014). *Journal of Micromechanics and Microengineering;* Rezaei, **Lueke**, Moussa. *Microsystem Technologies* 2013, 1-25) and a technical publication (Benfield, **Lueke**. *CMC Packaging Application Note* 2011).

The mechanical optimization methodology outlined in this thesis was successful in reducing the natural frequency of the piezoelectric energy harvester. This methodology can be applied to any energy harvesting scheme that requires a high out of plane displacement in order to maximize the energy harvested.

8.2   Suggested Future Work

This thesis has adapted a unique structural element, the fixed-fixed folded spring, as an alternative to the typical cantilever-based structural element. This has allowed for the reduction of the natural frequency of the structure significantly, however, the work could be extended in future research projects to further enhance the natural frequency reduction and power output. Possible extensions of this research include, and are not limited to the following:

- Increase of the PZT layer thickness to several micrometers, in order to increase the overall energy harvested per harvesting element. The increased film thickness will cause additional strain to be applied on the surfaces of the PZT film, causing a net increase in power output. Minimize the area of the PZT film to focus the strain applied to the PZT film during actuation.

- The development of active frequency tuning systems that could tune the natural frequency of the harvester by applying a known force to the harvester. This force would pre-stress the harvester, causing a change in stiffness and shift in natural frequency. A shape memory alloy actuator may be useful for the application of this external tuning force. This would allow the specific harvester to be tuned to a specific application *in-situ*.

- The use of a polymeric structural material, instead of silicon, to further drive down the natural frequency of the harvester.

- Further manipulating the geometry and arrangement of the Class II Harvester designs to allow for non-symmetric placement of proof masses. Offsetting proof masses could possibly allow for larger deflections and applied strains to the piezoelectric elements, increasing the effectiveness of torsion-based systems.

- Apply the folded spring methodology to other vibration-based harvesting technologies that require high displacement, low frequency, out-of-plane vibration for maximized energy harvesting. This may include electromagnetic and out-of-plane electrostatic-based harvesting schemes.

Through the mechanical optimization of the frequency-based performance of the piezoelectric energy harvester, it will be possible to facilitate the further development of the energy harvesting in general. In order to develop energy harvesting systems to augment and improve of traditional power schemes for wireless MEMS-based sensors and devices in consumer and industrial applications, the harvesters must be able to convert low frequency ambient vibration into electricity. This work gives an alternative methodology to the currently available methodologies in order to facilitate harvesting from low frequency vibrations.

Introduction

The simulation undertaken in this thesis allowed for an understanding of the mechanical behavior of the folded spring structure in response to various input vibrations. The simulations themselves were undertaken with ANSYS© Multiphysics, using a variety of analysis types, geometries, and element types. Due to the complexity of the geometry of the harvesters studied, it was necessary to utilize the command line input method for ANSYS, since defining the geometry in the code was not trivial. In this appendix, an example input file will be examined in detail.

Example Input File

Each design of harvester had its own specific input file which was used for all types of analysis. The input file for each harvester design only varies in the geometry portion at the beginning of the input file. For each design, the parametric definition of the keypoints used in area generation need to be specifically defined to provide the proper area to extrude. Additionally, every analysis/option used in the code throughout the development of the project is kept in the general code, just deactivated with exclamation marks when appropriate. In the following example input file, the function of each section of the file will be sequentially discussed.

Material Properties and Geometry:

```
/prep7
/com,  Material properties (Si):
/com,
/com, Stiffness, MN/m^2
/com, [c11 c12 c12  0 ]
/com, [c12 c11 c12  0 ]
/com, [c12 c12 c11  0 ]
/com, [ 0  0  0 c44]
/com,
c11= 165.7e9
c12= 63.9e9
```

```
c44= 79.6e9

!Parametric Geometry
A=150e-6
B=1500e-6
C=150e-6

!Element Type
et,1,98,2

!Define Coordinate Systems
!Regular
local,11
!Silicon Material Planes
local,12,,,,,45
local,13,1
! Material 2 = Silicon Anisotropic Elasticity Matrix
tb,ANEL,2,,,0
tbda,1,c11,c12,c12
tbda,7,c11,c12
tbda,12,c11
tbda,16,c44
tbda,19,c44
tbda,21,c44
MP,DENS,2,2328

csys,11

!Do Loop To Increment Thickness
!*do,F,5,70,5
!D is thickness
!D=F*1e-6

!Thickness if not using Do Loop
D=35e-6

!Silicon Folded Spring Footprint
k,1,0,-100e-6
k,2,A,-100e-6
k,3,A,B
k,4,(A+C),B
k,5,(A+C),0
k,6,(2*C+3*A),0
k,7,(2*C+3*A),B
k,8,(3*C+3*A),B
k,9,(3*C+3*A),0
k,10,(4*C+5*A),0
k,11,(4*C+5*A), (B+A+100e-6)
k,12,(4*C+4*A), (B+A+100e-6)
k,29,(4*C+4*A),A
k,30,(3*C+4*A),A
k,31,(3*C+4*A),(B+A)
k,32,(2*C+2*A),(B+A)
k,33,(2*C+2*A),A
k,34,(C+2*A),A
k,35,(C+2*A),(B+A)
```

```
k,36,0,(B+A)

!Silicon Areas
a,1,1,2,3,4,5,6,7,32,33,34,35,36
a,7,8,9,10,11,12,29,30,31,32
aadd,1,2

AGEN, ,all, , , ,100e-6, , , ,1
ARSYM,X,all, , , ,0,0
ARSYM,Y,all, , , ,0,0

Adele,1
Adele,4

!Move Folded Springs and Add Masses
AGEN, ,2, , , 700e-6,-800e-6, , , ,1
AGEN, ,3, , ,-700e-6,800e-6, , , ,1
RECTNG,800E-6,-800E-6,800E-6,-800e-6,

!Offset Areas into Volumes
voffst,2,D
voffst,3,D
voffst,1,500e-6

allsel,all
vglue, all
```

As seen above, the definition of the geometry and material properties is the largest section in the code. The first section defines the constants used in the input file, including the stiffness coefficients of the stiffness matrix and the chosen beam width, beam length, and overlap gap, consistent with the definition used in Figure 3.10. The element type is also defined. It was found that Solid 98 was a suitable element for this analysis. The material properties, such as the anisotropic stiffness matrix of the silicon and the density were defined. Next, the thickness of the folded springs, parameter D, was defined. There are two specific methods that could be used to define the thickness. If the analysis is meant to run once, at a constant thickness, the simple definition of "D=35e-6" could be used to set the thickness to a set value of 35 μm. If the thickness of the folded springs was to be incremented, a "Do Loop" was built into the code to increment the thickness, run the analysis, record the results, increment the thickness, and continue the cycle.

The geometry of the folded springs is then parametrically defined using previously defined constants, A, B, and C. Each keypoint is defined with a simple equation using these three variables. This allows for the geometry to be altered easily and consistently with only altering a few values in the code. This was particularly useful during the OAT sensitivity analysis, where a "Do Loop" could be used to increment one parameter at a time in the geometry. The areas of the folded springs are then constructed from the keypoints. The areas are then translated into the desired spacial location and copied (if need be). The area of the proof mass is then generated. Each area is then offset to produce the required volumes. The volumes are then glued together to create the three dimensional representation of the energy harvester.

Meshing and Boundary Conditions

```
!Full Geometry Mesh and Matprops

!Silicon
VATT,2
esys,12
ESIZE,100e-6,0,
Vmesh,all
allsel,all

!Boundary Conditions

csys,11

Nsel,s,loc,y,(-(B+A+1000e-6))
D,all,ux,0
D,all,uy,0
D,all,uz,0


Nsel,s,loc,y,(B+A+1000e-6)
D,all,ux,0
D,all,uy,0
D,all,uz,0

!Loads if needed

Nsel,s,loc,z,0
Nsel,r,loc,y,0
F,all,Fz,1e-6


!Nsel,s,loc,z,(D+I+J+K+M+N)
!Nsel,r,loc,x,((8*C+9*A)/2)
```

```
!Nsel,r,loc,y,((B+A)/2)
!F,all,FZ,.1

allsel,all
```

This section of the input file deals specifically with defining the material properties previously defined to the model, meshing, and applying boundary conditions and loads. First, the volume created in the previous section of the input file has material properties applied to it. Next the volume is meshed. To ensure a suitable mesh density, a convergence analysis should be undertaken to determine the appropriate mesh density to provide a valid solution.

After the volume is meshed, the fixed-fixed boundary conditions are applied to the roots of the folded spring. Depending on the analysis that is undertaken a load may or may not be needed. For a modal analysis, a specific load is not required. For a harmonic or transient analysis, a load must be applied. In the input file above, two methods of applying the required load are defined. The first is applying a point load at the node closest to the origin of the coordinate system, which coincides with the middle of the top surface of the proof mass. The second method selects the nodes in a given XYZ defined area according to the ranges defined. In the case in the input file, also shown in Figure 1, for demonstration purposes, the load is applied along the midline of the proof mass. Care must be taken while applying the nodal force in this manner to ensure the proper total load is applied to the structure.
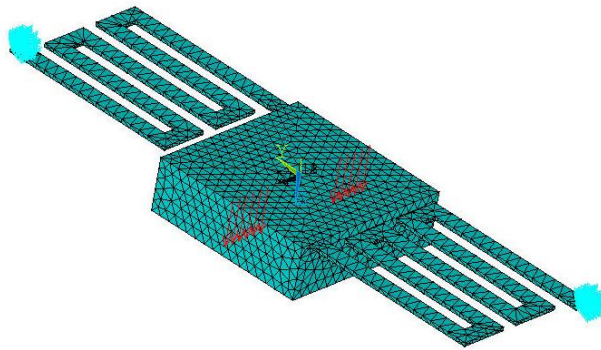
Figure 1 – Meshed Design A Folded Spring Energy Harvester. Boundary conditions are shown as blue triangles at either terminus of folded beam. Applied load shown as downward red arrows along midline of proof mass.

Analysis Types

```
!Modal Analysis
!/STATUS,SOLU
!/SOLUTION
!ANTYPE,MODAL  !!
!MSAVE,0
!*
!MODOPT,LANB,5
!EQSLV,SPAR
!MXPAND,5, , ,0
!LUMPM,0
!PSTRES,0

Solve

!Harmonic Analysis
Allsel,all
/SOLU
ANTYPE,HARMIC
HROPT,FULL
HROUT,OFF
OUTPR,BASIC,1
NSUBST,50
HARFRQ,,1000
KBC,1
SOLVE
FINISH
```

In the simulation work undertaken in this thesis, there were two main analysis types used. As shown in the above section of the input file, the first analysis type was a modal analysis. This specific analysis uses a Lanczos Algorithm to extract the first 5 natural frequencies and mode shapes. The second

analysis type used was a harmonic analysis. This allowed for a direct simulation of the testing method used in the thesis to experimentally determine the natural frequencies of the fabricated harvesters using the Laser Doppler Vibrometer. The applied load was varied in the frequency domain according to the bounds and step size defined in the input file. In the input file, exclamation marks were used to enable/disable specific analyses in order to allow for batch processing.

Post Processing

```
! Extract Displacement From Specific Point at each Frequency Step and Write to Txt File
when using Do Loop
/post26
Nsel,s,loc,z,0
Nsel,r,loc,y,-20e-6,20e-6
Nsel,r,loc,x,-20e-6,20e-6
*get,nresult,node,0,num,max,
Nsol,2,nresult,u,z
STORE,MERGE
*GET,size,VARI,,NSETS
*DIM,UZ2,ARRAY,size,2,1, , ,

VGET,UZ2(1,1),1, ,0
VGET,UZ2(1,2),2, ,0
*CFOPEN,CaseB%D%,txt
*VWRITE,UZ2(1,1),UZ2(1,2)
(F8.2,T10,E18.6,T10)

*CFCLOSE

!Reset Model for next Do Loop
!/prep7
!Vclear,all
!Vdele,all
!Adele,all
!Ldele,all
!Kdele,all

!*enddo
```

The final portion of the input file dealt specifically with post processing of the results for batch processing with "Do Loops". If the goal was to simulate the harvester in the GUI environment, this portion of the code would not be used. This portion of the code allows for the capture of a specific value (in this case a displacement in the Z direction) and export into a text file to for later analysis.

The location of the specific nodal result of interest must be known before running the input file in batch mode. The routine will capture the nodal result and write it to a specifically named text file. To allow for the next iteration of the "Do Loop", the model is completely cleared and then the loop incremented.

Overview and Purpose

The purpose of the Aqua Regia Etch System (ARES) is to allow the safe and repeatable etching of Titanium and Platinum films for microfabrication purposes. The etch process involves a heated 3:1 mixture of hydrochloric and nitric acids etching exposed Titanium and Platinum films. A by-product of this microfabrication process is chlorine gas, which can be a safety hazard. Therefore, it is necessary to properly handle and dispose the chlorine gas produced from this reaction. The exhaust gasses are bubbled through a gas wash bottle in order to dissolve the hazardous chlorine gas into a weak hydrochloric acid. The etch system is completely self contained, having its own inlets for deionized water for dilution/quenching, power for hotplate, and vacuum for exhaust removal; and outlets for aspirated waste solution and vacuum exhaust. This system allows for the controlled, repeatable, cost effective, and safe etching of Platinum and Titanium in for microfabrication purposes in a laboratory environment, without placing those working in the laboratory at risk.
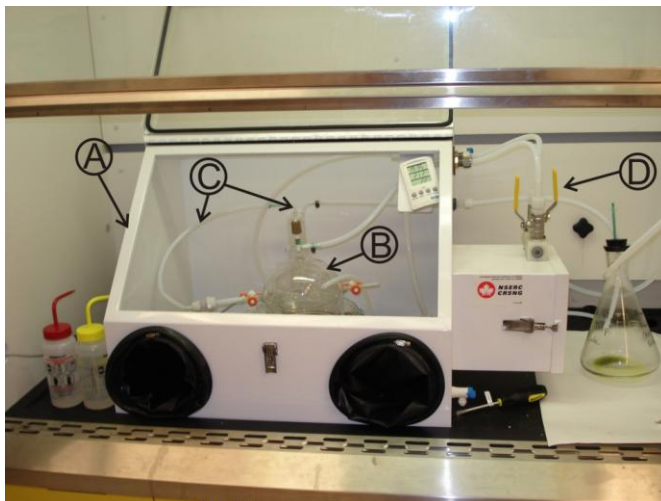
Major Subsystems of the ARES:

Figure 1 – ARES with Labelled Subsystems (A: Glovebox, B: Reaction Chamber,
C: Exhaust Handling System, D: Aspiration/Rinse System)

The ARES, as shown above in Figure 1, is composed of four major subsystems: the glovebox (A), the reaction chamber (B), the exhaust handling system (C), and the aspiration/rinse system (D). These systems all operate concurrently in order to etch Platinum and Titanium films.

A. Glovebox

As can be seen in the above figure, the whole reaction system is contained within a glovebox. The ARES can operate independently of fumehood, if properly vented with vacuum. In addition, the glovebox gives an added layer of protection to the user of the system. The glovebox allows for the use of chemically resistant black butyl gloves while operating the ARES. The gloves are fixed to the port holes on the glovebox using a suitably large pipe clamp. Black butyl is highly chemical resistant, and will protect the operator from accidental exposure to a small volume of liquid Aqua Regia.
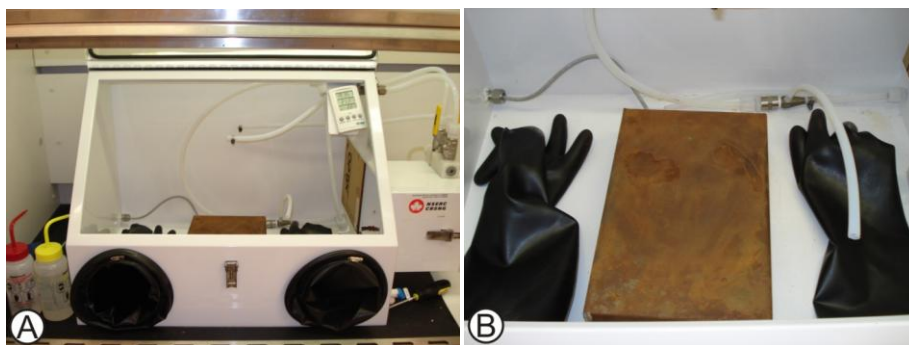
Figure 2 – Interior of the Glovebox, Showing the Gloves and Hotplate (Reaction Chamber/Wash Bottle Removed)

A hotplate is used to heat the chemical solution in the reaction chamber. Since the potential for some leakage from the reaction chamber exists during etching, a folded sheet steel cowl is used to protect the hotplate. Any material with reasonable thermal conductivity would be suitable. However, with the addition of a metal cowl to the system, the hot plate set point temperature should be calibrated to apply the appropriate reaction temperature to the glassware previous to processing. Power is provided to the hotplate inside via a cord threaded through a Swagelok fitting on the left side of the glovebox as can be seen in Figure 2A. In addition, this cord passes through a protective splash guard that rests on top of the hotplate, as well as the access port of the fumehood. The cord is plugged into the receptacle on the front of the fumehood when the hot plate is required.
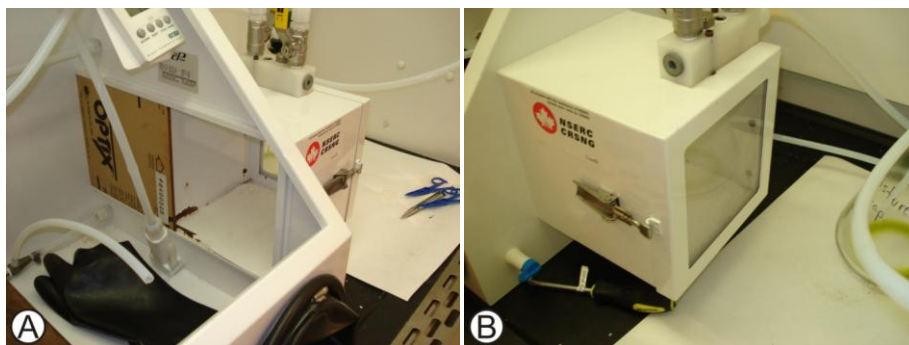

Figure 3 – Glovebox Passthrough

The glovebox also has a very useful pass-through load lock. In the case of the ARES, this load lock is useful for storing the chemicals (before processing) and empty glassware (after processing) preventing the reactants from mixing outside of the reaction chamber. The location of the load lock is very convenient for this purpose while manipulating the etch rig with the black butyl gloves.

B. Reaction Chamber

Figure 4 – Reaction Chamber on Hotplate, Connected and Ready for Use

The Aqua Regia etch takes place in the reaction chamber of the ARES. The reaction chamber itself consists of three pieces of glassware, nested to ensure that a vacuum induced airflow draws the produced chlorine gas off of the inner most piece of glassware, as shown below in Figure 5. The reaction between the Aqua Regia and the Titanium and Platinum takes place inside the glassware arrangement shown below:
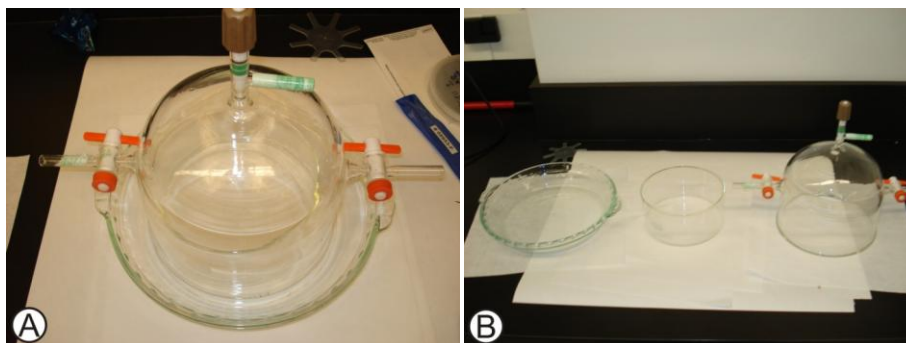

Figure 5 – Nested Glassware Reaction Chamber

The inner most glassware is a 1.75 L Pyrex crystallization dish. This crystallization dish is large enough to accommodate a single 6" silicon wafer or a 5" square photolithography mask. The second piece of glassware, which is placed over top of the crystallization dish, is a custom-made bell jar. The bell jar is slightly wider than the crystallization dish. The bell jar has been customized to allow for vacuum and deionized water inlets. During operation, air and expelled chlorine gas is drawn across the top of the reaction beaker and bubbled through a gas scrubber (behind the bell jar). The orange stopcock valves are used to throttle the flow rates of air inside the bell jar. Usually the valves are left open, but if need be, the flow can be manipulated. The brown pin valve at the top of the bell jar controls the inlet deionized water, which will quench the reaction when required. The top valve is connected to the manifold of the rinse/aspiration system via Teflon tube and a Swagelok connection. The outer most glassware is a circular Pyrex dish that acts as the catch-all for water drips during quenching. During processing, the whole nested glassware setup is heated by the hotplate below.
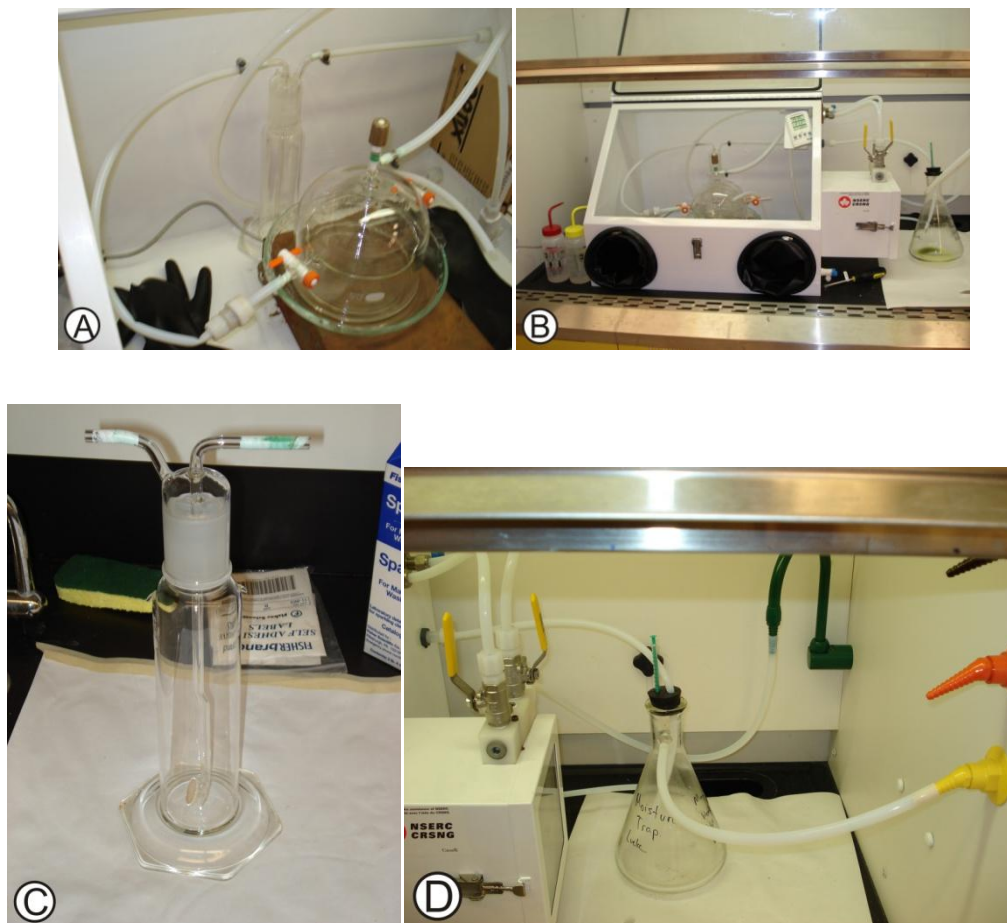
C. Exhaust System

Figure 6 – Exhaust System

The exhaust system of the ARES dissolves the chlorine gas exhaust from the reaction chamber using a gas wash bottle. The system as a whole is shown in Figure 6B. The bell jar of the reaction chamber is connected to the gas wash bottle by Teflon tubing and pipe clamps as shown above in Figure 6A. In the gas wash bottle, as shown in Figure 6C, the exhaust chlorine gas is bubbled through deionized water, producing a weak hydrochloric acid. The exhaust of the gas wash bottle is then routed to the outside of the glovebox through a stainless steel Swagelok connection to a vacuum flask using Teflon tubing. This vacuum flask, as shown in Figure 6D, acts as a moisture trap to prevent liquids to be drawn into the house vacuum. The vacuum flask is connected to house vacuum with Teflon

tubing. The flow rate of the exhaust system is controlled by the amount of suction provided by the house vacuum, and the throttling stopcock valves on the bell jar.
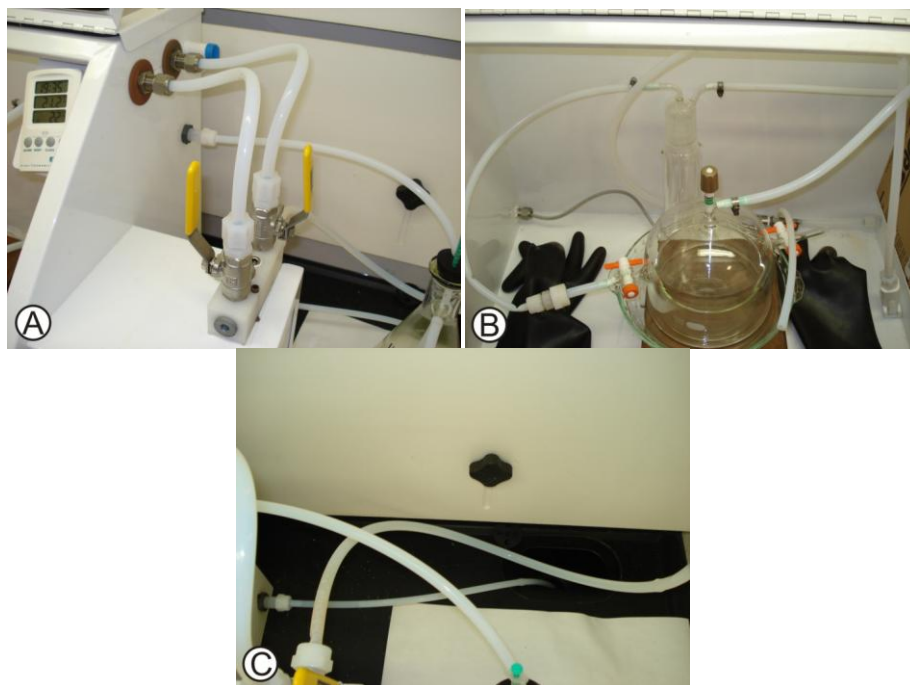
D. Aspiration/Rinse System

Figure 7 – Aspiration/Rinsing System

The aspiration/rinse system of the ARES has two separate loops controlled by a Teflon manifold with two ball valves, shown in Figure 7A. The rinse loop of the system is controlled by the nearest valve in Figure 7A, and can be seen in Figure 7B connecting the manifold to the top pin valve of the bell jar through a Swagelok connection. This loop allows for the quenching/rinsing of the Aqua Regia solution without having to lift/move the bell jar, with simply opening two valves in succession. The aspiration loop of the system is controlled by the back valve of the manifold in Figure 7A.The line is passed through into the glovebox using a Swagelok connection. A Teflon "T" intersection allows for a Teflon rinse gun, as seen in Figure 7B, to be used to additionally rinse the glassware if required. The Teflon "T" intersection is then connected to a stainless steel 10:1 aspirator using Teflon tubing. The aspirator is essentially a venturi that creates

suction on a secondary line (shown in Figure 7B) which is used to remove and dissolve the quenched Aqua Regia from the reaction chamber. The waste solution is then removed from the system through another Swagelok connection, and then is routed to the drain, as shown in Figure 7C. The aspiration loop can be open the whole time the ARES is in use, the rinse loop should be closed until quenching is required

Capabilities of the Aqua Regia Etch System:

1. The ARES system can provide repeatable etching of Platinum/Titanium films using a heated solution of Aqua Regia with an etch rate of approximately 12-15 nm/min, in comparison to 3.6 nm/min reported by Williams *et al.* [1].

2. The ARES system can provide a heated Aqua Regia Etch, which increases the etch rate of the reaction. Heating the solution increases the formation of chlorine gas. The ARES system is specifically designed to handle these increased gasses, allowing for increased etch rates.

3. The ARES system allows for quick and safe disposal of the Aqua Regia solution after processing (3:1 Hydrochloric to Nitric Acids). The solution can be diluted up to 17.5:1 (depending on amount of Aqua Regia used) in the reaction chamber with no "hands-on" interaction with the solution. Additionally, while being aspirated, the solution is diluted an additional 10:1 (current aspirator). This brings the dilution to approximately 175:1. The aspirator dilution ratio can be altered by using a different aspirator.

Personal Protection Equipment Required:

Stage 1: Equipment Preparation:

- Nitrile Gloves

- Lab Coat

- Safety Glasses

Stage 2: Chemical Preparation:

- Nitrile Gloves

- Lab Coat

- Face Shield

- Chemical Apron

- Safety Glasses

- Chlorine Exposure Tag

Stage 3: Etching:

- Nitrile Gloves

- Lab Coat

- Safety Glasses

- Black Butyl Gloves (attached to glovebox)

- Chlorine Exposure Tag

Stage 4: Cleaning/Tear Down:

- Nitrile Gloves

- Lab Coat

- Safety Glasses

Operational Procedure:

Stage 1: Equipment Preparation

- Ensure that the glassware that is being used is clean and dry.

- Ensure that the gas wash bottle is approximately 2/3rd full with clean deionized water, and that the proper connections to the wash bottle are made. The wash bottle is meant for "one-way" operation, so ensure that the vacuum line vacuums air into the moisture trap, not liquid. Ensure that the moisture trap is connected to the gas wash bottle; such that any water droplets do not make it into the vacuum system.

- Check that the connections to the bell jar are made correctly. The deionized water quench line should be connected to the top of the bell jar, while the exhaust line to the gas wash bottle should be connected to one outlet of the bell jar. Keep both orange stopcock valves open to promote airflow, and the brown pin valve closed until the quenching needs to take place.

- Ensure that the inlet to the water manifold of the ARES is connected to the DI water connection. Ensure that the Aspirator outlet hose is securely placed into the sink.

- Ensure that the hotplate is set to 275 C, and that it is turned on. Unplug the hotplate. You will not be able to turn the hotplate on by pressing the on button when everything is in place. The 275 C set point on the hot plate is necessary to achieve approximately 90 C inside the innermost Pyrex dish. This can be calibrated by heating water in the innermost Pyrex dish and measuring the water temperature.

- Turn on vacuum, about 1/4th a turn. The goal is to get achieve a vigorous bubbling in the wash bottle, while not vacuuming up liquid into the moisture trap. Check suction/airflow through bell jar.

- Close the quenching valve on the DI water manifold. Open the aspiration valve on the DI water manifold. Turn on deionized water, fully. The

system is fairly low pressure, and connections will hold. Water should flow all the way through the system, and into the fumehood sink.

- Check that the aspirator has suction. If the aspirator has no suction, remove the aspirator hose and check for calcium/scale blockage in the inlet of the aspirator.

- Turn water off.

Stage 2: Chemical Preparation

- Label 2 beakers, one beaker for Nitric Acid, one beaker for Hydrochloric Acid. Measure out 100 mL of hydrochloric acid, and 50 mL of nitric acid. Follow the appropriate precautions for pouring/handling chemicals.

- Place the beakers inside the load lock of the glove box, such that they are in easy reach of the butyl gloves.

Stage 3: Etching

- With the butyl gloves, lift the bell jar gently, pour hydrochloric acid into crystallization dish (inner most beaker where reaction takes place), then pour nitric acid into solution. The solution will be clear/slightly yellow.

- Turn on the hot plate by plugging it in. Heating the solution allows for increased etch rates, selectivity, and control of the etch process.

- Replace bell jar; leave the solution to age/heat/mix for 10 minutes. Etching will not take place well without aging the solution. The solution should be a deep gold at this point with slow bubbling taking place.

- After the solution ages, insert the wafer into the Aqua Regia. Agitate the solution to immerse the wafer into the solution. The wafer will float on the surface of the etchant otherwise.

- Once etching begins, it is necessary to agitate the solution. Bubbles will form on the platinum surface of the wafer, which prevents further etching taking place. This will cause spotty etching if allowed to stay on the surface of the wafer. Therefore constant agitation is required to allow for consistent etching.

- The etch will take place at 12-15 nm/min. For the films we typically etch, it will take between 19-25 minutes. Once etching is complete, open the brown pin valve on the top of the bell jar. Turn on the quench DI water. Fill the beaker to the top to quench/stop the reaction. This will dilute the solution at least 1:10.

- Turn on the DI water fully. Turn on the aspirator valve on the DI water manifold. Lift the bell jar and insert the aspirator tube into the solution. This will further dilute the solution 1:12 and dispose the solution into the fumehood sink. Once complete, fill and aspirate again.

- Unplug the hot plate.

- Turn off the DI water.

- Turn off the vacuum.

- Disconnect the water and vacuum connections to the ARES.

Stage 4: Cleaning/Tear Down

- Disconnect all connections to the bell jar.

- Move the bell jar and nested glassware to the laboratory sink. Remove the wafer, rinse wafer with DI and set aside.

- Clean glassware thoroughly. Hang/stow glassware to dry.

- Remove remaining connection to gas scrubber bottle. Aspirate contents of the gas washer bottle.

- Leave gas washer bottle to dry inside glove box.

Additional Notes:

- CMOS grade or better, full strength chemicals are required for this process. Lower quality/concentration chemicals will cause slower and less selective etch rates. Increased selectivity causes easier patterning of the target films.
- All manipulation of the chemical process occurs at least through one layer of protection (nested glassware, etc). Additionally, the controls of the ARES allow for the easy control of the etch process, without having to directly interact with the Aqua Regia solution.

References:

1. Williams, K.R.; Gupta, K.; Wasilik, M. Etch rates for micromachining processing - Part II. *Journal of Microelectromechanical Systems* **2003**, *12*, 761-778.